National Library of Canada
Bibliothèque nationale du Canada

Canadian Theses Service
Service des thèses canadiennes

Ottawa, Canada
K1A 0N4

NOTICE

The quality of this microform is heavily dependent upon the quality of the original thesis submitted for microfilming. Every effort has been made to ensure the highest quality of reproduction possible.

If pages are missing, contact the university which granted the degree.

Some pages may have indistinct print especially if the original pages were typed with a poor typewriter ribbon or if the university sent us an inferior photocopy.

Previously copyrighted materials (journal articles, published tests, etc.) are not filmed.

Reproduction in full or in part of this microform is governed by the Canadian Copyright Act, R.S.C. 1970, c. C-30.

AVIS

La qualité de cette microforme dépend grandement de la qualité de la thèse soumise au microfilmage. Nous avons tout fait pour assurer une qualité supérieure de reproduction.

S'il manque des pages, veuillez communiquer avec l'université qui a conféré le grade.

La qualité d'impression de certaines pages peut laisser à désirer, surtout si les pages originales ont été dactylographiées à l'aide d'un ruban usé ou si l'université nous a fait parvenir une photocopie de qualité inférieure.

Les documents qui font déjà l'objet d'un droit d'auteur (articles de revue, tests publiés, etc.) ne sont pas microfilmés.

La reproduction, même partielle, de cette microforme est soumise à la Loi canadienne sur le droit d'auteur, SRC 1970, c. C-30.

NL-339 (r. 88/04)

Canada

THE UNIVERSITY OF ALBERTA

ION-MOLECULE REACTION STUDIES OF: METHYL CATION AFFINITIES AND HYDROGEN BONDING IN PROTONATED IONS

©

BY

GORDON ROBERT NICOL

A THESIS
SUBMITTED TO THE FACULTY OF GRADUATE STUDIES AND RESEARCH
IN PARTIAL FULFILMENT OF THE REQUIREMENTS FOR THE DEGREE
OF DOCTOR OF PHILOSOPHY

DEPARTMENT OF CHEMISTRY
EDMONTON ALBERTA
FALL 1988

Permission has been granted to the National Library of Canada to microfilm this thesis and to lend or sell copies of the film.

The author (copyright owner) has reserved other publication rights, and neither the thesis nor extensive extracts from it may be printed or otherwise reproduced without his/her written permission.

L'autorisation a été accordée à la Bibliothèque nationale du Canada de microfilmer cette thèse et de prêter ou de vendre des exemplaires du film.

L'auteur (titulaire du droit d'auteur) se réserve les autres droits de publication; ni la thèse ni de longs extraits de celle-ci ne doivent être imprimés ou autrement reproduits sans son autorisation écrite.

ISBN 0-315-45454-7

THE UNIVERSITY OF ALBERTA

RELEASE FORM

NAME OF AUTHOR Gordon Robert Nicol

TITLE OF THESIS

Ion-Molecule Reaction Studies of Methyl Cation Affinities and
Hydrogen Bonding in Protonated Ions .

DEGREE FOR WHICH THESIS WAS PRESENTED DOCTOR OF PHILOSOPHY

YEAR THIS DEGREE WAS GRANTED FALL 1988

Permission is hereby granted to THE UNIVERSITY OF ALBERTA LIBRARY to reproduce single copies of this thesis and to lend or sell copies for private, scholarly or scientific research purposes only.

The author reserves other publication rights, and neither the thesis nor extensive extracts from it may be printed or otherwise reproduced without the authors written permission.

(SIGNED) ....Gordon Nicol

PERMANENT ADDRESS:

P.O. Box 165
Tide Head, NB
E0K 1K0

EDMONTON, ALBERTA

(FALL 1988)

THE UNIVERSITY OF ALBERTA

FACULTY OF GRADUATE STUDIES AND RESEARCH

The undersigned certify that they have read, and recommend to the Faculty of Graduate Studies and Research, for acceptance, a thesis entitled ION-MOLECULE STUDIES of METHYL CATION AFFINITIES AND HYDROGEN BONDING IN PROTONATED IONS. submitted by GORDON ROBERT NICOL in partial fulfilment of the requirements for the degree of DOCTOR OF PHILOSOPHY.

P. Kebarle
Supervisor

Loren G. Hepler

H B Dunford

Gary Horlick

External Examiner

Date Oct 13. 88

ABSTRACT

The extent of proton transfer from $H_3O^+(H_2O)_h$ to compounds B was studied with a pulsed electron high pressure mass spectrometer. The sensitivity of analytes B in an atmospheric pressure ionization mass spectrometer is porportional to the extent of proton transfer reaction $H_3O^+(H_2O)_h + B = BH^+(H_2O)_b + (h-b+1) H_2O$. The analytes can be divided into three groups: 1) bases with gas-phase basicities (GB) greater than 200 kcal/mol, mostly nitrogen bases, have high and relatively uniform sensitivities and the sensitivity is dependant on the kinetics of the proton transfer reaction. 2) bases with GB less than 200 kcal/mol, mostly oxygen bases, have sensitivities that increase with increasing GB. These bases were found to reach proton transfer equilibria with the water hydrates and their sensitivity was dependant on the equilibrium constant. 3) The third group consists mostly of carbon bases which show a very low sensitivity with respect to their GB. This is due mainly to the low stability of the $BH^+(H_2O)_b$ hydrates.

Symmetric hydrogen bond strengths were measured for HCl, HBr, MeCl and MeBr and are compared to hydrogen bond strengths of other heteroatoms. The trend of increasing hydrogen bond strength with electronegativity was observed. With poly functional compounds there is the possibility of internal hydrogen bonding. The thermodynamics of inter- as well as the intra-molecular hydrogen bonding in α,ω-dialcohols were studied. The ΔH° and ΔS° for the formation of the proton bound dimer of the α,ω-diacohols indicated the formation of a second ring.

Methyl cation affinities (MCA) were measured for several bases B. The relative values were anchored to the value for the $MCA(N_2)$. The MCA(B) follow in general the proton affinities. The rate constants for the methyl cation transfer were measured and were found to be equal to the ADO collision rates constants at large exothermicity and decreased below collision rates at low exothermicity.

The electron affinity (EA) of C_6F_6 was determined to be 14.8 ± 2.5 kcal/mol. The reaction between $C_6F_6^-$ and O_2 was also studied. The rate constant was found to be 8.7 x10^{-11} molec^{-1} cm^3 s^{-1} at 70C. At temperatures greater than 150C electron detachment from $C_6F_6^-$ occurred. From the temperature dependance of the rate of electron detachment an EA of 15.6 ± 2.6 kcal/mol was estimated.

ACKNOWLEDGEMENTS

I wish to acknowledge the time and effort from Dr. Kebarle during the five years of my studies here. His patience and advice have been greatly appreciated.

I would like to thank the members of the glass blowing, electronics, and the machine shop for their help during my stay. Especially Hubert and Henry, without whose help I would have had many more headaches.

I would also like to thank the members of the group and friend in the department for their support and discussions. Thanks also go to Milan for help with the word processing program. Special thanks to my wife whose patience and support, especially during the last year, was necessary in order to keep my sanity.

TABLE OF CONTENTS

CHAPTER . . . . PAGE

1. Introduction to Ion-Molecule Reactions 1

    1.1 Introduction 1

    1.2 Types of Ion-Molecule Reactions 2

    1.3 Ion-Molecule Collision Theory 8

    1.4 The Present Study 18

2. Experimental 19

    2.1 General 19

    2.2 Overall Description of the Apparatus 20

    2.3 Gas Handling Plant 22

    2.4 Electron Gun 25

        2.4a Electron Gun for the Magnetic Sector Mass Spectrometer 25

        2.4b Electron Gun for Quadrupole Mass Spectrometer 31

    2.5 High Pressure Ion Source 33

    2.6a Ion Detection and Data Storage and Handling 36

    2.6b Mass Analysis 37

    2.7 Ion Sampling 38

    2.8 Experimental Procedure 40

3. Kinetics and Thermodynamics of the Protonation Reaction: $H_30^+(H_2O)_h$

    $+ B = BH^+(H_2O)_b + (h-b+1) H_2O$ 42

    3.1 Introduction 42

    3.2 Experimental 45

    3.3 Results and Discussion 46

        3.3a Factors Responsible for the Different Proton Transfer . . . .

        Efficiencies from $H_3O^+(H_2O)_h$ to Compounds B 46

3.3b Thermodynamics of Proton Transfer 59

3.3c Kinetics of the Proton Transfer to Nitrogen, Oxygen and Carbon Bases 69

3.3d Kinetics of Proton Transfer, $AH^+ B = BH^+ + A$, to Carbon Bases B 77

4. Hydrogen Bond Strength of HCl, HBr and MeCl, MeBr 88

4.1 Introduction 88

4.2 Experimental 90

4.3 Results and Discussion 92

5. Hydrogen Bonding in α,ω-dialcohols 110

5.1 Introduction 110

5.2 Experimental 111

5.3 Results and Discussion 112

5.3a Protonation of a,w-dialcohols 112

5.3b Proton Bound Dimer of α,ω-dialcohols 126

6. Methyl Cation Affinities 131

6.1 Introduction 131

6.2 Experimental 133

6.3 Results and Discussion 134

6.3a Rate Constants for Me^+ Transfer Reactions from Me_2F^+ and Me_2Cl^+ to Bases B 147

6.3b Thermochemical Data on Me^+ affinities 155

6.3c Relationships Between Proton and Methyl Cation Affinities 160

6.3d Unique Features of Individual Methyl Cation Affinities 167

7. The Electron Affinity of Perfluorobenzene, C_6F_6, and the Reaction of

$C_6F_6^-$ with O_2 170
7.1 Introduction 170
7.2 Experimental 170
7.3 Results and Discussion 171
7.3a Electron affinity of C_6F_6 171
7.3b Reaction of $C_6F_6^-$ with O_2 175
Appendix A 192
A.1 MCA program for the Analysis of Data from the EG&G MCS-913 Multi Channel Scaler 192
A.1a Main Menu A 194
A.1b Main Menu B 195
A.2 Information on Specific 199
A.2a F:6 to get Profile Information 199
A.2b How to Plot Profiles 201
A.2c How to Normalize Ion Profiles 203
A.2d How to get Profile Intensity Ratios 205
A.2e How to Print Ion Profiles 206
A.3 Functions available for the analysis of Ion Profiles 207
A.4 Help Menus 211
A.5 Programs for calculations not available in the MCA Program 211
References 213

LIST OF FIGURES

FIGURE . . . . PAGE
1.1 Schematic representation of an ion-molecule collision system 9
1.2 Plot of V_{eff} against r for the $[N_2]^+/[N_2]$ ion-molecule system 11
1.3 Variation of the ion trajectory as a function of the impact parameter, b 13
1.4 Plot of the dipole locking constant, c, against $u_D/\alpha^{1/2}$ for temperatures between 150 and 650K 17
2.1 Block diagram of Pulsed High Pressure Mass Spectrometer 21
2.2 Schematic diagram of the gas handling plant 23
2.3 Schematic diagram PHPMS Apparatus with 90° Magnetic Sector 26
2.4 Pulsing sequence with typical voltages and durations 30
2.5 Schematic diagram of the pulsed electron gun for the quadrupole mass spectrometer 32
2.6 Schematic diagram of the low pressure ion scource for the quadrupole mass spectrometer 35
2.7 Mass calibration curves for quadrupole mass spectrometer 39
3.1 Sensitivity, relative to pyridine, in APCI source for analytes B as a function of gas phase basicity, GB(B), at room temperature 47
3.2. Typical time dependence of kinetic controlled ions 51
3.3 Rate constant determination for the proton transfer: $H_3O^+(H_20)_h + B = BH^+(H_2O)_b + h\text{-}b\text{+}1\ H_2O$ 52
3.4 Typical time dependence of the thermodynamically controlled ions 55
3.5 Typical time dependence of the relative intensities for the low sensitivity compounds 57
3.6 Observed time dependence for B = furan at 198C 58

3.7 van't Hoff plots for n-1,n equilibria of hydration: $BH^+(H_2O)_{n-1} + H_2O = BH^+(H_20)_n$, for B = pyrrole, furan and thiophene 62

3.8 a) This figure shows the protonation site for pyrrole, furan and thiophene being the a carbon and not the heteroatom. b) shows the different resonance structures for $pyrroleH^+$ 64

3.9 A plot of the hydration energy of protonated B as a function gas phase proton affinity (PA(B)) 65

3.10 Plot of R_{eq}, an experimentally measure of the extent of reaction $H_3O^+(H_2O)_h + B = BH^+(H_2O)_b + (h-b+1)\ H_2O$, as a function of the gas phase basicity. 67

3.11 A comparison of experimentally determined R_{eq} from PHPMS and relative sensitivity ($H_2O = 1$) in the APCI source for room temperature and 1 torr water pressure 68

3.12 Rate constant determination for the reaction of individual protonated water clusters 72

3.13 Rate constant determinations for the reaction: $H_3O^+(H_20)_h$ + Pyrrole = $PyrroleH^+(H_2O)_b + h-p+1\ H_2O$ 76

3.14 Plot of experimentally determined rate constants for the reaction $H_3O^+(H_20)_h$ + Pyrrole = $PyrroleH^+(H_2O)_p + h-p+1\ H_2O$ against rate constants calculated assuming that for $h < 3$, $k = k_{ADO}$, for $h > 3$, $k = 0$ and for $h = 3$, $k = 0.4\ k_{ADO}$ 78

3.15 Rate constant determination for the proton transfer: $AH^+ + B = BH^+ + A$ 83

3.16 Plot of rate constant for the proton transfer: $AH^+ + B = BH^+ + A$ versus ΔG^o_{28} 84

3.17 Double minimum reaction coordinate for proton transfer reaction

3.23. 86

4.1 Typical plot of the ion intensities as a function of time for Scheme 2 with X = Cl 93

4.2 Typical plot of the ion intensities as a function of time for scheme 2 with X = Br 94

4.3 Van't Hoff plots for the reactions in Scheme 2 that were measured directly for X = Cl 95

4.4 van't Hoff plots for the reactions in Scheme 2 that were measured directly for X = Br 96

4.5 Typical plot of the ion intensities for the reaction: $HClH^+ + HCl = (HCl)_2H^+$ 103

4.6 Typical plot of the ion intensities for the reaction: $HBrH^+ + HBr = (HBr)_2H^+$ 104

4.7 Van't Hoff plot for the reaction: $HClH^+ + HCl = (HCl)_2H^+$ 105

4.8 Van't Hoff plot for the reaction: $HBrH^+ + HBr = (HBr)_2H^+$ 106

4.9 Plot of the equilibrium constant for reaction: $HBrH^+ + HBr = (HBr)_2H^+$, versus the partial pressure of HBr at several different temperatures 107

4.10 A plot of the average hydrogen bond strength for symmetrical proton bound dimers versus the electronegativity of the heteroatom involved 109

5.1 Mass spectrum of 1,8-octanediol 113

5.2 The time dependance for the observed ion intensities for the conditions: CH_4 = 3 torr, $C_6H_5CH_3$ = 3.8 mtorr, $C_6H_5OCH_3$ = 3.75 mtorr, 1,8-octanediol = 0.75 mtorr, Temp 478K 114

5.3 Temperature dependance of the equilibrium constants for the reaction:

$BH^+ + HO(CH_2)_nOH = HO(CH_2)_nOHH^+ + B$, where n=4 115

5.4 Temperature dependance of the equilibrium constants for the reaction:
$BH^+ + HO(CH_2)_nOH = HO(CH_2)_nOHH^+ + B$, where n = 6 116

5.5 Temperature dependance of the equilibrium constants for the reaction:
$BH^+ + HO(CH_2)_nOH = HO(CH_2)_nOHH^+ + B$, where n = 8 117

5.6 Temperature dependance of the equilibrium constants for the reaction:
$HO(CH_2)_nOHH^+ + B = BH^+ + HO(CH_2)_nOH$, where n = 10 118

5.7 A plot of the entropy change for cyclization against the
chain length 124

5.8 The temperature dependance of the equilibrium for the proton bound
dimer of $HO(CH_2)_nOH$ where n = 4, 6 and 8 127

6.1 Relative ion intensity time dependance after the electron pulse 135

6.2 At a CH_3F pressure which is 10 times higher than that used in Figure
6.1, $CH_3FCH_3^+$ and $CH_3N_2^+$ reach an equilibrium rapidly 137

6.3 Ion intensities observed with N_2 = 3.5 torr, CH_3F = 33 mtorr,
$(CF_3)_2CO$ = 11 mtorr, T = 400K 138

6.4 Example of a run where $CH_3FCH_3^+$, produced rapidly by reactions 6.3-
6.9 see Figure 6.1 and text, is used to transfer Me^+ to two bases:
CH_3Cl and SO_2Cl_2 which then engage in Me^+ transfer equilibria 140

6.5 The intensities of the water clusters formed when the cold trap
is not used 143

6.6 The mass spectrum for the run in Figure 6.4b 145

6.7 Free energy changes ΔG°_2 from equilibrium constants K_2 for reaction
6.2: $B'CH_3^+ + B = B' + CH_3B^+$ 146

6.8 Ion intensity time dependance in a run used to determine rate constant
k for the reaction: $CH_3FCH_3^+ + CH_3Cl = CH_3F + CH_3ClCH_3^+$ 148

6.9 Gas phase reaction coordinate for cationic S_N2 reaction 6.2 involving Me^+ transfer 151

6.10 Plot of proton affinity PA(B) against methyl cation affinity MCA(B) for bases of Table 6.3 161

6.11 Plot of PA(B) against MCA(B) including bases from Figure 6.10 and bases XH whose MCA(XH) can be evaluated from PA(CH_3X) see equation 6.27 163

6.12 Plot of PA(CH_3X) - PA(HX) against PA(HX) for X groups shown 165

6.13 Plot of PA(B) - MCA(B) against PA(B) reaches a constant value at high PA(B) 166

7.1 The time dependance of the ion intensities observed after a short (20 μs) electron pulse 172

7.2 Summary of ΔG°_1 determinations with the five different reference compounds B 174

7.3 Mass spectrum of the reaction mixture: CH_4 = 3 torr, C_6F_6 = 19 mtorr, no O_2 was added, Temperature 121C 176

7.4 The time dependance of the ion intensities observed for the conditions: CH_4 = 3 torr, C_6F_6 = 19.3 mtorr, O_2 = 1.68 mtorr, Temp 70C 178

7.5 A plot of the log of the normalized intensities of $C_6F_6^-$ against time for several different O_2 concentrations 180

7.6 A plot of the pseudo first order rate constants for reaction 7.7 against the partial pressure of O_2 181

7.7 A plot of the log of the normalized intensities of C_6F_6 against time for several different C_6F_6 concentrations 182

7.8 A plot of the pseudo first order rate constants for reaction 7.8 against

the partial pressure of C_6F_6 183
7.9 A plot of the intensity of $C_6F_6^-$ against time for several different temperatures 184
7.10 A plot of the pseudo first order rate constant for reaction 7.7 as a function of temperature 186
7.11 A plot of the rate of electron detachment as a function of temperature 187
7.12 Mass spectrum of the reaction mixture: CH_4 = 3 torr, C_6F_5CN = 1.6 mtorr, O_2 = 0.97 mtorr,T = 150C 189
7.13 Time dependance of the observed ion intensities for reaction 7.10 190
A.1 193
A.2 196
A.3 198
A.4 198
A.5 200
A.6 202
A.7 202
A.8 202
A.9 204
A.10 208

LIST OF TABLES

TABLE PAGE

2.1 Typical voltages for the electron gun in the magnetic sector mass spectrometer 28
2.2 Typical voltages for the electron gun in the quadrupole mass spectrometer 34
3.1 Total rate constant k_t and equilibrium ratio R_{eq} for proton transfer reactions 48
3.2 ADO rate constants for the reaction: $H_3O^+(H_2O)_h + B = BH^+(H_2O)_b +$ h-n+1 H_2O 54
3.3 $-\Delta G^\circ_{n-1,n}$ 60
3.4 ΔH° and ΔS° for the reaction: $BH^+(H_2O)_n + H_2O = BH^+(H_2O)_{n+1}$ 63
3.5 Relative Distrubition of n for $H_3O^+(H_2O)_n$ for different conditions 70
3.6 R_{eq} for the reaction: $H_3O^+(H_2O)_h + B = BH^+(H_2O)_b + (h-b+1)H_2O$ 71
3.7 Rate constants k_a for proton transfer to pyrrole under different conditions 74
3.8 Rate constants for the reaction: BH^+ + pyrrole = pyrrole·H^+ + B 80
4.1 ΔH° and ΔS° Values for Reactions in Scheme 2 97
4.2 ΔH° and ΔS° for the Reaction: $RXH^+ + RX = (RX)_2H^+$ 98
4.3 Equilibrium constants for the reaction measured in Scheme 2 for X = Br at several different temperatures 99
4.4 Calculation of ΔH°_3 101
4.5 Average hydrongen bond strength of symmetric proton bound dimers for several different heteroatoms 108
5.1 ΔH°_4 and ΔS°_4 for the reaction: BH^+ + diol = B + diol·H^+ 119
5.2 Cyclization of α,ω-dialcohols 122

5.3 Comparison of α,ω-diamines with α,ω-dialcohols 123

5.4 Entropy of n- and c- alkanes 125

5.5 ΔH°_8 and ΔS°_8 for the reaction: $BH^+ + B = B_2H^+$ 128

6.1 Reproducibility of equilibrium constants K_2 for different concentrations of B' and B 142

6.2 Rate constants k for reactions: $Me_2X^+ + B = MeX + MeB^+$ 149

6.3 Entropys used in calcuating ΔS° 153

6.4 MCA(RCl) 158

CHAPTER 1

Introduction to Ion-Molecule Reactions

1.1 Introduction

Much important chemistry takes place in solution and involves ions and ionic reaction intermediates. Although water is the most common solvent, many organic reactions require the use of other solvents, while biochemical systems are often dominated by the presence of lipids or proteins. When one works with a many solvent environment it becomes necessary to distinguish between the intrinsic (molecular) properties of the ion and the properties resulting from ion-solvent interaction. Of the important properties at the molecular level, structure and energy are the two major features. By studying reactions in the gas phase, it is possible to determine the molecular properties without the interference of the solvent.

The principal sources of gas phase ion thermochemistry are electron impact and photoionization measurements of ionization and appearance potentials as well as electron detachment thresholds. Early work of this type has been summarized by Franklin and Field (1) and more recent developments can be found in Rosenstock (2) and others (3-10). While these measurements are indispensable to gas phase ion thermochemistry, ambiguity as to the energy level of the reactants and the products involved in these measurements made for slow progress particular where ions like NH_4^+, H_3O^+, and CH_3COO^- were concerned.

Abundant gas phase ion thermochemistry was generated with the introduction of ion-molecule equilibrium measurements (11-16). Practically all the ion-molecule equilibria studied in the gas phase parallel important classes of ionic reactions in solution. Thus, the ion-molecule equilibria provides the energy changes for ionic reactions in solution. Comparison of the energetics with and without the presence of the solvent leads to knowledge of the energetics of the ion-solvent interaction.

1.2 Types of ion-molecule reactions

The types of ion-molecule reactions that have lead to abundant thermochemical data are shown in reactions 1.1 to 1.8.

Proton Transfer

$B_1H^+ + B = B_1 + BH^+$ [1.1]

$A_1^- + AH = A_1H + A^-$ [1.2]

Electron Transfer

$M_1^- + M = M_1 + M^-$ [1.3]

$M_1^+ + M = M_1 + M^+$ [1.4]

Hydride or Halide Transfer

$R_1^+ + RX = R_1X + R^+$ [1.5]

Alkyl Transfer

$RB_1^+ + B = B_1 + RB^+$ [1.6]

Ligand Exchange

$M^+L_1 + L = M^+L + L_1$ [1.7]

Ion-Ligand Association

$M^+L_{n-1} + L = M^+L_n$ [1.8]

Reactions 1.1 to 1.7 involve transfer (i.e. exchange) of a given group and can be represented by the general reaction 1.9.

$$A^+ + B = C^+ + D \qquad [1.9]$$
$$K_9 = [C^+][D]/[A^+][B]$$

The percentage of the neutrals species that are converted to ions is negligibly small. Therefore, the concentrations of the neutrals species, B and D, are constant throughout the experiment and their concentrations are known from the known composition of the reaction mixture. The relative concentrations of the ions are determined with the mass spectrometer. The equilibrium 1.8 is an association (clustering) process of the form represented by reaction 1.10. Again the equilibrium constant, K_{10}, is determined after the ions, A^+ and AB^+, are mass spectrometrically observed to reach equilibrium. Here we must keep in mind that the units for the concentration of the neutral species must be in and be consistent with the thermodynamic standard state.

$$A^+ + B = AB^+ \qquad [1.10]$$
$$K_{10} = [AB^+]/[A^+][B]$$

With both reactions 1.9 and 1.10, determination of the equilibrium constant leads to the free energy of the reaction (equation 1.11), and the temperature dependence of the equilibrium constants lead to the enthalpy (ΔH^o) and entropy (ΔS^o) via van't Hoff plots (equation 1.12).

$$\Delta G^\circ = -RT \ln K \qquad [1.11]$$

$$\ln K = -\Delta H^\circ/RT + \Delta S^\circ/R \qquad [1.12]$$

In some cases ΔS° can be estimated from statistical thermodynamics which allows ΔH° to be calculated from equation 1.13 and provides a method for determining the ΔH° without the necessity of extensive measurements at different temperatures.

$$\Delta H^\circ = \Delta G^\circ + T\Delta S^\circ \qquad [1.13]$$

Two major requirements for ion-molecule equilibrium measurements must be met: a) the ions must be in thermal equilibrium with the bath gas, b) sufficient time has to be given to the ion to reach chemical equilibrium. At the low pressures (10^{-6} torr) generally used in conventional analytical mass spectrometers, the ions reach the walls of the ion source in milliseconds and discharge. This is not enough time for the ions to reach chemical equilibrium. At pressures in the 3-5 torr range, used in the pulsed electron beam high pressure mass spectrometer (PHPMS), the ions experience many thousands of collisions with the bath gas before reaching the walls of the ion source. Thus, the ions are trapped because they have to diffuse through the bath gas and this provides time for the reaction to reach equilibrium. Also the collisions with the bath gas bring the ions to thermal equilibrium.

Ion-molecule equilibria of reaction 1.9 can be also measured with ion cyclotron resonance mass spectrometers (ICR) (13, 14). In this method the ions are trapped with the use of magnetic and electric fields. This type of trapping is very efficient but works only at low pressures (10^{-6} torr). Association reactions generalized by equilibrium 1.10, require third body stabilization and generally have too slow a rate at these pressures to be measured with ICR.

Reaction 1.1 involves the proton transfer from a protonated base to a neutral base. The proton transfer equilibria provide the relative gas phase basicities (GB) (or proton affinities, PA) of the neutral bases. In these and other exchange equilibria (reactions 1.1 to 1.7) the data generally are grouped by combining individual equilibria measurements into a ladder of equilibria (See Figure 6.7). In this fashion basicity differences between bases with widely differing basicities can be obtained through stepwise equilibrium measurements. Another advantage of this approach is the ability to establish the consistency of the results through thermodynamic cycles.

The proton affinity (PA) of a base is defined as the enthalpy of reaction 1.14. Since the proton affinity of ordinary bases are in the

$$BH^+ = B + H^+ \qquad [1.14]$$

order of 100-250 kcal/mol and the bond dissociation energies are in the order of 100 kcal/mol, it is impossible to observe thermal equilibrium of reaction 1.14 directly. Instead the proton transfer (reaction 1.1) between two bases must be used to measure the relative proton affinity. The relative proton affinity can be converted to the absolute proton affinity by incorporating an external standard into the equilibrium ladder. There are compounds whose basicities can be determined by electron impact or photoionization via thermodynamic cycles (1-10). Protonation of neutral pi bases leads to the energetics of carbocations. For example, the protonation of ethylene leads to the ethyl cation, $C_2H_5^+$, protonation of isobutene leads to the t-butyl cation, t-$C_4H_9^+$, and so on. Early work established a ladder from water to nitrogen bases including ammonia (17-19). The external standard chosen was isobutene (i.e. $\Delta H^\circ_f(t\text{-}C_4H_9^+)$), which proved to be unreliable. Extension of the ladder to lower basicities and particular to ethylene by McMahon (20) has allowed the use of the more reliable standard $C_2H_5^+$ (2, 7, 21). This new standard was incorporated into the available proton transfer data by Lias (22). Most recently the ladder has been extended downwards to methane (23). The proton affinity ladder contains over 300 bases from weak bases like methane to very strong bases such as 1,8-bis(dimethylamino)naphthlene.

Reaction 1.2 involves the proton transfer to anions and leads to the relative acidity of the acids AH. Like the proton affinities, the relative acidities can be converted to absolute acidities by the incorporation of an external standard into the equilibrium ladder. Using the well known (10) enthalpy and free energy for reaction 1.15, the acidity ladder can be connected to three excellent external standards.

$$HX_{(g)} = H^{+}_{(g)} + X^{-}_{(g)} \quad X= Cl, Br, I \qquad [1.15]$$

The acidity ladder contains some 500 compounds which are principally oxygen, carbon, and nitrogen acids.

Reactions 1.3 and 1.4 are electron transfer equilibria. Reaction 1.3 involves the electron transfer from a negative ion to a neutral molecule. Most commonly the measurements involve singlet state neutral molecules with low lying vacant orbitals such that the M^{-} ion is a doublet radical anion. Thus, equilibrium 1.3 provides thermochemical data for this very important class of compounds. McIver (24) first measured these equilibria and measurements by Caldwell and Kebarle (25) have successfully connected the ladder to several external standards.

The electron transfer reaction 1.4 involves positive ions and provides relative ionization potentials. Since photoionization and photoelectron spectroscopy provide good ionization potentials, these equilibria 1.4 have not been extensively used. Important and interesting results have been obtained by Meot-Ner (26) for the polynuclear aromatic hydrocarbons. These charge transfer measurements are particular useful when the adiabatic ionization potential involves a large geometric change and cannot be reached by spectroscopic means.

Reaction 1.5 represents hydride and halide transfer equilibrium. These reactions provide a useful route to the energetics of carbocations. Hydride transfer equilibria were first measured by Field (27, 28). A number of chloride transfer equilibria have been measured recently by Sharma et al (29).

The thermochemistry of quaternary ammonium ions like Me_4N^+ or tertiary oxonium ions like Me_3O^+ and halonium ions Me_2X^+ has become accessible through the measurement of alkyl cation transfer and specifically methyl cation transfer equilibria. (See chapter 6.)

The equilibria 1.7 and 1.8 involve reactions between ions and ligand molecules. The ions may be inorganic species, such as alkali or halide ions, or organic anions and cations. These equilibria provide the thermochemistry of ion-ligand coordination and the sequential solvation of an ion by solvent molecules. Reviews of this work are available (16, 32, 33).

Gas phase ion-molecule equilibria measurements may be used to provide abundant thermochemical data for ions in solution. Born cycles involving parallel reactions in the gas phase and solution leads to relative solvation energies for the ions. The interpretation of these results is aided by ion-solvent molecule (clustering) studies in the gas phase like those of reactions 1.7 and 1.8 where L and L_1 are solvents molecules such as H_2O, CH_3OH or CH_3CN.

1.3 Ion-Molecule Collision Theory

In studying the kinetics of ion-molecule reactions, it is necessary to be able to compare the experimental rate constants to collision rates. In this section some models for the calculation of ion-molecule collisions rates are examined.

A variety of theories and models has been developed to describe gas phase ion-molecule reactions. These have been extensively reviewed (34, 35). A series of electrostatic models, based upon the classical electrostatic polarization model of Langevin (36), has been developed which are relatively simple, but have been highly successful in predicting the rate constants of numerous ion-molecule reactions. Because the ion is treated as a point charge, these models can be applied to reactions involving positive ions, negative ions or electrons. It is important to note that the models deal only with the physical situation of a "capture collision" and do not in any way account for the variety of chemical reactions.

From the pure polarization theory, the collision cross section of an ion-molecule pair with a given relative velocity can be calculated. Both the ion and the neutral molecule are assumed to be point particles with no internal energy. Consider an ion and molecule approaching each other with a relative velocity v and impact parameter b, as shown in Figure 1.1. The classical potential energy at an ion-molecule separation r is given by

$$V(r) = -(\alpha q^2)/(2r^4) \qquad [1.16]$$

where α is the polarizability of the neutral and q the charge on the ion. Hence, for $r <$ infinity, the relative energy of the system E_r is a sum of the instantaneous kinetic energy $E_{kin}(r)$ and the potential energy $V(r)$

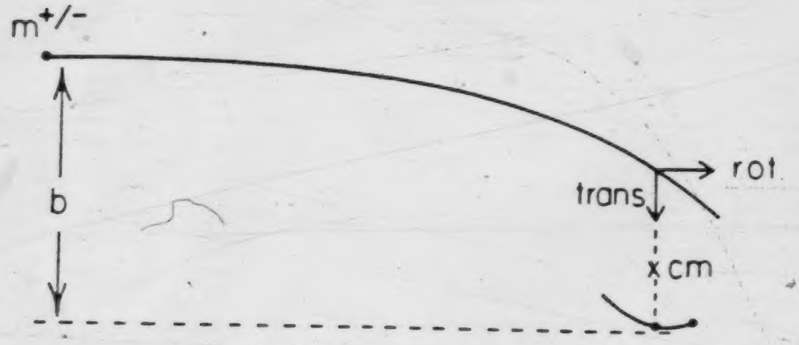
m+/-
b
rot.
trans
x cm

Figure 1.1 Schematic representation of an ion-molecule collision system.

$$E_r = 1/2\mu v^2 = E_{kin}(r) + V(r) \qquad [1.17]$$

where μ is the reduced mass. From Figure 1.1, it is apparent that there are two components to the kinetic energy term

$$E_{kin}(r) = E_{trans}(r) + E_{rot}(r) \qquad [1.18]$$

where $E_{trans}(r)$ is the translational energy along the line of centers of the collision and $E_{rot}(r)$ is the energy of relative rotation of the particles. The rotational energy of the system is given by

$$E_{rot}(r) = L^2/2\mu r^2 = (\mu v^2 b^2)/(2r^2) \qquad [1.19]$$

where L is the classical orbiting angular momentum of the two particles. This rotational energy is associated with an outwardly directed centrifugal force. Thus, the effective potential energy of the ion-molecule system is the sum of the central potential energy V(r) and the centrifugal potential energy $E_{rot}(r)$;

$$V_{eff}(r) = -(\alpha q^2/2r^4) + (\mu v^2 b^2/2r^2) \qquad [1.20]$$

The total relative energy of the system is then

$$E_r = E_{trans}(r) + V_{eff}(r) \qquad [1.21]$$

A plot of $V_{eff}(r)$ against r at constant E_r for several values of the impact parameter is given in Figure 1.2. For $b = 0$, there is no contribution from the centrifugal potential and $V_{eff}(r)$ is attractive for all values of r. ~~Hence the system~~ passes through the scattering center (i.e., $r = 0$). When $b > 0$, the centrifugal potential terms in $V_{eff}(r)$

The material on this page has been removed because of the unavailability of copyright permission. The diagram of V_{eff} against r for the $[N_2]^+/[N_2]$ system can be found in "Gas Phase Ion Chemistry" vol 1, Bowers, M.T. Ed., Academic Press, New York, (1979).

creates a so-called "centrifugal barrier" to a capture collision. For the special case in which the centrifugal barrier height equals E_r ($b = b_c$ in Figure 1.2), V_{eff} at r_c is equal to E_r. Thus from equation 1.21, $E_{trans}(r) = 0$, and the particles will orbit the scattering center with a constant ion-molecule separation r_c (Figure 1.3). For all impact parameters $b < b_c$, a capture collision will occur. A capture collision is defined as one in which the particles have appropriate energy and impact parameters to pass through $r = 0$. For $b > b_c$, the centrifugal barrier prevents capture and the particles are merely scattered at large r, as shown for several trajectories in Figure 1.3. All ions that pass through the circle, in Figure 1.3, when approaching the molecule will pass through $r = 0$ (i.e., capture collision will occur). The area of the circle is called the capture collision cross section, σ, for a given relative velocity v:

$$\sigma(v) = \pi b_c^2(v) \qquad [1.22]$$

To evaluate the capture cross section at a given relative velocity, one has to calculate the critical impact parameter such that the maximum value of V_{eff} is equal to E_r (See Figure 1.2). This condition occurs when $dV_{eff}(r)/d(r) = 0$ and $E_r = V_{eff}(r)$ at $r = r_c$:

$$dV_{eff}(r)/dr = 0 = -(\mu v^2 b^2)/(r^3) + (2\alpha q^2)/(r^5) \qquad [1.23]$$

$$V_{eff}(r) = E_r = -(\alpha q^2)/(2r^4) + (\mu v^2 b^2)/2r^2) \qquad [1.24]$$

Equations 1.23 and 1.24 give

$$r_c = (q/b_c)(2\alpha/E_r)^{1/2} \qquad [1.25]$$

$$b_c = (2q^2\alpha/E_r)^{1/4} \qquad [1.26]$$

The material on this page has been removed because of the unavailability of copyright permission. The plot of the variation of the ion trajectory as a function of the impact parameter can be found in Gioumousis, G. and Stevenson, D.P. J. Chem. Phys., 1958 **29**, 294.

and

$$r_c = b_c/(2^{1/2}) \qquad [1.27]$$

Finally, the capture cross section and rate constant are given by

$$\sigma(v) = (2\pi q/v)(\alpha/\mu)^{1/2} \qquad [1.28]$$

$$k_c = v\sigma(v) = 2\pi q(\alpha/\mu)^{1/2} \qquad [1.29]$$

The capture rate constant described here, often referred to as the Langevin rate constant, is predicted to be independent of the relative velocities of the particles and the temperature of the system. For simple systems involving low-energy collisions between ions and non-polar molecules, this model has been found to agree quite well with experimentally determined rate constants (34, 35) but underestimates the rate constants for most ion-polar molecule collisions. Although the Langevin model assumes that the polarization of the molecule is spherically symmetric, it may be successfully applied to molecules whose polarization is anisotropic because thermal rotation of such molecules "averages " the polarizability components to the mean polarizability (38).

For ion-molecule collisions involving molecules which have a permanent dipole moment, μ_D, the permanent dipole will act in conjunction with the ion-induced dipole to increase the capture collision cross section and the rate constant (34, 39, 40). Equation 1.30 describes the ion-dipole potential, $V_D(r)$, where θ is the angle the dipole makes with the line of the centers of the collision. In a manner similar to that discussed in connection with the Langevin model, an effective potential may be defined as shown in equation 1.31.

$$V_D(r) = -(q\mu_D/r^2)\cos\theta \qquad [1.30]$$

$$V_{eff}(r) = -(\alpha q^2)/(2r^4) - (q\mu_D/r^2)\cos\theta + (\mu v^2 b^2)/2r^2 \qquad [1.31]$$

In the locked-dipole (LD) model for ion-molecule reactions (39, 40), the effective potential defined in equation 1.31 is simplified by assuming that the dipole aligns perfectly with the ion field so that $\theta = 0°$ and $\cos\theta = 1$. Using an approach similar to the Langevin model, results in a rate constant for thermal velocities given by

$$k_{LD}(\text{therm}) = (2\pi q/\mu^{1/2})[\alpha^{1/2} + \mu_D(2/\pi kT)^{1/2}] \qquad [1.32]$$

where k is the Boltzmann constant and T is the absolute temperature. Experimental determinations of the rate constants for ion-molecule reactions involving dipolar molecules have shown that the LD model overestimates the influence of the dipole of the molecule on the reaction rate (34, 41). Thermal rotation of the molecule acts to disrupt the alignment of the ion and the dipole so that full alignment is achieved for only a fraction of the time. Hence, k_{LD}(therm) may be viewed as the upper limit for the capture collision rate constant.

Bowers and Laudenslager (42) made the first attempt to estimate experimentally the degree of locking of the dipole. They measured thermal energy charge transfer rate constants from various rare gas ions to three geometric isomers of difluoroethylene. All three isomers have essentially the same average polarizability and ionization potential, but they have considerably different dipole moments: trans, 0.0D; cis, 2.32D; and 1,1, 1.38D. Thus, an incremental increase in the rate constant with increasing polarity of the molecule presumably reflects the degree of locking of the dipole. If a parameter c with values between 0 and 1 represents the effectiveness of the locking of the dipole (or the average value of cosθ), the rate constant can be expressed as

$$k_{ADO}(\text{therm}) = (2\pi q/\mu^{1/2})[\alpha^{1/2} + c\mu_D(2/\pi kT)^{1/2}] \qquad [1.33]$$

This model is referred to as the Average Dipole Orientation (ADO) theory. Parameterization of the ADO model has shown that at constant temperature, c is significantly less than one and is a function of $\mu_D/\alpha^{1/2}$ only (43, 44), as shown in Figure 1.4. In practice, appropriate values for c may be readily selected from plots, such as Figure 1.4, in order to predict the rate constant for capture collisions for a given ion-molecule pair. Experimentally, the ADO model has been shown to be relativly accurate, frequently predicting rate constants to within 20% of their measured values (34).

The level of accuracy of the ADO model has been found to be adequate for a variety of purposes, such as distinguishing between efficient and inefficient ion-molecule reactions. However, many more elaborate ion-molecule collision models have been developed in order to improve the accuracy or to describe specialized situations. The ADO model has been improved to yield the AADO model which includes conservation of angular momentum throughout the ion-molecule interaction (45). This is a consideration which becomes increasingly important as the dipole of the molecule increases. A model describing ion-molecule collisions, where the molecule exhibits a permanent quadrupole, has been developed along the same lines as the ADO model, and is called the Average Quadrupole Orientation (AQO) model (46). A molecular quadrupole generally has less influence on the ion-molecule collision than the does molecular dipole and may often be neglected. Each of the

The material on this page has been removed because of the unavailability of copyright permission. The plot of the locking constant against $\mu_D/\alpha^{1/2}$ for temperatures between 150 and 650K can be found in Su, T. and Bowers, M.T., Int. J. Mass Spectrom. Ion Phys., 1975, **17**, 211.

models described in this section treats the ion as a non-polarizable point charge, real ions are polarizable so that induced-dipole/induced-dipole interactions may also affect the ion-molecule collision rate (47).

1.4 The Present Study

In the present work, we are looking at several different types of ion-molecule reactions. The different studies arose out of interesting results and side reactions in other studies within the research group. Chapter 3 involves proton transfer reactions from partially solvated protons to bases with gas-phase basicities greater than water. These proton transfer reactions give important information about the relative sensitivities of bases in atmospheric pressure chemical ionization mass spectrometry as well as a number of other areas of chemistry such as solvation and atmospheric chemistry. In chapters 4 and 5 we look at hydrogen bonding in the gas phase. In chapter 4 we look at the proton bound dimer of HCl, MeCl, HBr, and MeBr while in chapter 5 we studied the inter- and intramolecular hydrogen bond in dialcohols. In chapter 6 we studied the methyl cation affinities of several bases and the relationship between proton and methyl cation affinities. Chapter 7 is a study of the electron affinity of C_6F_6 and the reactions between the $C_6F_6^-$ anion and oxygen. Appendix A is the manual for the MCA program developed in collaboration with Norman Osborn for the IBM-PC.

CHAPTER 2

EXPERIMENTAL

2.1 General

Measurements of equilibrium constants and rate constants of gas phase ion molecule reactions were carried out with a pulsed electron beam high pressure mass spectrometer (PHPMS). The pressure in the PHPMS ion source was maintained between 2 and 5 torr. A high capacity pumping system was required in order to keep the pressure outside the ion source low ($<10^{-4}$ torr), even when the ion source is at several torr pressure. The low pressure outside the ion source was required in order to avoid the occurence of ion-molecule collisions in the region between the ion source and the detector. At pressures less than 10^{-4} torr the mean free path of an ion (m/e= 16) is longer than the distance from the ion source to the detector. Since the ion detection is done outside the ion source, it is important that the ratio of intensities sampled is a true representation of the ion concentrations ratio in the ion source. At the high pressures used in the ion source, high energy electrons (2000 eV) were needed to penetrate the ion source and ionize the gaseous sample.

The PHPMS can be divided into three parts: the electron gun where the high energy electrons are produced; the ion source which serves as a reaction chamber; and the detection system with which mass analysis of all the ions is obtained and the ion intensities are determined.

The investigations described in this thesis were conducted on two different mass spectrometers. The main difference between the two instruments is the mass analyzer; the first has a magnetic sector for mass analysis while the second has a quadrupole mass analyzer. Also, the electron guns were of somewhat different designs. The magnetic sector mass spectrometer was constructed in this laboratory by Payzant (48), while the quadrupole mass spectrometer was constructed by Durden (49) and modified by Lau (50). A brief description of the instruments will be given here.

2.2 Overall Description of the Apparatus

A block diagram of the PHPMS is shown in Figure 2.1. The electron gun, ion source and the mass detection system are housed in the vacuum chamber which is pumped by high capacity diffusion pumps. When there was no sample in the ion source, the pressure in the vacuum chamber was normally 10^{-7} to 10^{-8} torr. With a pressure of 3 torr in the ion source, the pressure in the vacuum chamber was between 10^{-4} torr and 10^{-6} torr. This pressure decreased along the vacuum chamber due to the differential pumping between the ion source chamber and the mass analyzer.

The pulsing of the electron beam was controlled by the master pulse generator and the pulse amplifier. Ions which remained in the ion source after the observation period could be removed before the start of a new electron beam pulse by pulsing the voltage on the repeller electrode in the ion source. This pulse was obtained from a pulse generator connected to a second pulse amplifier. Sample preparation was carried out in a gas handling plant and the reaction mixture was allowed flow to the ion source. Ions diffusing out of the ion source, through the ion exit slits, were accelerated and mass analyzed by a magnet or quadrupole according to their mass to charge (m/e) ratio and then detected by a secondary electron multiplier. The signal from the detector was amplified and individual pulses were counted by the rate meter and the multichannel scaler. The time dependence of the ion intensities was obtained by synchronizing the sweep of the multichannel scaler with the start of an electron pulse.

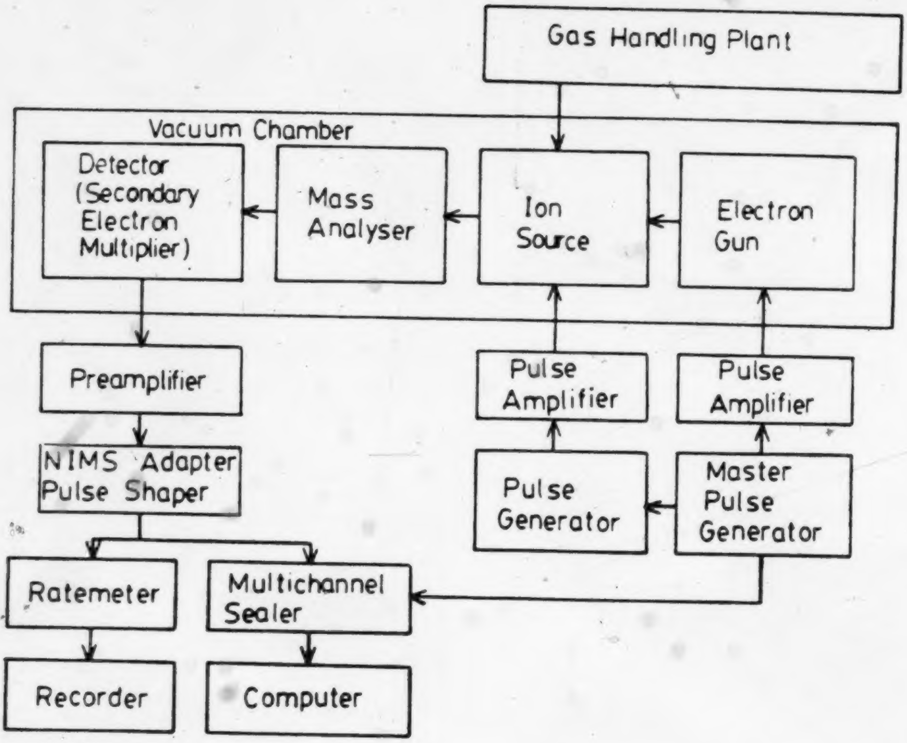
Gas Handling Plant
Vacuum Chamber
Detector (Secondary Electron Multiplier)
Mass Analyser
Ion Source
Electron Gun
Preamplifier
Pulse Amplifier
Pulse Amplifier
NIMS Adapter Pulse Shaper
Pulse Generator
Master Pulse Generator
Ratemeter
Multichannel Sealer
Recorder
Computer

Figure 2.1 Block Diagram of the Pulsed High Pressure Mass Spectrometer.

Individual components of the mass spectrometer are described in the following sections.

2.3 Gas Handling Plant

The gas handling plants on both mass spectrometers were essentially the same. A schematic diagram of the gas handling plant is shown in Figure 2.2. The 5l bulb is used as a reservoir for the reaction mixture. The major components of the reaction mixture were introduced into the 5 liter bulb through valve 4 or 5. The minor reactants were introduced into the bulb directly by injecting them with a syringe through a septum attached to the 5 liter bulb. The pressures of the major gases were measured with a validyne pressure gauge at valve 6. The pressures of the minor components were calculated from the number of moles injected into the 5l bulb. After the mixture had time to equilibriate it was allowed to flow through valve 7 and into the ion source and then return from the ion source through valve 8. Impurities, even at the part per million level, can cause a great deal of difficulty. Incorporation of all-metal valves into the gas handling plant enabled the system to be baked at high temperatures to remove compounds that have absorbed onto the walls. The septum in the 5 l bulb was also changed when introducing a new series of compounds.

The main difference in the two gas handling plants was the position of the pressure gauge for measuring the pressure in the ion source. In the gas handling plant with the magnetic sector instrument, the pressure was measured in the glass line between the ion source and valve 8 and the pressure was regulated by the small valve 7 between the ion source and the manifold of the gas handling plant. In the gas handling plant with the quadrupole instrument the pressure was read in the manifold (valve 6) of the gas handling plant which meant that the pressure was regulated by the

Figure 2.2

Schematic Diagram of the Gas Handling System

1	valve to 5 liter bulb
2	valve to the diffusion pump
3	valve to the rough pump
4,5	inlet valves
6	valve to the validyne pressure gauge
7	valve to the ion source
8	valve from the ion source
a	to gas cylinders
b	to ion source
c	from ion source
d	validyne manometer
e	rough pump
f	diffusion pump
g	ion gauge

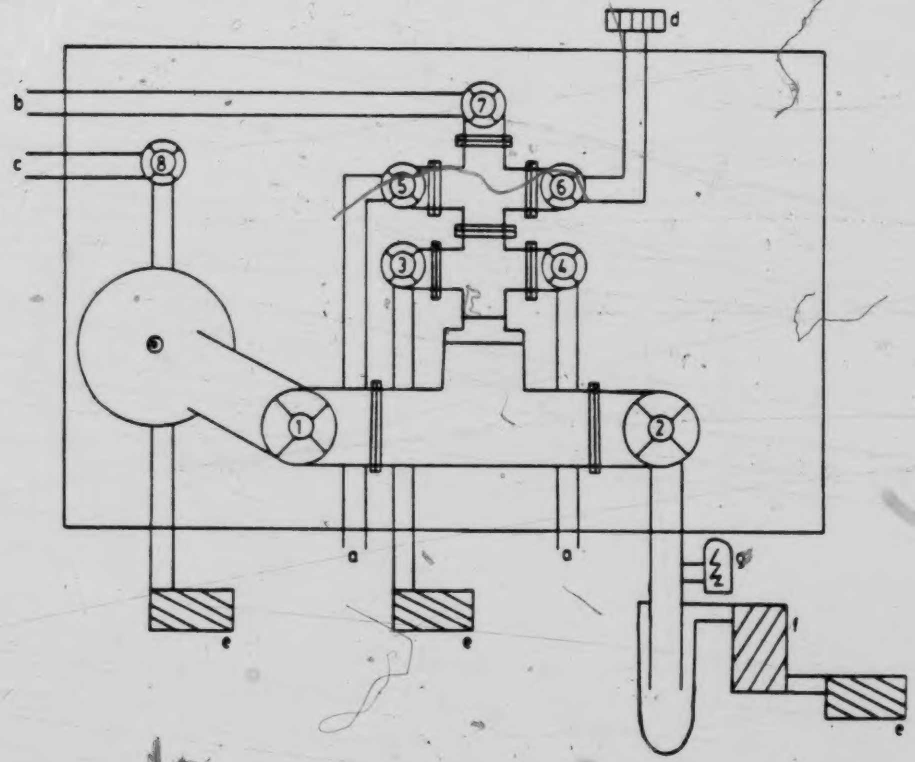
d
b
7
c
8
5
6
3
4
1
2
a
a
g
f
e
e
e

large valve 1 at the five liter bulb. In both cases the pressure in the ion source could be kept constant to within 1 percent during an experiment without a great deal of difficulty. A second difference was the absence of inlet valve 5 in the gas handling plant with the magnetic sector instrument. The temperature in the gas handling plant was usually kept at approximately 150C. This ensured complete vaporization of most of the liquids and solids injected into the 5l bulb.

The glass lines leading from the gas handling plant to the ion source were wrapped with heating tape and kept at about 100C so that the bases would not condense out on the walls of the glass lines. On the inlet to the ion source a cold trap could be used to trap out impurities such as water or low volatility impurities. When the cold trap was not being used it was heated along with the rest of the inlet line.

The gas handling plant was pumped with a rotary pump to a pressure of less than 1 torr and then an Edwards diffusion pump with a liquid nitrogen cold trap was used to reduced the pressure to about 10^{-6} torr.

2.4 Electron Gun

2.4a Electron Gun for the Magnetic Sector Mass Spectrometer

A schematic diagram of the electron gun assembly used with the magnetic sector mass spectrometer is shown in Figure 2.3. Electrons emitted from a heated filament [1] were accelerated and focussed by various electrode plates and lenses [2-6] along the z axis towards the ion source. Two pairs of deflection plates [7,8] were used to deflect the electron beam in the x and y axes in order to position the electron beam on the electron entrance slit of the ion source. In order to produce high energy (2 kV) electrons for ionization of the gas sample in the high pressure ion source, the

FIGURE 2.3

Schematic Diagram PHPMS Apparatus with 90° Magnetic Sector[a]

Pulsed Electron Gun	
1	filament
2	drawout
3	extractor
4,5,6	einzel lens
7,8	electron deflection plates in X and Y directions
9	electric and magnetic shield
Ion Source	
10	ion source block with heaters
11	wire mesh electric shield
12	electron entrance slit flange
13	electron trap and repeller
14	ion exit slit flange
15	gas inlet and outlet tubes
Ion Acceleration Tower	
16-21	cylindrically symetrical electrodes for ion acceleration
22,22a	collimating and ion deflection slits
Vacuum system	
23	mass analyser tube
24	lead to 6" diffusion pump
25	lead to 4" diffusion pump

[a] Adapted from reference (51)

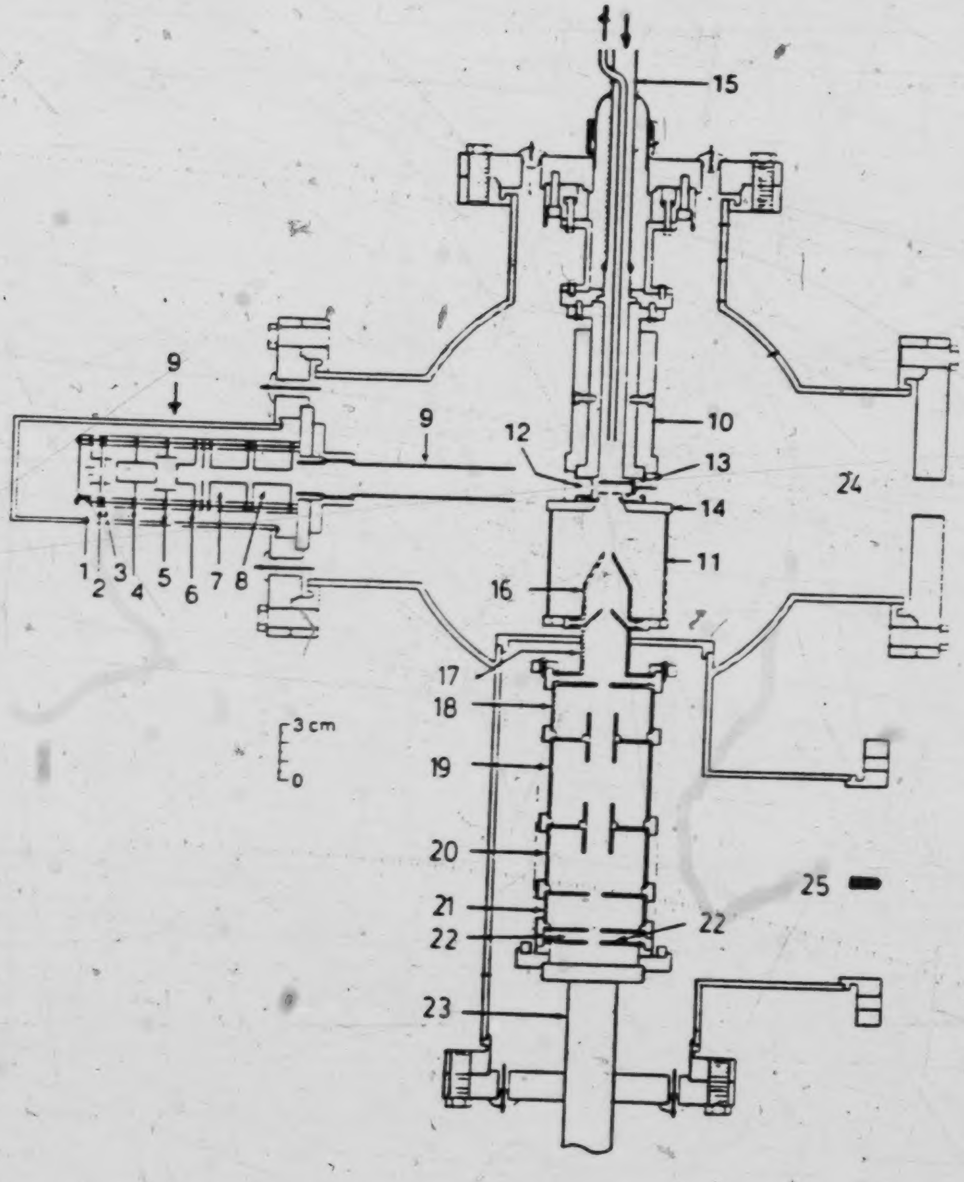
3 cm

TABLE 2.1

Typical voltages for the electron gun in the magnetic sector mass spectrometer.

Electrode[a]		Voltage (Volts) Positive ions	Voltage (Volts) Negative ions
1		0	-2800
2		50	-2750
3		200	-2600
4		1950	-1430
5		350	-2750
6[b]		1950	-1430
7	X_1	1925	-1440
	X_2[b]	1950	-1450
8	X_1	1965	-1430
	X_2[b]	1950	-1450
Ion source		2000	-1200

a) numbers refer to Figure 2.3

b) fixed voltages. All other voltages are variable filament was kept at -2000 V relative to the ion source. Typical voltages are given in Table 2.1. The long distance from the ion source to the filament meant that the filament was not exposed to the high pressure gas near the ion source; and this resulted in a longer life for the filament. Also, a the ion source temperature could be controlled better in this manner since the hot filament would not heat the ion source, and the temperature of the ion source could be controlled solely by the ion source heaters.

Focusing of the electron beam was done with the system under vacuum. A metal plate with a small hole in front of the electron entrance slit was mounted on the ion source. The outer surface of this metal plate was coated with a phosphor (Type P-31 Sylvania) embedded in sodium silicate. The electron beam was first deflected onto the plate by varying the voltages on the deflection plates [7,8] and then focused to give a sharp spot. The focussed electron beam was then deflected onto the electron entrance slit. The final position was attained by adjusting the deflection voltages until a maximum current was read on the electron trap current microammeter. Some minor adjustments were usually made once the gas was admitted to the ion source in order to maximize the ion current.

All experiments were performed with a pulsed electron gun. A schematic diagram of the pulsing sequence is shown in Figure 2.4. The pulsing was achieved by varying the potential of the drawout electrode at regular intervals. Electrons could only pass the drawout electrode [2] when this electrode was at a positive potential relative to the filament. In the pulsing mode the drawout electrode was kept at -40 volts relative to the filament. Upon receiving a triggering pulse from the master pulse generator, the floating pulse amplifier would alter the potential on the drawout electrode to about 50 volts positive relative to the filament for the desired length of the electron pulse (6-160 μs). This allowed the electrons to pass through the drawout

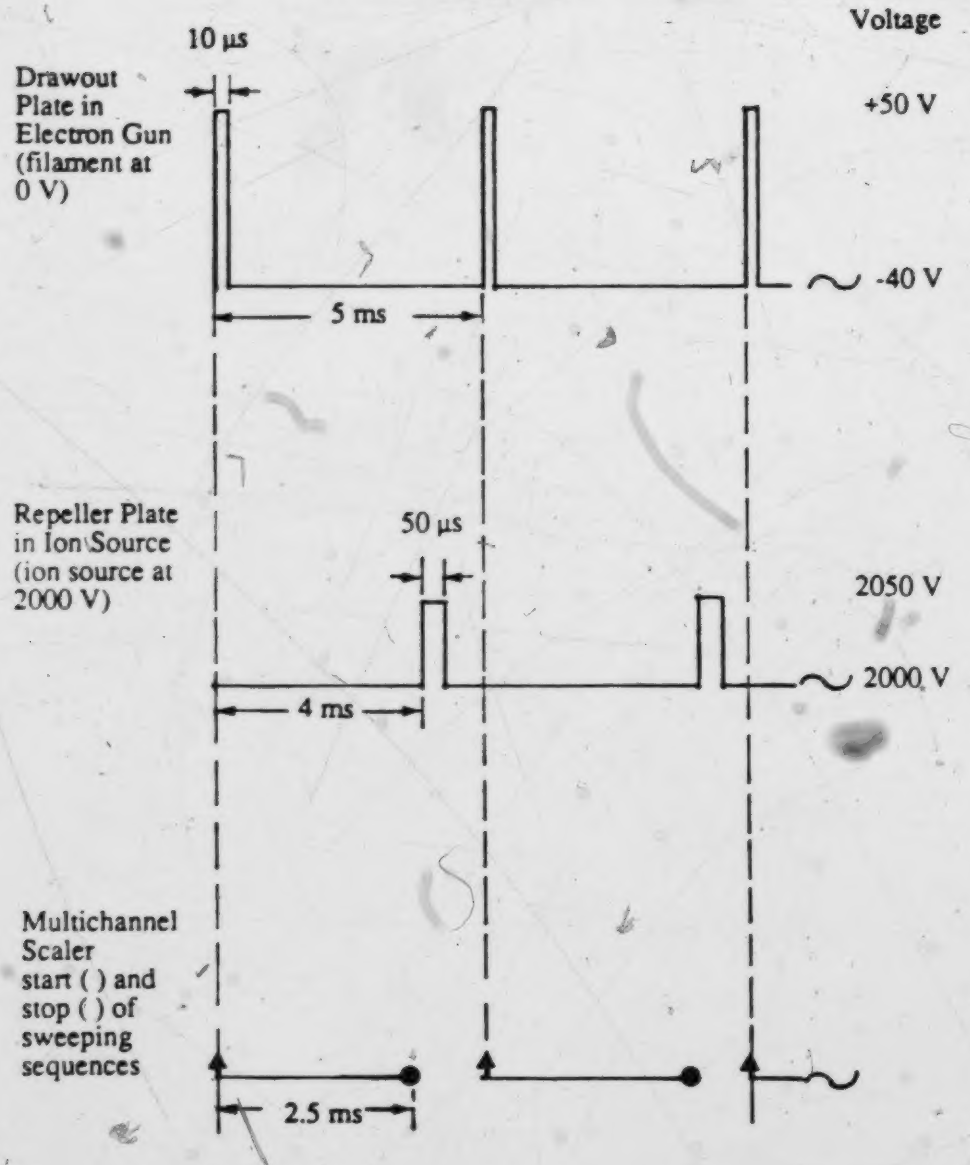
Voltage
10 µs
Drawout Plate in Electron Gun (filament at 0 V)
+50 V
-40 V
5 ms
Repeller Plate in Ion Source (ion source at 2000 V)
50 µs
2050 V
2000 V
4 ms
Multichannel Scaler start ( ) and stop ( ) of sweeping sequences
2.5 ms

Figure 2.4 Pulsing sequence with typical voltages and durations.

electrode for only the preset period of time, after which the drawout electrode would return to its original potential of -40 volts to the filament until the next cycle was initiated by the master pulse generator. The frequency of the cycles was controlled by the master pulse generator at about 5 ms/cycle. The duration of the "on" time for the electron beam was controlled by the pulse amplifier which also controlled the exact voltage of the drawout electrode.

The triggering pulse from the master pulse generator served two other purposes. It could be used to send a delayed pulse to the repeller in the ion source to sweep all the ions to the wall before starting the next electron pulse. This was achieved with a second floating pulse amplifier together with a delay pulse generator externally triggered by the master pulse generator. The repeller pulse was typically of 50 μs duration and at some 20-40 volts positive (for positive ions) relative to the ion source. Also, the master pulse generator triggered the sweep of the multichannel scaler to allow a time dependance of the ion intensities to be observed after the ionizing pulse.

2.4b Electron gun for quadrupole mass spectrometer

A schematic diagram of the electron gun used with the quadrupole mass spectrometer is shown in Figure 2.5. The pulsing circuitry was identical for both electron guns. The major difference between the electron gun for the magnetic setror mass spectrometer and the present electron gun is in the focussing of the electron beam. The electron beam in the magnetic instrument was focussed by electrostatic fields whereas in the second electron gun, the electron beam was focussed by electromagnetic fields. Stronger focussing effects were achieved by magnetic fields resulting in a higher intensity of the electron beam in the ion source.

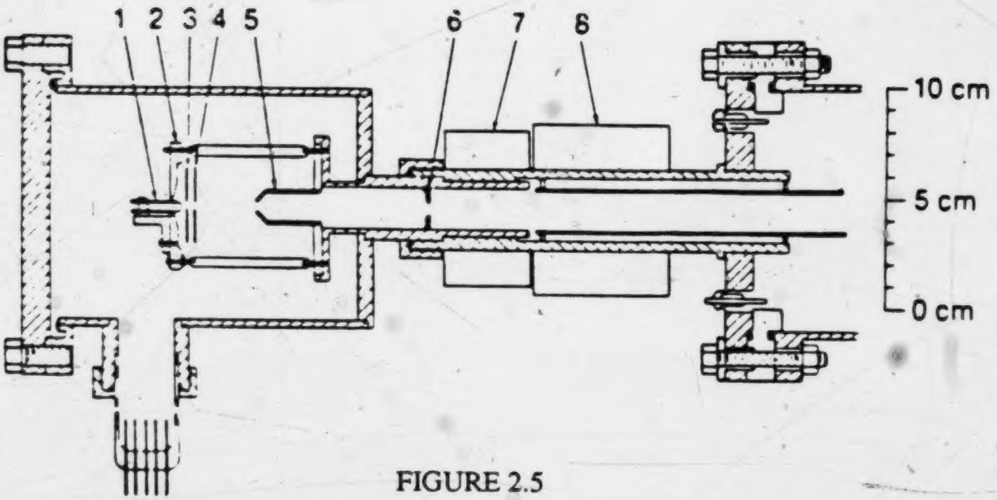

FIGURE 2.5

Schematic diagram of the pulsed electron gun for the quadrupole mass spectrometer.[a]

1	filament
2	filament support
3	drawout electrode
4	extractor electrode
5	accerlation
6	collimation electrode
7	solenoid providing axial magnetic field for electron collimation
8	TV yoke for X and Y deflection of electron beam

[a] Adapted from reference (50)

During the operation of the second electron gun, the filament [1] and the filament support [2] were kept at -2 kV. Electrons from the heated filament were accelerated between the support plate [2] and the drawout electrode [3]. They were slightly focused by the extractor electrode [4] before being accelerated towards the grounded cone [5]. The electron beam was focused by the solenoid coil [7] (1000 turns of 22 AWG copper wire with 0.5 to 1.5 amps generally required for focussing). Horizontal and vertical positioning of the electron beam to the ion source was achieved by a television tube yoke [8]. The solenoid of the yoke was controlled by a low voltage (7 volts) gas chromatograph dc supply modified to give two independent outputs in order to control the x and y axes. The solenoid coil [7] and the TV yoke [8] were put outside the vacuum chamber. The walls of the vacuum chamber within the coil and TV yoke were made of brass to minimize the disturbance of the magnetic fields.

Focussing of the electron gun was done in the same manner as for the magnetic sector electron gun. The typical operating voltages of the second electron gun are shown in Table 2.2.

2.5 High Pressure Ion Source

A schematic diagram of the ion source is shown in Figure 2.3. The design of the ion source was very similar for both instruments, the only difference being the presence of a low pressure ion source with the quadrupole instrument (See Figure 2.6). The ion source was machined from a non-magnetic stainless steel tube. One end of the tube was attached to the base of the assembly. There were two holes on the other end of the tube perpendicular to the main axis. These two holes were sealed by flanges which carried the electron entrance slit [12] and the electron trap [13], which could also be used as a repeller. The top of the ion source was sealed by a small "hat

TABLE 2.2

Typical voltages for the electron gun in the quadrupole mass spectrometer.

Electrode[a]		Voltage (volts)	Amperage
1[b]		-2000	
2[b]		-2000	
3		-1950	
4		-1700	
5		0	
6		0	
7			1.0 A
8	X		5.3 mA
	Y		10. mA

a) refers to numbers in Figure 2.5

b) fixed voltage. All other are variable voltages

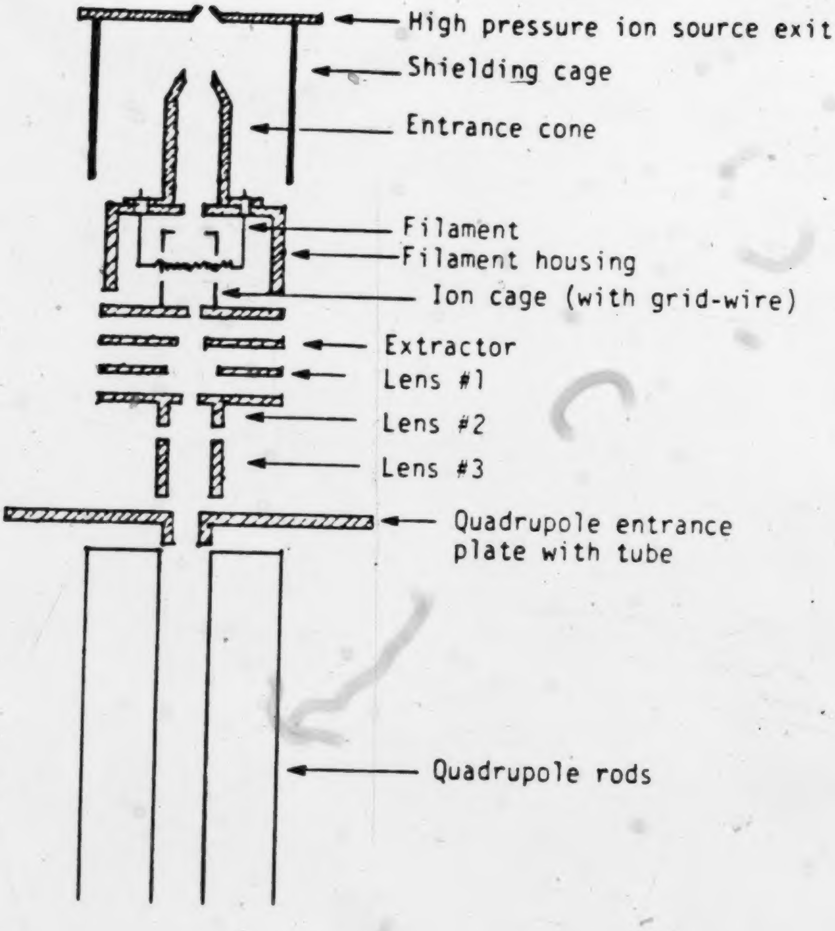
High pressure ion source exit
Shielding cage
Entrance cone
Filament
Filament housing
Ion cage (with grid-wire)
Extractor
Lens #1
Lens #2
Lens #3
Quadrupole entrance plate with tube
Quadrupole rods

Figure 2.6 Schematic diagram of the low pressure ion scource for the quadrupole mass spectrometer. Adapted from reference (50)

shaped" flange which carried the ion exit slit [14]. "O"-rings made of 0.25 - 0.50 mm gold wire were used in sealing the flanges to the ion source. The volume of the ion source was about 1.5 cm^3.

The ion exit slit and the electron entrance slit were made by spot welding two small pieces of stainless steel razor blade across a 1 mm diameter hole on the respective demountable flanges. Typical dimensions of the ion exit slit and the electron entrance slit were 20 μm x 1 mm and 15 μm x 1 mm respectively.

The ion source was heated by inserting 6 cartridge heaters (Hotwatt Inc., Danvers Mass.) into circular channels in the ion source block [10]. The temperature of the gas in the ion source was determined by measuring the temperature of the ion source wall with an iron/constantan thermocouple placed firmly in a small diameter hole drilled into the ion source block. As the thermocouple was held against the end of the hole which terminated near the inner wall of the ion source cavity, it was assumed that this arrangement led to correct reading of the ion source temperature.

2.6a Ion Detection and Data Storage and Handling

The ions were counted after detection with a secondary electron multiplier (Spiraltron 4219 EIC, Gallileo Electric Optics). The electron pulses from the secondary electron multiplier were amplified and counted with conventional devices. An example of the type of devices given here is for the quadrupole mass spectrometer. A similar arrangement was used with the magnetic sector instrument. The electron pulses were amplified with a SSR Model 1120 amplifier/discriminator (Princeton Research Corp) having a rise time of 6 x 10^{-9} seconds and a minimum gain of 2300. The amplifier/discriminator was designed to permit resolution of electron pulses separated by as little as 10^{-8} s, with sufficient sensitivity to detect individual secondary pulses representing less than 10^6 electron charges. The discrimator sensitivity had a range of 25mV to 250mV and allowed a gate level to be set such that only the signal pulses were transmitted while the low level noise pulses were rejected. The amplifier/discriminator could be used for pulse rates up to 10^7 per second. This resolution was sufficient for this application as the normal pulse rate was 10^4 per second. The output pulses from the amplifier/discriminator were fed into the SSR model 1127 NIM adapter (Princeton Research Corp.) which converted the discriminated pulses into uniform 5V, 10 ns pulses. The uniform pulses were collected with a multiscaler and dedicated computer. The computer interfaced to the quadrupole instrument was an IBM PC with the ORTEC-MCS 913 on an IBM PC plug in card. The typical noise level observed was about 10 counts per second. On the magnetic sector instrument, a LeCroy 3500 computer with a LeCroy multiscaler interface MCS 3521A was used.

2.6b Mass Analysis

The mass analysis in PHPMS is similar to mass analysis on conventional mass spectrometers. Since very adequate descriptions can be found in the literature (51, 52) it will not be discribed here except for the discussion of mass discrimination.

The ion transmission of magnetic sector instruments, using constant acceleration voltage and magnetic scanning, changes (decreases) only very slightly with (increasing) mass and therefore no correction was made when the magnetic sector instrument was used.

The ion transmission of quadrupole mass analyzers is strongly dependant on the parameters used (resolution, etc.) and mass scans at constant U/V lead to a rapid fall off of transmission with increasing mass (51). In order to correct for this change in mass transmission, a mass calibration curve must be obtained. The most convenient calibration was obtained with the use of the low pressure ion source, see

Figure 2.6. A standard calibrant such as perfluorotributlyamine was bled via the high pressure ion source, with the high pressure filament turned off, into the low pressure vacuum chamber, such that a constant pressure (10^{-6} torr) of the gas was obtained. The electron impact mass spectrum of the gas was recorded and compared to the mass spectrum of the same gas obtained from a magnetic sector instrument. Plots of the ion intensity ratios of the normalized mass spectra obtained with the two instruments resulted in curves which gave the mass dependant transmission of the quadrupole. Typical curves for the quadrupole are shown in Figure 2.7. The quadrupole ion intensities were corrected by multiplying each mass with the mass correction term, (1/transmission) obtained from the transmission curve. From Figure 2.7b we can see that the transmission falls off more rapidly as the resolution increases.

In order to reduce the loss of transmission at high mass, the ion source voltage was linearly increased as the mass was increased. This increase in ion source voltage reduces the time the heavier mass ions spend in the quadrupole, and increases the transmission of the ion, but at the same time reduces the resolution of the instrument at high mass.

2.7 Ion Sampling

In these experiments we assumed that the population outside the ion source is a true representation of the population inside the ion source. In order for this to be true two conditions must be met. First, the diffusion coefficient of the ions in the ion source must be the same and second, the gas flow through the ion exit slit must be molecular.

The first condition is required to ensure that the population is uniform throughout the ion source as only the flux of ions to a region near the ion exit slits is

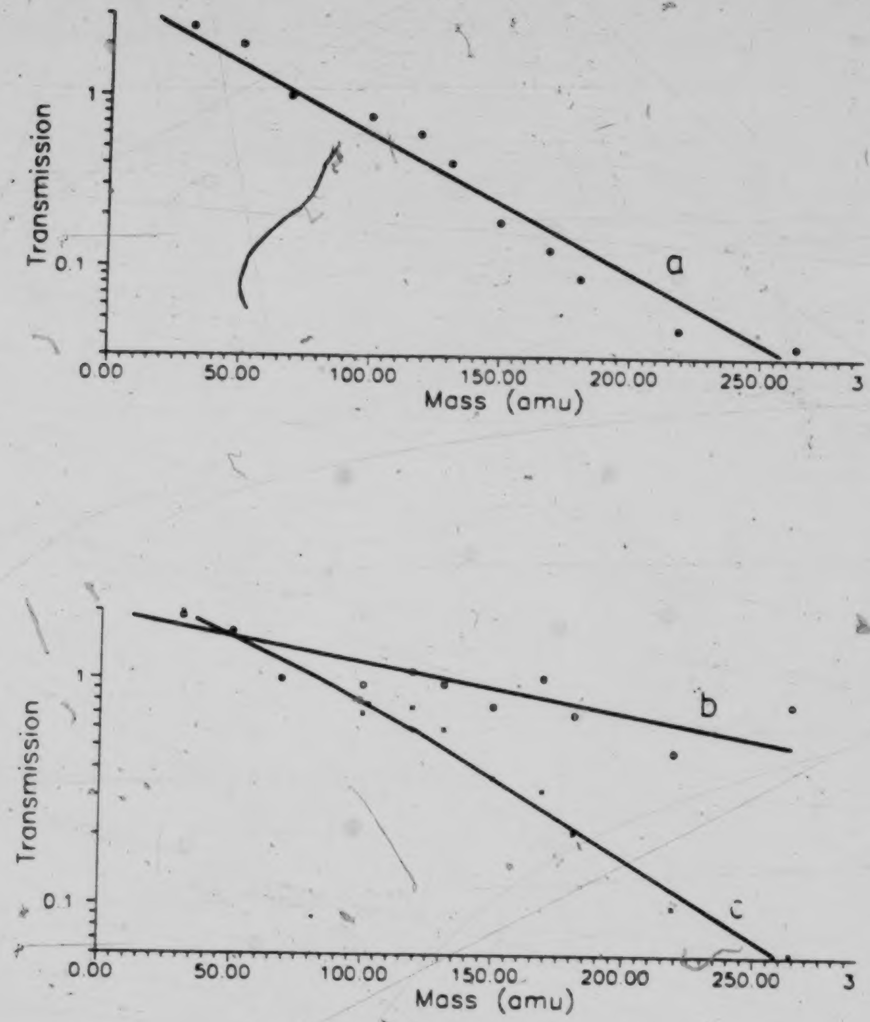

Figure 2.7 Mass calibration curve for the quadrupole mass spectrometer. Transmission is equal to the ratio of the normalized intensity of the quadrupole divided by the normalized intensity of the magnetic instrument. a) High mass Q-head b) Low mass Q-head. Resolution set at M/ΔM = 100 c) Low Mass Q-head. Resolution set at M/ΔM = 175.

sampled. The diffusion coefficient of an ion is inversely proportional to the square root of the reduced mass of the ion and gas molecules. With methane (M.W.= 16) as the bath gas, the differences in the reduced mass for ions with considerably higher masses will be insignificant. If we look at two ions of mass 50 and 200, the square root of the reduced mass is 3.48 and 3.36 respectively. This is a difference of less than 4%. In most cases the difference will be even smaller as the ions studied will have masses that are closer together.

The second condition requires molecular flow through the ion exit slits. Under molecular flow the ions do not undergo collisions while effusing through the slits and therefore no serious distortion of the ion population will occur. Also, molecular flow is needed to avoid cooling due to adiabatic expansion of the gas into vacuum. Molecular flow occurs when the mean free path of the molecules is larger than the dimension of the orifice. The mean free path, l, of methane is given by equation 2.1

$$l = 1/(2\pi d^2 n) \qquad [2.1]$$

where d is the molecular diameter of the gas and n is the number density of the gas. The mean free path of methane at 3 torr and 300 K is 1.4×10^{-3} cm. The dimensions of the ion exit slit are 2.0×10^{-3} cm x 0.1 cm. This should result in the flow through the ion exit slits being near molecular.

2.8 Experimental Procedure

The general procedure for the collection of ion intensity profiles is given here. The reaction mixture was allowed to mix in the 5 liter bulb for 15-20 minutes. After the mixture reached thermal equilibrium in the bulb it was allowed to flow through the ion source at a pressure of about 3 torr. Once the pressure in the ion source had stabilized, the focus of the electron beam was fine tuned by adjusting the focus of the beam until the maximum intensity of an ion was obtained. The ion used in the focusing was usually the most intense ion. Once the focusing was completed a mass spectrum was recorded. Ions of interest for which intensity profiles would be collected were identified from the mass spectrum.

During the collection of an ion intensity profile, the pressure of the ion source was kept constant to within one percent. This could be readily achieved for the duration of a single run as long as the pressure had stabilized prior to the run. A similar pressure was maintained as each subsequent ion profile was collected. For example, if the first ion profile was collected at an ion source pressure of 3 torr, then the subsequent profiles would be collected between the pressures of 2.97-3.03 torr. 5000-20000 scans,i.e. electron pulses, were used to obtain the intensity-time profile for a given ion. The larger number of scans was used for ions of low intensity. 512 channels of the multiscaler were used for each ion profile. With a dwell time for each channel of 4 μs, this gave a window of about 2 ms for the collection of the ion intensity profile. This window could be lengthened or shortened by changing the dwell time for each channel or by changing the number of channels that were used for the collection of the ion intensity profile. Once the ion intensity profile was collected it was stored in the computer to be analyzed at a later time.

CHAPTER 3

Kinetics and Thermodynamics of the protonation reaction: $H_30^+(H_2O)_h + B = BH^+(H_2O)_b + (h\text{-}b+1)\ H_2O$ where B are Nitrogen, Oxygen, and Carbon Bases.[1]

3.1 Introduction

Studing ion molecule reactions in the gas phase leads to thermochemical information that is free of solvent effects. By comparing the data from the gas phase to that for the same reaction in solution leads to infromation on the ion-solvent interaction (12,53). The of proton transfer reactions from partially solvated ions provides an insight into the effects of solvation on the proton transfer reaction. In the following study we look at the effects of solvation on the kinetics and thermodynamics of the proton transfer reaction.

The reason for this study arose out of an experimental study of the sensitivity of various compounds in a commercial atmospheric pressure chemical ionization (APCI) analytical mass spectrometer (54, 55). In the APCI source trace organic analyte compounds present in atmospheric air, B, are protonated by the reagent ions $H_3O^+(H_2O)_h$ to form BH^+ ions. Ionization of moist air initiates a sequence of ion/molecule reactions that result, within milliseconds, in the formation of hydronium ion water clusters, $H_3O^+(H_2O)_h$. A simplified reaction scheme is given by equations 3.1-3.5. The hydronium ion-water clusters undergo successive clustering.

$$e^- + N_2 = N_2^+ \overset{N_2}{=} N_4^+ \overset{O_2}{=} O_2^+ \qquad [3.1]$$

$$e^- + O_2 = O_2^+ \overset{O_2}{=} O_4^+ \qquad [3.2]$$

$$O_2^+, O_n^+ + H_2O = O_2^+(H_2O) \qquad [3.3]$$

$$O_2^+(H_2O) + H_2O = O_2^+(H_2O)_2 = H_3O^+(OH) + O_2 \qquad [3.4]$$

$$H_3O^+(OH) + H_2O = H_3O^+(H_2O) + OH \qquad [3.5]$$

$$H_3O^+(H_2O) + H_2O = H_3O^+(H_2O)_2 \qquad [3.6]$$

$$H_3O^+(H_2O)_{h-1} + H_2O = H_3O^+(H_2O)_h \qquad [3.7]$$

In this way an equilibrium cluster distribution is attained. At 25C and with 5 torr partial pressure (Relative humidity, RH = 21%) the majority of the clusters contain from 5 to 8 water molecules at thermal equilibrium (56). These hydronium ion-water cluster ions are the main reagent ions in positive ion APCI and protonate molecules with gas-phase basicities (GB) higher than that of water according to the general reaction 3.8.

$$H_3O^+(H_2O)_h + B = BH^+(H_2O)_b + (h-b+1)H_2O \qquad [3.8]$$

$$BH^+(H_2O)_{h-1} + H_2O = BH^+(H_2O)_h \qquad [3.9]$$

At the relatively high water pressure arising from the ambient humidity of the laboratory air (5 torr) and the low analyte pressures (10^{-6} torr), the protonation reaction 3.8 is relatively slow compared to the hydration (clustering) reaction 3.7 of H_3O^+ and reaction 3.9 for BH^+. Thus the reagent ions, $H_3O^+(H_2O)_h$, are at their equilibrium hydrate populations and the protonation of B is followed by the rapid achievement of the $BH^+(H_2O)_b$ equilibrium populations.

The APCI method is very well suited for the detection of trace compounds such as pollutants in air. However, it suffers from the problem that the sensitivity of different classes of compounds can be very different. In particular some environmentally important compounds like mercaptans, thioethers, thiophenes and halobenzenes are detected with very low sensitivity.

It was the purpose of this study to determine the reasons for the different sensitivities exhibited by different classes of compounds and to find better conditions to correct for these problems. While the study was done to understand the factors governing the APCI sensitivities, the findings are of more general interest. The change in reactivity of ion clusters like $H_3O^+(H_2O)_h$ with the degree of hydration, or general solvation, are of fundamental significance (57-63). Also the stability of the hydrates $BH^+(H_2O)_b$ are important in determining the sensitivities and this fact leads into the general area of gas phase ion solvation (16).

The efficiency of protonation by $H_3O^+(H_2O)_h$ of compounds B present as traces in the atmosphere is not only of interest in the analytical APCI technique. The $H_3O^+(H_2O)_h$ species are the major naturally occurring ions in the tropo- and stratosphere as well as the D region of the ionosphere (64). The $BH^+(H_2O)_b$ ions resulting from protonation of traces of B can be detected with air or rocket borne mass spectrometers and can be used as probes for the presence of traces of B (64). Examples of possible atmospheric B are CH_2O, CH_3OH, HNO_3, and NH_3. In order to relate the observed abundance of $BH^+(H_2O)_b$ to the unknown concentration of B one needs to understand the kinetics and thermodynamics of the protonation reactions. A laboratory study of the protonation of B by $H_3O^+(H_2O)_h$ undertaken with the purpose of identifying the possible core ions BH^+ and thus the precursors of the stratospheric ions (64), was reported by Ferguson and co-workers (65). Their investigation dealt only with B= CH_3OH and CH_2O and $H_3O^+(H_2O)_h$ with $h \leq 3$, since these were relevant in the stratosphere. The present work provides data for a larger number of compounds and for higher values of h. Thus, it extends the laboratory data towards conditions present in the lower stratosphere and particularly the troposphere.

3.2 Experimental

The experiments were preformed on a pulsed high pressure mass spectrometer which utilized a quadrupole (described in chapter 2) for mass analysis and an ion counting and multiscalar system for real time resolution of the ion signal.

The experiments were generally performed at 3 torr total pressure. Ultrahigh purity (99.99%) methane was used as the major gas. The water used was from the departmental distilled water reservoir and then redistilled with potassium dichromate. Reagent grade analytes were used without further purification with the exception of furan and thiophene which were distilled with the retention of the middle fraction.

Typical conditions in the PHPMS were P_{CH4} = 2 torr, P_{H2O} = 1 torr and P_B = 10^{-5} torr. The total pressure in the ion source was usually kept at 3 torr and the temperature at 32C. Approximately 4 x10^{-5} torr of CCl_4 was added to all the reaction mixtures. The dissociative electron capture, $e^- + CCl_4 = Cl^- + CCl_3$, leads to ambipolar positive ion-negative ion diffusion which is slower than positive ion-electron diffusion and improves the condition for the measurements (66). For some experiments the pressures and temperatures were varied in order to change the distrubtion of the reactants. These conditions are described in the results and discussion section.

3.3 Results and Discussion

3.3.a Factors Responsible for the Different Proton Transfer Efficiencies from $H_3O^+(H_2O)_h$ to Compounds B

The sensitivities of several bases relative to a high sensitivity compound (pyridine = 1) measured in a commercial atmospheric pressure chemical ionization (APCI) mass spectrometer (54) are plotted against their gas phase basicity in Figure 3.1. The bases in this figure can be divided into three groups. Compounds with gas phase basicity, GB, greater than 200 kcal/mol have high sensitivities which are relatively constant. This group is made up of mostly nitrogen bases and will be called the K group (kinetic control). The reason for the names will be discussed later. The second group consists of bases whose sensitivities vary with the gas phase basicities (GB < 200 kcal/mol). These bases are mainly oxygen bases. This group is called the T group (thermodynamic control). The third group is all the bases that have low sensitivities compared to bases with similar GB. This group is called the L group and is made up of mainly carbon bases.

The sensitivities for some representative compounds are shown in Table 3.1. The sensitivities of these compounds is proportional to the extent of the proton transfer from $H_3O^+(H_2O)_h$ to B in reaction 3.8.

$$H_3O^+(H_2O)_h + B = BH^+(H_2O)_b + (h-b+1)H_2O \qquad [3.8]$$

The conditions in the APCI MS for which these bases were studied were P_{air} = 700 torr, P_{H2O} = 7 torr (natural humidity) and $P_B < 10^{-6}$ torr, ion reaction time approximately 300 μs and room temperature. Reaction 3.8 was studied in a PHPMS for the bases in Table 3.1. The conditions in the APCI could not be reproduced but at

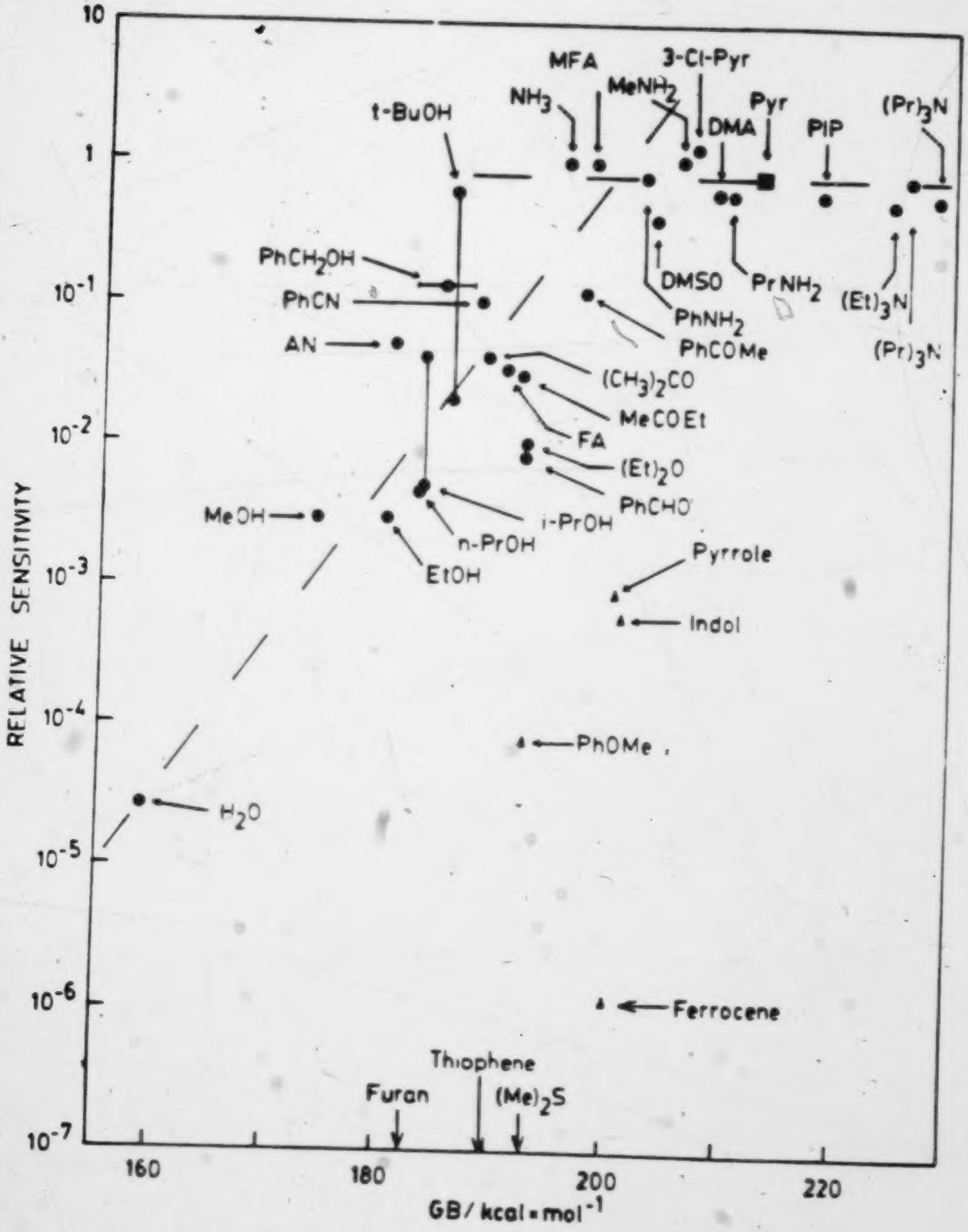

Figure 3.1 Sensitivity, relative to pyridine, in APCI source for analytes B as a function of gas phase basicity, GB(B), at room temperature.

TABLE 3.1

a) for reaction 8 at 32C, 1 torr H_2O, 2 torr CH_4

b) gas phase basicities at 27C from Lias et al (22)

c) total rate constants for proton transfer from $H_3O^+(H_2O)_h$ to B. Since h = 4 and h = 5 are dominant and of nearly equal concentrations k_a corresponds mainly to the proton transfer from these two hydrates.

d) $R_{eq} = \dfrac{\Sigma I\{H_3O^+(H_2O)_h\}\ P_B}{\Sigma I\{BH^+(H_2O)_b\ P_{H2O}}$

Observed at proton transfer equilibrium, for 32C and 1 torr water pressure and variable B pressure.

e) rate constant for proton transfer from $H_3O^+(H_2O)_3$ to B in (molecules^{-1} s^{-1} cm^3)x10^9. From Bohme (57)

f) Sensitivities observed with APCI apparatus at same temperature but 7 torr H_2O from Sunner (54). K, T, L stand for Kinetic, Thermodynamic control Low sensitivity, respectively.

g) Rate constants could not be measured at this temperature and water pressure since equilibrium shifted too far in favour of $H_3O^+(H_2O)_h$

h) R_{eq} could not be determined due to the presence of low concentration high GB impurities in pyrrole.

i) Free energy change for reaction: $H_3O^+(H_2O)_6 + B = BH^+(H_2O)_6 + H_2O$ at 32C.

j) thio = thiophene, pyr = pyrrole, py = pyridine, pip = piperidine.

TABLE 3.1

Total Rate Constant k_a and Equilibrium Ratio R_{eq} for Proton Transfer Reactions[a]

B	GB(B)[b]	R_{eq}[d]	$\Delta G^{o}_{6,6}(PT)$[i]	$K_a(PT)$[c]	$K_8(PT)$[e]	SENS[f]
MeOH	174	340	-6	g	1.7	$3X10^{-3}$T
EtOH	180	2730	-7	1.9	1.7	$3X10^{-3}$T
MeCN	181	8500	-8	3.0	-	$6X10^{-2}$T
furan	185	<4	(+27)	g	-	$<10^{-7}$ L
t-BuOH	186	27500		1.7	-	-- T
Me_2CO	189	31000	-6	3.0	2.9	$2X10^{-2}$T
thio	190	<7	(+23)	g	-	$<10^{-7}$ L
Et_2O	192	15000	(-7)	1.4	-	10^{-2} T
pyr[j]	200	h	(+8)	0.003	-	10^{-3} L
3-Clpyr	207	$8x10^6$	(-6)	1.6	-	1.2 K
py[j]	213	$>10^7$	-11	1.7	-	1 K
pip[j]	218	$>10^7$	(-16)	2.0	-	0.9 K

the conditions of P_{total} = 2.5-4.5 torr, P_{H2O} up to 1 torr and P_B down to 10^{-5} torr were found to give valuable insights into the factors responsible for the different sensitivities of the different groups of bases.

An ion profile for a typical K group compound, pyridine is shown in Figure 3.2. The $H_3O^+(H_2O)_h$ ions, which are in rapid clustering equilibrium (reaction 3.10) and thus at constant ratio, are not shown individually. All the H_3O^+ hydrates decrease at the same rate due to proton transfer to pyridine (reaction 3.8). The protonation products of reaction 3.9 are rapidly hydrated and reach equilibrium via reaction 3.11.

$$H_3O^+(H_2O)_h + H_2O = H_3O^+(H_2O)_{h+1} \quad [3.10]$$

$$BH^+(H_2O)_b + H_2O = BH^+(H_2O)_{b+1} \quad [3.11]$$

$$BH^+ + B = B_2H^+ \quad [3.12]$$

Reaction 3.12 accounts for the formation of the proton bound dimer, B_2H^+, which is evident in Figure 3.2. It is also apparent that the $H_3O^+(H_2O)_h$ ions disappear completely while the B_2H^+ and $BH^+(H_2O)_b$ reach equilibrium at long times. With the higher pressures of water, lower analyte pressures and a 300 µs residence time found in the APCI source one expects the B_2H^+ ion to be a minor product and the $BH^+(H_2O)_b$ will be the major product.

Plots of lnI vs time for the ion intensities from the normalized plots, as in Figure 3.3, lead to the average pseudo first order rate constant $v_a = k_a[B]$, for the proton transfer of reaction 3.8 from this value, the average rate constant k_a for reaction 3.8 can be evaluated since the [B] is known. The rate constant for pyridine is $k_a = 1.7 \times 10^{-9}$ molecules^{-1} s^{-1} cm^3 for the conditions in Figure 3.1, this is close to the orbiting collision limit, i.e. k_{ADO}, which can be evaluated with the average dipole orientation theory (See Chapter 1).

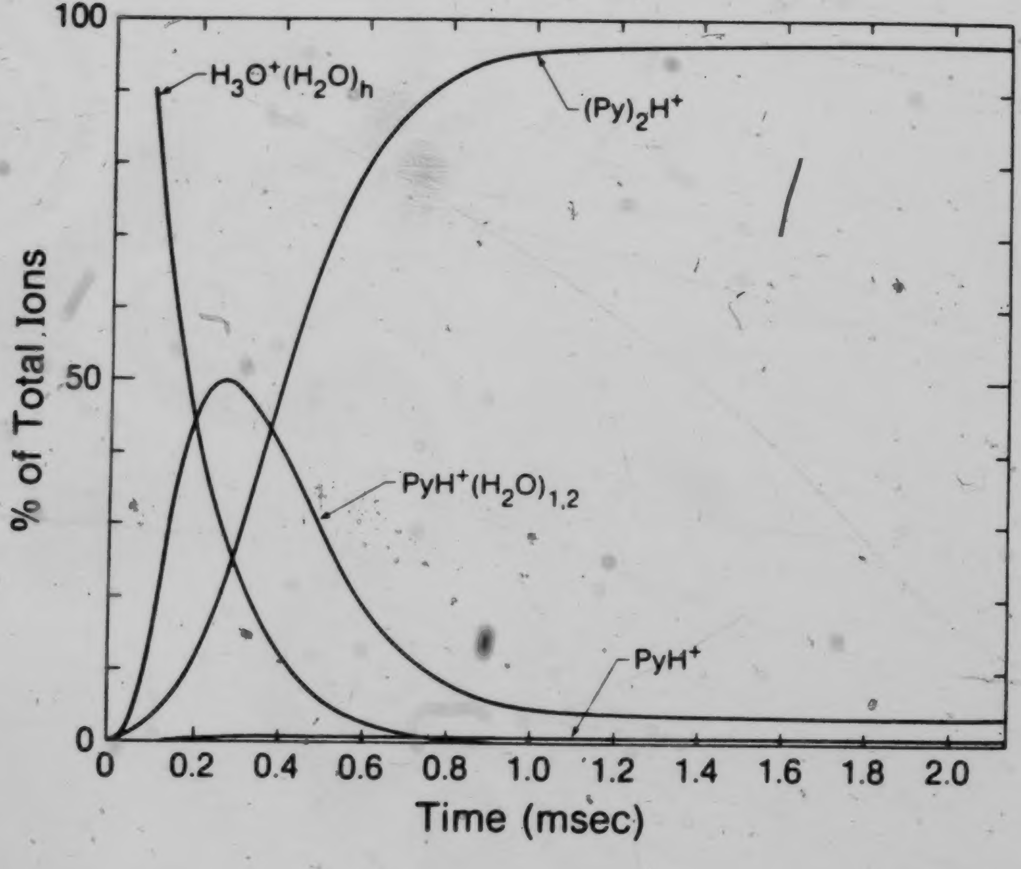

Figure 3.2 Typical time dependence of kineticly controlled ions. Conditions: T_{is} 32C, P_{CH4} = 2 torr, P_{H2O} = 1.1 torr and $P_B = 10^{-4}$ (B = pyridine). The $H_3O^+(H_2O)_h$ ions maintain hydration equilibrium as they protonate B.

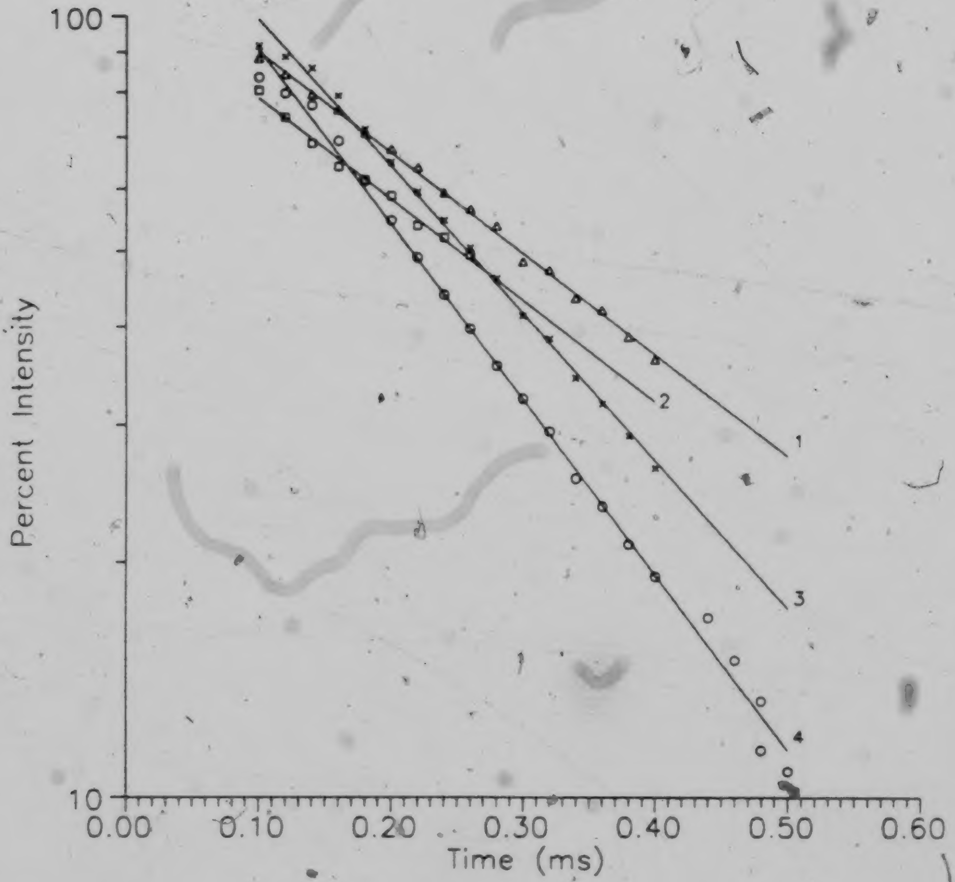

Figure 3.3 Rate constant determination for the proton transfer: $H_3O^+(H_20)_h + B = BH^+(H_2O)_b + h\text{-}b+1\ H_2O$, where B= a) diethyl ether; b) acetone; c) piperdine; and d) pyridine. Conditions: $T_{is} = 305K$, $P_{CH4} = 2$ torr, $P_{H2O} = 1.1$ torr, P_B =(a = 7 x10^{-5}; b = 6 x10^{-5}; c = 8 x10^{-5}; d = 1 x10^{-4}) torr. Deduced rate constants (a = 1.4; b = 3.2; c = 2.0; d = 1.7) x10^{-9} molecules^{-1} cm^3 s^{-1}.

At much lower [B] ($P_B = 10^{-6}$ torr, [B] = 3×10^{10} molecules cm^{-3}) and shorter reactions times (t = 300us) found under APCI conditions, the proton transfer, reaction 3.8, will be very incomplete; i.e. only a small fraction of the $H_3O^+(H_2O)_n$ ions will have had time to react. This fraction can be calculated with equation 3.13.

$$\frac{\Delta H_3O^+(H_2O)_n}{H_3O^+(H_2O)_n} = k_1[B]\,t \qquad [3.13]$$

Substitution of the numerical values leads to a value of 1.5×10^{-2}, indicating that less than 2% of the $H_3O^+(H_2O)_n$ ions react under APCI conditions. Because the [B] and the reaction time is the same for all bases the only difference is the rate constant. That is the extent of the proton transfer reaction has a kinetically controlled upper limit. The sensitivity for bases such as pyridine will depend upon the rate constant for reaction 3.8. The similar sensitivities for these compounds is due to the similarity in the rate constant for reaction 3.8 (see Table 3.2) expected for collision limited rates (34). For reactions that occur at every collision, exhibited by the K group compounds, there is a maximum rate constant, k_{ADO}.

Figure 3.4 shows a typical ion profile for the T group with B = acetone. Proton transfer leads to rapid decrease in the $H_3O^+(H_2O)_h$ ions and an increase in $BH^+(H_2O)_b$ followed by the formation of B_2H^+ and $B_2H^+(H_2O)_b$ ions. This is similar to the situation with pyridine except that the $H_3O^+(H_2O)_h$ ions do not disappear but reach an equilibrium with the $BH^+(H_2O)_b$ ions after about 500 us. From the initial decrease of the $H_3O^+(H_2O)_h$ ions, an average rate constant $k_a = 3.2\times10^{-9}$ molecules^{-1} s^{-1} cm^3 (Figure 3.3) can be obtained. This is in agreement with the expected collision limited rate (k_{ADO}) (See Table 3.2). Rate constants for other compounds of the T group are also in Table 3.2 and one can see that all are in agreement with the collision limited rate.

TABLE 3.2

ADO Rate Constants for the Reaction:

$$H_3O^+(H_2O)_h + B = BH^+(H_2O)_b + h\text{-}n\text{+}1\ H_2O$$

$$k_{ADO} = (2\pi q/\mu^{1/2})(\alpha^{1/2} + c\mu_D(2/(\pi kT))^{1/2})$$

B	$\mu(g)^c$	c	$\mu_D \text{x} 10^{18a}$	a^b	$k_{ADO} \text{x} 10^{9d}$	$k_a \text{x} 10^{9d}$
MeOH	24.2	0.219	1.71	3.23	1.5	
EtOH	31.5	0.195	1.73	5.50	1.6	2.2
MeCN	29.1	0.260	3.97	4.86	2.7	3.0
Furan	40.5	0.081	0.71	8.29	1.1	
tBuOH	42.5	0.169	1.67	10.0	1.7	1.7
Me_2CO	36.7	0.229	2.86	7.0	2.0	3.2
Thiophene	45.7	0.034	0.51	11.3	1.3	
Et_2O	42.5	0.148	1.30	8.97	1.3	1.4
Pyrrole	40.1	.200	1.84	7.48	1.5	0.032
DMSO	43.8					2.1
Pyridine	44.1		2.2			1.6
piperidine	45.9		1.19			2.1

a) Dipole moment in Debye.

b) Polarizablity in angstroms^3.

c) for calculation of μ a value of n = 4.5 was used. This corresponds to the average value of n at 32C and 1 torr water pressure.

d) in molecules^{-1} cm^3 s^{-1}

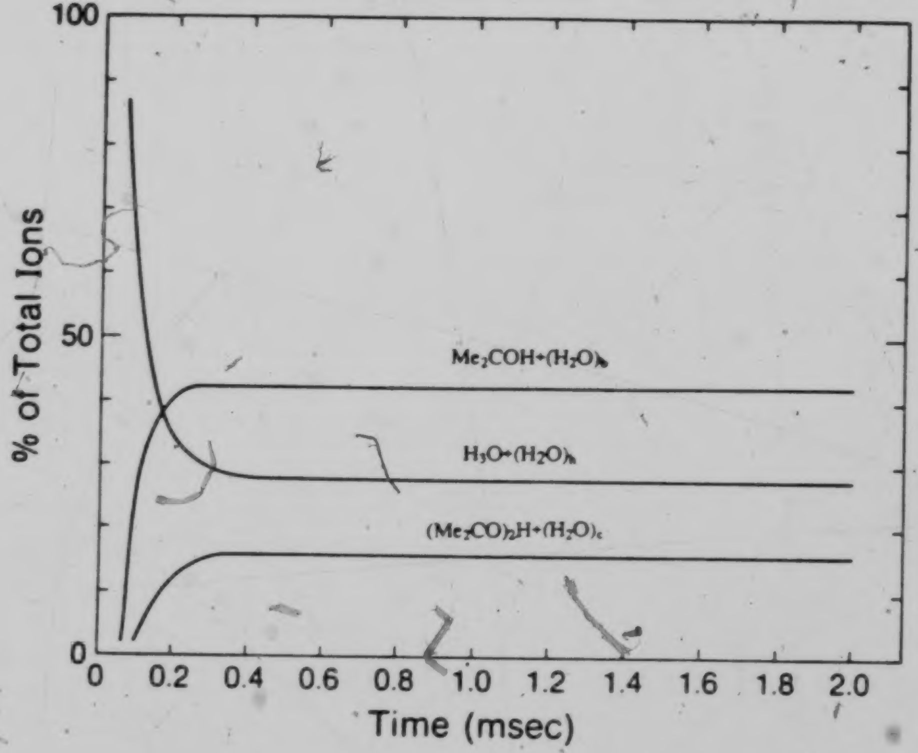

Figure 3.4 Typical time dependence of the thermodynamically controlled ions. Conditions: T_{is} = 32C, $P_{CH4} \geq 2$ torr, P_{H2O} = 1.1 torr and $P_B = 6 \times 10^{-5}$ torr (B = acetone). The $H_3O^+(H_2O)_h$ maintain hydration equilibrium as they proton transfer to B. The water hydrates and the acetone hydrates reach equilibrium at approximately 0.5 ms.

For the high water pressures and low analyte pressures in the APCI source, the proton transfer equilibria will be shifted farther to the reactants than for the conditions in Figure 3.4. Under the APCI conditions the equilibrium is attained faster than in Figure 3.4 due to the large concentration of water; that is, the equilibrium will be reached in less than 300us. This means that the extent of proton transfer for reaction 3.8 for compounds like acetone will be controlled by the thermodynamics of reaction 3.8. Although the K and T group compounds are protonated at the same rate, k_{ADO}, The extent of the proton transfer to the T group compounds is limited because an equilibrium is reached where the back reaction occurs and lowers the attainable sensitivity. For the T group, sensitivity is thus determined by the equilibrium constant which is in turn determined by the reaction thermodynamics.

The ion profile for a low sensitivity compound, B = furan, is shown in Figure 3.5. The proton transfer equilibrium for reaction 3.8 is reached rapidly and the $BH^+(H_2O)_b$ ions at equilibrium are much less abundant than was the case for acetone even though in the present case the P_B is 5 times larger and the water pressure is 10 times smaller. The proton transfer equilibrium is shifted much farther to the $H_3O^+(H_2O)_h$ side than for acetone even though the two compounds have essentially the same GB (Table 3.1). Similar results were obtained with the PHPMS for other L group compounds which are characterized by thermodynamic control but the equilibrium is shifted far to the water side. At higher temperatures where the hydration is much weaker we see the equilibrium shift in favour of furan (Figure 3.6).

A decisive clue to the reason for the unfavorable equilibrium position for the L group compounds was the observation that the hydrates $BH^+(H_2O)_b$ of these compounds have very low b, b = 0 or 1, compared to the T group where b = 3 and 4 for acetone. The consequences of the lower stability of the hydrates for the L group are discussed later.

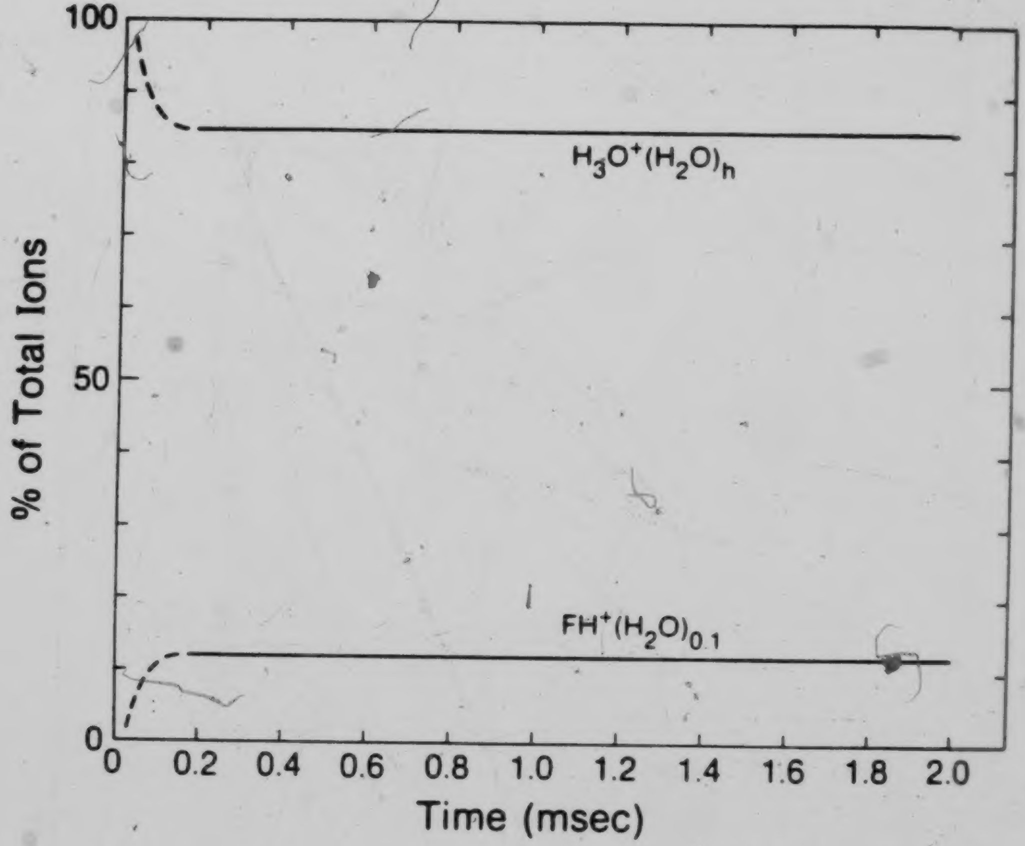

Figure 3.5 Typical time dependence of the relative intensity of the ions for the low sensitivity compounds. Conditions: T_{is} = 32C, P_{CH4} = 3 torr, P_{H2O} = 0.1 torr and P_{Furan} = 3 x10^{-4} torr. The $H_3O^+(H_2O)_h$ maintain hydration equilibrium as they proton transfer to B. The protonated water and the furan hydrate ions reach an equilibrium in approximately 0.1 ms. The reason for the unfavorable position of the equilibrium is the inefficient hydration of the protonated furan ions (see text).

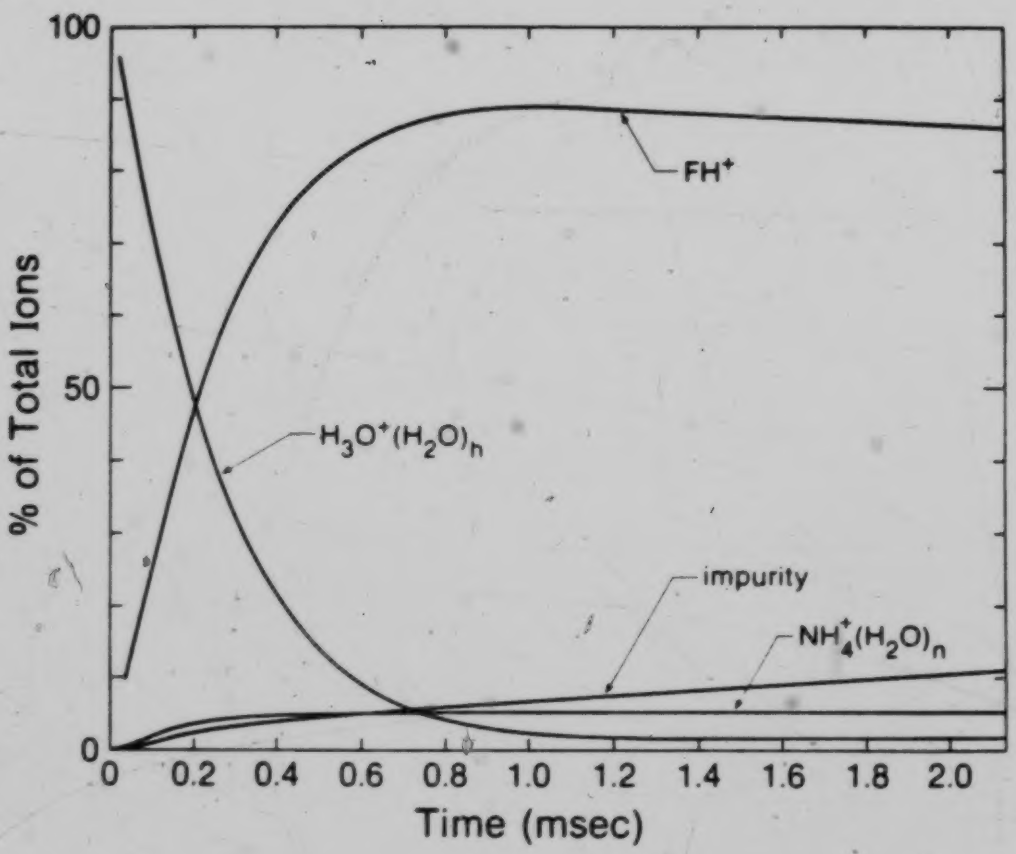

Figure 3.6 Observed time dependence for B = furan at 198C. Conditions: T_{is} = 198C, P_{CH4} = 2 torr, P_{H2O} = 1.1 torr and P_{Furan} = [illegible]x10^{-3} torr. The $H_3O^+(H_2O)_h$ maintain hydration equilibrium as they proton transfer to B. Proton transfer equilibrium is shifted in favour of furan due to the lower values of h in $H_3O^+(H_2O)_h$.

3.3b Thermodynamics of proton transfer

The extent of proton transfer from $H_3O^+(H_2O)_h$ to B occurring in a limited time is dependent on the kinetics and the thermodynamics of reaction 3.8. The thermodynamics of the reaction will be discussed first as it is of significance to the kinetics also.

$$H_3O^+(H_2O)_h + B = BH^+(H_2O)_b + (h-b+1)H_2O \qquad [3.8]$$

$$\Delta G^\circ_8 = GB(H_2O) - GB(B) + \Delta G^\circ_{h,0}(H_3O^+) - \Delta G^\circ_{b,0}(BH^+) \qquad [3.14]$$

$$M^+(H_2O)_n = M^+ + n\,H_2O \qquad \Delta G^\circ_{15} = -\Delta G^\circ_{n,o}(M^+) \qquad [3.15]$$

$$M^+(H_2O)_{n-1} + H_2O = M^+(H_2O)_n \quad \Delta G^\circ_{16} = \Delta G^\circ_{n-1,n}(M^+) \qquad [3.16]$$

$$\Delta G^\circ_{n,0}(M^+) = \Delta G^\circ_{n-1,n}(M^+) + ...+ \Delta G^\circ_{1,0}(M^+) \qquad [3.17]$$

$$\Delta G^\circ_{n-1,n}(M^+) = -\Delta G^\circ_{n,n-1}(M^+) \qquad [3.18]$$

The thermodynamic data required for the evaluation of the $BH^+(H_2O)_b$ concentrations relative to the $H_3O^+(H_2O)_h$ concentrations at proton transfer equilibrium, reaction 3.8, are given in equation 3.14. Comprehensive information on the GB(B) is available in the literature (22). The $\Delta G^\circ_{0,n}$ for H_3O^+ and a number of BH^+ have also been determined previously and a recent compilation of such data is available (67). The thermodynamic data used for some of the representative compounds are given in Table 3.3.

No hydration data were available for the BH^+ ions of B = pyrrole, furan, and thiophene, which are of special interest since they are typical of low sensitivity compounds, (See Table 3.1), whose BH^+ hydrate very poorly.

The hydration equilibria for these BH^+ were studied in separate experiments. Equilibrium constants $K_{n-1,1}$ were obtained at different temperatures. The resulting

TABLE 3.3

$-\Delta G^{o}_{n-1,n}$[b]

B	GB(B)[a]	0,1	1,2	2,3	3,4	4,5	5,6
HOH	159	24.2	12.8	9.2	5.4	3.8	2.7
MeOH	174	18.4	12.1	6.9	4.9	3.5	2.6
EtOH	180	16.1	10.7	6.3	4.6	3.3	(2.5)[d]
MeCN	181	16.1	9.8	8.0	4.6	3.3	2.3
furan[c]	185	4.4[c]	-	-			
Me_2CO	189	12.6	6.5	6.0	4.2	3.1	(2.1)[d]
thiophene	190	3.9[c]					
Et_2O	192	11.8	(6.1)[d]	(5.6)[d]	(3.9)[d]	(2.9)[d]	(1.9)[d]
pyrrole[c]	200	6.9[c]	3.1[c]	(1.0)[d]	(0.0)[d]	(-1.0)[d]	(-1.5)[d]
pyridine	213	7.2	3.6	2.3	(1.3)[d]	(0.7)[d]	(0.0)[d]

a) From gas phase basicities compilation of Lias (22) in kcal per mole at 300K

b) Free energy of hydration of BH^+, see eq.9, in kcal/mol. Standard state 1 atm. 300K. From compilation of Keesee (67). $\Delta H^{o}_{n-1,n}$ and $\Delta S^{o}_{n-1,n}$, allowing evaluation of $\Delta G^{o}_{n-1,n}$ at other temperatures than those available in Keesee (67).

c) Determinations from present work (see table 3.4)

d) Rough estimate on the basis of available lower $\Delta G^{o}_{n-1,n}$ and fall off of $\Delta G^{o}_{n-1,n}$ with increasing n observed for other similar compounds in Table 3.2

van't Hoff plots are shown in Figure 3.7 and the $\Delta H^\circ_{n-1,n}$ and $\Delta S^\circ_{n-1,n}$ obtained from these plots are given in Table 3.4. (These values are in agreement with Hiraoka and co-workers (69) which were published later) As expected the hydration energies of these ions are much lower than bases of similar GB in the T group. For example the $\Delta G^\circ_{0,1}$ at 300K for protonated furan is 4.4 kcal/mol while the corresponding values for protonated MeCN and Me_2CO, which are approximately the same GB, are 16.1 and 12.6 kcal/mol respectively (See Table 3.3). The low hydrations energies for pyrrole, furan and thiophene are expected since these compounds do not protonate on the "lone" pair of the basic heteroatom: N, O, S respectively but on the ring (69-71).

The occurrence of ring protonation predominantly in the α position (See Figure 3.8) was demonstrated by Honriet, Schwarz, Schleyer and coworkers (70) on the basis of experimental (ICR) studies of the protonation of these compounds and theoretical calculations (MMDO and MNDO). These compounds are not n donors but pi donors and thus carbon bases. As a consequence of the low electronegativity of carbon and the charge delocalization, (see resonance structures of Figure 3.8), there is only a small positive charge on the hydrogen(s) and this leads to weak hydrogen bonding in $BH^+\cdots OH_2$. Another example of such weak hydration due to carbon protonation is that of substituted benzenes which were studied earlier in this laboratory (72).

It is interesting to note that protonated pyrrole hydration energies are much stronger than furan and thiophene (See Table 3.3). It has been shown for protonated oxygen and nitrogen bases that the strength of the hydrogen bond with water decreases as the gas phase basicity of the base increases (See Figure 3.9). With the GB of pyrrole being greater than that of furan and thiophene one would expect the hydration energy to be smaller. Hiraoka and coworkers (69) have explained this by showing that the hydrogen bound to the nitrogen has a greater positive charge than

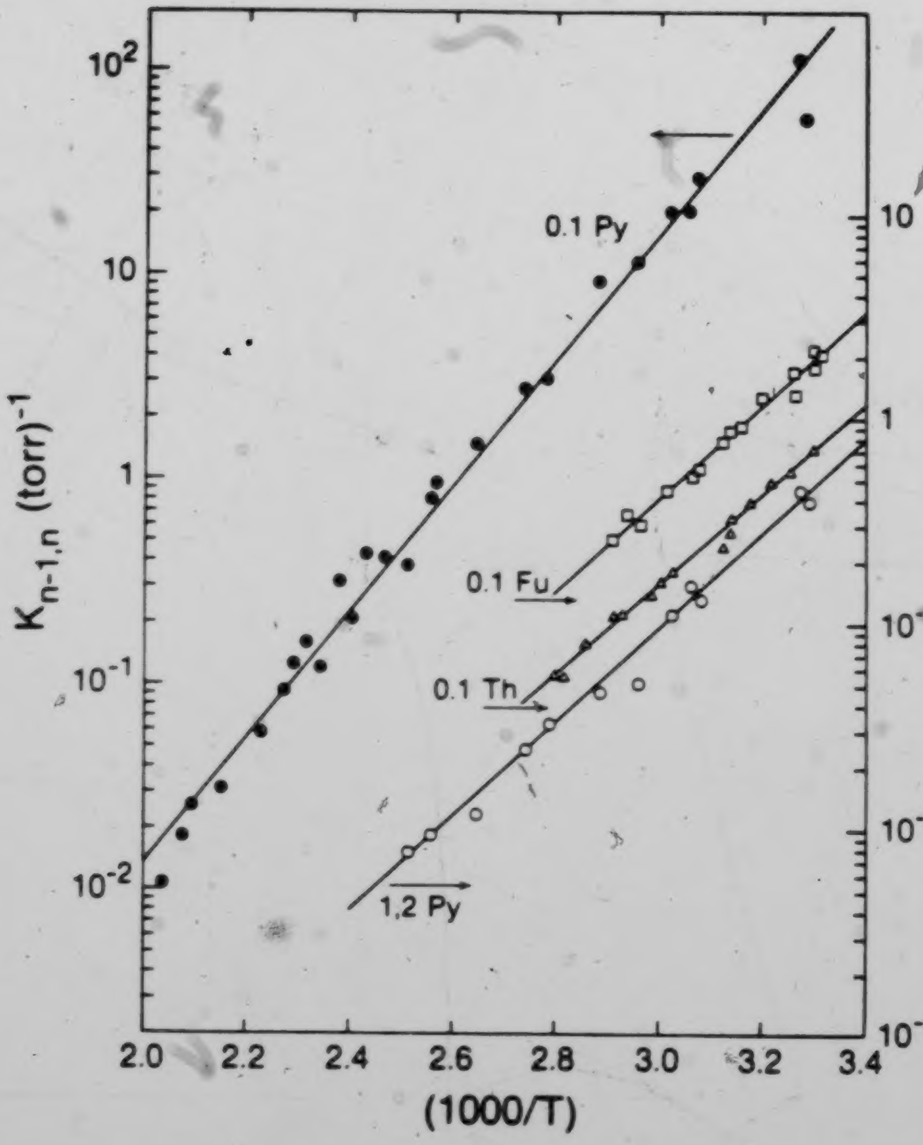

Figure 3.7 van't Hoff plots for n-1,n equilibria of hydration: $BH^+(H_2O)_{n-1} + H_2O = BH^+(H_20)_n$, for B = pyrrole, furan and thiophene. The resulting $\Delta H^\circ_{n-1,n}$ and $\Delta S^\circ_{n-1,n}$ values are given in Table 3.4

TABLE 3.4

ΔH° and ΔS° for the reaction:

$BH^+(H_2O)_n + H_2O = BH^+(H_2O)_{n+1}$

	$-\Delta H^{\circ a}$		$-\Delta S^{\circ b}$	
B\n,n+1	0,1	1,2	0,1	1,2
Pyrrole	14.0	10.4	23.3	22.6
Thiophene	10.4		20.6	
Furan	10.4		19.9	

a kcal/mol

b cal/mol K. Standard state 1 atm.

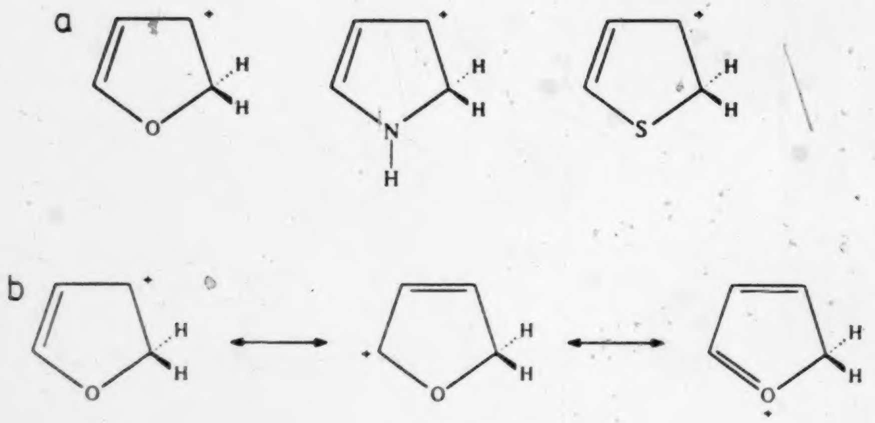
a
+
H
H
O
+
H
H
N
H
+
H
H
S
b
+
H
H
O
+
H
H
O
H
H
O
+

Figure 3.8 a) The figure shows the protonation site for pyrrole, furan and thiophene to be the α carbon and not the heteroatom. b) shows the different resonance structures for furan·H$^+$.

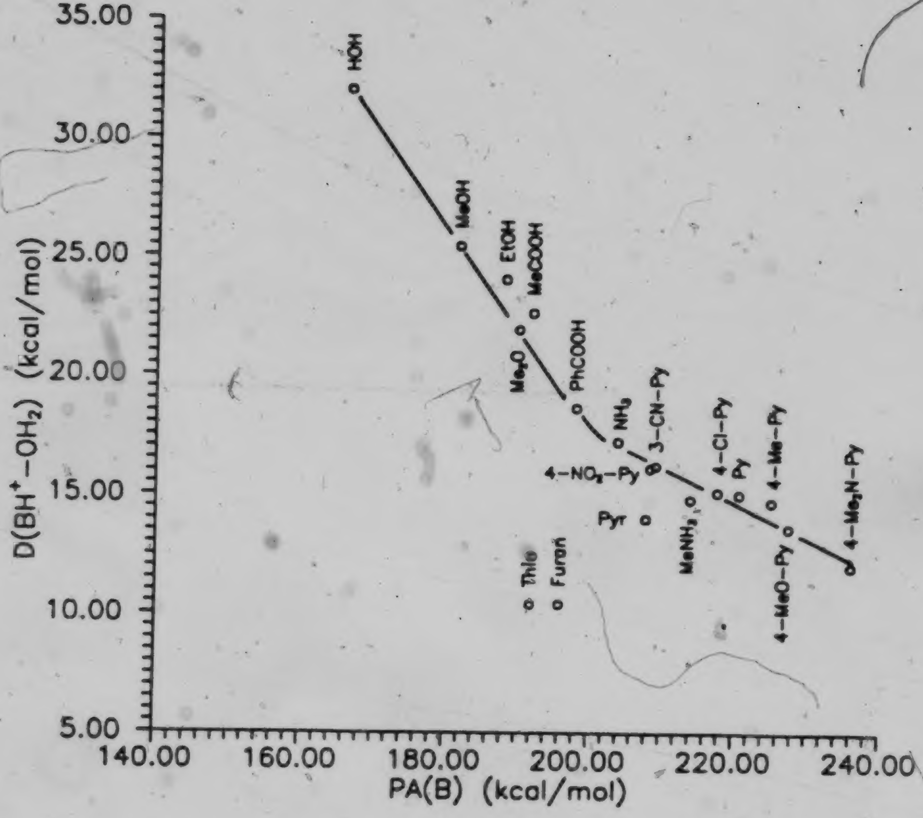

Figure 3.9 A plot of the hydration energy of protonated B as a function of gas phase proton affinity (PA(B)). The strength of the hydrogen bond decreases as the PA(B) increases. PA(B) are taken from Lias et al (22), hydration energies are taken from Keesee (67) and Davidson (68). Py = pyridine.

the carbon atom hydrogens, which is probably due to the greater electronegativity of nitrogen relative to that of carbon. It is also possible that for pyrrole.H$^+$, hydration promotes a proton migration to the nitrogen. Evidence for H$^+$ migration was given in earlier work for substituted anilines (72).

$$R_{eq} = \frac{\Sigma I\{H_3O^+(H_2O)_h\}\ P_B}{\Sigma I\{BH^+(H_2O)_b\}\ P_{H2O}} \qquad [3.19]$$

Given in Table 3.1 are also "equilibrium ratios" R_{eq}. These are defined in equation 3.19 and were measured experimentally with the PHPMS. The sum over the hydrates were obtained by summing over the corresponding ion intensities at equilibrium. It can be shown that if the water pressure is kept constant the equilibrium ratio, R_{eq}, will be constant. The R_{eq} shown in Table 3.1 are for 300K and 1 torr water pressure. The R_{eq} expresses the extent of proton transfer to B at equilibrium for variable B pressures. They are proportional to the sensitivities for the T group and L compounds for the APCI. The reason for the difference between the sensitivities for the K group and the R_{eq} measured by the PHPMS is the long residence time in the ion source of the PHPMS and this longer time causes most of the bases to be under thermodynamic control.

The R_{eq} for the poorly hydrating compounds of the low sensitivity group L are seen to be particularly low (See Table 3.1). The dependance of R_{eq} on GB(B) is shown in Figure 3.10 and follows the same trends as the results obtained with the APCI apparatus (54) which were observed at a higher water pressure (P_{H2O} = 7 torr) and are in very good agreement for the APCI results at P_{H2O} = 1 torr (Figure 3.11).

Since the hydration exothermicity for the addition of an other water molecule to $H_3O^+(H_2O)_n$ exceeds the exothermicity for the addition of water to $BH^+(H_2O)_n$ at all n, (See Table 3.2 for $\Delta G^o_{n-1,n}$ values), it is obvious that the proton transfer

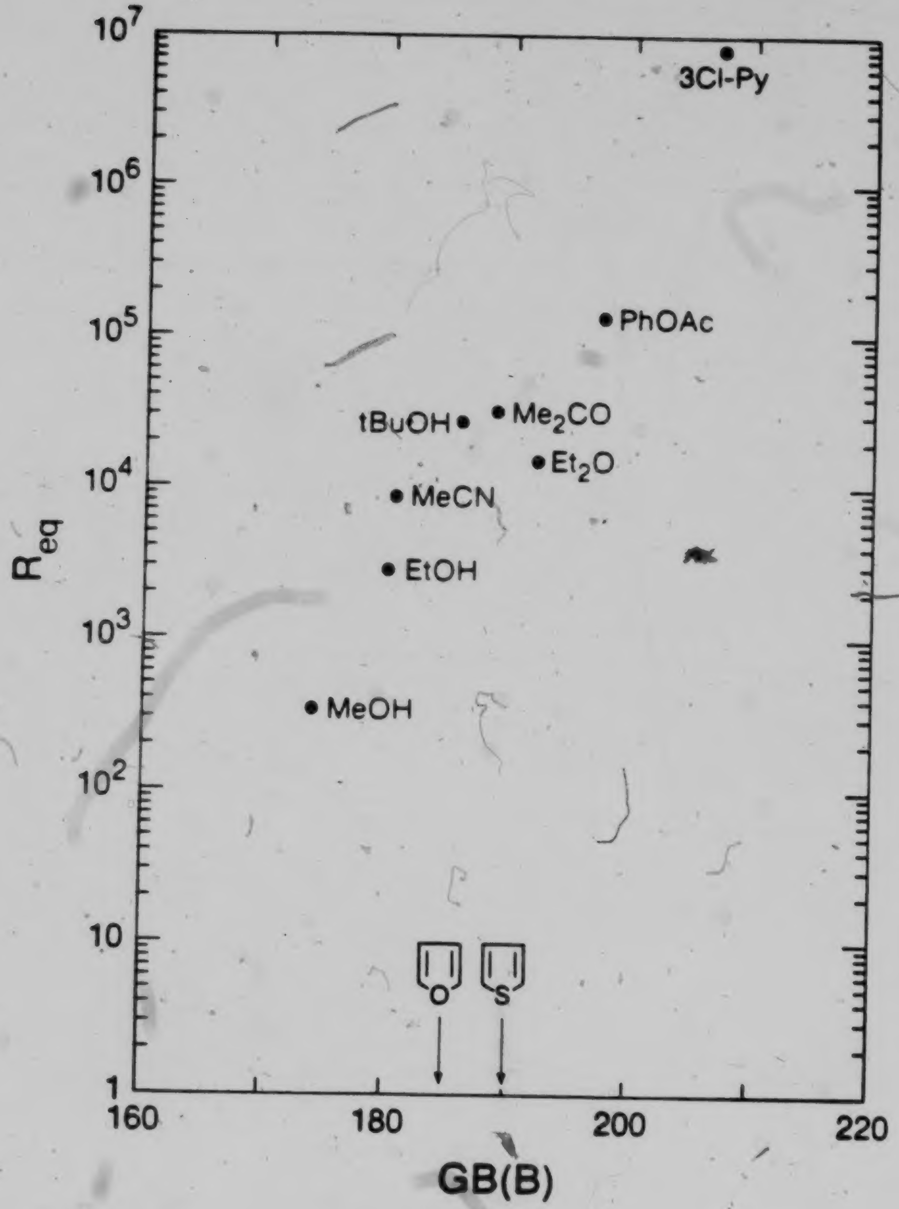

Figure 3.10 Plot of R_{eq}, an experimentally measure of the extent of reaction $H_3O^+(H_2O)_h + B = BH^+(H_2O)_b + (h-b+1)\ H_2O$, as a function of the gas phase basicity.

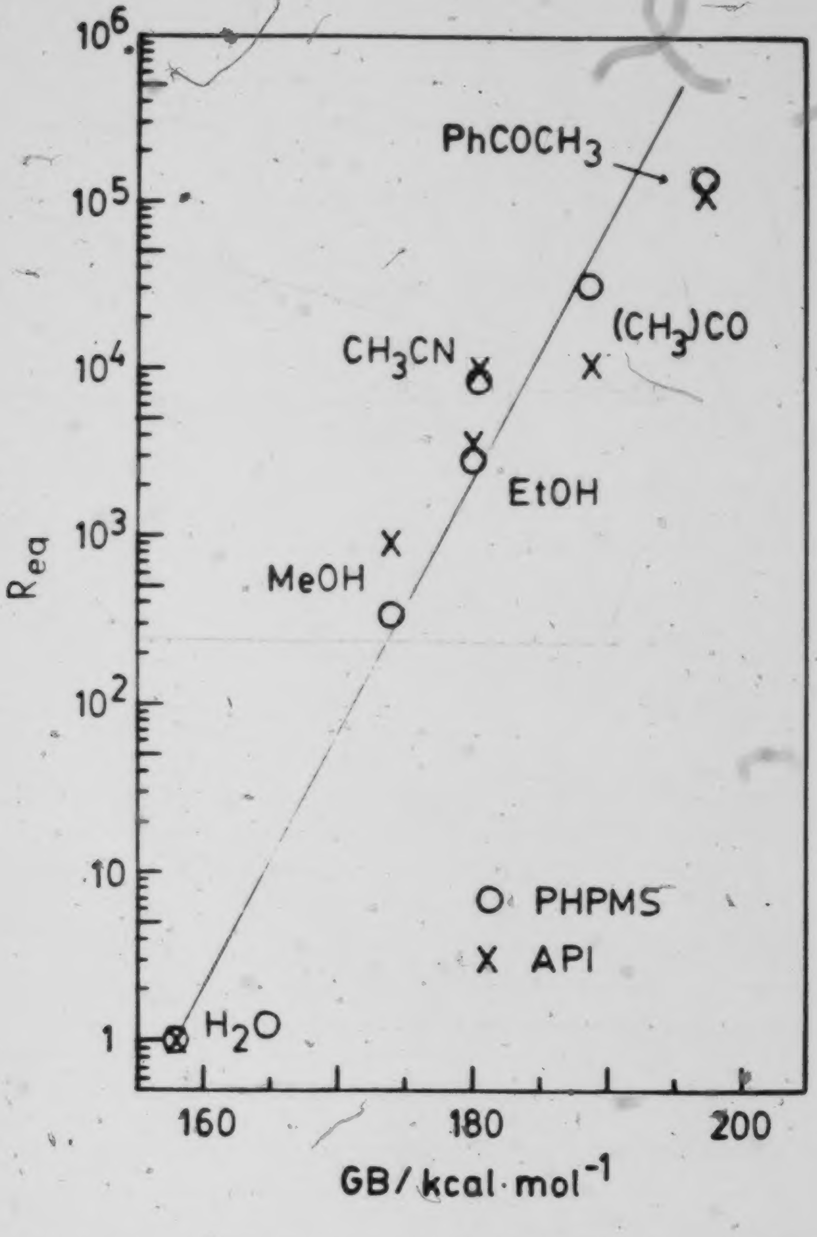

Figure 3.11 A comparison experimentally determined of R_{eq} from PHPMS and relative sensitivity (H_2O = 1) in the APCI source for room temperature and 1 torr water pressure.

equilibria will shift to be more in favour of the BH^+ hydrates when lower H_3O^+ hydrates are present as reactants. This can be achieved either by working at a higher temperature or by working at lower water pressures where only the lower H_3O^+ hydrates are stable. The effect of lowering the water pressure is not as large as the effect of higher temperature. In Table 3.5 the average number of hydrates is shown for a wide range of water pressures and temperatures. It is quite apparent that in order to achieve higher sensitivities it would be better to increase the temperature rather than lowering the water pressure. Table 3.6 shows the R_{eq} for MeOH for several different water pressures. The R_{eq} values change by only a factor of 2 over an order of magnitude change of water pressures. The R_{eq} value for thiophene changes by a factor of 1000 from 30C to 300C even though the water pressure has been increased by a factor of 10. Dramatic increases in sensitivity for the L group compounds could be achieved in the APCI method by performing the analysis of atmospheric air at elevated temperatures (55). The reason for the larger increase in sensitivity with changes in temperature as opposed to a change in water pressure is due to the sensitivity of hydration to temperature. The average value of h for 1 torr water pressure is 4.5 while that at 50 mtorr is 3.4. The average value of h at 1 torr and 198C is 2.1. This drastic change in h is the cause for the large increase in sensitivity.

3.3c Kinetics of the proton transfer to nitrogen, oxygen and carbon bases

As mention earlier, the proton transfer kinetics involved a hydration equilibrium assembly of $H_3O^+(H_2O)_h$. Plots of the $\ln[H_3O^+(H_2O)_h]$ vs. time for any h gave the same slope, $-v_a$, (See Figure 3.12) due to the fast equilibrium between the clusters, where v_a is the average pseudo first order rate constant $v_a = k_a[B]$. Rate constants k_a obtained with this procedure are given in Table 3.1 and the plots are shown in Figure 3.3 for several bases.

TABLE 3.5

Relative Distrubition of n for $H_3O^+(H_2O)_n$

for different conditions[a]

Temp	32C				
n\P_{H2O}[b]	50	100	200	500	1000
0	-	-	-	-	-
1	-	-	-	-	-
2	0.2	0.1		-	-
3	58.7	40.9	24.2	9.2	3.6
4	39.0	54.0	63.8	60.9	47.2
5	1.7	4.9	11.6	27.7	42.9
6	-	0.1	1.3	2.1	6.0
7	-	-	-	0.1	0.3
average n	3.4	3.6	3.8	4.2	4.5

Temp	54C		105C	198C
n\P_{H2O}[b]	100	1000	1000	1000
0	-	-	-	-
1	-	-	-	3.3
2	3.2	1.0	4.8	82.0
3	78.5	30.9	89.0	14.7
4	18.3	53.6	6.1	-
5	-	14.4	0.1	-
6	-	-	-	-
average n	3.2	3.8	3.0	2.1

a) Values calculated from thermodynamic data in reference (67)

b) Pressure in mtorr.

TABLE 3.6

R_{eq} for the reaction:

$$H_3O^+(H_2O)_h + B = BH^+(H_2O)_b + (h\text{-}b+1)H_2O$$

$$Req = \frac{\Sigma IBH^+(H_2O)_b \; P_{H2O}}{\Sigma IH_3O^+(H_2O)_h \; P_B}$$

	R_{eq}				
P_{H2O}[a]	50	100	200	500	1000
MeOH	650	600	520	400	340
EtOH		7900	3100	2960	2730
MeCN		26000	16000	9000	8500
tBuOH		33000	36000	37000	28750
Me_2CO			40000	30000	31000
Thiophene	55	20			
Et_2O				30500	15000
3-Cl-pyridine					$8x10^6$

P_{H2O}[a]	100	1000
T_{is}	30C	300C
Thiophene	20	22600

a Pressure in mtorr. Temperature 30C

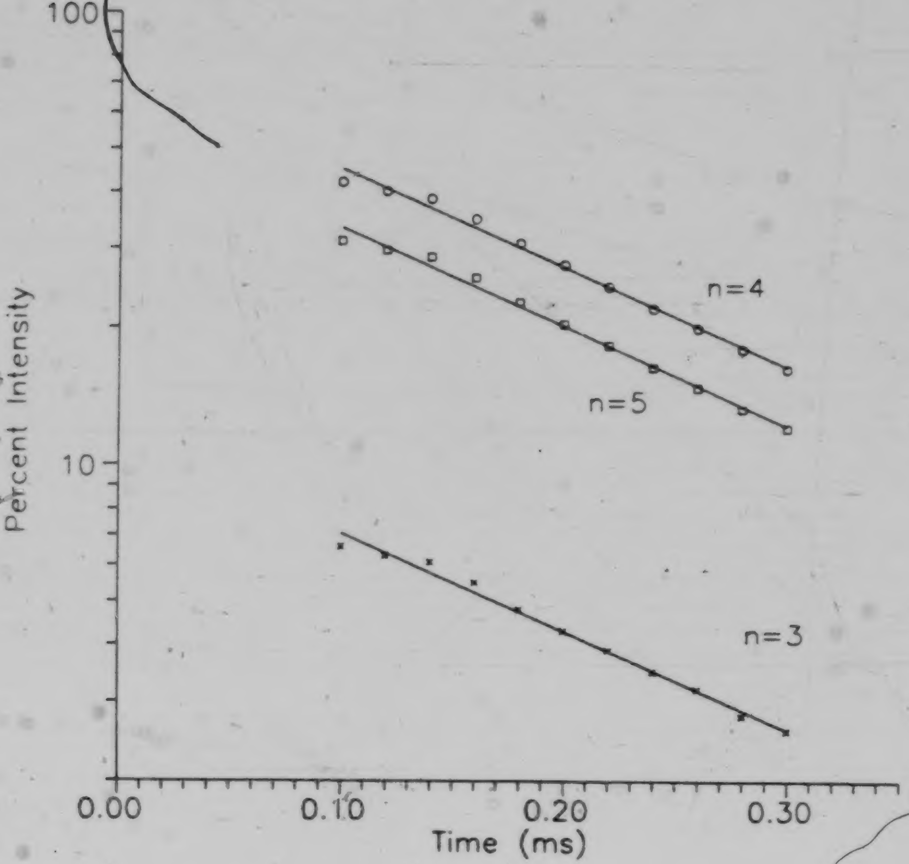

Figure 3.12 Rate constant determination for the reaction of individual protonated water clusters with pyridine: a) $H_3O^+(H_2O)_3$, b) $H_3O^+(H_2O)_4$, c) $H_3O^+(H_20)_5$. Conditions: T_{is} = 305K, P_{CH4} = 2 torr, P_{H2O} = 1.1 torr and $P_B = 10^{-4}$ torr B = pyridine. All water clusters decrease at the same rate because of the fast equilibrium between them.

The two major $H_3O^+(H_2O)_h$ ions at 1 torr and 32C are h = 4 and 5 each at about 45% of the total ion current with no base added. For hydrate distributions under different conditions for pyrrole see Table 3.7. Bohme et al (57-61) have measured rate constants for proton transfer from $H_3O^+(H_2O)_h$ to B at low H_2O pressures and high B pressures where the hydration equilibria were slow and the proton transfer is fast. This allowed rate constant determination for proton transfer from $H_3O^+(H_2O)_h$ with a given h and data for h= 0 to 3 were obtained. The rate constants for several oxygen bases (CH_2O, HCOOH, CH_3OH, C_2H_5OH, $HCOOCH_3$, CH_3COOH, $(CH_3)_2O$, $(CH_3)_2CO$) were measured. It was found that these were close to the collision rate, k_{ADO}, and decreased very little (20%) as h was increased (See Table 2 in Bohme (57)). Bohme's data for h = 3 are given in Table 3.1, wherever compounds examined in both investigations occur. It can be seen that Bohme's and the present rate constants values are close. Since the major reactants for the present study are h = 4 and 5, the present results extend the observation of collision rates to these higher hydrates.

Considering the general reaction for the proton transfer to B, reaction 3.8, a multiplicity of rate constants $k_{h,b}$ exist depending on the reactant $H_3O^+(H_2O)_h$ and the product $BH^+(H_2O)_b$. Neither Bohme's work (57-61) nor the present study allow for independent observation of the effect of b. In the absence of such direct information a meaningful examination of the proton transfer rates can be obtained through a consideration of the hydrate reaction 3.20 where n = b. The forward and reverse rates of this reaction can be expected to be able to maintain the proton transfer equilibrium and therefore one can relate directly the kinetics to the thermodynamics via equation 3.21.

TABLE 3.7

Rate constants k_a for proton transfer to pyrrole under different conditions

T_{is}	32C				
P_{H_2O}[a]	0.05	0.1	0.5	1.1	
k_a[b]	5.3	2.7	1.2	0.3	
n	%$H_3O^+(H_2O)_n$[c]				$\Delta G^o_{n,n}$[e]
0	0	0	0	0	-
1	0	0	0	0	-
2	0.7	0.7	0.1	0.01	-14.7
3	58.7	47.5	14.9	7.9	-6.1
4	38.3	47.5	61.1	50.3	-0.7
5	2.2	4.3	22.7	37.1	+4.1
6	0	0	1.2	4.4	+7.8

T_{is}	54C			105C		198C	
P_{H_2O}[a]	0.1	1.0		1.0		1.0	
k_a[b]	1.7	5.1		5.9		11.	
n			$\Delta G^o_{n,n}$[d]		$\Delta G^o_{n,n}$[d]		$\Delta G^o_{n,n}$[d]
0	0	0	-41.3	0	-41.4	0	-41.4
1	0	0	-24.28	0.1	-24.3	5.4	-24.1
2	2.3	0.3	-14.6	5.9	-15.1	81.8	-15.6
3	78.9	27.4	-7.0	80.3	-8.7	12.8	-11.0
4	18.3	60.2	-2.4	13.7	-5.7		
5	0.4	11.8	+0.7	0.1	-3.1		

a) Pressure in torr

b) in (molecules^{-1} cm^3 s^{-1}) x 10^{+10}

c) Measured abundances of $H_3O^+(H_2O)_n$ at hydration equilibria

d) Free energy for the proton transfer reaction with equal hydrates, see equation 3.12, in kcal/mol at 32C.

$$H_3O^+(H_2O)_n + B = BH^+(H_2O)_n + H_2O \qquad [3.20]$$

$$K_{20} = K_{n,n} = k_f/k_r \quad \Delta G^\circ_{n,n}(PT) = -RT\ln K_{n,n} \qquad [3.21]$$

Bohme (57) found that the rate constant, k_f, for proton transfer to oxygen bases remained close to the collision rate constant $k_c = k_{ADO}$ right down to near zero exothermicity, i.e. $\Delta G^\circ_{n,n}(PT)<0$, although only a few cases were examined and n was less than 3. The present results for EtOH, MeCN, Me_2CO, Et_2O and nitrogen bases are in accordance with this result. $\Delta G^\circ_{6,6}(PT)$ is given in Table 3.1 for the reactions. The sixth hydrate is probably the relevant one at 1 torr and 32C since $H_3O^+(H_2O)_6$ is the largest hydrate of significant concentration (See Table 3.5). In all of the above cases, $-\Delta G^\circ_{6,6}(PT)$ is negative and the k_a are near k_c. Unfortunately examples where $-\Delta G^\circ_{6,6}(PT)$ was close to zero were not obtained.

The carbon bases, furan and thiophene, have large positive $\Delta G^\circ_{6,6}(PT)$. The proton transfer equilibria were shifted far to the left, i.e., in favour of the reactants (See small R_{eq} in Table 3.1), so that the rate constants k_a could not be measured for these carbon bases. A rate constant, $k_a = 3\text{x}10^{-11}$ molecules^{-1} s^{-1} cm^3, could be obtained only for pyrrole, see Table 3.1.

When k_a becomes considerably less than k_c, proton transfer only from the lower hydrates is indicated. That is, transfer from $H_3O^+(H_2O)_n$ to the base B occurs only for n's which the proton transfer $\Delta G^\circ_{n,n}(PT)$ is still exothermic.

Kinetic measurements for the proton transfer were also made at lower water pressures where the value of h will be smaller. The plots used to determine rate constants for pyrrole at different water pressures are shown in Figure 3.13. The rate constants are given in Table 3.7 together with the $\Delta G^\circ_{n,n}(PT)$ for all the relevant $H_3O^+(H_2O)_h$ present under these conditions. $k_c = k_{ADO}$ for pyrrole can be calculated as: $k_{ADO} = 1.6\text{x}10^{-9}$ molecules^{-1} s^{-1} cm^3 (see Table 3.2). The measured k_a increases by

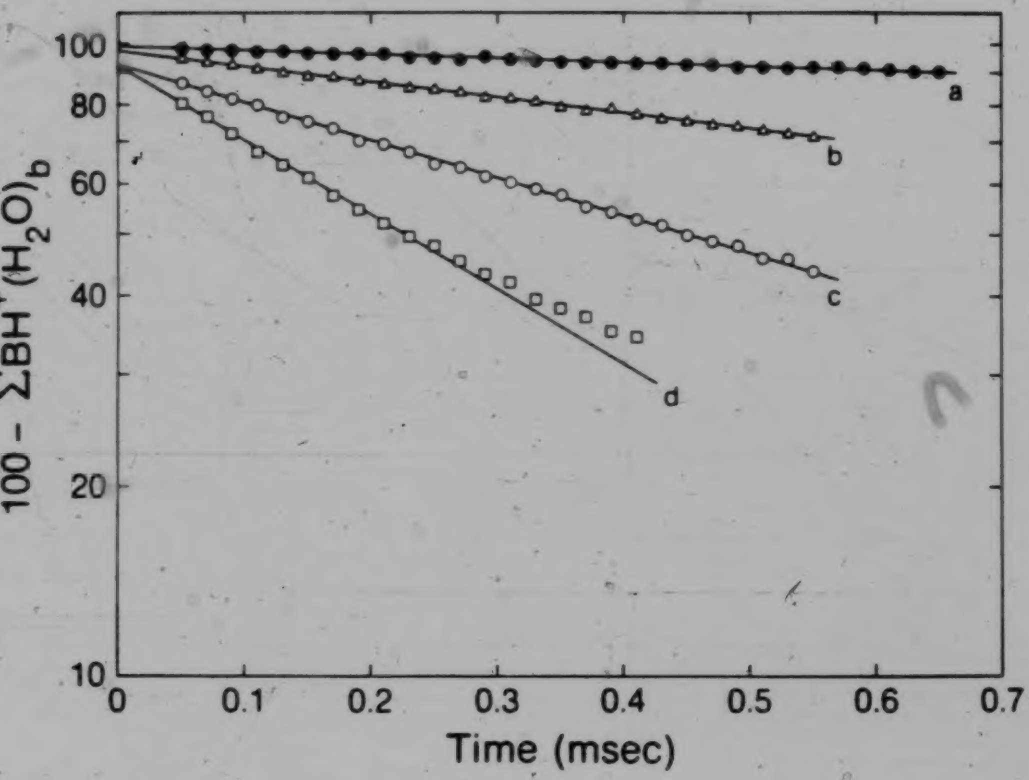

Figure 3.13 Rate constant determinations for the reaction: $H_3O^+(H_2O)_h$ + Pyrrole = Pyrrole$\cdot H^+(H_2O)_b$ + h-b+1 H_2O. All runs at 32C and P_{total} = 3 torr and 1.5×10^{-4} torr pyrrole. Variable water pressures: a) 1.1; b) 0.5; c) 0.1; d) 0.05 torr. Resulting k_a found in Table 3.7.

a factor of 10 as the water pressure is decreased by a factor of 10 but still remains far below the collision rate $k_c = k_{ADO} = 1.6\times10^{-9}$ molecules^{-1} s^{-1} cm^3. The rate constant increases as we increase the temperature. This is due to the decrease in the value of h in the water hydrates.

Examining the k_a and the corresponding $H_3O^+(H_2O)_h$ distributions one finds that the data can be fitted if one assumes that proton transfer from $H_3O^+(H_2O)_3$ occurs at 0.4 of the collision rate and that all larger clusters do not react, i.e. the rate from h = 4 or larger is negligible, also all smaller clusters with h = 2 or less react at collision rates. This is shown in Figure 3.14. Measurement of k_a at 1 torr water pressure and 198C where $H_3O^+(H_2O)_h$ where h = 0-2 is 87% of the total hydrates led to k_a = 1.4×10^{-9} molecules^{-1} s^{-1} cm^3, which is near the collision rate and supports the assumption that proton transfer for $h < 3$ occur at collision rates.

Proton transfer from the h = 3 corresponds to a $\Delta G^\circ_{3,3}(PT) = -6.1$ kcal/mol at 300K (See Table 3.7). This is a substantial exothermicity and it might appear surprizing that the reaction is slow even though the exothermicity is substantial. The low rate is most likely due to the fact that a pyrrole is a carbon base. Brauman (73) has shown that the proton transfer reaction 3.22 involving delocalized negatively charged bases B$^-$ proceeds at rates slower than collision rates. Experiments described in this next section will examine whether exothermic proton transfer form AH$^+$ to B (pyrrole) slows down as the exothermicity is decreased.

$$AH + B^- = A^- + BH \qquad [3.22]$$

3.3d Kinetics of proton transfer, AH$^+$ B = BH$^+$ + A, to carbon bases B

It was established in the previous section that the proton transfer reaction from $H_3O^+(H_2O)_h$ to carbon base B (pyrrole) is slower than the collision limit at relatively

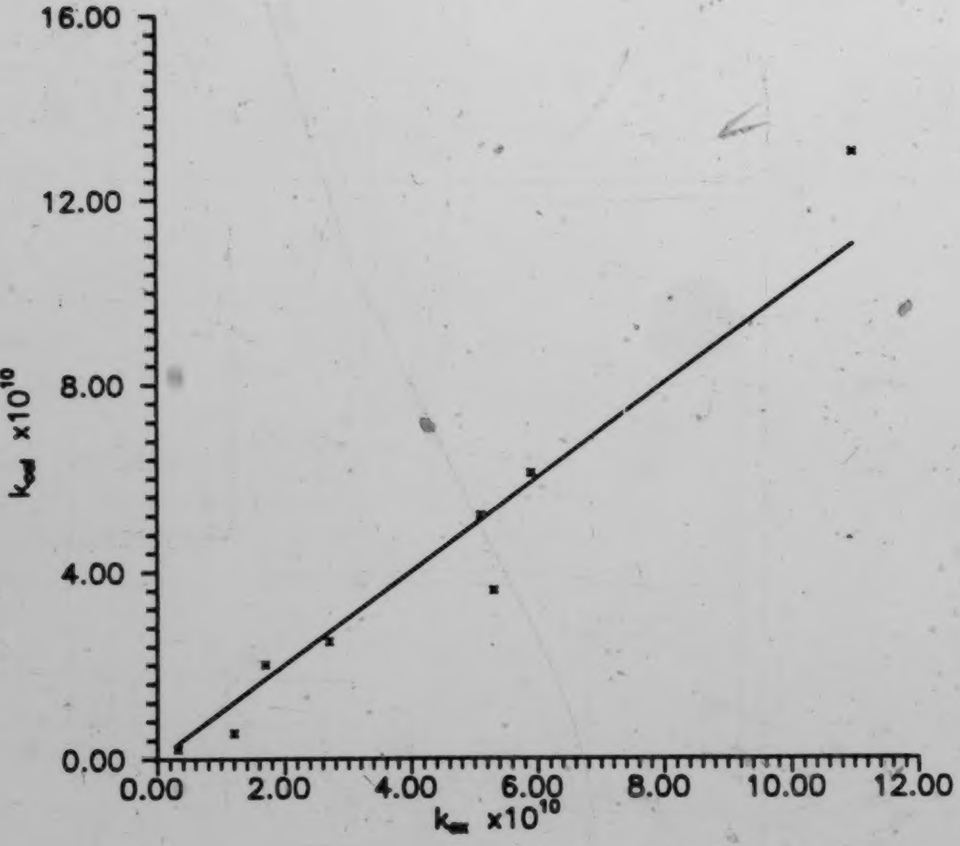

Figure 3.14 Plot of experimentally determined rate constants for the reaction $H_3O^+(H_20)_h$ + Pyrrole = Pyrrole·$H^+(H_2O)_p$ + (h-p+1) H_2O against rate constants calculated assuming that for $h < 3$ $k = k_{ADO}$, for $h > 3$ $k = 0$ and for $h = 3$ $k = 0.4$ k_{ADO}.

$k_{cal}=k_{ADO}[\Sigma(\%H_3O^+(H_2O)_{0,1,2}) + 0.4\ \%H_3O^+(H_2O)_3]$

high exothermicities, while proton transfer to oxygen bases remains near the collision rates even for exothermicities that are close to zero. In this section we describe proton transfer measurements for reaction 3.23 where different protonated compounds A are involved in proton transfer to pyrrole.

$$AH^+ + B = BH^+ + A \qquad [3.23]$$

$$AH^+ + A = A_2H^+ \qquad [3.24]$$

Using A with different gas phase basicities leads to proton transfer reactions with different exothermicities. The experimentally rate constants are summarized in Table 3.8. The measurements were preformed at near constant temperature (232 to 238C). The elevated temperatures were required in order to suppress the formation of the proton bound dimer (See reaction 3.24). For some compounds significant concentrations of A_2H^+ were present even at these elevated temperatures. Since the concentrations of A were sufficiently high, AH^+ and A_2H^+ remained in equilibrium while the slower proton transfer reaction to B, via reaction 3.23, proceeded. This was the case for diethyl ether and methanol. For diethyl ether the protonation of pyrrole by the dimer is endothermic, and therefore, the rate constant was determined by assuming that only the AH^+ reacted while A_2H^+ and AH^+ remained in equilibrium. Looking at a reaction where the dimer is in equilibrium with the monomer and only the monomer reacts with compound C (reaction 3.25). The rate law is described by equation 3.26.

$$B_2H^+ = BH^+ \xrightarrow{k_3[C]} CH^+ \qquad [3.25]$$

$$\frac{d[BH^+]}{dt} = -\frac{d[B_2H^+]}{dt} - k_3[C][BH^+] \qquad [3.26]$$

TABLE 3.8

Rate constants[a] for the reaction:

pyrrole·H$^+$ + B = BH$^+$ + pyrrole

B	Δ(GB)	k(x10^{10}) (cm^{3}molec^{-1}s^{-1})	k$_{ado}$(x10^9)
Diisopropylether	3.0	0.54	1.42
acetophenone[b]	3.1	0.48	1.37
n-butylether	5.0	0.92	1.35
benzaldehyde[b]	8.2	0.95	1.40
diethylether	8.2	1.18	1.52
(methanol)$_2$	8.7	18.5	1.94
anisole[b]	8.1	0.046	1.40
m-xylene	12.5	0.42	1.41
toluene	18.6	0.80	1.45

a) Measurements at temperatures between 232-238C.

b) Earlier work (72) established that acetophenone and benzaldehyde are oxygen protonated while anisole is ring protonated.

Because the equilibrium between the dimer and the momomer is fast, the ratio of the concentrations of dimer to momomer is constant (equation 3.27) and the rate of loss of the dimer will be equal to the rate of loss of the momomer times this constant (equation 3.28)

$$B_2H^+/BH^+ = R \qquad [3.27]$$

$$\frac{Rd[BH^+]}{dt} = \frac{d[B_2H^+]}{dt} \qquad [3.28]$$

Substituting equation 3.28 into equation 3.26 gives equation 3.29

$$\frac{d[BH^+]}{dt} = \frac{-Rd[BH^+]}{dt} - k_3[C][BH^+] \qquad [3.29]$$

Rearranging and integrating gives equations 3.30 and 3.31

$$(1+R)\ \frac{d[BH^+]}{dt} = -k_3[C][BH^+] \qquad [3.30]$$

$$d\ln[BH^+] = \frac{-k_3[C][BH^+]dt}{1+R} \qquad [3.31]$$

This shows that a normal plot of lnI against time gives the pseudo first order rate constant equal to the slope times (1+R).

For methanol, the dimer equilibrium reaction 3.24, was shifted almost completely in favour of the A_2H^+ side and the rate of protonation was evaluated by assuming that it occurred only from the dimer A_2H^+. The proton transfer from A_2H^+ is exothermic for A = methanol (See Table 3.8). The compounds for which $-\Delta G^\circ_{23}$ was small led to the achievement of proton transfer equilibrium. In these cases (diisopropyl ether, acetophenone and di-n-butyl ether) the rate constants were obtained from the ion concentration changes on approach to equilibrium i.e. with the inclusion of the reverse rate. When the reaction approaches equilibrium it can be shown that the rate of change of concentration is proportional to the sum of the forward and reverse rates (reaction 3.32).

$$(v_f + v_r)t = \ln\{([AH^+]_0 - [AH^+]_e)/([AH^+]_t - [AH^+]_e)\} \qquad [3.32]$$

where v_f and v_r are the pseudo first order rate constants in the forward and reverse directions respectively. With $v_f = k_f\,[B]$ and $v_r = k_r\,[A]$ and the equilibrium constant

$$K_{eq} = k_f/k_r = \frac{[BH^+]_e[A]}{[AH^+]_e[B]} \qquad [3.33]$$

we get

$$v_r = v_f\,[AH^+]_e/[BH^+]_e \qquad [3.34]$$

substituting $[AH^+]_e/[BH^+]_e = R$ and equation 3.34 into equation 3.32 we get

$$(1+R)v_f t = \ln([AH^+]_0 - [AH^+]_e) - \ln([AH^+]_t - [AH^+]_e) \qquad [3.35]$$

therefore a plot of $\ln([AH^+]_t - [AH^+]_e)$ against time will have a slope equal to the $v_f(1 + R)$. An example of this treatment is given in Figure 3.15.

The rate constants of Table 3.8 are plotted in Figure 3.16 versus the free energy change ΔG°_{23} of the proton transfer reaction 3.23. The rate seems to fall into two groups depending on if the bases, AH^+, are oxygen or carbon protonated. The oxygen protonated AH^+ lead to higher rates for the same exothermicity. In both

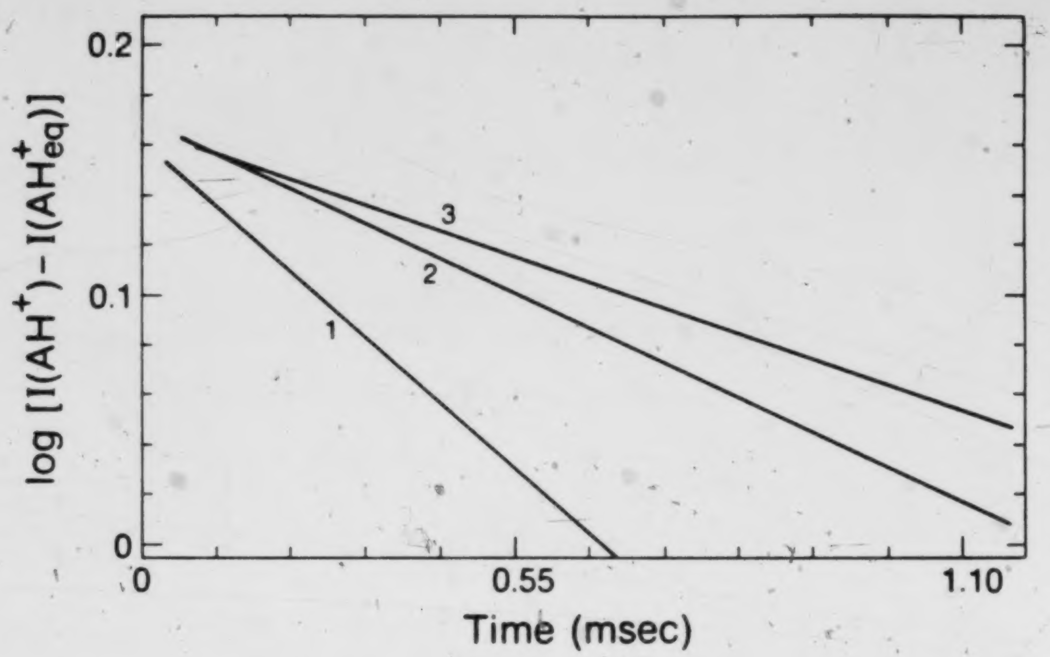

Figure 3.15 Rate constant determination for the proton transfer: $AH^+ + B = BH^+ + A$, where A = acetophenone and B = pyrrole. Since this reaction reaches equilibrium, rate constants were derived from concentration changes assuming reversible reaction (see text). $I(AH^+) = 100\%$ at $t = 0$, $I(AH^+)$ is intensity at equilibrium in %. Runs 1-3 $P_{pyrrole} = (0.59, 0.30, 0.15)$ mtorr. rate constants $k = (0.48, 0.43, 0.50) \times 10^{-9}$ $molecules^{-1}\ cm^3\ s^{-1}$.

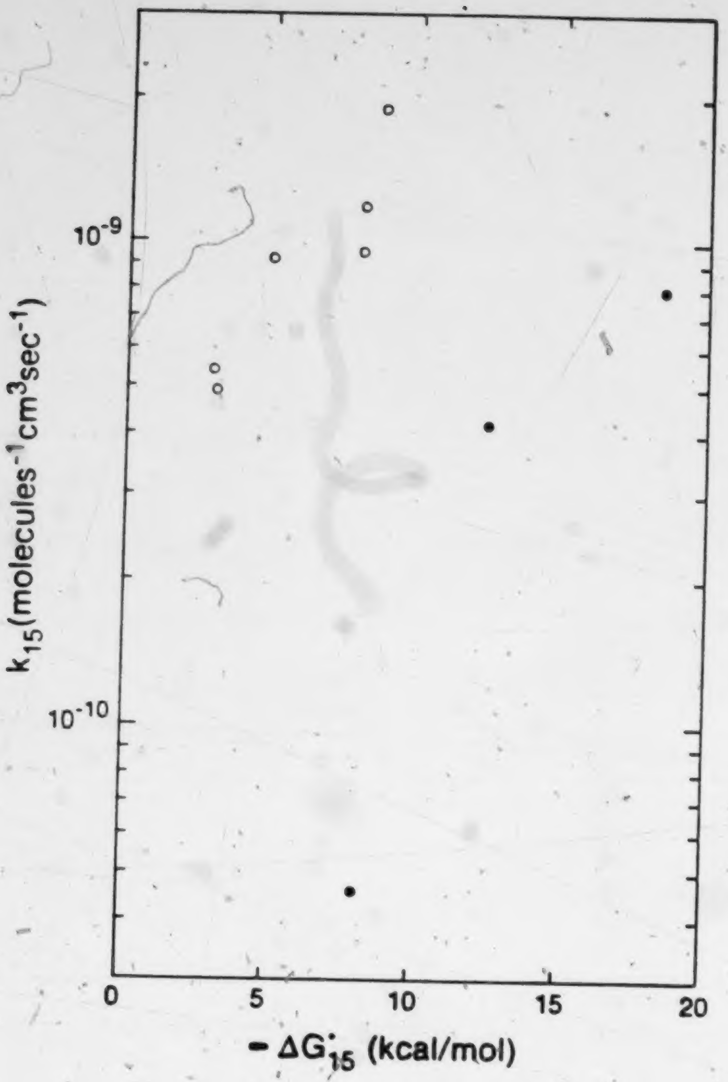

Figure 3.16 Plot of rate constant for the proton transfer: $AH^+ + B = BH^+ + A$ versus ΔG°_{28} B = pyrrole ○A are oxygen bases; ●A are carbon bases.

groups the rate constants were found to decrease as the exothermicity goes to zero. These results can be rationalized on the basis of the double minimum reaction coordinate model (74-76) shown in Figure 3.17. Since the observed rates of reaction were not exceedingly slow, E_{diff} is expected to be negative. Therefore, the rate constants will increase as the absolute value of E_{diff} increases. For the cases where AH^+ is an oxygen acid, E_{diff} is expected to be larger and the rate faster for two reasons. The well depth $E_w = \Delta E(AH^+\text{-}B)$ will be deeper and the barrier ΔE^* should be smaller than is the case for carbon acids AH^+. The expected poorer bonding of carbon acids AH^+ to water due to the relative lack of positive charge on the hydrogen(s) was discussed earlier and the same reasons will lead to weak bonding of AH^+ to B. In general, the barriers ΔE^* for proton transfer are low when both A and B are oxygen or nitrogen bases, however large barriers are expected when either A or B is a carbon base (73) and even larger when both A and B are carbon bases.

The increase of k_{23} with exothermicity, i.e. increase of $-\Delta E^{\circ}_{rxn}$ for both oxygen and carbon acids AH^+, is also expected. This is generally observed whenever ion-molecule reactions proceed at rates considerably lower than the collision rate (77). The decrease of ΔE^* with increasing exothermicity is incorporated into theoretical treatments such as the Marcus equation (80, 81).

In light of the results in Table 3.8 and Figure 3.16, the observed slow down of proton transfer from $H_3O^+(H_2O)_h$ to pyrrole and presumably other carbon bases with decreasing exothermicity is seen to be part of a general trend when oxygen acids AH^+ engage in proton transfer to carbon bases.

The above results show that proton transfer from $H_3O^+(H_2O)_h$ to carbon bases like pyrrole, furan and thiophene in inefficient on two counts. First, due to the poor exothermicity of hydration of $BH^+(H_2O)_b$, the proton transfer equilibria are shifted in favour of $H_3O^+(H_2O)_h$. Second, the kinetics of proton transfer reaction 3.20 slow

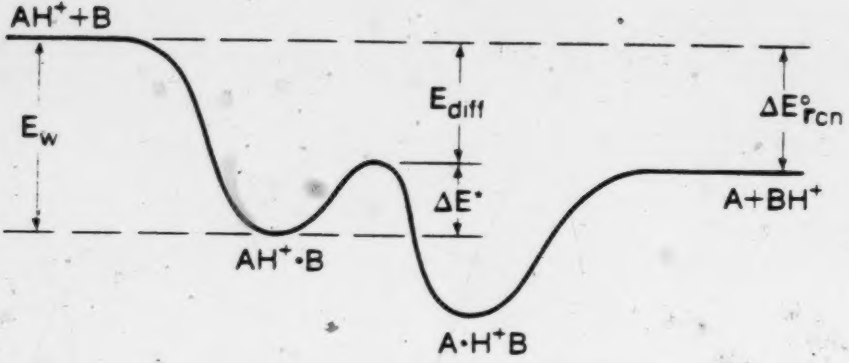
AH⁺+B
E_w
E_diff
ΔE°rcn
ΔE*
A+BH⁺
AH⁺·B
A·H⁺B

Figure 3.17 Double minimum reaction coordinate for proton transfer reaction 3.23. Notation used is that of Brauman (81).

down as the exothermicity decreases. Under atmospheric (APCI) conditions only the first factor is of importance. Due to the unfavorable thermodynamics the proton transfer equilibria are shifted almost completely in favour of the $H_3O^+(H_2O)_h$. Even though the rate constant for the proton transfer in the forward direction may be slow, the proton transfer is thermodynamically controlled. It should be remembered that the relaxation time *t* for achievement of the equilibrium depends on the sum of the forward and reverse rates. Even though both k_f and k_r are smaller than the case for the oxygen bases, the reverse rate is very fast due to the relatively large water concentration and the thermodynamics of the proton transfer equilibria will be important.

$$1/t = k_f[B] + k_r[H_2O] \qquad [3.36]$$

I would like to acknowledge the assistance of Dr. Jan Sunner who performed the experiments on the Atmospheric Pressure Mass Spectrometer.

Chapter 4

Hydrogen Bond Strength of HCl, HBr and MeCl, MeBr.

4.1 Introduction

Although there have been many investigations into the hydrogen bond strengths in neutral molecules, there has been relatively few investigations into the hydrogen bond strength in ionic species of the form, AH^+B. The ionic hydrogen bond strengths are much stronger than the hydrogen bonds in neutral dimers and are referred to as "strong hydrogen bonds" (83, 84). The strength of the ionic hydrogen bonds results from a combination of electrostatic, polarization, exchange repulsion, charge transfer and coupling components, of which the first two are the most significant in hydrogen bonding (82-85). The physical factors that contribute to ionic hydrogen bonding interactions have been investigated quantitatively by several theoretical methods. (68, 72, 82-86)

The strong intermolecular hydrogen bond, formed by the binding of two n-donor bases to a labile proton, plays an important role in a variety of bimolecular reactions, including acid and base induced elimination reactions and nucleophilic displacement reactions. The growing body of gas phase data from both experimental (67) and ab initio methods (88) recently available for hydrogen bonded cluster ions also provides insight into the nature of solvation of ions in both protic and aprotic solvents. To date most of the data available is on the proton bound dimers of oxygen and nitrogen n-donor bases. From these data one can see interesting trends. In symmetric proton bound dimers the hydrogen bond strength increases in the order $(PH_3)_2H^+$ (89), $(H_2S)_2H^+$ (90), $(NH_3)_2H^+$ (91), $(H_2O)_2H^+$ (56). From these trends it is evident that the hydrogen bond strength in symmetric proton bound dimers increases from left to right across the periodic table and decreases from top to bottom along a column in the periodic table.

Previous studies of H_2O, CH_3OH, and $(CH_3)_2O$ (92, 93) as well as NH_3, CH_3NH_2, $(CH_3)_2NH$, and $(CH_3)_3N$ (94) have shown little or no effect on the hydrogen bond strength in the symmetric proton bound dimer with methyl substitutions. Observations by Yamdagni and Kebarle (95) and Meot-ner and Sieck (96) show that the hydrogen bond strength for symmetric proton bound dimers of the nature $-NH^+--N-$ is constant at 23 ± 2 kcal/mol for dimers that range from $(NH_3)_2H^+$ to dimers of such large, and hindered, species as $((n\text{-}C_4H_9)_3N)_2H^+$. Similarly, the hydrogen bond strength of $-OH^+--O-$ dimers is constant at 32 ± 2 kcal/mol for dimers ranging from $(H_2O)_2H^+$ to dimers of a large variety of alcohols, ethers, and ketones (92, 93, 97).

In this study the hydrogen bond strength of the symmetric proton bound dimer of RX, reaction 4.1, is examined.

$$RXH^+ + RX = (RX)_2H^+ \quad R = (H, CH_3)\ X = (Cl, Br) \qquad [4.1]$$

$$CH_3XH^+ + CH_3X = CH_3XH^+CH_3X \qquad [4.2]$$

$$CH_3XH^+CH_3X = CH_3XCH_3^+ + HX \qquad [4.3]$$

The study of the symmetric proton bound dimer (reaction 4.2) for methyl halides cannot be studied directly due to a rapid nucleophilic displacement reaction 4.3 which make the simultaneous observation of CH_3XH^+ and $CH_3XH^+CH_3X$ impossible. In order to overcome this problem McMahon and Kebarle (98) postulated that if the methyl halide was a strong hydrogen bond acceptor, despite its low Bronsted basicity, then it should be possible to find a species, B, with a proton affinity greater than the methyl halide, but with a poorer hydrogen bonding ability. Measurement of the clustering equilibrium leading to the proton bound dimer of such a species, and determination of the subsequent displacement equilibria by the methyl halide from this proton bound dimer, would lead to the energetics of $CH_3XH^+CH_3X$ (See Scheme 1). McMahon and Kebarle (98) found SO_2 to be such a compound for the determination of the symmetric proton bound dimer of methyl fluoride. In this chapter, this method is extended to the determination of the hydrogen bond strength in the symmetric proton bound dimer of methyl chloride and methyl bromide. The hydrogen bond strength in the symmetric proton bound dimers of hydrogen chloride and hydrogen bromide are also examined.

4.2 Experimental

The experiments were performed on a Pulsed Electron Beam High Pressure Mass Spectrometer (PHPMS) with a magnetic sector which is described in Chapter 2. The experimental conditions were similar to those used in other work (66). The reagents used were of the highest available purity and were used without further purification. CH_4 was used as the bath gas at approximately 3 torr with the pressures of the bases ranging from 0.1-50 mtorr.

The gas mixture entering the ion source passed through a cold trap located on the gas inlet line to the ion source. The temperature of the cold trap was kept at -128 C (n-pentane slush). The temperature of the trap was selected to freeze out water vapor but to be warm enough not to freeze out the bases of interest.

In general, the concentrations of the bases were varied and the resulting equilibrium constants measured to obtain an average K_{eq}. Also, the equilibrium constants were measured at several different ion source pressures to ensure the equilibrium constant was not pressure dependent. This was repeated at every temperature to determine the temperature dependence of the equilibrium constants.

SCHEME 1

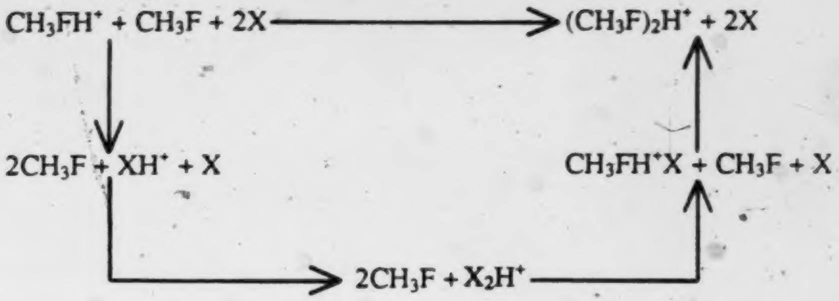
$CH_3FH^+ + CH_3F + 2X$
$(CH_3F)_2H^+ + 2X$
$2CH_3F + XH^+ + X$
$CH_3FH^+X + CH_3F + X$
$2CH_3F + X_2H^+$

Scheme 1. General reaction scheme proposed by McMahon and Kebarle (16).

SCHEME 2

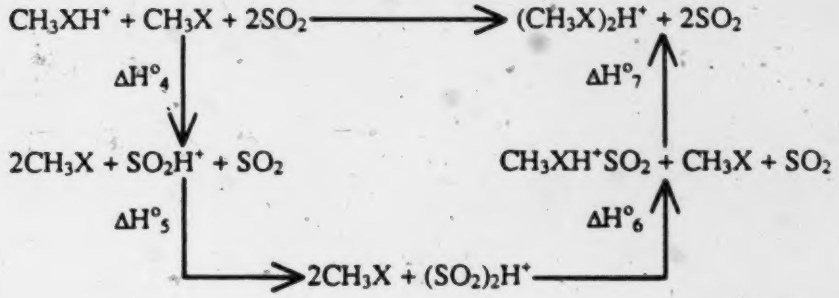
$CH_3XH^+ + CH_3X + 2SO_2$
$(CH_3X)_2H^+ + 2SO_2$
ΔH°_4
ΔH°_7
$2CH_3X + SO_2H^+ + SO_2$
$CH_3XH^+SO_2 + CH_3X + SO_2$
ΔH°_5
ΔH°_6
$2CH_3X + (SO_2)_2H^+$

Scheme 2. Reaction scheme for measuring the hydrogen bond strength of the proton bound dimer of the methyl halides. X = Cl and Br. The values for the individual reactions are given in Table 4.1.

4.3 Results and discussion

Direct determination of reaction 4.2, leading to the proton bound dimer of CH_3X, where X=Cl, Br, was impossible because of the rapid nucleophilic displacement reaction 4.3, which made simultaneous observation of CH_3X and $(CH_3X)_2H^+$ impossible. In order to overcome this problem a reaction scheme was used similar to that of McMahon and Kebarle for CH_3F (98). As with methyl fluoride, a base with a proton affinity similar to that of methyl chloride (and methyl bromide) and a weaker hydrogen bond acceptor was required. SO_2 was used even though its proton affinity is less than that of either methyl halide of interest. The reason it was tried was due to its success in measuring the proton bound dimer of methyl fluoride. Also, with the proton affinity being lower and the hydrogen bond strength expected to be similar, the $(CH_3X)_2H^+$ dimer was expected to be more stable than the $(SO_2)_2H^+$ dimer. Measurement of the equilibria outlined in Scheme 2 would then lead to the hydrogen bound strength of the methyl chloride and methyl bromide proton bound dimers.

In Figures 4.1 and 4.2 are typical plots for the reactions in Scheme 2. In these plots the exchange equilibria between the methyl halide and the SO_2 proton bound dimers is evident. An equilibrium between the CH_3XH^+ and $(CH_3X)_2H^+$, where X = Cl and Br is also observed. Because both the monomer and the dimer are present the equilibrium constant can be measured directly as well as via the cycle in Scheme 2. The equilibrium constants were determined at several different temperatures and the van't Hoff plots are shown in Figure 4.3 and 4.4 for CH_3Cl and CH_3Br respectively with the ΔH° and ΔS° for the reactions given in Table 4.1. The ΔH°_2 and ΔS°_2 for the symmetric proton bound dimer of the methyl halides are given in Table 4.2. Table 4.3 illustrates the type of consistency obtained for the equilibria with CH_3Br where the concentrations of the bases were varied.

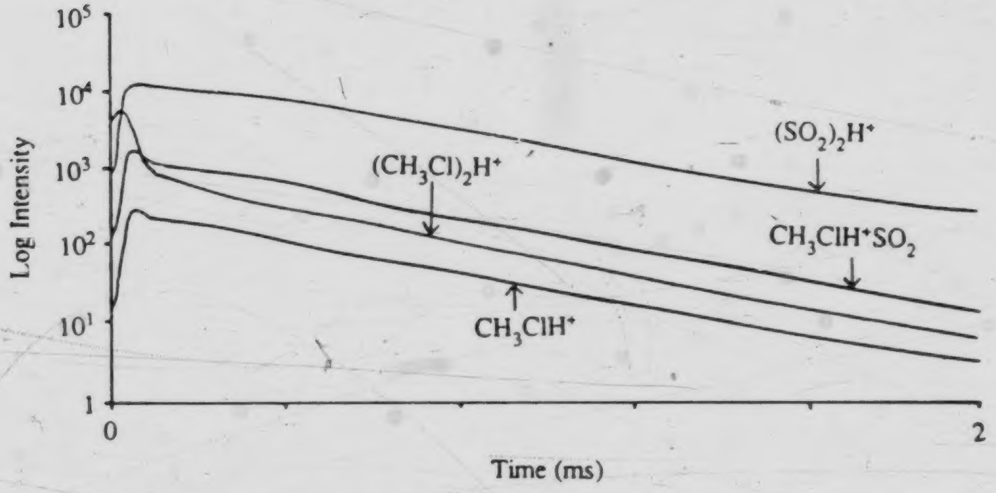

Figure 4.1 Typical plot of the ion intensities as a function of time for Scheme 2 with X = Cl. Conditions: CH_4 = 3.5 torr, CH_3Cl = 1.08 mtorr, SO_2 = 54.0 mtorr, Temperature 426K.

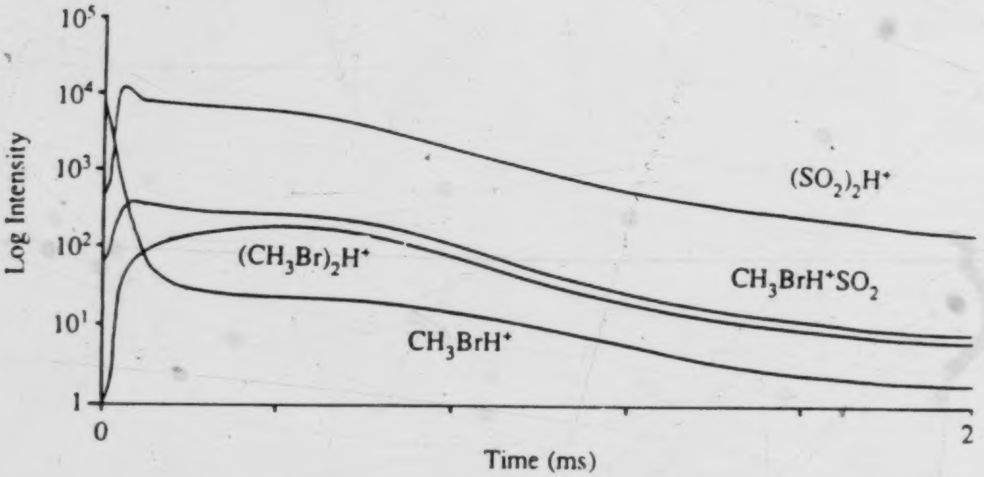

Figure 4.2 Typical plot of the ion intensities as a function ~~of~~ time for Scheme 2 with $X = Br$. Conditions: CH_4 = 3.1 torr, CH_3Br = 0.192 mtorr, SO_2 = 1.92 mtorr, Temperature 331K.

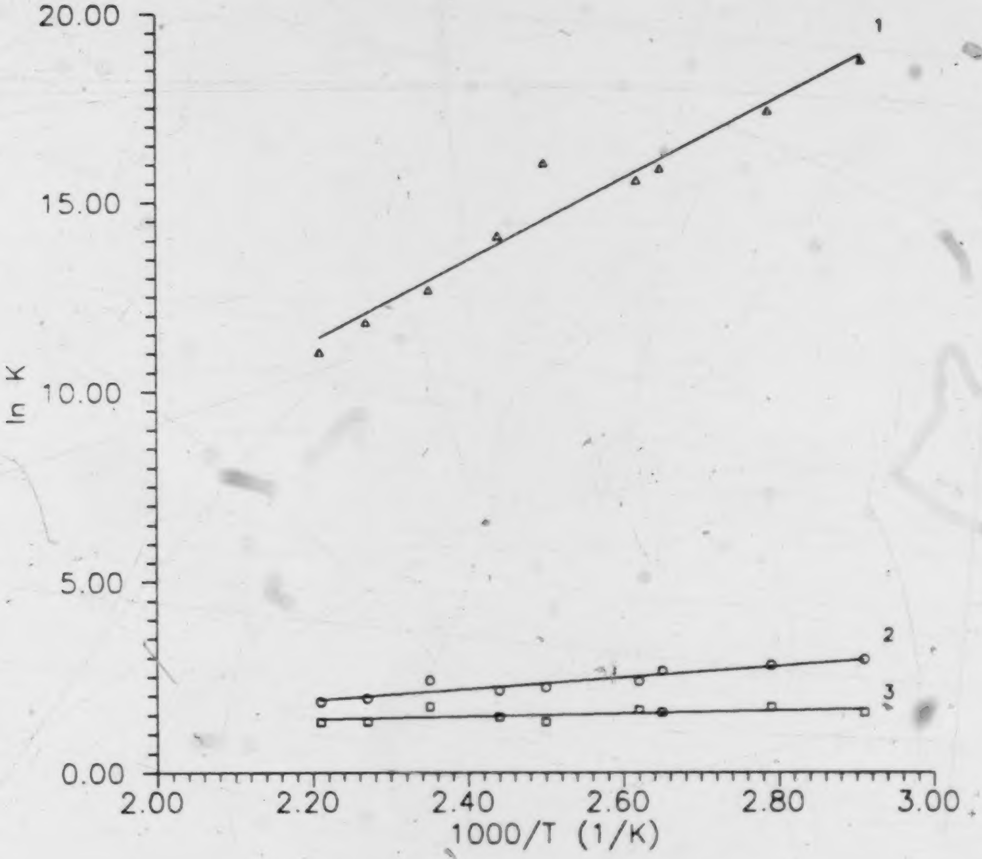

Figure 4.3 Van't Hoff plots for the reactions in Scheme 2 that were measured directly for X = Cl. The ΔH° and ΔS° are found in Table 4.1. The reactions are: 1) $CH_3ClH^+ + CH_3Cl = (CH_3Cl)_2H^+$ 2) $CH_3Cl + CH_3ClH^+OSO = (CH_3Cl)_2H^+ + SO_2$ 3) $CH_3Cl + (SO_2)_2H^+ = CH_3ClH^+OSO + SO_2$

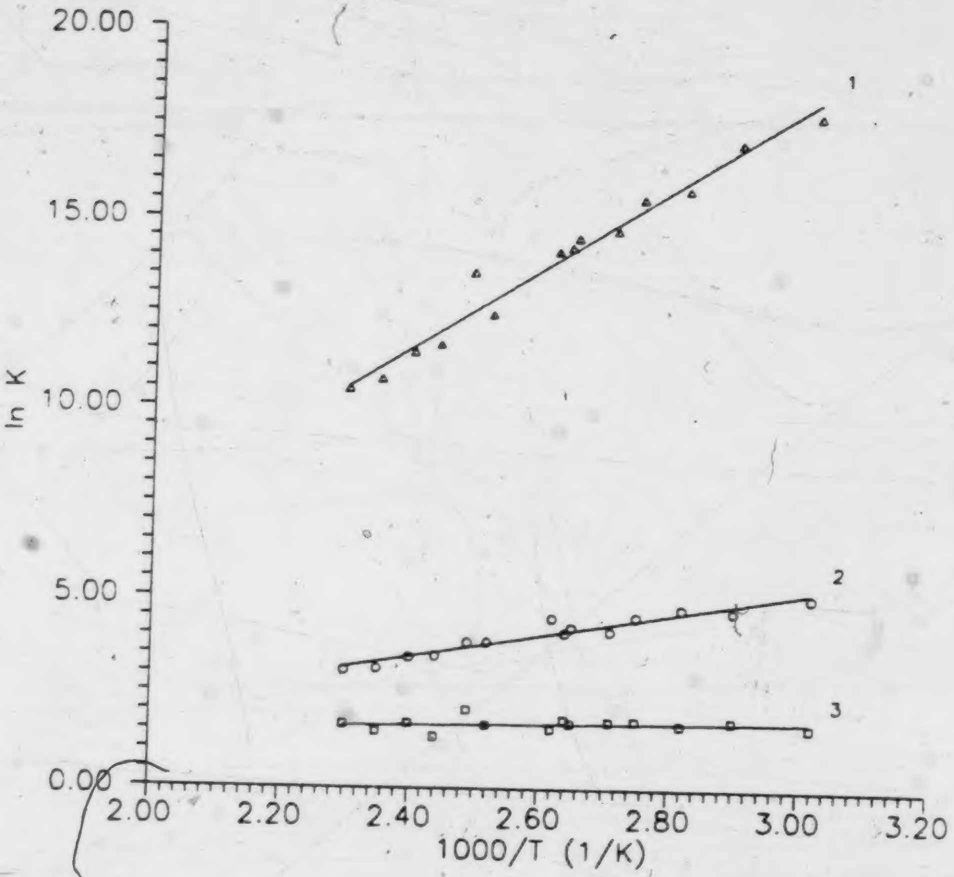

Figure 4.4 van't Hoff plots for the reactions in Scheme 2 that were measured directly for X = Br. The ΔH° and ΔS° are found in Table 4.1. The reactions are: 1) $CH_3BrH^+ + CH_3Br = (CH_3Br)_2H^+$ 2) $CH_3Br + CH_3BrH^+OSO = (CH_3Br)_2H^+ + SO_2$ 3) $CH_3Br + (SO_2)_2H^+ = CH_3BrH^+OSO + SO_2$

TABLE 4.1

ΔH° and ΔS° Values for Reactions in Scheme 2[a]

X =	Cl	Br
ΔH°_4[b]	6.9	8.0
ΔH°_5[c]	-23.2	-23.2
ΔH°_6	-0.8	-0.6
ΔH°_7	-3.1	-5.6
ΔH°_2	-20.2	-21.4
ΔS°_4[d]	2	2
ΔS°_5[c]	-27.4	-27.4
ΔS°_6	0.3	1.8
ΔS°_7	-3.6	-6.6
ΔS°_2	-28.7	-30.2

a) ΔH° in kcal/mol, ΔS° in cal/mol K. Measured $\Delta H^\circ \pm 2$ kcal/mol and $\Delta S^\circ \pm 5$ cal/mol K

b) Proton affinity of CH_3X from the methyl cation affinity of HX, where X = Cl, Br, from data given in chapter 3 and McMahon et al (30). PA of SO_2 = 155.3 kcal/mol from McMahon (23)

c) Values from McMahon (98)

d) calculated from S° values in Benson (75). For protonated species S° values estimated by $S^\circ(CH_3XH^+) = S^\circ(CH_3OH)$ and $S^\circ(SO_2H^+) = 57$ arbitrary estimate.

TABLE 4.2

ΔH° and ΔS° for the Reaction

$RXH^+ + RX = (RX)_2H^+$

R	X	ΔH° (kcal/mol)	ΔS° (cal/mol K)
CH_3	Cl	$-20.2^{a} \pm 3$	$-29.7^{a} \pm 5$
		$-21.3^{b} \pm 2$	$-25.2^{b} \pm 5$
CH_3	Br	$-21.4^{a} \pm 3$	$-31.2^{a} \pm 5$
		$-21.5^{b} \pm 2$	$-28.8_{b} \pm 5$
H	Cl	$-19.5^{b} \pm 2$	$-26.4^{b} \pm 5$
H	Br	$-18.4^{b} \pm 2$	$-24.9^{b} \pm 5$

a) calculated from cycle represented in Scheme 2

b) measured directly

TABLE 4.3

Equilibrium constants for the reactions measured in Scheme 2 with X = Br at several different temperatures.

P_{SO_2}[a]	P_{CH_3Br}[a]	K_6	K_7	K_2[b]
Temperature 425K				
25	0.51	18.0	3.3	3.2×10^4
55	1.1	21.0	3.4	3.9×10^4
13	1.3	18.8	4.3	3.7×10^4
Temperature 362K				
10	0.51	110	6.5	1.2×10^7
32	0.53	92.6	6.3	8.1×10^6
11	1.1	90.4	5.0	6.2×10^6
33	2.2	112	6.6	7.3×10^6
Temperature 331K				
1.9	0.19	141	5.9	5.9×10^7
25	0.49	143	5.2	5.8×10^7
10	1.0	144	4.5	4.3×10^7

a) pressure in mtorr.

b) standard state 1 atm.

The ΔH°_4 (Scheme 2) can be calculated from the proton affinities of SO_2 and the methyl halides. PA(SO_2) = 155.3 kcal/mol (23) while PA(CH_3X) = 162.2 kcal/mol and 163.3 kcal/mol, for X = Cl and Br respectively, as determined from the methyl cation affinities of HX in Chapter 6 and McMahon et al (30). ΔH°_5, the hydrogen bond strength of SO_2 proton bound dimer, was determined to be -23.2 kcal/mol by McMahon and Kebarle (98). ΔH°_6 and ΔH°_7 were measured and the values are given in Table 4.1. From these values the hydrogen bond strength can be determined to be 20.2 kcal/mol for CH_3Cl and 21.4 kcal/mol for CH_3Br. These can be compared to the direct measurement of reaction 4.2 of 21.3 kcal/mol and 21.5 for CH_3Cl and CH_3Br respectively.

When an attempt was made to study reaction 4.2 without adding a second base, an equilibrium between the protonated methyl halide and the proton bound dimer was not observed due to the rapid nucleophilic displacement reaction 4.3. The thermodynamics of reaction 4.3 indicates that the nucleophilic displacement is actually endothermic. ΔH°_3 = 7.6, 11.5, 12.2 for X = F, Cl, Br respectively (See Table 4.4). Despite the fact that reaction 4.3 is endothermic, it causes the direct determination of the equilibrium of reaction 4.2 to be impossible because the exothermicity of reaction 4.2 is large enough to make the nucleophilic displacement reaction 4.3 proceed (see Tables 4.2 and 4.4). At the low pressures used, the energy released on formation of the proton bound dimer complex is not immediately removed by third body collisions and is thus available for use in overcoming the barrier to reaction 4.3 (75, 78, 99).

By using SO_2 and forming the symmetric proton bound dimer of the methyl halide through exchange equilibria, the methyl halide symmetric proton bound dimer was formed with less exothermicity than was required to proceed with the nucleopholic displacement reaction 4.3 (See Table 4.1 and 4.4). These

TABLE 4.4

Calculation of ΔH°_{3}

$HX + CH_3^+ = CH_3XH^+$ [4.8]

$CH_3X + CH_3^+ = CH_3XCH_3^+$ [4.9]

$CH_3XH^+ + CH_3X = CH_3XH^+CH_3X$ [4.2]

$CH_3XH^+CH_3X = CH_3XCH_3^+ + HX$ [4.3]

$\Delta H^{\circ}_3 = \Delta H^{\circ}_f(CH_3XCH_3^+) + \Delta H^{\circ}_f(HX) - \Delta H^{\circ}_f(CH_3XH^+CH_3X)$ [1]

$\Delta H^{\circ}_f(CH_3XCH_3^+) = \Delta H^{\circ}_9 + \Delta H^{\circ}_f(CH_3^+) + \Delta H^{\circ}_f(CH_3X)$ [2]

$\Delta H^{\circ}_f(CH_3XH^+CH_3X) = \Delta H^{\circ}_2 + \Delta H^{\circ}_f(CH_3X) + \Delta H^{\circ}_f(CH_3XH^+)$ [3]

$\Delta H^{\circ}_f(CH_3XH^+) = \Delta H^{\circ}_8 + \Delta H^{\circ}_f(HX) + \Delta H^{\circ}_f(CH_3^+)$ [4]

Substituting [2], [3] and [4] into [1] gives

$\Delta H^{\circ}_3 = \Delta H^{\circ}_9 - \Delta H^{\circ}_2 - \Delta H^{\circ}_8$

X	ΔH°_2[a]	ΔH°_8[b]	ΔH°_9[b]	ΔH°_3
F	-32	-34	-58.4	7.6
Cl	-21.8	-55.2	-65.5	11.5
Br	-20.0	-58.9	-66.8	12.1

a) values from this work and reference (98).

b) values from Chapter 3.

exothermicities (3.1 kcal/mol for methyl chloride and 5.6 kcal/mol for methyl bromide) were well below the 11.5 kcal/mol and 12.2 kcal/mol needed for reaction 4.3 for CH_3Cl and CH_3Br respectively to proceed spontaneously.

$$HXH^+ + HX = (HX)_2H^+ \quad X = Cl, Br \qquad [4.10]$$

In addition to the study of the methyl halides, the hydrogen bound strength for the hydrogen halide proton bound dimer (reaction 4.10) was also studied in order to examine the effect of methyl substitution on the strength of the hydrogen bond. Figures 4.5 and 4.6 are typical plots for HCl and HBr respectively. From plots such as these, the equilibrium constants for reaction 4.10 were calculated. The van't Hoff plots obtained by measuring the equilibria at different temperatures are shown in Figures 4.7 and 4.8. Figure 4.9 shows that the equilibrium constants are invariant with the partial pressure of the base and shows the reproducibility of the equilibrium constants. The ΔH°_{10} and ΔS°_{10} values for these reactions can be found in Table 4.2.

A number of fundamental trends in the properties are evident from the data in Table 4.2. It is apparent that the hydrogen bond strength of the methyl halide does not vary significantly with the methyl substitution. Also, the average strength of the symmetric proton bound dimer decreases upon going from X = Cl to Br as was expected. Examination of the symmetric proton bound dimer bond strengths for several different heteroatoms, P, S, N, O, F, Cl, Br, (See Table 4.5) shows the trend of increasing hydrogen bond strength from left to right and top to bottom along the periodic table. Also evident is an increase in the hydrogen bond strength with increasing electronegativity of the heteroatom, as suggested by Desmeales and Allen (88) (See Figure 4.10).

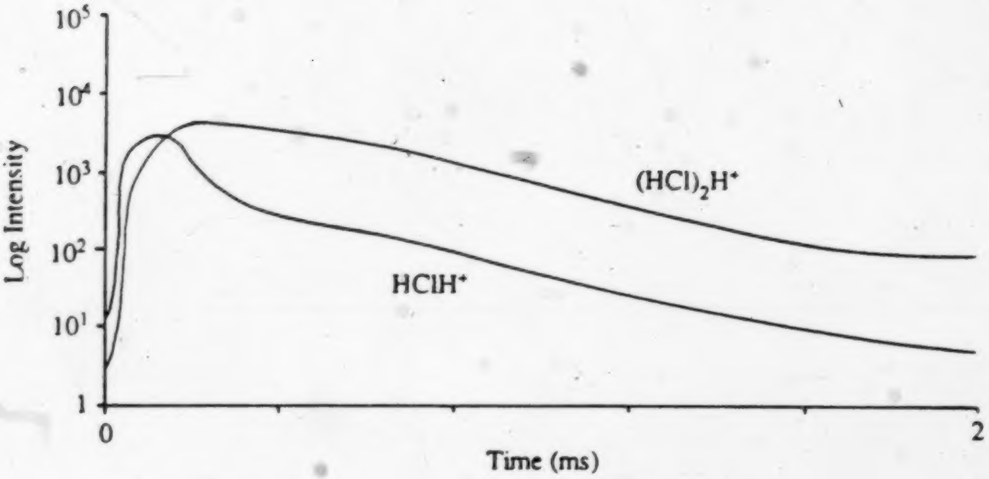

Figure 4.5 Typical plot of the ion intensities for the reaction: $HClH^+ + HCl = (HCl)_2H^+$. Conditions: CH_4 = 4.0 torr, HCl = 24.7 mtorr, Temperature 394K.

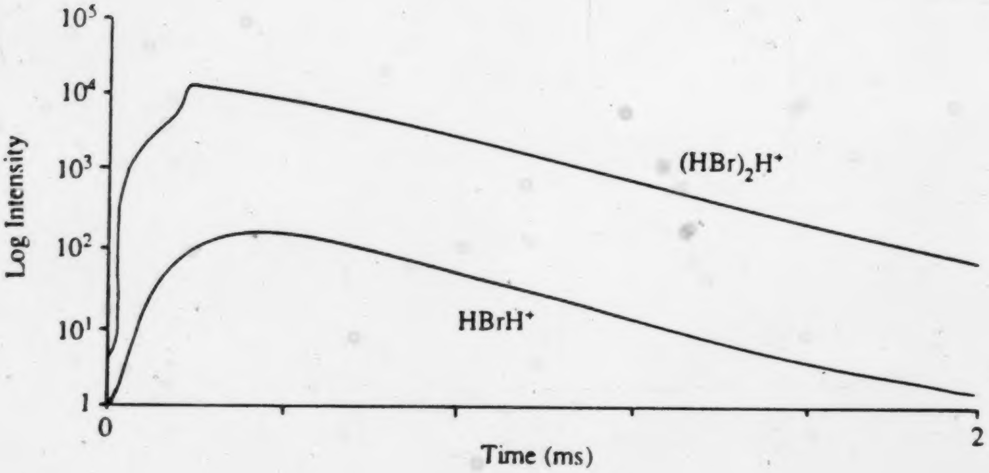

Figure 4.6 Typical plot of the ion intensities for the reaction: $HBrH^+ + HBr = (HBr)_2H^+$. Conditions: CH_4 = 3.0 torr, HBr = 1.34 mtorr, Temperature 421K.

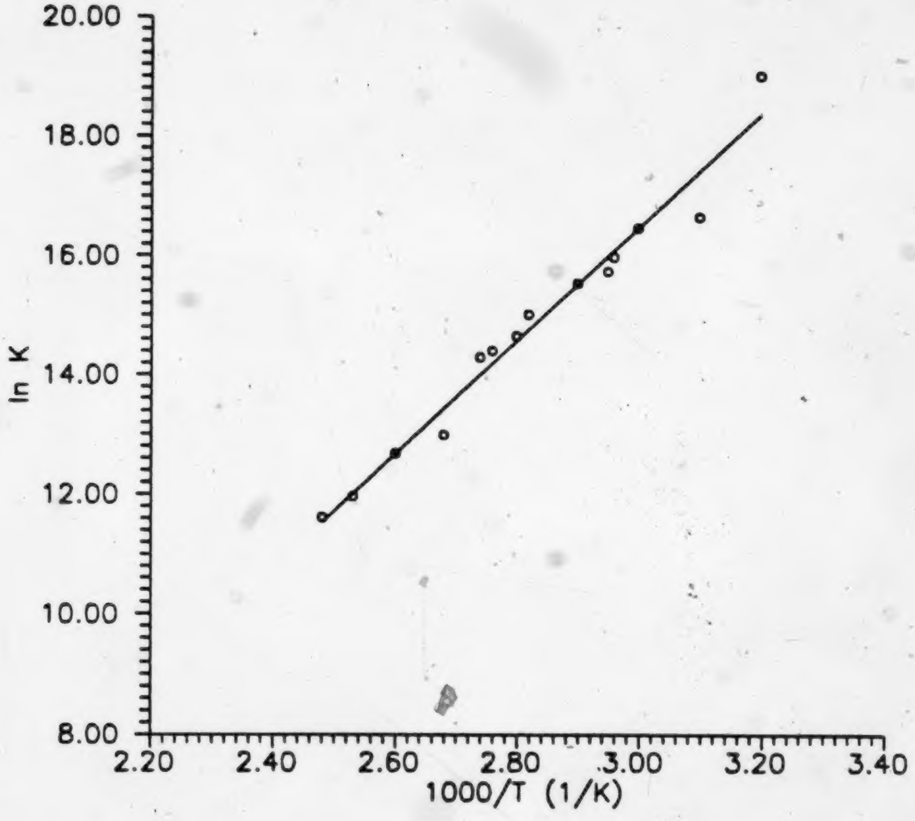

Figure 4.7 Van't Hoff plot for the reaction: $HClH^+ + HCl = (HCl)_2H^+$. The values for ΔH° and ΔS° are given in Table 4.2.

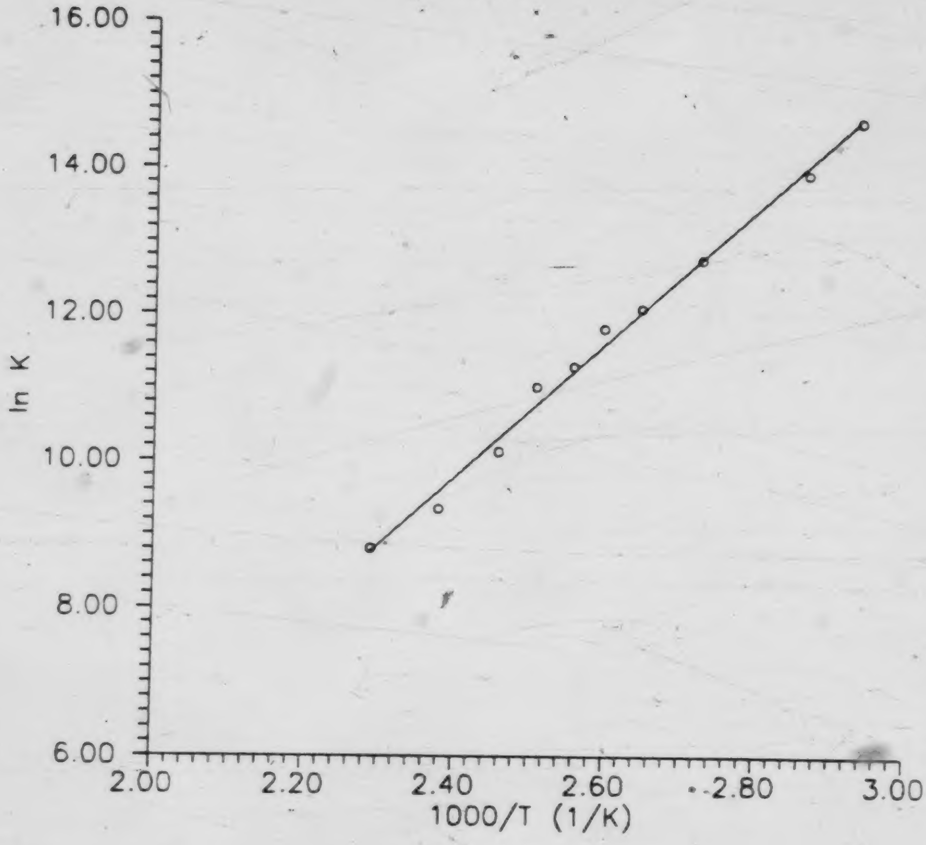

Figure 4.8 Van't Hoff plot for the reaction: $HBrH^+ + HBr = (HBr)_2H^+$. The values for ΔH° and ΔS° are given in Table 4.2.

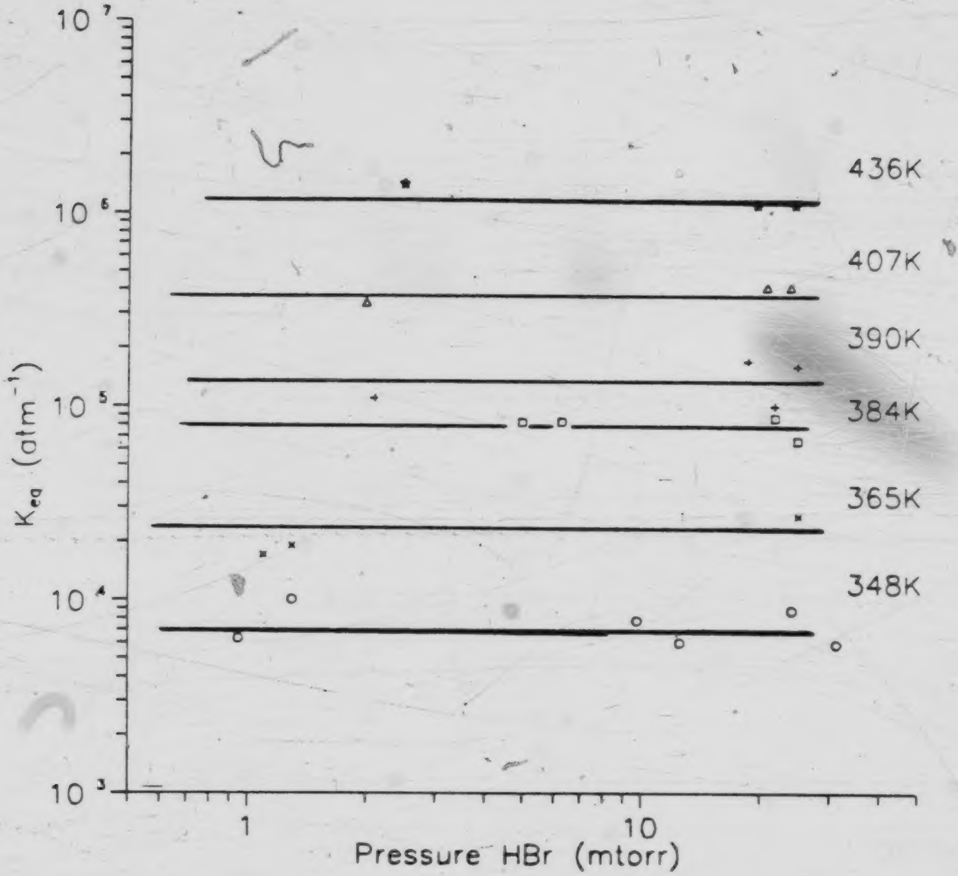

Figure 4.9 Plot of the equilibrium constant for reaction: $HBrH^+ + HBr = (HBr)_2H^+$, versus the partial pressure of HBr at several different temperatures. This plot indicates the reproducibility of the equilibrium constants.

TABLE 4.5

Average hydrongen bond strength of symmetric proton bound dimers for several different heteroatoms

	N	O	F
H-Bond strength[a]	23	32	32
Electronegativity[b]	3.0	3.4	4.0
	P	S	Cl
H-Bond Strength[a]	11.5	15.4	21
Electronegativity	2.2	2.6	3.2
			Br
H-Bond Strength[a]			20
Electronegativity			3.0

a) values in kcal/mol. values for N and O from Meot-Ner (93), F from McMahon and Kebarle (98), P from Long and Franklin (56), S from Hiraoka and Kebarle (90), Cl and Br from the present work. P, S and F are for one value only. P and S for the hydrogen bond strength of PH_3 and H_2S respectively while F is from the hydrogen bond strength of CH_3F.

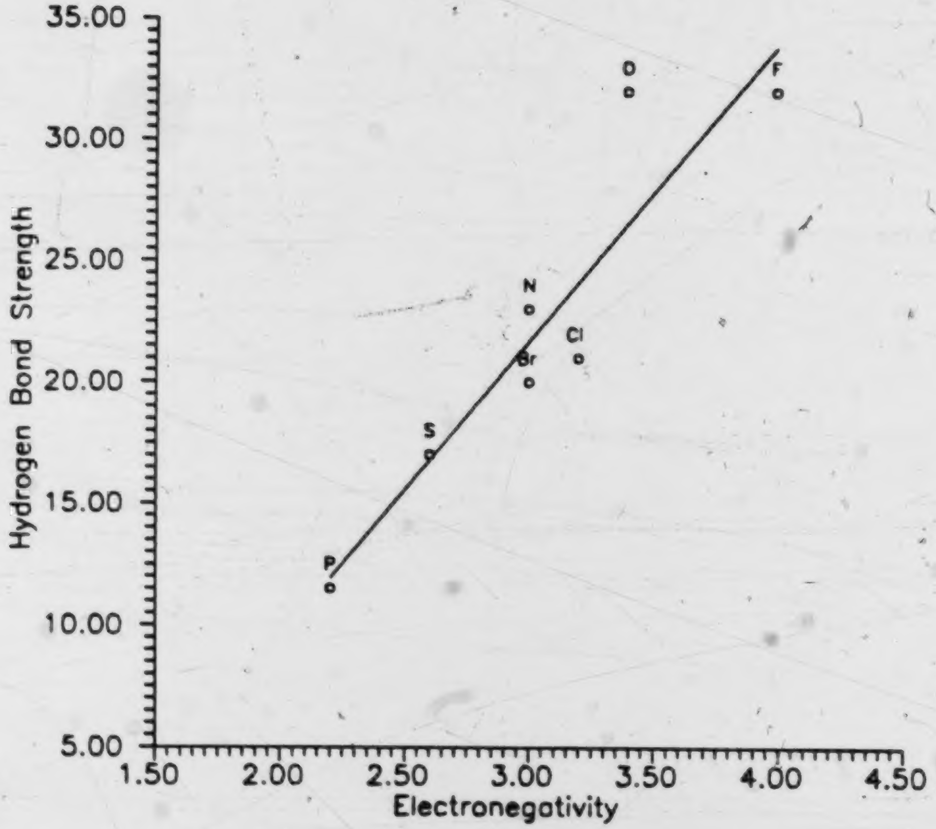

Figure 4.10 A plot of the average hydrogen bond strength for symmetrical proton bound dimers versus the electronegativity of the heteroatom involved. For P and S the value of only the proton bound dimer of Phosphine (56) and Hydrogen sulfide (91) were used. The values for O and N were taken from Meot-Ner (94) for the average hydrogen bond strength. For F the value for CH_3F (98) was used. Cl and Br were the average of the values presented in this work.

Chapter 5

Hydrogen Bonding in α,ω-dialcohols

5.1 Introduction

In the preceding chapter, it was demonstrated that strong hydrogen bonding is common in the gas phase and that some hydrogen bond strengths may be as high as 32 kcal/mol. In molecules which have more than one functional group, such as $H_2N(CH_2)_nNH_2$, there is the possibility of a strong internal hydrogen bond forming after protonation. This intramolecular hydrogen bond has the potential to stabilize the ion and increase the proton affinity of the molecule significantly.

Protonation of polyfunctional molecules is of interest due to the possibility of such intramolecular solvation. The resulting cyclization is shown in reaction 5.1. A larger enthalpy change was observed for reaction 5.1 than for reaction 5.2 where no intramolecular solvation can occur (95). Furthermore, reaction 5.2 should have a small entropy change, typical for simple proton transfer reactions, while reaction 5.1 should have a substantial entropy loss due to the loss of internal freedom on cyclization.

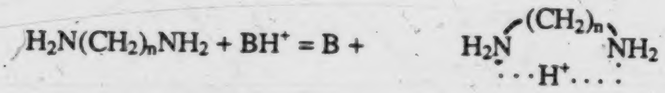

$$H_2N(CH_2)_nNH_2 + BH^+ = B + \overset{(CH_2)_n}{H_2N \cdots H^+ \cdots NH_2} \quad [5.1]$$

$$CH_3(CH_2)_nNH_2 + BH^+ = B + CH_3(CH_2)_nNH_3^+ \quad [5.2]$$

This type of intramolecular solvation has been seen in diamines (19, 95), polyamines (100, 101), amino alcohols (101), halogenated amines (19), diaminonaphthalenes (102), polyethers (103, 104), crown ethers (103, 105), diketones (103), some cyclohexanediols (106) and amides and aminoacid derivatives (107).

These occurrences suggest that intramolecular solvation is common in gas phase ions and that it should be present in many molecules which have two or more functional groups. The multiple interactions of a protonated ion with polar functions of an enzyme are seen as the major energy factor in biochemical proton transfer reactions (108). Despite the common occurrence, the entropy and enthalpy of the intramolecular solvation have been studied in only a few molecules. Kebarle et al. have examined diamines (95) and crown ethers (105), Meot-Ner has looked at some polyamines and amino alcohols (100), poly ethers, crown ethers and diketones (103) and amides and aminoacid derivatives (107). In this study, protonation of a series of dialcohols is examined. These molecules are of particular interest since the hydrogen bond strength with oxygen bases is nearly 10 kcal/mol stronger than for nitrogen bases (95, 96). This stronger bonding should be evident in the PA of the dialcohols and possibly also in the entropy of cyclization.

5.2 Experimental

The proton transfer and clustering equilibria were determined on a pulsed high pressure mass spectrometer with a quadrupole mass analyzer, which is described in Chapter 2. The procedures were the same as in earlier studies (66). The solid dialcohols were dissolved in reagent grade methanol and the solution was injected into the 5 l bulb. Toluene was also added to the reaction mixture, in a relatively large concentration, in order to generate $C_6H_5CH_3{\cdot}H^+$ which was able to protonate the dialcohols relatively gently. If the exothermicity of the protonation was very large the dialcohol would fragment with the loss of a water molecule.

The temperature dependence of the equilibrium constants was determined by flowing the same mixture through the ion source and varying the temperature slowly. The time dependence of the ion intensities were measured at each temperature. The temperature of the ion source did not vary by more than one degree during the acquisition of the ion profiles. No attempt was made to determine the reproducibility of the equilibrium at each temperature. For most cases two different base ratios were used, one at low temperatures and one at high temperatures.

5.3 Results and Discussion

5.3a Protonation of α,ω-dialcohols.

Figure 5.1 shows a typical mass spectrum for the protonation of 1,8-octanediol. The conditions were: CH_4 = 3 torr, $C_6H_5CH_3$ = 3.8 mtorr, Anisole = 3.75 mtorr, 1,8-octanediol = 0.75 mtorr, T = 478K. Even with the toluene and anisole added, some loss of water from the protonated dialcohol was still observed, [see peak (MH^+-H_2O)]. Figure 5.2 shows the time dependance of the observed ion intensities for the mass spectrum shown in Figure 5.1. Equilibrium is reached only after 1 ms, even though the concentration of the dialcohol is relatively high. This indicates a slow proton transfer reaction.

The proton transfer equilibrium constant, K_3, was determined for reaction 5.3 at different temperatures, where B is a reference base with a known proton affinity and n = 4, 6, 8 and 10.

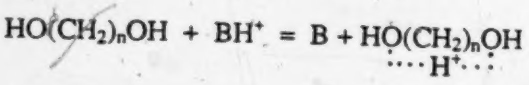

$$HO(CH_2)_nOH + BH^+ = B + \underset{\cdots\cdots H^+\cdots\cdots}{HO(CH_2)_nOH} \qquad [5.3]$$

Van't Hoff plots for reaction 5.3 for n = 2, 4, 6, 8 are shown in Figures 5.3-5.6. The ΔH°_3 and ΔS°_3 values along with the derived proton affinities of the dialcohols are given in Table 5.1.

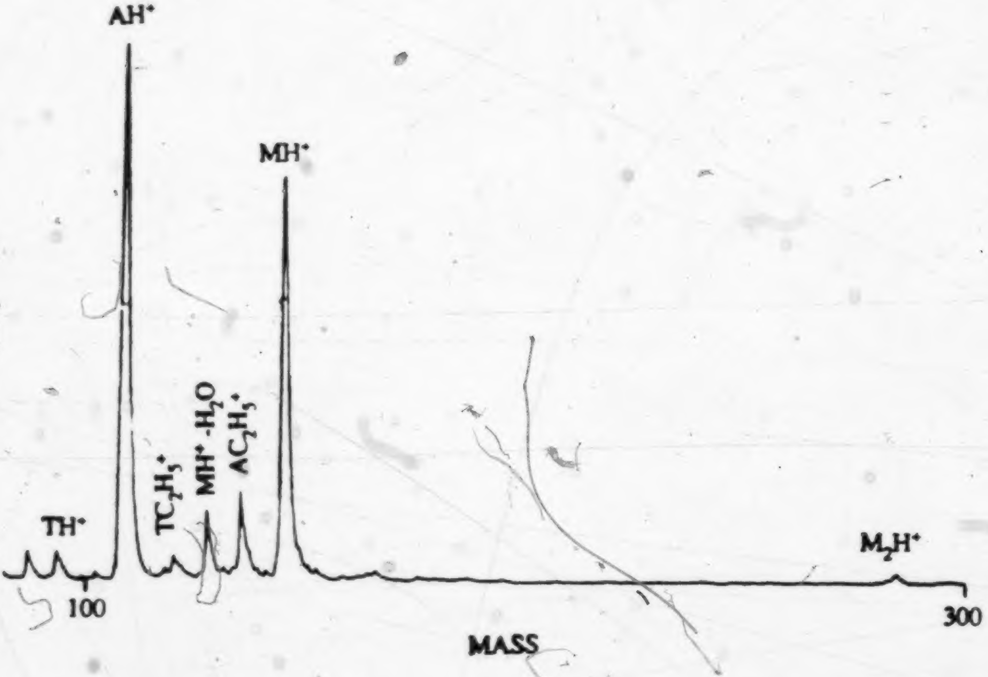

Figure 5.1 Mass spectrum of 1,8-octanediol. Conditions: CH_4 = 3 torr, $C_6H_5CH_3$ = 3.8 mtorr, $C_6H_5OCH_3$ = 3.75 mtorr, 1,8-octanediol = 0.75 mtorr, Temp 478K. T = toluene, A = anisole, M = 1,8-octanediol. Even with the toluene added there is still some loss of water from the protonated dialcohol.

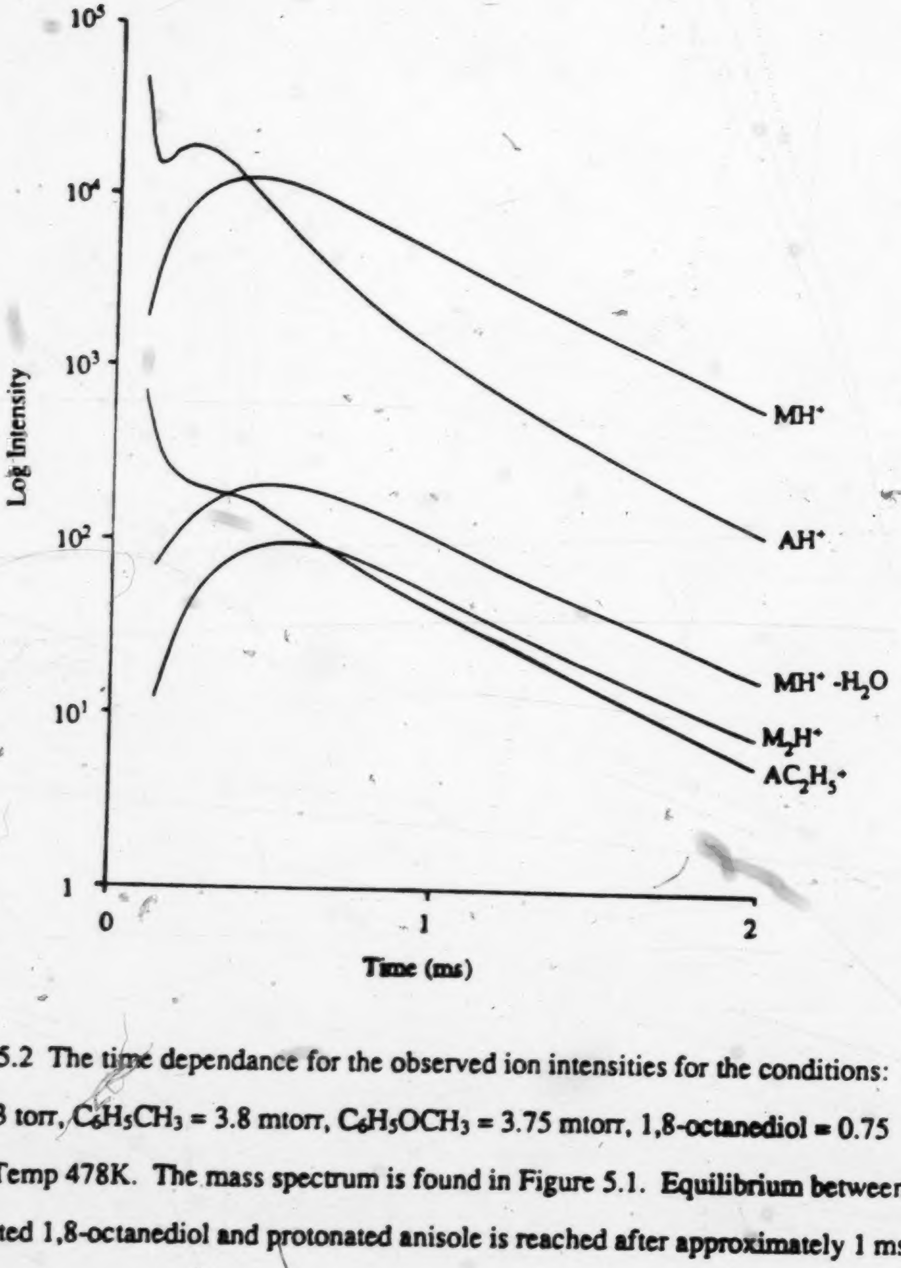

Figure 5.2 The time dependance for the observed ion intensities for the conditions: CH_4 = 3 torr, $C_6H_5CH_3$ = 3.8 mtorr, $C_6H_5OCH_3$ = 3.75 mtorr, 1,8-octanediol = 0.75 mtorr, Temp 478K. The mass spectrum is found in Figure 5.1. Equilibrium between protonated 1,8-octanediol and protonated anisole is reached after approximately 1 ms.

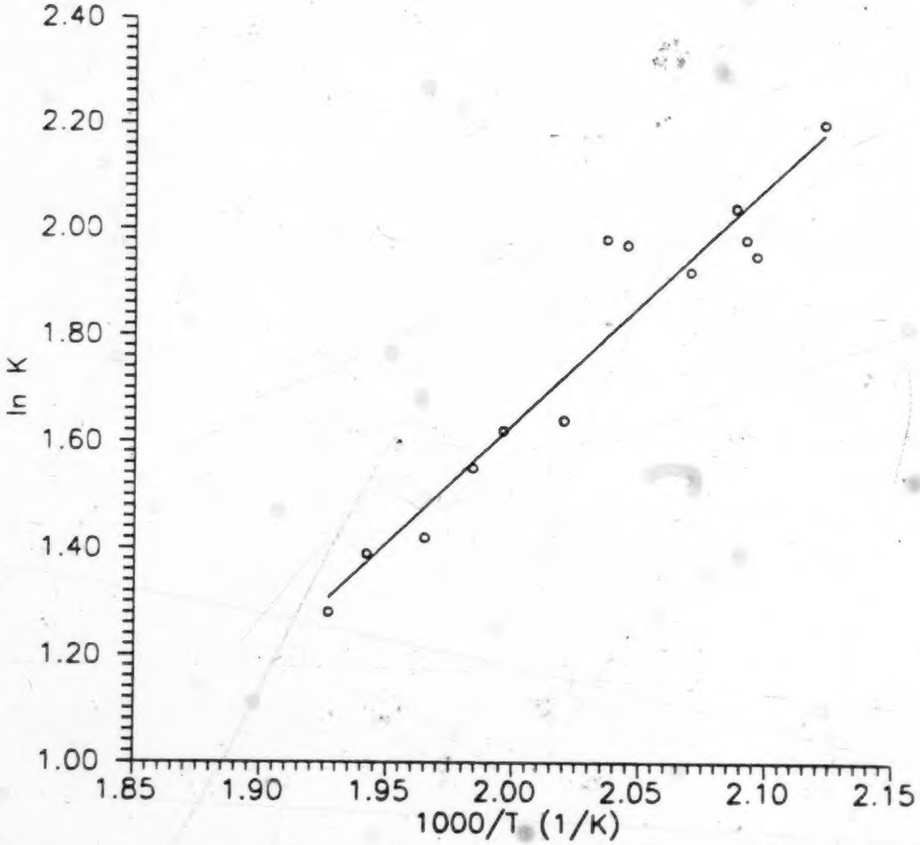

Figure 5.3 Temperature dependance of the equilibrium constant for the reaction: $BH^+ + HO(CH_2)_nOH = HO(CH_2)_nOHH^+ + B$, where n = 4, B = acetophenone. The ΔH° and ΔS° are found in Table 5.1.

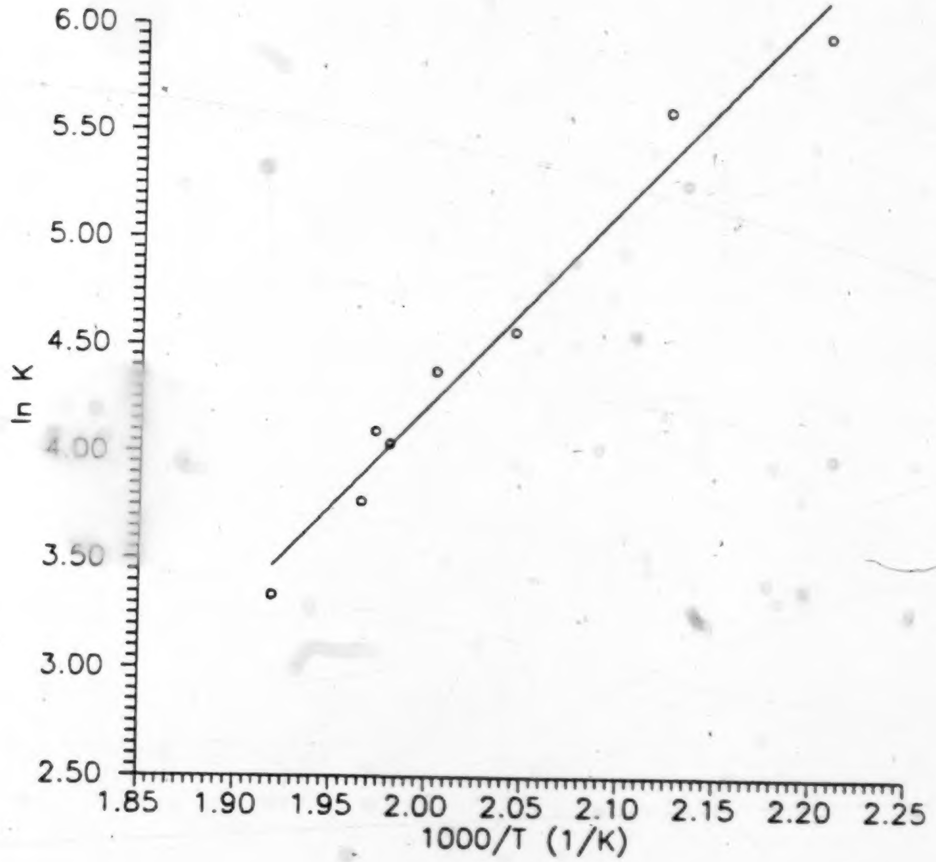

Figure 5.4 Temperature dependance of the equilibrium constant for the reaction: $BH^+ + HO(CH_2)_nOH = HO(CH_2)_nOHH^+ + B$, where $n = 6$, B= anisole. The ΔH° and ΔS° are found in Table 5.1.

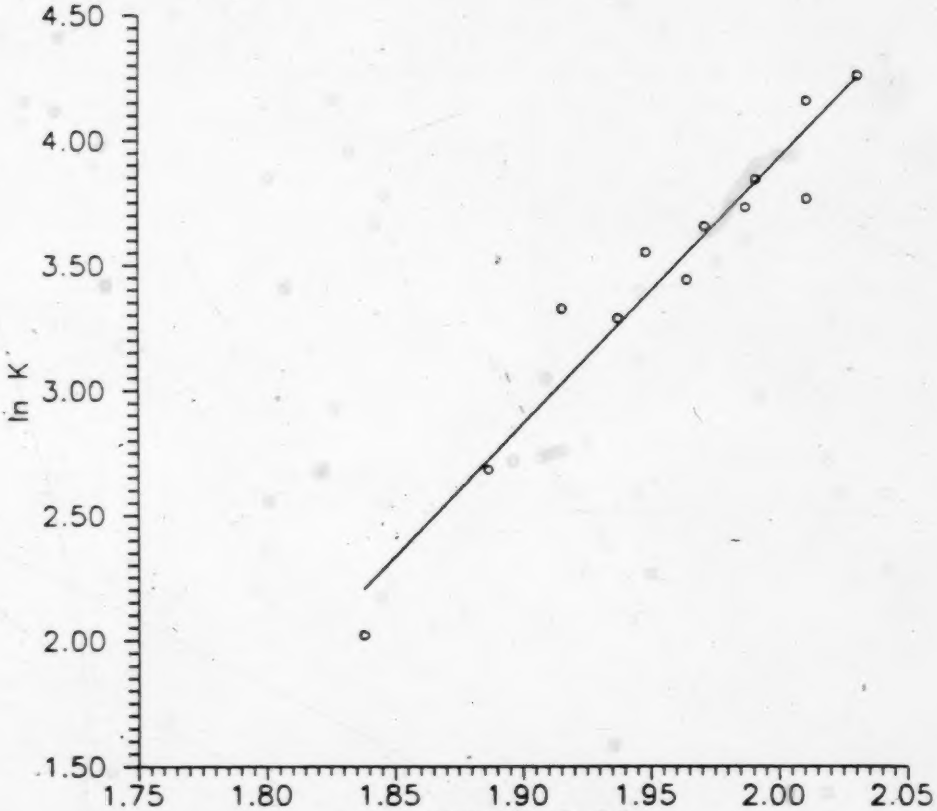

Figure 5.5 Temperature dependance of the equilibrium constant for the reaction: $BH^+ + HO(CH_2)_nOH = HO(CH_2)_nOHH^+ + B$, where $n = 8$, B = anisole. The ΔH° and ΔS° are found in Table 5.1.

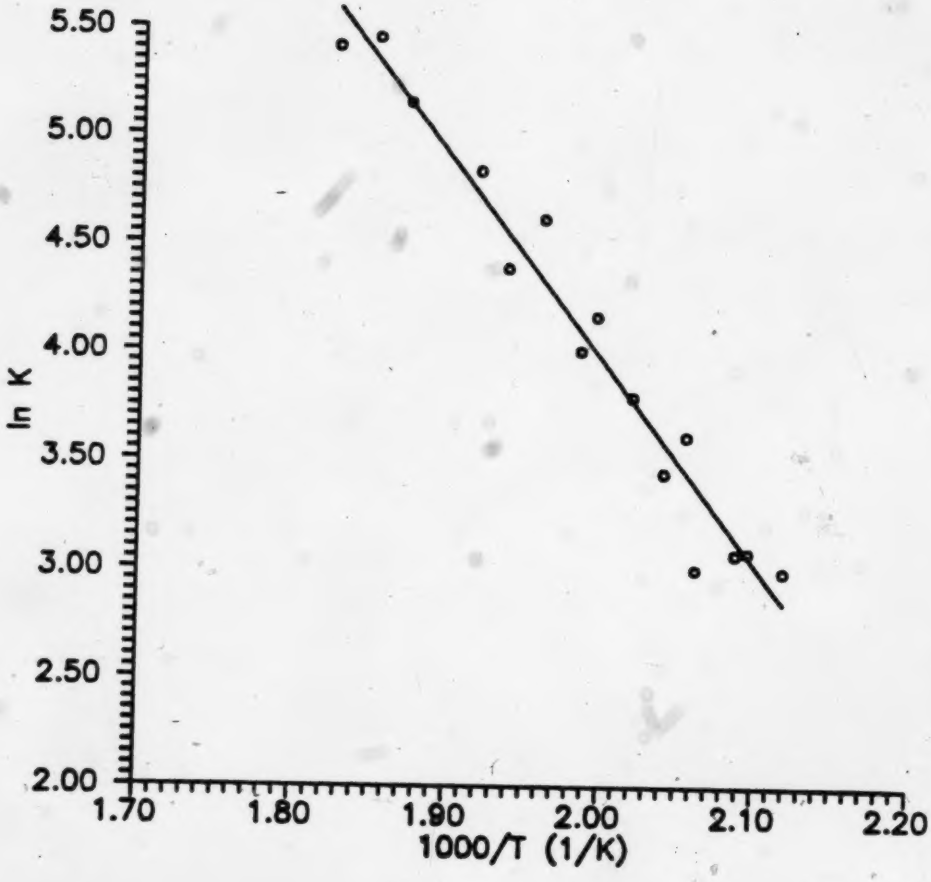

Figure 5.6 Temperature dependance of the equilibrium constant for the reaction: $HO(CH_2)_nOHH^+ + B = BH^+ + HO(CH_2)_nOH$, where n = 10, B = aniline. The $\Delta H°$ and $\Delta S°$ are found in Table 5.1.

TABLE 5.1

ΔH°_4 and ΔS°_4 for the reaction:
$BH^+ + \text{diol} = B + \text{diol}\cdot H^+$

diol	B	PA(B)[a]	ΔH°_4[a]	ΔS°_4[b]	PA(diol)[a]
1,4-butanediol	acetophenone	205.4	-8.9	-14.5	214.3
1,6-hexanediol	anisole	200.3	-18.4	-28.3	218.7
	acetophenone	205.4	-11.2	-22.0	216.6
1,8-octanediol	anisole	200.3	-21.0	-34.2	221.3
1,10-decanediol	aniline	209.9	-18.6	-45.1	228.5

a) in kcal/mol. Measured $\Delta H^\circ_4 \pm 3$ kcal/mol. PA(B) from Lias (22).

b) in cal/mol K. Measured $\Delta S^\circ_4 \pm 5$ cal/mol K

As can be seen from Table 5.1, there is a significant entropy change associated with the proton transfer reaction 5.3. As mentioned earlier, for most proton transfer reactions there is little or no entropy change. The relatively large, entropy change for the dialcohols must then be due to a substantial change in structure and indicates the formation of a cyclic structure. One can assume that the protonation takes place in two steps where the initial proton transfer step, reaction 5.4, is followed by cyclization, reaction 5.5.

$$HO(CH_2)_nOH + BH^+ = B + HO(CH_2)_nOH{\cdot}H^+ \qquad [5.4]$$

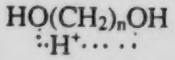

$$HO(CH_2)_nOH{\cdot}H^+ = \underset{\vdots\cdot H^+\cdots\cdots\vdots}{HO(CH_2)_nOH} \qquad [5.5]$$

The entropy change for reaction 5.4 should be nearly zero; therefore, we can assume $\Delta S_3 = \Delta S_5$, i.e., the entropy change in reaction 5.3 must be due primarily to the cyclization process.

The enthalpy change ΔH°_5 can be estimated by comparing the proton affinity of the dialcohol $HO(CH_2)_nOH$ with that of a monoalcohol $CH_3(CH_2)_nOH$, (see equation 5.6).

$$\Delta H_5 = \Delta H_6 = PA(HO(CH_2)_nOH) - PA(CH_3(CH_2)_nOH) \qquad [5.6]$$

As an upper limit to the exothermicity of the cyclization one can take ΔH_7, the enthalpy change for the formation of the proton bound dimer where $k+1 = n/2$.

$$CH_3(CH_2)_kOH_2^+ + CH_3(CH_2)_kOH = (CH_3(CH_2)_kOH)_2H^+ \qquad [5.7]$$

The difference between ΔH_7 and ΔH_5 will indicate the extent of ring strain in the cyclization.

$$\Delta H_{\text{ring strain}} = \Delta H_6 - \Delta H_7 \qquad [5.8]$$

The strength of the proton bound dimer for a large series of oxygen bases (92, 93, 109) has been shown to be 32 ± 2 kcal/mol. Using $\Delta H^\circ_7 = -32$ kcal/mol and equation 5.8, we can now calculate the ring strain. The values calculated along with the proton affinities used in equation 5.6 are found in Table 5.2.

Comparing the ΔH_{cyc} for the dialcohols and the diamines, which were measured earlier in this laboratory (95), (See Table 5.3) we see as expected that the ΔH_{cyc} is greater for the alcohols than the amines. This is due to the fact that the hydrogen bond strength of protonated dimers of alcohols is higher than that for amines (32 kcal/mol versus 23 kcal/mol) (95, 96). Also we see that the ring strain is greater for the alcohols than the amines. This is probably due to the greater contraction of the ring caused by the stronger and shorter hydrogen bond in the dialcohols.

Figure 5.7 shows ΔS°_3 as a function of chain length. The increase in the entropy change as the chain length increases is the same trend as is seen when comparing the S° values of n-alkanes and cycloalkanes (See Table 5.4). With the neutral alkanes the entropy change increases by about 3 cal/mol K per CH_2 unit, while the entropy change for the cyclization of the dialcohol increases by 5 cal/mol K per CH_2 unit.

From the results in Table 5.2 we can see that an intramolecular hydrogen bond can stabilize a protonated ion by up to 36 kcal/mol for large dialcohols. As was mentioned earlier, the average hydrogen bond strength for oxygen bases is about 32

TABLE 5.2

Cyclization of α,ω-dialcohols[a]

	$-\Delta S_{cyc}$[b]	ΔH_{cyc}[c]	Strain[d]	PA(diol)	PA(mono)[e]
1,4-butanediol	14.5	22.3	9.7	214.3	192
1,6-hexanediol	28.3	26.7	4.3	218.7	192
1,8-octanediol	34.2	29.3	2.7	221.3	192
1,10-decanediol	45.1	36.5	-4.5	228.5	192

a) in kcal/mol except ΔS_{cyc} in cal/mol K

b) $\Delta S_{cyc} = \Delta S^{\circ}_3$ see text

c) ΔH_{cyc} = PA(diol) - PA(mono)

d) Strain = 32 - ΔH_{cyc} See text.

e) PA(mono) is the proton affinity of the monoalcohol. These values have been estimated by extrapolation from the PA of smaller chain alcohols. PA of monoalcohols are from Lias (22).

f) The negative strain obtained for the 1,10-decanediol probably results from an underestimate of PA(mono) and from the uncertainty in DH_{cyc}. Expermential error in ΔH° from van't Hoff plots are in the range of ± 3 kcal/mol. Also Shaefer (110) has calculated the hydrogen bond strength for $H_3O^+H_2O$ to be 35 kcal/mol and Hiraoka (111) has experimental results agree with this value. This suggests that the value of 32 kcal/mol for the average bond strength in symmeteric proton bound dimers may be low.

TABLE 5.3

Comparison of α,ω-diamines with α,ω-dialcohols[a]

B	ΔH_{cyc}[b]	ΔS_{cyc}[c]	Strain[d]
1,4-butanediol	22.3	14.5	8.8
1,4-butanediamine[e]	18.7	17.1	4.3
1,6-hexanediol	26.7	28.3	6.4
1,6-hexanediamine[e]	18.7	20.0	4.3

a) in kcal/mol except ΔS_c in cal/mol

b) $\Delta H_{cyc} = PA(X(CH_2)_nX) - PA(CH_3(CH_2)_nX)$

c) $\Delta S_{cyc} = \Delta S^o_3$ see text.

d) Strain = $32 - \Delta H_c$ for dialcohols. See text.
$23 - \Delta H_c$ for diamines. See text.

e) values from Kebarle (95)

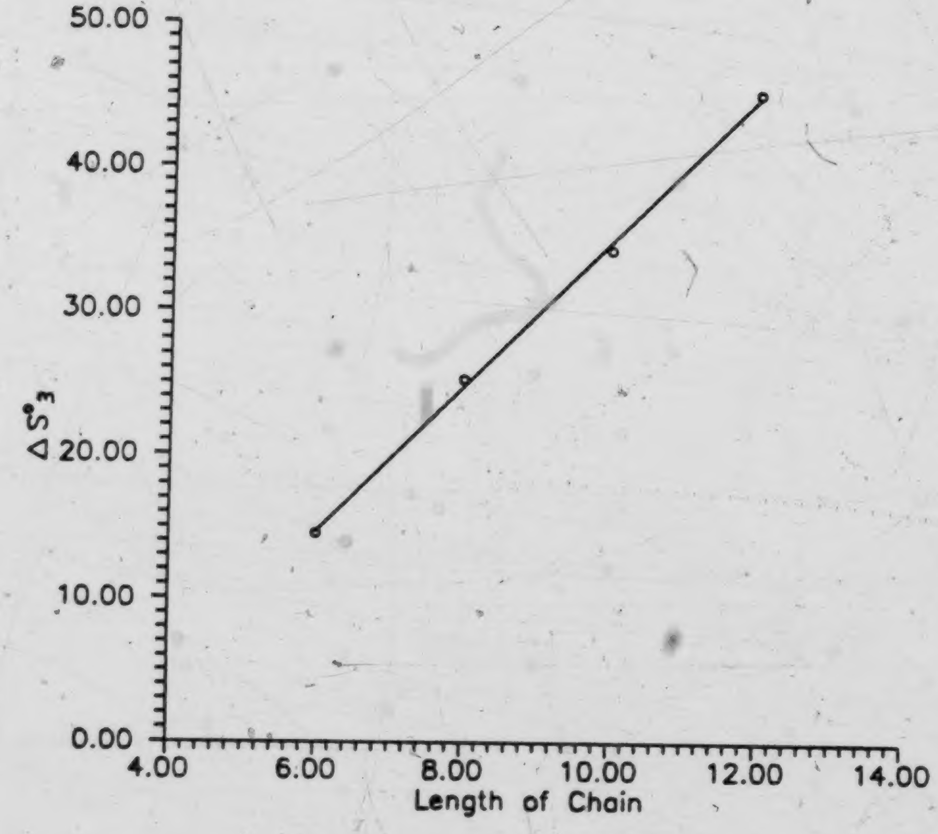

Figure 5.7 A plot of the entropy change for cyclization against the chain length. This is the same trend as seen for the neutral alkanes (Table 5.4).

TABLE 5.4

Entropy of n- and c- alkanes[a]

Temp 300K	S^{ob} n-alkane	c-alkane	S^{o}_{c}-S^{o}_{n}
propane	64.6	56.8	7.8
butane	74.3	63.5	10.8
pentane	83.6	70.1	13.5
hexane	92.0	71.4	20.6
heptane	102.5	82.0	20.5
octane	111.8	87.9	23.9

a) values in cal/mol K.

b) S° values from Stull (112)

kcal/mol. This would indicate that for large polyfunctional bases, where the ring formed by the internal hydrogen bond is not strained, the intramolecular hydrogen bond can be as strong as when two smaller alcohols are bridged by the proton.

5.3b Proton Bound Dimer of Dialcohols

In addition to the protonated dialcohol ions, the proton bound dimer of the dialcohols (reaction 5.9) was also observed in these experiments. The temperature dependance of the equilibrium constant, K_9, is shown in Figure 5.8. The ΔH°_9 and ΔS°_9 are found in Table 5.5.

$$HO(CH_2)_nOHH^+ + HO(CH_2)_nOH = (HO(CH_2)_nOH)_2H^+ \qquad [5.9]$$

As was mentioned earlier, the hydrogen bond strength of the proton bound dimers of oxygen bases are 32 ± 2 kcal/mol. The values in Table 5.5 show that the strengths of the proton bound dialcohols dimers fall within the expected values for oxygen bases. Because the monomer of the protonated dialcohol has an intramolecular hydrogen bond, it may be expected that the strength of the proton bound dimer will be weaker than average if the protonated dialcohol monomer remains cyclic after the clustering. If the protonated monomer opened up during the clustering we would also expect to see a smaller ΔH°_9, as the opening of the ring is an endothermic reaction.

$$H_2NCH_2CH_2CH_2NH_3^+ + H_2O = H_2NCH_2CH_2CH_2NH_3^+ \cdot H_2O \qquad [5.10]$$

$$CH_3CH_2CH_2NH_3^+ \cdot H_2O + H_2O = CH_3CH_2CH_2NH_3^+ (H_2O)_2 \qquad [5.11]$$

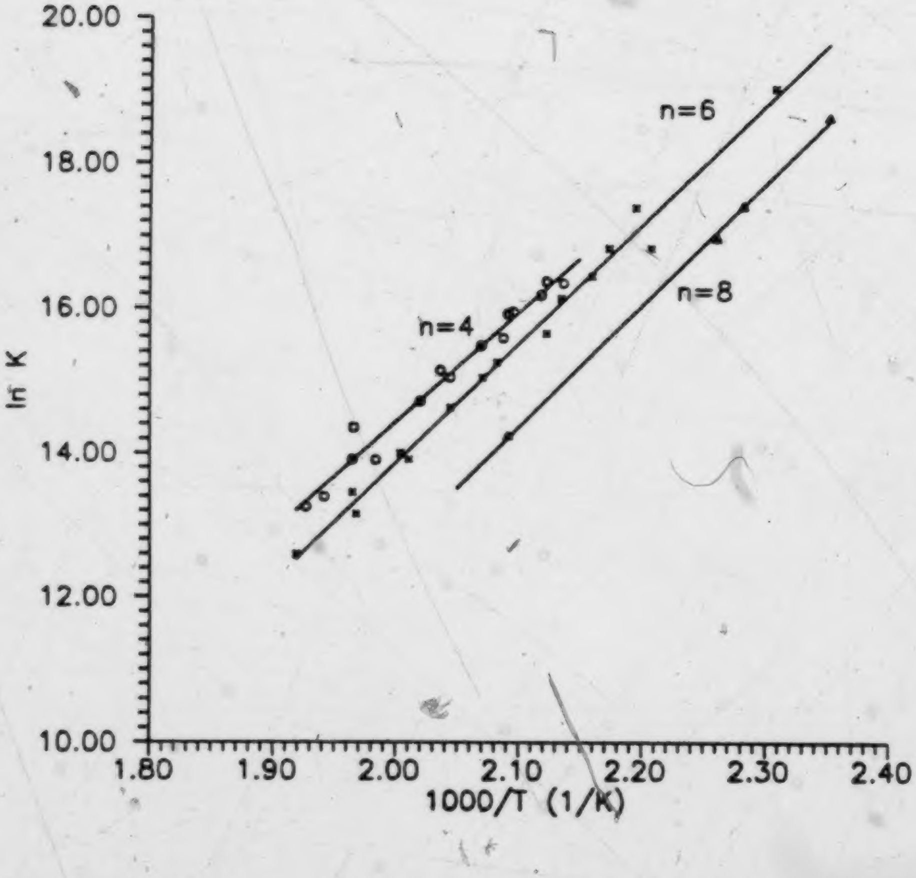

Figure 5.8 The temperature dependance of the equilibrium for the proton bound dimer of $HO(CH_2)_nOH$ where n = 4, 6 and 8 (reaction [5.8]). The ΔH° and ΔS° are found in Table 5.5.

TABLE 5.5

ΔH°_8 and ΔS°_8 for the reaction:
$BH^+ + B = B_2H^+$

B	$\Delta H^\circ_8{}^a$	$\Delta S^\circ_8{}^b$
1,4-butanediol	-30.0	-31.3
1,6-hexanediol	-32.6	-37.7
1,8-octanediol	-33.3	-41.5

a) in kcal/mol $\Delta H^\circ_8 \pm 3$ kcal/mol.

b) in cal/mol K standard state 1 atm. $\Delta S^\circ_8 \pm 5$cal/mol K.

Meot-ner (100) reported that the $\Delta H^\circ_{0,1}$ for hydration of protonated 1,3-propanediamine, reaction 5.10, was almost the same energy as $\Delta H^\circ_{1,2}$ for hydration of n-propylamine, reaction 5.11. Therefore, we would expect ΔH°_9 to be similar to the ΔH° for the clustering of a second neutral molecule (about 20 kcal/mol) and not the first molecule (32 kcal/mol).

If the dialcohol opens up during clustering reaction 5.9, one would expect that the entropy decrease of the overall process will be small. The opening of the ring would have a positive entropy effect, while the clustering itself would have a negative entropy effect. Most clustering reactions have a $-\Delta S = 25$-30 cal/mol K. If we assume that the entropy change due to the clustering of the dialcohols with no change in cyclization is -25 cal/mol K, then from the entropy change in the proton bound dimer reaction (Table 5.1), we can conclude that the dialcohol does not open up upon clustering. Also, with the large entropy changes for the clustering, especially for 1,8-octanediol, it would seem that there is loss of entropy in addition to the loss of translational entropy of a simple clustering reaction.

From the ΔH°_8 and ΔS°_8 values (Table 5.5), the indication is that during the clustering reaction the protonated monomer dialcohol does not open up. In addition, it seems that the second dialcohol also forms a ring. This is indicated by the higher dimerization enthalpy (ΔH°_8) and larger entropy (ΔS°_8) change than would be expected if there was only a simple clustering taking place. However, from the entropy changes, it is probable that the second ring formation is not as tight as for the protonated dialcohol. The entropy change for the cyclization of the protonated 1,6-hexanediol is about 25 cal/mol K while the entropy for the proton bound dimer reaction is 38 cal/mol K. The entropy value of 38 cal/mol K for the dimer reaction is too small to account for a cyclization entropy similar to the protonated monomer as well as the entropy loss due to the loss of translation freedom. A possible structure for the proton bound dimer of the dialcohols is

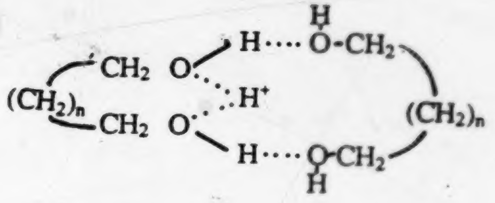

Structure I

Morton and Beauchamp (104) saw the proton bound dimer of protonated diethers, $CH_3O(CH_2)_nOCH_3$, for molecules having $n < 5$. For $n > 5$ there were no proton bound dimers observed. The molecules with small n have a fairly large ring strain and will open easily to form unbridged dimers. The molecules which have large n have small ring strain and require a large energy to open the ring and with no acidic hydrogens for the neutral to bond with the proton bound dimer of the diether was not observed. With the dialcohols, the ring does not have to open in order for the proton bound dimer to form. The oxygen atoms on the neutral can hydrogen bond to the hydrogen atoms on the protonated species not involved in the intramolecular hydrogen bond as in the Structure I proposed above.

I would like to acknowledge assistance of Dr. Jan Sunner who measured the PA of 1,6-hexanediol with respect to acetophenone as well as his helpful discussion.

Chapter 6

Methyl Cation Affinities[1]

6.1 Introduction

In this chapter thermochemical data is presented for the methyl cation (Me^+) affinities of bases B, MCA(B), which correspond to the enthalpy change ΔH°_1 for the gas phase reaction 6.1. The ΔH°_1 values were obtained through determinations of the methyl cation transfer equilibria 6.2 which are cationic S_N2 reactions. The resulting free energy changes, $\Delta G^\circ_2 = -RTlnK_2$ were combined into a continuous scale. The ΔG°_2 changes were measured to obtain ΔH°_2 by estimates of the small ΔS°_2 changes so that a scale of interconnected values of ΔH°_2 changes, was obtained also. It was possible to convert the relative methyl cation affinities to absolute methyl cation affinities by incorporating a compound into the methyl cation affinity ladder whose MCA was available from the literature. In this manner MCA(B) for some 25 bases were obtained.

$$BCH_3^+ = B + CH_3^+ \qquad [6.1]$$

$$BH^+ = B + H^+ \qquad [6.1a]$$

$$BCH_3^+ + B' = B + B'CH_3^+ \qquad [6.2]$$

$$BH^+ + B' = B + B'H^+ \qquad [6.2a]$$

The above methodology is analogous to that used for the determination of proton affinities via measurements of proton transfer equilibria 6.2a. Proton transfer equilibria measurements have led to proton affinities of literally thousands of compounds (22, 23, 113, 114). On the other hand previous MCA determinations have been very limited, yet methylation reactions, like reaction 6.2, are of importance in an extremely wide range of chemistry. To indicate this scope, one may mention: (a) $Me^+.B$ formation by the reverse of reaction 6.1 in interstellar clouds where B may be Ne, H_2, O_2, CO, CO_2 etc. and the transfer of Me^+ to other B via bimolecular reactions 6.2 and its presumed significance to interstellar molecular synthesis (114, 115). (b) Methylation and alkylation in organic synthesis undertaken in solution with use of diazonium ions (116, 119), MeN_2^+ and RN_2^+ or halonium ions (120) $MeXR^+$. (c) Carcinogenicity of alkylating agents which are believed to owe their activity to conversion to highly reactive diazonium cations which alkylate nucleophilic sites on DNA (121).

Although the present studies are in the gas phase, they can be of significance also for understanding of the processes occurring in solution. Furthermore, comparison between the energy changes in the gas phase and solution can be expected to provide important insights into solvent effects. Certainly this approach has proven most fruitful in the studies of Bronsted acidities and basicities. Also, the gas phase thermochemistry data relate directly to energy changes obtained by quantum chemical computation which provide essential complementary information on structure and energy (121-123).

The experimental gas phase studies of MCA's were initiated by Beauchamp (124). Significant development using both ICR and high pressure mass spectrometric techniques has occurred since and will be considered in the discussion.

6.2 Experimental

Most of the experiments were performed on the magnetic sector PHPMS which is described in Chapter 2. The experimental conditions are similar to those used for other work (66). The chemicals used were of reagent grade and were used without further purification. N_2 was used as the bath gas at approximately 3 torr with the pressures of the bases from 0.1-150 mtorr. The temperature in the ion source was kept at 400K. At this elevated temperature the formation of ion clusters such as Me^+B_2 is much reduced and does not interfere with equilibria measurements.

The gas mixture entering the ion source was passed through a cold trap located on the gas inlet line to the ion source. This trap was used to remove water vapor from the gas mixture. The temperature of the cold trap was varied from -77C to -160C depending on the volatility of the bases being used. The temperature was chosen to be high enough to selectively remove water from the gas flow without condensing the bases of interest.

The concentrations of the bases were changed and the resulting equilibria measured to obtain an average equilibrium constant. Also the pressure in the ion source was varied to ensure the equilibrium was not pressure dependant. The average equilibrium constant also gave an indication of the reproducibility of the equilibrium constants.

Some of the measurements were performed with an ion cyclotron resonance (ICR) spectrometer which has been described in detail previously (125, 126). These measurements were preformed by Dr. McMahon and J. Hovey at the University of Waterloo.

6.3 Results and Discussion

Many of the Me$^+$ transfer equilibria were achieved by producing first the dimethylfluoronuim ion, $CH_3FCH_3^+$, and using this ion as the primary reagent ion in the Me$^+$ transfer. The ion intensities observed in a PHPMS experiment used to elucidate the reaction sequence leading to $CH_3FCH_3^+$ are given in Figure 6.1. The major gas in the reaction mixture is nitrogen, which upon electron impact ionization gives N_2^+ and N^+ (reaction 6.3). In the absence of CH_3F, all the initial N_2^+ and N^+ is converted to N_4^+ and N_3^+ (reactions 6.4, 6.5) respectively within 50 μs, such that a distribution of N_4^+ to N_3^+ of 80:20 results (127). In the present case, (See Figure 6.1), due to the low pressure of CH_3F the same conversion occurs almost to completion. Therefore, the ions reacting with CH_3F are mainly N_4^+ and N_3^+ in a 80:20 ratio. It is probable that the dominant N_4^+ produces mostly the fluoromethyl cation,CH_2F^+, ions by dissociative charge transfer reaction 6.6 (See Figure 6.1).

$$e^- + N_2 = N_2^+ + N^+ \qquad [6.3]$$

$$N_2^+ + N_2 = N_4^+ \qquad [6.4]$$

$$N^+ + N_2 = N_3^+ \qquad [6.5]$$

$$N_4^+ + CH_3F = 2N_2 + CH_2F^+ + H \qquad [6.6]$$

$$= 2N_2 + CH_3F^+ \qquad [6.6a]$$

$$CH_3F + CH_2F^+ + M = CH_3FCH_2F^+ + M \qquad [6.7]$$

$$CH_3F + CH_3FCH_2F^+ = CH_3FCH_3^+ + CH_2F_2 \qquad [6.7a]$$

$$CH_3FCH_3^+ + N_2 = N_2CH_3^+ + CH_3F \qquad [6.8]$$

$$CH_3F^+ + CH_3F = CH_3FH^+ + CH_2F \qquad [6.9]$$

$$CH_3FH^+ + CH_3F = CH_3FCH_3^+ + HF \qquad [6.9a]$$

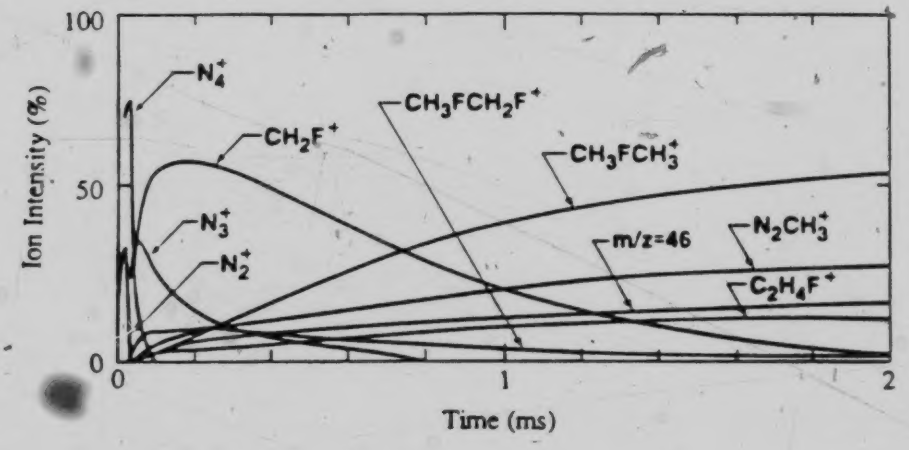

Figure 6.1 Relative ion intensity time dependance after the electron pulse. Gases in the ion source: N_2 = 3.5 torr, CH_3F = 0.4 mtorr, T = 400K. Reaction sequence reactions 6.3 -6.9, see text, leads to the major products $CH_3FCH_3^+$ and $CH_3N_2^+$.

The fluoromethyl cation is known (128) not to undergo bimolecular reactions with CH_3F. In the present case, the disappearance of this cation should be due to the third body dependent association reaction with CH_3F shown in reaction 6.7. This reaction is followed by nucleophilic displacement reaction 6.7a which leads to the desired dimethylfluoronium cation. In the presence of the large excess of N_2 some endothermic Me^+ transfer occurs via reaction 6.8, a reaction that is reversible but has not reached equilibrium in Figure 6.1. When larger pressures of CH_3F are used, the ions engaged in the reversible reaction 6.8 become dominant quite early and reach equilibrium much faster (See Figure 6.2). Runs under such concentration conditions were used to determine the equilibrium constant K_8.

Some CH_3F^+ is also produced by charge transfer from N_4^+ (See reaction 6.6a). This ion could be observed when the CH_3F pressures were lower than that used in Figure 6.1. The CH_3F^+ disappeared rapidly, presumably by the sequence of bimolecular reactions 6.9 and 6.9a which also lead to $CH_3FCH_3^+$. These reactions proceed at near Langevin collision rates (See Beauchamp (129) and Harrision (130)).

The ion intensities shown in Figure 6.3 illustrate the measurement of an equilibrium between $CH_3FCH_3^+$ and a base B = perfluoroacetone, which has an MCA that is higher than that of CH_3F. The use of the relatively high partial pressure for CH_3F lead to the rapid production of the dimethylfluoronuim, $CH_3FCH_3^+$. The equilibrium is reached only after approximately 1 ms (see Figure 6.3) even though the perfluoroacetone pressure is relatively high.

$$CH_3FCH_3^+ + (CF_3)_2CO = CH_3F + (CF_3)_2CO^+CH_3 \qquad [6.10]$$

This result indicates that the rate constant, k_{10}, for the forward direction is considerably slower than the collision rate limit ($k_{10} = 2\times10^{-11}$ molecules^{-1} cm^3 s^{-1}). It

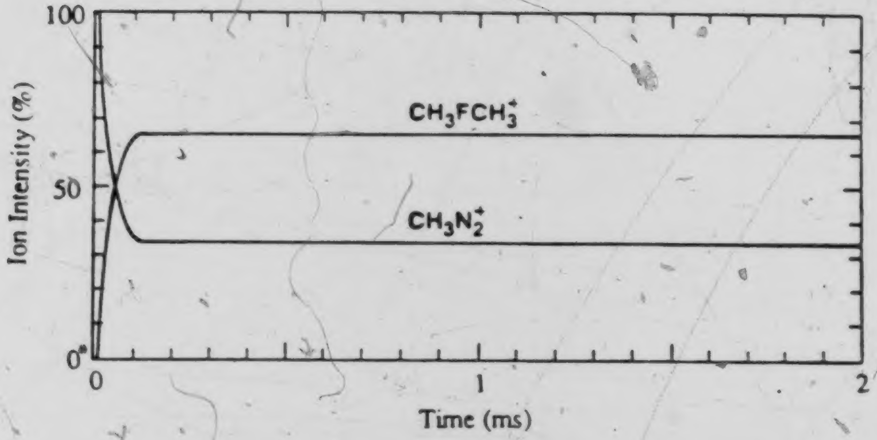

Figure 6.2 At a CH_3F pressure which is 10 times higher than that used in Figure 6.1, $CH_3FCH_3^+$ and $CH_3N_2^+$ reach an equilibrium rapidly. N_2 = 3.5 torr, CH_3F = 5 mtorr.

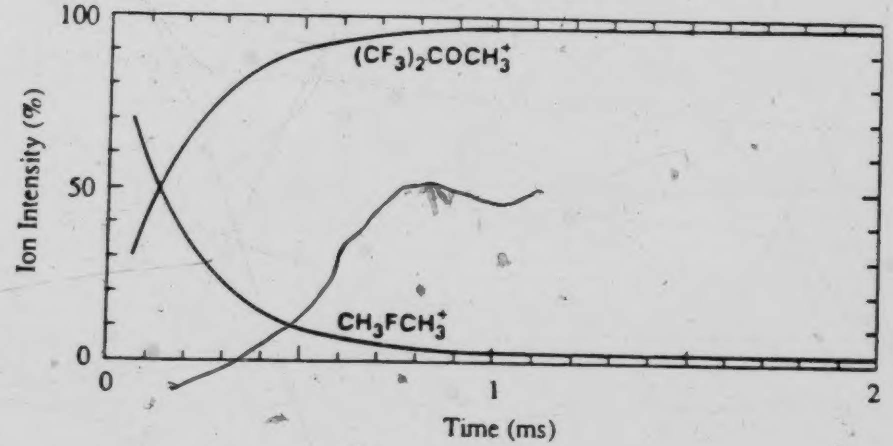

Figure 6.3 Ion intensities observed with N_2 = 3.5 torr, CH_3F = 33 mtorr, $(CF_3)_2CO$ = 11 mtorr, T = 400K. The equilibrium: $CH_3FCH_3^+ + OC(CF_3)_2 = CH_3F + CH_3OC(CF_3)_2^+$ is reached rather slowly even though the pressure of $(CH_3)_2CO$ is relatively high. This is due to the low rate constant of the reaction.

is shown in a later section that this is not an isolated case; a good fraction of the exothermic Me^+ transfer reactions proceed at rates which are considerably below the collision rate. Slow Me^+ transfer rates makes the equilibria measurements more difficult since other faster competitive reactions such as proton transfer may influence the concentration change of the ions engaged in the Me^+ transfer equilibrium. For bases of the form HX, where X = OH, OCH_3, NH_2, etc., the methyl cation affinities could not be measured due the relative rapid proton transfer from CH_3XH^+ after the initial Me^+ transfer (see reactions 6.11, 6.12).

$$CH_3^+ + HX = CH_3XH^+ \qquad [6.11]$$

$$CH_3XH^+ + B = CH_3X + BH^+ \qquad [6.12]$$

In the previous example CH_3F is one of the bases engaged in the equilibrium. Many of the Me^+ transfer equilibria were measured where CH_3F was not one of the bases engaged in the equilibrium. In other experiments, mixtures containing CH_3F and two bases were used where $CH_3FCH_3^+$ served merely as the source of CH_3^+. In these cases, the gas mixture typically contained N_2 as the major gas and relatively high pressures of CH_3F (50-100 mtorr) while the two bases would be in the 1-5 mtorr range. Under these conditions, reactions 6.6-6.9 rapidly produce the $CH_3FCH_3^+$ which then transferred the Me^+ to the two bases. An example of such a run is given in Figure 6.4a where the two MeB^+ are $CH_3ClCH_3^+$ and $CH_3SO_2Cl_2^+$. Equilibrium 6.13 was not achieved for this particular set of conditions, but under adjusted conditions the two bases could be brought to equilibrium as shown in Figure 6.4b.

$$CH_3ClCH_3^+ + SO_2Cl_2 = CH_3Cl + CH_3SO_2Cl_2^+ \qquad [6.13]$$

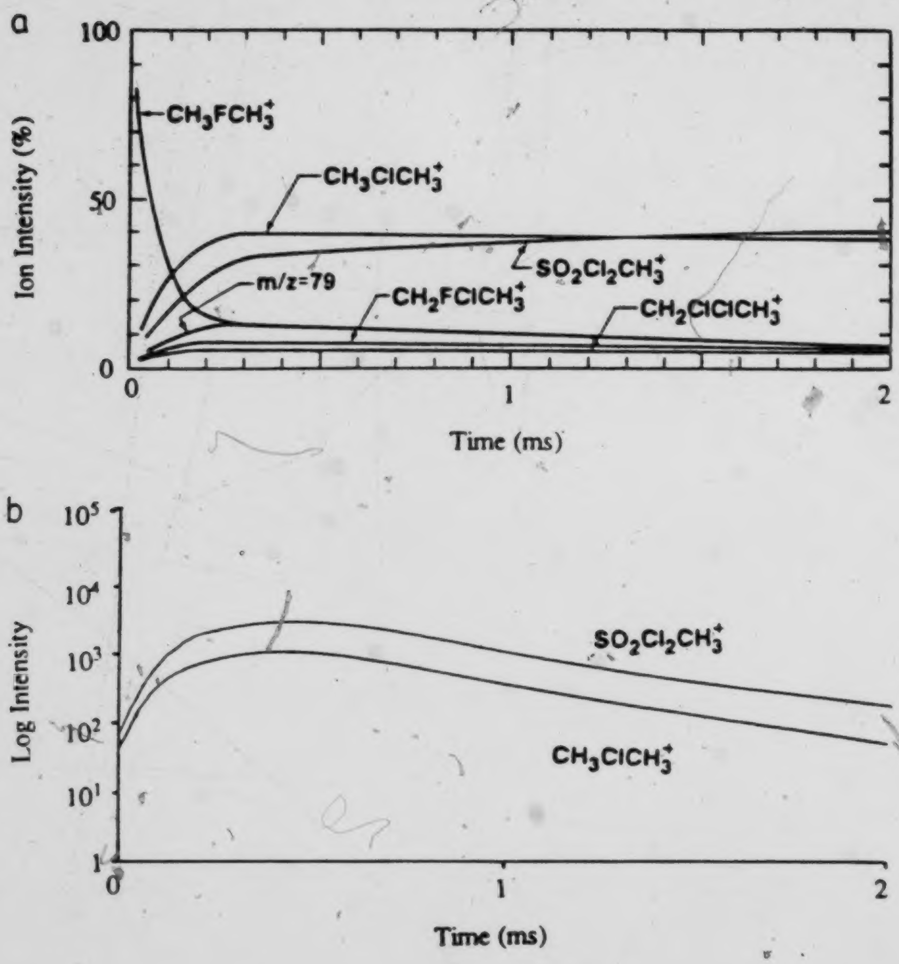

Figure 6.4a Example of a run where $CH_3FCH_3^+$, produced rapidly by reactions]6.3]-[6.9] see Figure 6.1 and text, is used to transfer Me^+ to two bases: CH_3Cl and SO_2Cl_2 which then engage in Me^+ transfer equilibria. N_2 = 3.5 torr, CH_3F = 100 mtorr, CH_3Cl = 1 mtorr, SO_2Cl_2 = 1.7 mtorr, T = 400K. No equilibrium is reached in this run.

b) An example of a run where an equilibrium is reached for the two bases CH_3Cl and SO_2Cl_2. N_2 = 4.0 torr, CH_3F = 122 mtorr, CH_3Cl = 1.2 mtorr, SO_2Cl_2 = 4.0 mtorr.

In general, the reliability of the equilibrium constants was checked by measuring these constants for each reaction several times with different base concentrations and ratios. For example, Table 6.1 illustrates the type of reproducibility obtained with the measured equilibrium constant of reaction 6.13.

The measurement of the Me^+ transfer equilibria was considerably more difficult than PHPMS proton transfer measurements. For proton transfer experiments, conditions could be achieved where the two protonated species to be measured represented better than 80% of the total ion concentration. Furthermore, the proton transfer equilibria almost always proceeded at collision rates in the exothermic direction. In the MCA equilibria, in addition to the two MeB^+ ions of interest, often there were many other ions produced by unidentified side-reactions.

A large number of peaks are observed in the mass spectrum when water is not excluded from the reaction mixture. Figure 6.5 shows the time dependence for the ion profiles for a mixture of N_2 and MeF with no precautions taken against water. The methyl cation transfer from the dimethyl flouronium ion to water produces $CH_3H_2O^+$, which can react further with MeF to give $(CH_3)_2O^+$ and eventually $(CH_3)_3O^+$ (reactions 6.14-6.16).

$$CH_3FCH_3^+ + H_2O = H_2OCH_3^+ HF \quad [6.14]$$

$$CH_3OH_2^+ + CH_3F = (CH_3)_2OH^+ + HF \quad [6.15]$$

$$(CH_3)_2OH^+ + CH_3F = (CH_3)_3O^+ + HF \quad [6.16]$$

Using the heats of formation from Lias (22) for $\Delta H°_f(CH_3OH_2^+) = 135.5$ kcal/mol, $\Delta H°_f((CH_3)_2OH^+) = 130.0$ kcal/mol, $\Delta H°_f(MeF) = -56$ kcal/mol and $\Delta H°_f(HF) = -65$ kcal/mol we find that reaction 6.15 is exothermic by approximately 14.5 kcal/mol. A similar reaction scheme can be proposed starting with $H_3O^+H_2O$ and replacing all the

TABLE 6.1

Reproducibility of equilibrium constants K_2 for different concentrations of B' and B.[a]

$P(CH_3Cl)^b$	$P(SO_2Cl_2)^b$	K_2
5.3	1.7	1.1
4.4	1.4	0.8
1.2	4.0	1.1
0.8	2.7	1.6
1.2	9.9	1.6
1.2	12.6	0.8
1.0	10.7	1.2

a) for reaction: $CH_3ClCH_3^+ + SO_2Cl_2 = CH_3SO_2Cl_2^+ + CH_3Cl$, at 400K.

b) Ion source pressure in mtorr.

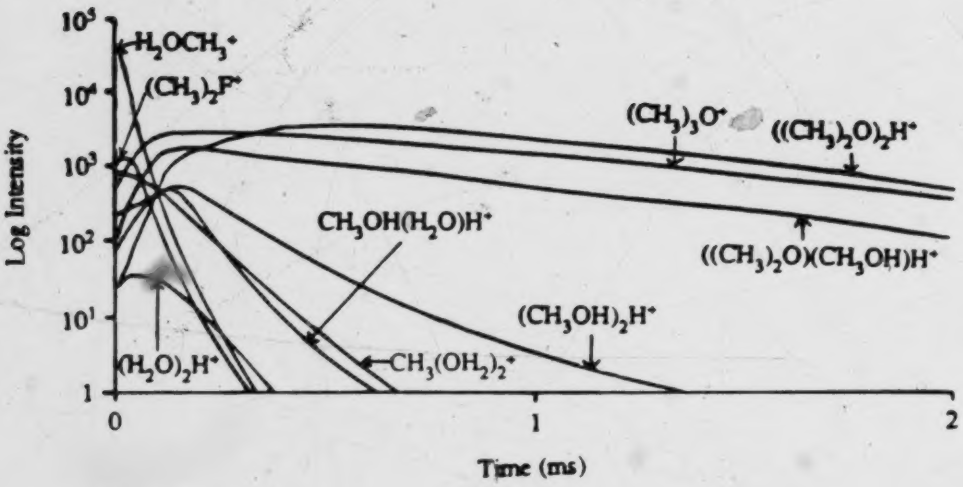

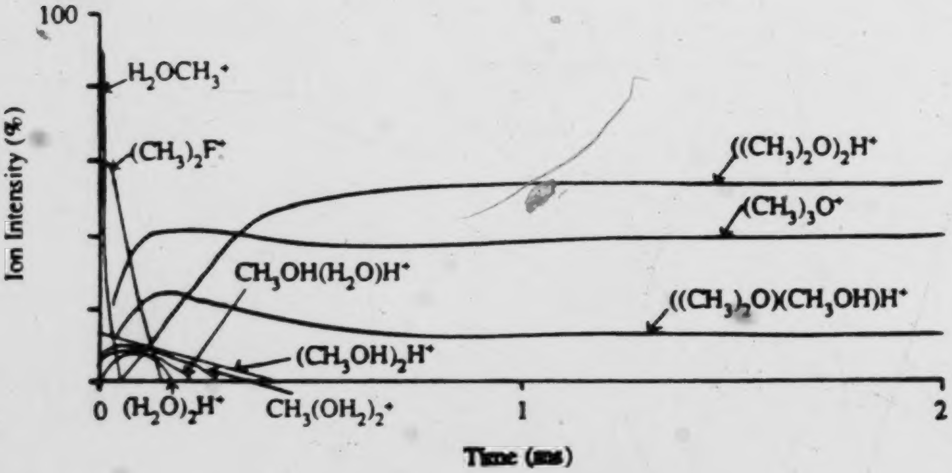

Figure 6.5 The intensities of the water clusters formed when the cold trap is not used.

Conditions: N_2 = 3.5 torr, CH_3F = 15 mtorr, no water was added.

the labile hydrogens with methyl groups, ending with $((CH_3)_2O)_2H^+$ (reactions 6.17, 6.18).

$$H_3O^+H_2O + CH_3F = CH_3OH_2^+H_2O + HF \qquad [6.17]$$

$$CH_3OH_2^+H_2O + CH_3F = \cdots = ((CH_3)_2O)_2H^+ + HF \qquad [6.18]$$

This problem with water clusters can generally be avoided by adding a cold trap to the gas inlet line to freeze out the water vapor. In Figure 6.6 the mass spectrum for the time dependance plots in Figure 6.4b is shown. In the mass spectrum the MeB^+ ions are the major peaks but a large number of smaller peaks are also present. Even with a acetone slush (-98C) cold trap some of the water clusters persist in the mass spectrum. For these reasons we have assigned somewhat larger uncertainties to the MCA results. In the most unfavorable cases, relative errors in the ΔG°_2 measurements of $\pm$ 1 kcal/mol cannot be excluded.

The equilibrium constants, K_2, for the general Me^+ transfer reaction 6.2 determined by the measurements described above were used to obtain the corresponding ΔG°_2 values. The resulting ladder of interconnected ΔG°_2 values is shown in Figure 6.7. Both the PHPMS results obtained at 400K and the ICR results at 300K are included in this ladder. Even though the results are at different temperatures, the ΔG°_2 can be compared directly because the ΔS°_2 are generally small which means that the temperature effect on ΔG°_2 is small. In general there is good agreement between the PHPMS results and the ICR results, the data for CF_3Cl are within 0.6 kcal/mol; SO_2F_2 is within 0.2 kcal/mol; and the HCl value comes out to be the same (See Figure 6.7).

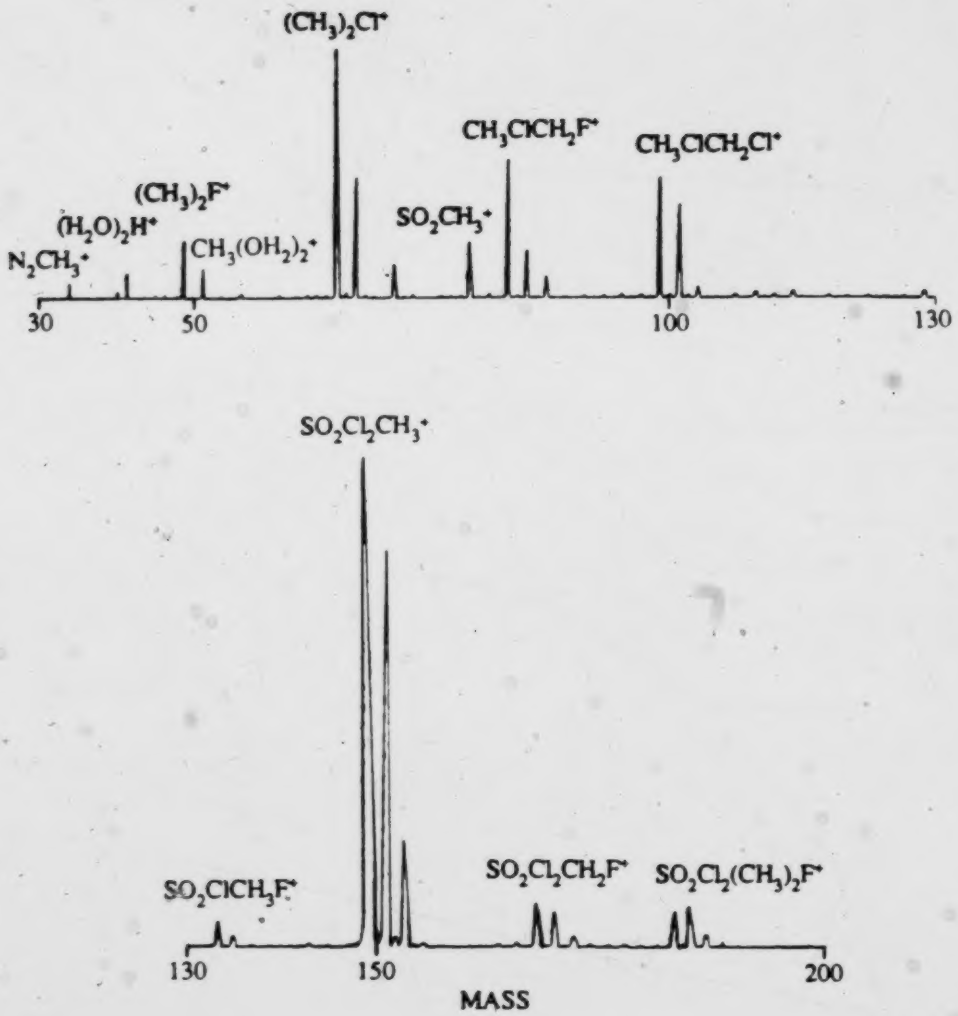

Figure 6.6 The mass spectrum for the run in Figure 6.4b. N_2 = 4.0 torr, CH_3F = 122 mtorr, CH_3Cl = 1.2 mtorr, SO_2Cl_2 = 4.0 mtorr.

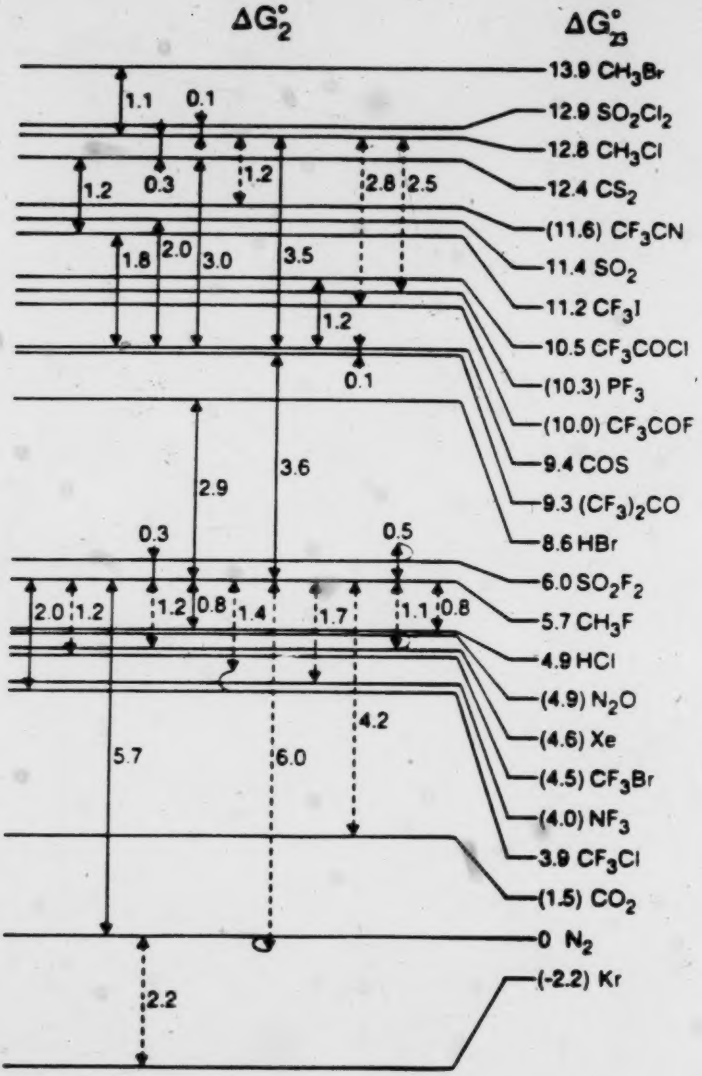
ΔG°2
ΔG°23
13.9 CH3Br
12.9 SO2Cl2
12.8 CH3Cl
12.4 CS2
(11.6) CF3CN
11.4 SO2
11.2 CF3I
10.5 CF3COCl
(10.3) PF3
(10.0) CF3COF
9.4 COS
9.3 (CF3)2CO
8.6 HBr
6.0 SO2F2
5.7 CH3F
4.9 HCl
(4.9) N2O
(4.6) Xe
(4.5) CF3Br
(4.0) NF3
3.9 CF3Cl
(1.5) CO2
0 N2
(-2.2) Kr
1.1
0.1
0.3
1.2
1.2
2.8
2.5
1.2
1.8
2.0
3.0
3.5
1.2
0.1
2.9
3.6
0.3
0.5
2.0
1.2
1.2
0.8
1.4
1.7
1.1
0.8
5.7
6.0
4.2
2.2

Figure 6.7 Free energy changes ΔG^o_2 from equilibrium constants K_2 for reaction 6.2: $B'CH_3^+ + B = B' + CH_3B^+$. Solid arrows PHPMS data at 400K, dashed arrows ICR data at 300K. ΔG^o_{23} values obtained from summation of ΔG^o_2 corresponding to free energy changes for reaction 6.23: $N_2CH_3^+ + B = N_2 + CH_3B^+$.

6.3a Rate constants for Me^+ transfer reactions from Me_2F^+ and Me_2Cl^+ to bases B.

The rate constants for several Me^+ transfer reactions from $CH_3FCH_3^+$ to different bases were determined in a number of special experiments. In these experiments the pressure of the CH_3F was relatively high, such that the formation of $CH_3FCH_3^+$ by reactions 6.6-6.9 was rapid, while the pressure of B was relatively low, so that the kinetics of the Me^+B production by Me^+ transfer from $CH_3FCH_3^+$ occurred within the window of the PHPMS. The results from a typical run are shown in Figure 6.8, which gives the logarithmic plot of the absolute intensities and a linear plot of the relative ion concentrations. The logarithmic plot gives a good picture of low intensity ions that are also present while the linear "normalized" plot provides a picture of the main events, i.e. the reaction 6.19.

$$CH_3FCH_3^+ + CH_3Cl = CH_3ClCH_3^+ + CH_3F \qquad [6.19]$$

A plot of the natural logarithm of the normalized $CH_3FCH_3^+$ intensity against time gave a straight line with slope, v_{19}, equal to the pseudo first order rate constant. The known concentration of $B = CH_3Cl$ was then inserted into equation 6.20 to obtain k_{19}, the rate constant for the Me^+ transfer.

$$k = v/[B] \qquad [6.20]$$

The results of the kinetic determinations are summarized on Table 6.2. Included in the table are previously determined rate constants (78) involving Me^+ transfer from the dimethylchloronium ion to bases B (See equation 6.21).

$$CH_3ClCH_3^+ + B = CH_3Cl + CH_3B^+ \qquad [6.21]$$

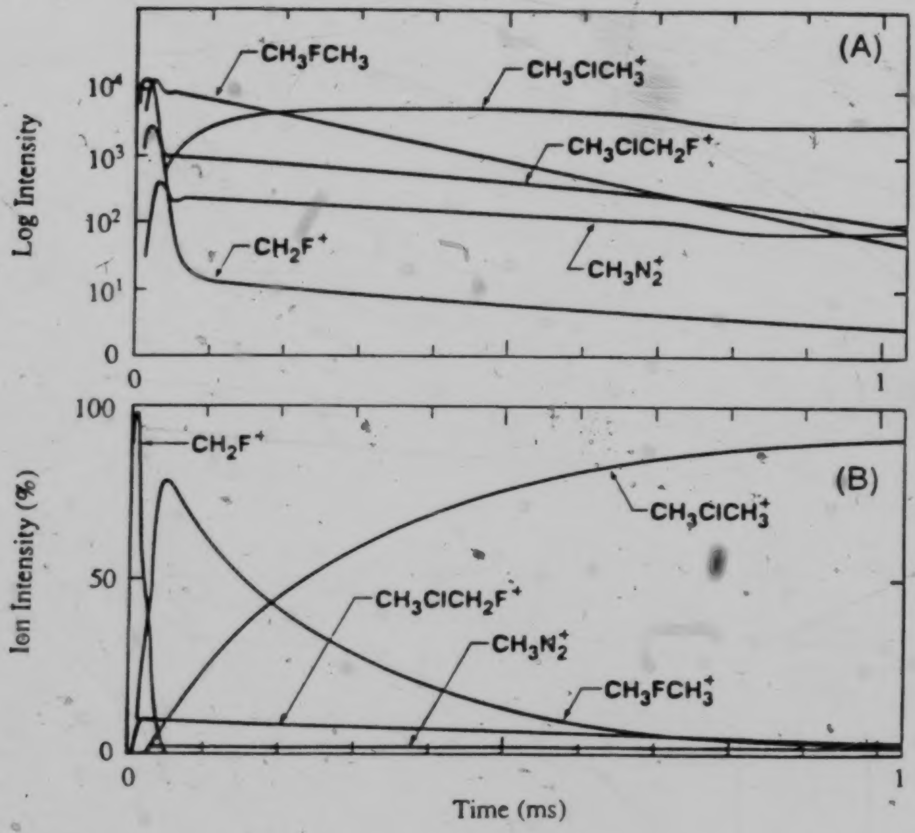

Figure 6.8 Ion intensity time dependance in a run used to determine rate constant, k, for the reaction: $CH_3FCH_3^+ + CH_3Cl = CH_3F + CH_3ClCH_3^+$. In Figure 8a the logarithm of the measured ion intensity in counts per channel are shown. The linear decrease of the $CH_3FCH_3^+$ ion is due to the pseudo first order Me^+ transfer reaction. Figure 8b shows the corresponding relative intensities in a linear plot.

TABLE 6.2

Rate constants k for reactions:

$Me_2X^+ + B = MeX + MeB^+$

X	B	k x10[9c]	-ΔG°[d]
F[a]	CH_3Cl	1.4	7.1
	CS_2	1.4	6.4
	SO_2Cl_2	1.0	7.2
	SO_2	0.3	5.7
	SO_2ClF	0.3	5.7[e]
	$(CF_3)_2CO$	0.02	3.6
Cl[b]	$(CH_3)_3N$	1.2	64
	NH_3	0.8	43
	$(CH_3)_2O$	1.1 (0.47)[f]	31
	C_2H_5OH	0.5	27
	$CH_3C_6H_5$	0.05	34
	C_6H_6	0.002	33

a) temperature 400K, present work

b) temperature 315K, from Sen Sharma (78)

c) in molecules^{-1} cm^3 s^{-1}

d) Free energy change of reaction in kcal/mol. For F from Figure 6.4 and Table 6.3. For Cl from Sen Sharma (78).

e) estimate based on the assumption that ΔG° for SO_2ClF should be between SO_2Cl_2 and SO_2F_2 but closer to SO_2Cl_2, (see Figure 6.4).

f) temperature 400K, from Sen Sharma(78).

For the reactions involving Me^+ transfer from Me_2F^+, the rate constants are close to the ADO collision limit (See Chapter 1) at higher exoergicities of reaction and gradually decrease to considerably below the collision limit as the transfer exoergicity decreases. Thus, for B = $(CF_3)_2CO$ at an exoergicity of 6.6 kcal/mol, the observed rate is about 100 times slower than the collision limit. A similar trend is observed with the data for Me^+ transfer from Me_2Cl^+, but in this case the rate decrease occurs at much higher exoergicities.

It is most likely that the Me^+ transfer reactions 6.21 and 6.22 proceed by an S_N2 mechanism involving "backside attack" and inversion of the methyl group.

A double minimum potential well is expected (75, 78, 131, 132) for the reaction coordinate in the gas phase, as shown in Figure 6.9. Theoretical calculations also have indicated that a double minima reaction coordinates occurs in the transfer of Me^+ from $MeOH_2^+$ to H_2O and MeOH (122). The height of the central barrier in Figure 6.9 is the dominant factor controlling the rate of the Me^+ transfer reactions. When the barrier is small so that the gap ($-\Delta E_g$) is large, the reaction proceeds at collision rates. For reactions with a large barrier where the gap is small, the rate is slow and decreases as the temperature is increased (negative temperature dependance) (78), see for example the data for Me_2Cl^+ and B = Me_2O (78). Where the central barrier is sufficiently high for ΔE_g to be positive, the reaction will exhibit an activation energy barrier leading to a very slow reaction with a positive temperature dependance, as was the case for benzene (78).

Neglecting entropic factors, a direct relationship between the rate and the gap width can be expected. ΔE_g is expected to increase monotonically with an increase in the reaction exoergicity and thus with the MCA(B) only when a series of related bases B is involved (81, 133). For example the n-donor bases, EtOH to Me_3N (See Me_2Cl^+ results in Table 6.2) represent a group. The carbon bases, toluene and

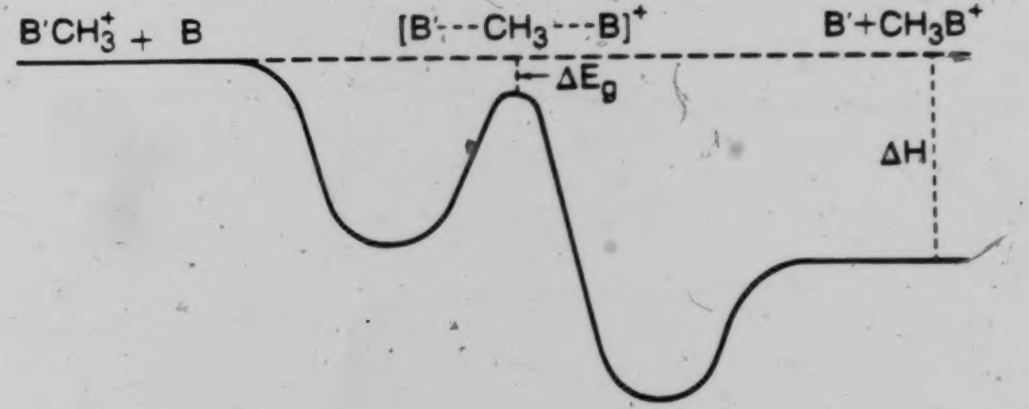

Figure 6.9 Gas phase reaction coordinate for cationic S_N2 reaction 6.2 involving Me$^+$ transfer. The energy difference between the intermediate B'CH$_3$B$^+$ and the reactants B'CH$_3^+$ and B called ΔE_g, controls the rate. A large $-\Delta E_g$ leads to collision rates, a small $-\Delta E_g$ leads to negative temperature dependance and below collision rates.

benzene, fall into another group which is far less nucleophilic. Substantial reaction exothermicity still occurs for the latter group due to resonance stabilization (charge delocalization) present in the products but not in the transition state (78).

The observed decrease of rates for the Me^+ transfer from Me_2F^+ to B with decreasing exoergicity of the reactions, decreasing MCA(B), is expected. Even though the nucleophilic centers on the bases are fairly dissimilar, these are systems in which selective resonance stabilization of only the products does not occur to any extent. The experimental observation that for Me_2F^+ the rates remain close to collision rates down to very low exothermicities while for Me_2Cl^+ they begin to decrease even at 30 kcal/mol exothermicities (B = Me_2O), can not be attributed to different nucleophilicities of the bases used in the two groups as Me_2O is more nucleophilic than all the bases of the Me_2F^+ group. Obviously the difference must be due to differences between Me_2F^+ and Me_2Cl^+. Reaction of Me_2F^+ would lead to a larger gap ($-\Delta E_g$) relative to reactions with Me_2Cl^+ when the same base is involved because Me_2F^+ is the higher energy ion. The observed greater reactivity of Me_2F^+ relative to Me_2Cl^+ is in line with the lower MCA of MeF relative to the MCA of MeCl (See Figure 6.7 and Table 6.3). The generalization that for similar B the reactivity of MeB^+ in electrophilic Me^+ transfer reactions increases with decreasing MCA(B) may be expected to hold. In summary, the present kinetic results for the Me^+ transfer reaction 6.22 are consistent with the assumption that $-\Delta E_g$ (See Figure 6.9) and thus the rates increase with increasing MCA of B and decreasing MCA of B', when they are limited by the passage over the barrier. This relationship is expected to hold well when a series of related B and B' are involved. Such a series of related bases would be CH_3X where X = F, Cl, Br, I.

TABLE 6.3

a) Entropies at 298K in cal mol^{-1} K^{-1} from Benson (75) except where otherwise indicated, ΔG°_{23} at 300K, ΔH°_{23}, MCA(B) all in kcal/mol.

b) Estimated using group equivalents, Benson (75).

c) Estimated entropy of CH_3B^+ based on entropy for isoelectronic neutral shown. Values for isoelectronic neutrals from Benson (75) except where otherwise indicated.

d) from Stull et al. (112).

e) Assumed to be the same as ΔS°_{23} for reaction 6.13 involving CH_3Cl.

f) Assumed to be the same as ΔS°_{23} for reaction 6.23 involving CH_3F.

g) Assumed to be the same as ΔS°_{23} for HCl.

h) Arbitrary estimate.

k) External standard, Beauchamp et al. (129).

l) from Sen Sharma (23).

m) Estimates based on bracketing literature data leading to PA(CH_3Cl) = 158 ± 6 kcal/mol and PA(CH_3Br) = 164.5 ± 3 kcal/mol see text.

TABLE 6.3

B	S°(B)[a]	So(CH_3^+B)[c]		$\Delta S°_{23}$	$\Delta G°_{23}$	$\Delta H°_{23}$	$\Delta H(Me^+B)$
CH_3Br	-	-		-2.6[f]	14.1	14.3	66.8
SO_2Cl_2	-	-		-2.[h]	13.1	13.7	65.6
CH_3Cl	56.0	-		-2.1[f]	13.0	13.6	65.5 (64)[l]
CS_2	56.8	-		1.6	12.3	11.8	63.7
SO_2	59.3	-		-2.[h]	11.6	12.2	64.1
CF_3I	-	-		-1.3$_e$	11.3	11.6	63.5
CF_3COCl	-	-		-2.[h]	10.7	11.7	63.6
OCS	55.3	CH_3NCS	69.3[d]	1.6	9.3	8.8	60.7
$(CF_3)_2CO$	-	-		-2.[h]	9.5	10.1	62.0
HBr	47.5	-		4.4[h]	8.2	7.0	58.9(59.8±3)[m]
SO_2F_2	67.7	-		-2.[h]	6.3	6.9	58.8
CH_3F	53.3	$(CH_3)_2O$	63.7	-2.0	5.9	6.5	58.4
HCl	44.6	CH_3SH	61.0[d]	4.0	4.7	3.3	55.2 (51±6)[m]
N_2O	52.5	CH_3NCO	65.1[b]	0.2	5.1	4.5	56.4
Xe	40.5	CH_3I	60.7[d]	7.8	4.8	2.5	54.4
CF_3Br	73.4[b]	-		-1.3[e]	4.7	5.2	57.1
NF_3	62.3	CH_3CF_3	68.7[b]	-6.0	4.2	6.0	57.9
CF_3Cl	69.0[b]	CF_3SCH_3	80.3[b]	-1.1	4.2	4.5	56.4
CO_2	51.1	CH_3NCO	65.1[b]	1.6	1.5	1.0	52.9
N_2	45.8	CH_3CN	58.1[d]	0.	0.	0.	(51.9)[k]
Kr	39.2	CH_3Br	58.8[d]	7.2	-2.2	-4.4	47.5

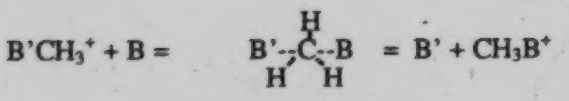

$$B'CH_3^+ + B = B'{-}{-}\overset{H}{\underset{H\ \ H}{C}}{-}{-}B = B' + CH_3B^+ \qquad [6.22]$$

It is notable that these simple relationships, which are easily spotted in the gas phase where the complicating effects of the solvent are absent, can be experimentally demonstrated only when the gas phase ion-molecule reaction rates are lower than the collision rates. In such cases the magnitude of the ΔE_g can often be determined (73, 75, 78, 132). This value is essential for the evaluation via a Born cycle of the solvation energy of the transition state of the corresponding reaction in solution (134) and this amounts to establishing quantitative relationships between the reaction in the gas phase and solution (134).

6.3b Thermochemical data on Me$^+$ affinities

The ΔG°_2 results for the Me$^+$ transfer equilibria 6.2, (See Figure 6.7) can be combined to provide a scale giving the ΔG°_{23} value for the transfer reaction 6.23. The resulting values for ΔG°_{23} are given in Figure 6.7.

$$N_2CH_3^+ + B = N_2 + CH_3B^+ \qquad [6.23]$$

N_2 is the only base for which a good literature value for the MCA is available and therefore this compound is used as the anchor point (primary standard) of the ladder. Beauchamp et al (135) have deduced on the basis of the photoionization appearance potential of $CH_3N_2^+$ from $CH_3N_2CH_3$, a heat of formation $\Delta H^\circ_f(CH_3N_2^+) = 209.4$ kcal/mol. From this value and $\Delta H^\circ_f(CH_3^+) = 261.2$ kcal/mol (136) one obtains the

$MCA(N_2)$ = 51.9 kcal/mol (See equation 6.24). This MCA is used in Table 6.3 to construct an absolute MCA scale in combination with the results from Figure 6.7.

$$N_2CH_3^+ = N_2 + CH_3^+ \quad \Delta H^\circ_{24} = MCA(N_2) = 51.9 \text{ kcal/mol (135)} \qquad [6.24]$$

Unfortunately photoionization appearance potentials do not always provide reliable ionic heats of formation so that ΔH°_{24} could be in error by a few kcal/mol.

Theoretical calculations (123, 137) have established that $CH_3N_2^+$ is linear. Unfortunately the $MCA(N_2)$ provided by these calculations differ widely depending on the basis set used. Ab initio calculations by Radom (123) have yielded $MCA(N_2)$ = 51.6 kcal/mol at the STO 3G level, in good agreement with Beauchamp (135), but calculations at the 4-31G level give a value of 28.5 kcal/mol. Simonetta et al (137) used a more flexible basis set which included polarization functions, to obtain an even lower value of 18.4 kcal/mol. For MNDO data see Ford and Schibner (121). Obviously, further extended basis set calculations including electron correlation and complete optimization would be very desirable.

In order to combine ΔH°_{24} with the free energy scale ΔG°_{23} of Figure 6.7, the ΔG°_{23} values of the Me^+ transfer must be converted to ΔH°_{23} values. In principle, ΔS°_{23} and ΔH°_{23} could be obtained by measuring the temperature dependance of the Me^+ transfer equilibria 6.2 and deriving ΔH°_2 and ΔS°_2 from van't Hoff plots. However, since the equilibria 6.2 were difficult to measure, even at one single temperature, this method was not adopted and instead the ΔS°_{23} were estimated. The $S^\circ(B)$ for most B are available in the literature (112, 138). In a few cases the $S^\circ(B)$ had to be estimated with the group equivalents method (138). All the $S^\circ(B)$ data used are given in Table 6.3. The $S^\circ(CH_3B^+)$ were assumed to be the same as those of the isoelectronic neutral. For example, $S^\circ(CH_3N_2^+)$ was assumed to be equal to

$S^\circ(CH_3CN)$. The $S^\circ(CH_3B^+)$ and the isoelectronic neutrals used are given in Table 6.3. ΔS°_{23} was then calculated from the S° values of the reactants and products. In cases where the S° of the isoelectronic neutral was not available, the ΔS°_{23} values were obtained by assuming that they are identical for homologous pairs. Thus, ΔS°_{23} for the reactions 6.25 were assumed to be identical.

$$N_2CH_3^+ + CH_3X = N_2 + CH_3XCH_3^+ \text{ (X= F, Cl, Br)} \qquad [6.25]$$

The ΔS°_{23} evaluated in this manner were used to obtain $T\Delta S^\circ_{23}$ for $T = 400$ and these combined with the PHPMS ΔG°_{23} led to a ΔH°_{23} scale. The ΔH°_{23} scale was anchored to the $\Delta H^\circ_1(N_2) = MCA(N_2) = 51.9$ kcal/mol (135) to give a $\Delta H^\circ_1(B) = MCA(B)$ scale.

The MCA(B) scale can be checked with available literature data at three points. The $MCA(CH_3Cl) = 64$ kcal/mol reported by Sen Sharma et al (139) and McManus (140) is close to the present value of 65.4 kcal/mol, Table 6.3. The Sen Sharma and McManus result is based on MINDO/3 calculations. The calculations by themselves would not have been convincing however, Sen Sharma et al (139), on the basis of determinations of the temperature dependence of equilibria 6.26, obtained via van't Hoff plots ΔH°_{26} and

$$R^+ + CH_3Cl = CH_3ClR^+ \quad \text{(R = Et, i-Pr, t-Bu)} \qquad [6.26]$$

from these and thermochemistry data deduced the MCA(RCl) given in Table 6.4. The relatively good agreement between the experimental MCA results (139) for RCl = EtCl, i-PrCl; t-BuCl and the MINDO/3 predicted values (139, 140), suggests that the MINDO/3 result for the $MCA(CH_3Cl)$ is reliable to within ± 3 kcal/mol.

TABLE 6.4

MCA(RCl)[a]

R	experimental	MINDO/3[b]
Me	65.4[c]	64
Et	71.[d]	72
i-Pr	77.[d]	79
t-Bu	81.[d]	85

a) all values in kcal/mol.

b) Theoretical calculations from references 27 and 28.

c) Experimental results from present work.

d) Experimental results from Sen Sharma (78).

Relationship 6.27 between the proton affinity of the methyl halide, CH_3X, and the Me^+ affinity of the corresponding hydrogen halide, HX, follows from the definition of the PA and MCA. The value of 104.5 kcal/mol for the difference between $\Delta H_f(H^+)$ and $\Delta H_f(CH_3^+)$ is based on the $\Delta H_f(H^+) = 365.7$ and the $\Delta H_f(CH_3^+) = 261.2$ kcal/mol (136).

$$\begin{aligned} PA(CH_3X) - MCA(HX) &= \Delta H_f(H^+) - \Delta H_f(CH_3^+) + \Delta H_f(CH_3X) - \Delta H_f(HX) \\ &= 104.5 + \Delta H_f(CH_3X) - \Delta H_f(HX) \qquad [6.27] \end{aligned}$$

The proton affinity of CH_3Cl has been established by Beauchamp et al (129) to be between $PA(C_2H_4)$ and $PA(C_2H_2)$. Using the PA values of 162.6 kcal/mol and 153.3 kcal/mol respectively, Lias (22), estimated $PA(CH_3Cl)$ to be 158 ± 6 kcal/mol and combined this value with $\Delta H_f(CH_3Cl) = -19.3$ kcal/mol and $\Delta H_f(HCl) = -22.1$ kcal/mol (141) to give, via 6.22, MCA(HCl) = 51 ± 6 kcal/mol. This value is in fair agreement with the present experimental result of 55.2 kcal/mol, Table 6.3.

The proton affinity of CH_3Br has been bracketed (23) between $PA(C_2H_4) = 162.2$ kcal/mol and $PA(H_2O) = 166.4$ kcal/mol (22) allowing an assignment of $PA(CH_3Br) = 164.5 \pm 3$ kcal/mol. This value combined with the $\Delta H_f(CH_3Br) = -8.5$ kcal/mol and $\Delta H_f(HBr) = -8.7$ kcal/mol (142) leads to MCA(HBr) = 59.8 ± 3 kcal/mol, which is in good agreement with the experimental value of 58.9 kcal/mol.

The above three comparisons with approximate MCA data from the literature are in support of the MCA ladder Table 6.3 and suggests an uncertainty in the absolute values of approximately ± 2 kcal/mol. Since MCA(HCl) and MCA(HBr)values determined in this investigation can be considered more accurate than the bracketed $PA(CH_3Cl)$ and $PA(CH_3Br)$ values, one can use equation 6.22 to determine the PA values from the MCA values. In this manner, PA(CH_3Cl) = 162.2 kcal/mol and PA(CH_3Br) = 163.3 kcal/mol are obtained.(See also McMahon (143).)

The present MCA scale, Table 6.3, extends to MCA = 70 kcal/mol. This value is somewhat below but close to where the MCA's for oxygen bases like ethers begin. Thus, from the known heats of formation of protonated dimethyl ether, $\Delta H_f((CH_3)_2OH^+)$ = 130 kcal/mol (22), one can calculate MCA(CH_3OH) to be 83.2 kcal/mol. Therefore, the availability of the present scale holds the promise that future Me^+ transfer equilibria measurements to bases with MCA in the 70-80 kcal/mol range will extend to MCA scale to oxygen and nitrogen bases. Thus, a complete scale of MCA based on equilibria covering a similar range to that for the PA's (22, 23, 113, 114) is made more likely by the availability of the present results. Also with higher MCA compounds the Me^+ transfer from $CH_3FCH_3^+$ should be near collision rate making the reactions easier to study.

6.3c Relationships Between Proton and Methyl Cation Affinities

An approximate relationship between PA(B) and MCA(B) can be expected. Thus, assuming that the H^+ and the CH_3^+ react with the same basic atom on B, the reaction is formally very similar since it consists of an electron pair donation from B to H^+ and CH_3^+. The PA(B) should be much larger than the MCA(B) on two counts. First, the B-H bond formed will be stronger than the B-CH_3 bond, and secondly, the electrostatic energy decrease due to the positive charge expansion from the small H^+ to BH^+ will be very much larger than that from the sizable CH_3^+ to CH_3B^+.

A plot of PA(B) from Lias (22) versus the MCA(B) determined in this work is shown in Figure 6.10. A fairly linearly relationship with a slope, p, equal to about 3 is observed. In order to examine the relationship over a wider range of data, MCA values for bases of the type HX, where X now stands for a basic group like OH,

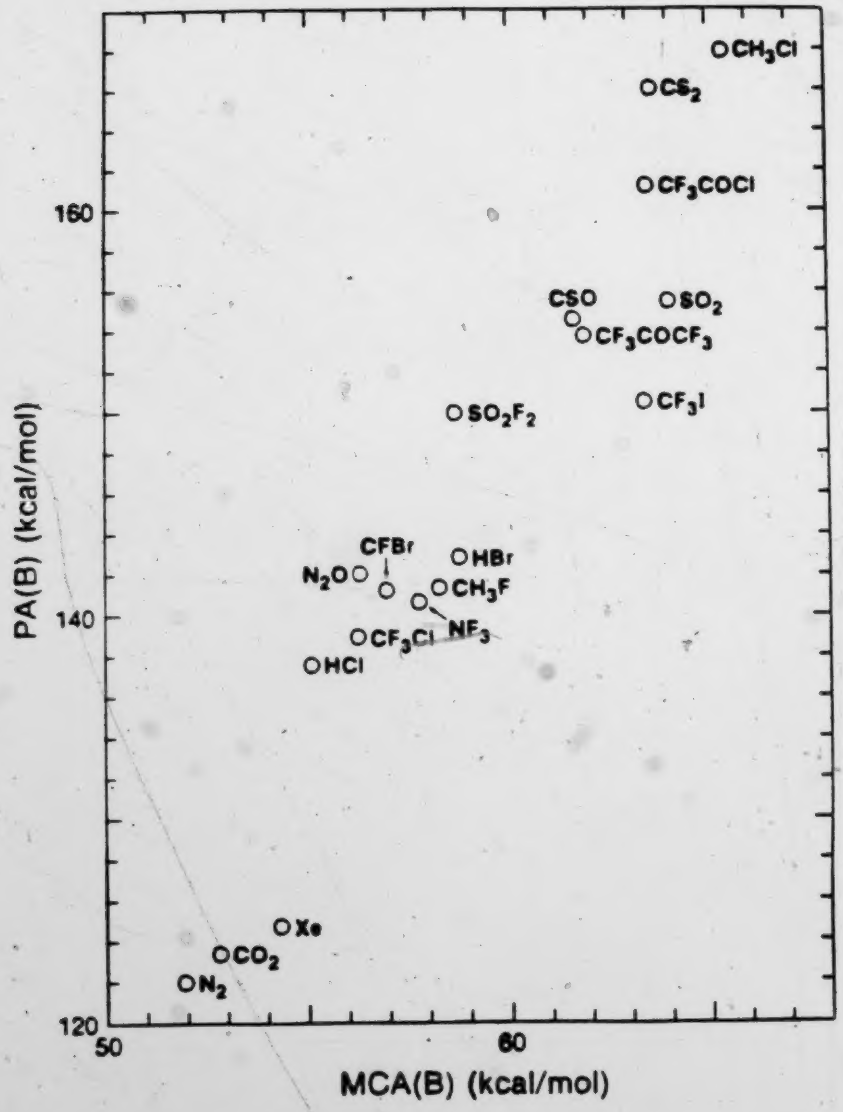

Figure 6.10 Plot of proton affinity PA(B) against methyl cation affinity MCA(B) for bases of Table 6.3. Slope = 3.

OCH_3, etc., were evaluated from thermochemical data (22, 142) with the use of equation 6.22. Also added are the MCA of acetone and dimethyl ether determined by Szulejko et al (144) of 92 kcal/mol and 95 kcal/mol respectively. The extended set is shown in the PA versus MCA plot in Figure 6.11. Figure 6.11 shows that when data covering a wider range of affinities, the plot may be divided into two distinct regions, with the transition occurring in the vicinity of H_2O. For bases weaker than water, the plot of PA versus MCA yields a slope of about 3. For bases stronger than water, a slope of approximately 1 is found.

Equation 6.28 can be derived from equation 6.27 as will be shown. The equation is exact only for bases HX, but a certain interpretative meaning will be obtained from the equation which is useful also for the general group B.

$$\mathrm{PA(HX)} - \mathrm{MCA(CH_3X)} = \mathrm{IE(H)} - \mathrm{IE(CH_3)} + \mathrm{BE(H\text{-}X)} - \mathrm{BE(CH_3\text{-}X)} - \Delta \mathrm{PA(CH_3)} \qquad [6.28]$$

Substitution of the definitions for the ionization energies, IE (See equation 6.29), bond dissociation energies, BE (See equation 6.30), and equation 6.31 which expresses the methyl substitution effect on the proton affinity of HX, into equation 6.27 leads directly to equation 6.28.

$$\mathrm{IE(H)} = \Delta H_f(\mathrm{H^+}) - \Delta H_f(\mathrm{H}) \qquad [6.29]$$

$$\mathrm{BE(H\text{-}X)} = \Delta H_f(\mathrm{H}) + \Delta H_f(\mathrm{X}) - \Delta H_f(\mathrm{HX}) \qquad [6.30]$$

$$\Delta \mathrm{PA(CH_3)} = \mathrm{PA(CH_3X)} - \mathrm{PA(HX)} \qquad [6.31]$$

Equation 6.28 can be given the following interpretation: as the base is protonated, a charge transfer occurs from H^+ to the base (measured by IE(H)) and a

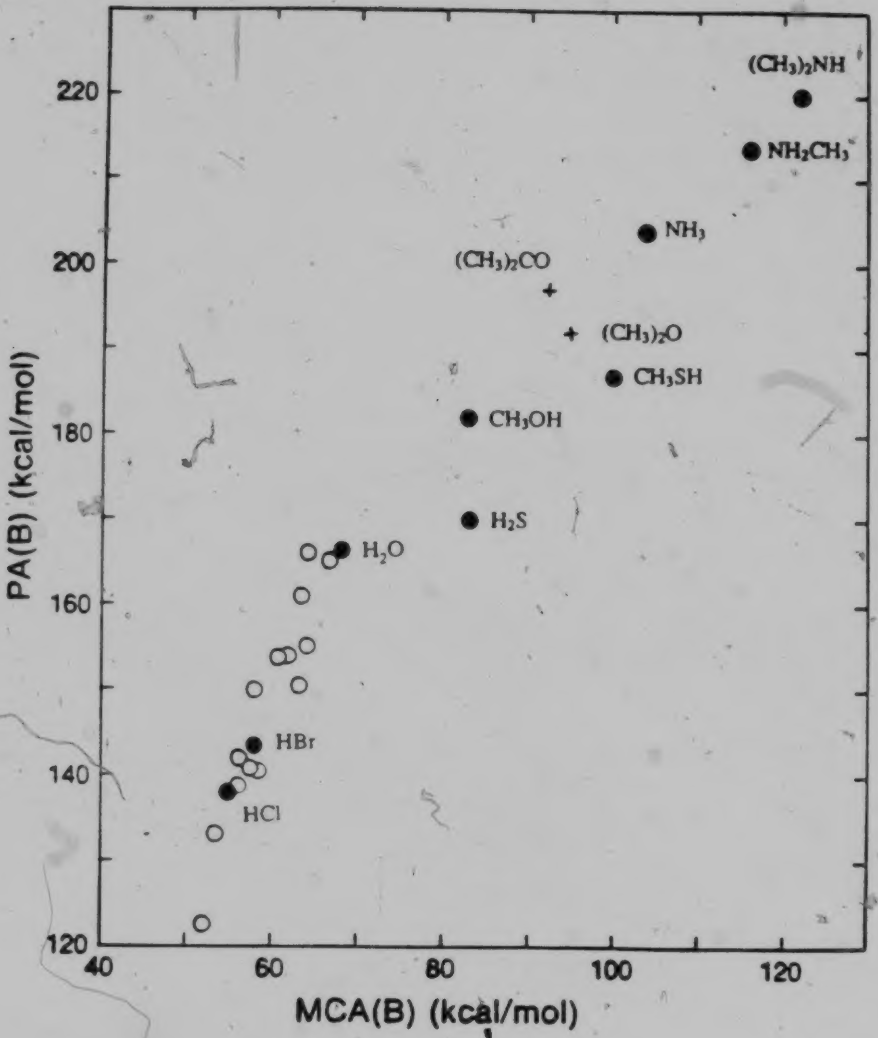

Figure 6.11 Plot of PA(B) against MCA(B) including bases from Figure 6.9 and bases XH whose MCA(XH) can be evaluated from PA(CH_3X) see equation 6.27. Slope changes from 3 at low MCA(B) to 1 at high MCA(B). ○ Bases from Table 6.3, ● Bases XH, + Bases from reference (144).

bond is formed measured by BE(H-X). The analogous terms IE(CH_3) and BE(CH_3-X) occur for the CH_3^+ addition to a base. However, the charge transfer from H^+ (respectively CH_3^+) to the base is not complete and therefore IE(H) (respectively IE(CH_3)) are terms that are too large. This "overestimate" is "corrected for" by the methyl substitution effect on the protonation, ΔPA(CH_3). This term measures the relative energy stabilization of the ion due to some positive charge remaining on the H and CH_3.

As the proton affinity of the bases increases, ΔPA(CH_3) decreases reaching a small value of a few kcal/mol. See the plot of ΔPA(CH_3) against PA(B) in Figure 6.12. This is expected since strongly basic groups (i.e. in amines) carry nearly all the positive charge and thus the relative charge remaining on the H or CH_3 is not so significant. The very small change of ΔPA(CH_3) at high PA values is responsible for the near linear region (slope = 1) of the PA versus MCA plot in Figure 6.11, since when ΔPA(CH_3) becomes constant, PA(HX) and MCA(HX) differ only by a constant (See equation 6.28).

A replot of the PA(B) and the MCA(B) data based on the functional dependence of equation 6.28 is shown in Figure 6.13. The PA(B) - MCA(B) versus PA(B) plot illustrates the asymptotic approach of the difference to an approximately constant value at high PA(B) values. This asymptotic region corresponds to the linear region with slope = 1 in the PA(B) versus MCA(B) plot in Figure 6.11.

Since the bond energy difference depends on the nature of the basic atom to which the bond is made, eg. F, O, N, S, etc., somewhat different asymptotic values are expected for series of bases with a given basic atom. Thus, two high PA limits are observed in Figure 6.13, the higher one corresponds to the nitrogen bases and the lower one corresponds to the sulfur bases. It will be interesting to see how the plot

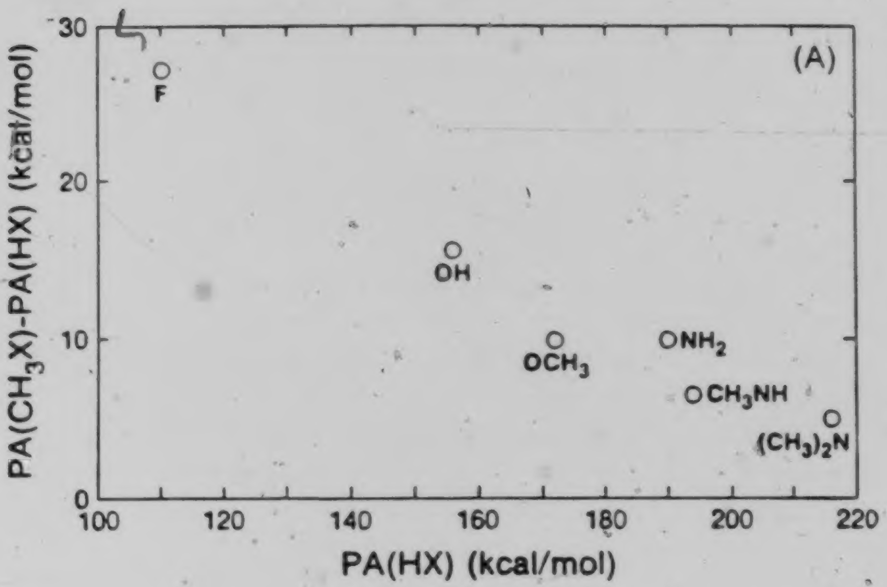

Figure 6.12 Plot of PA(CH$_3$X) - PA(HX) against PA(HX) for X groups shown.

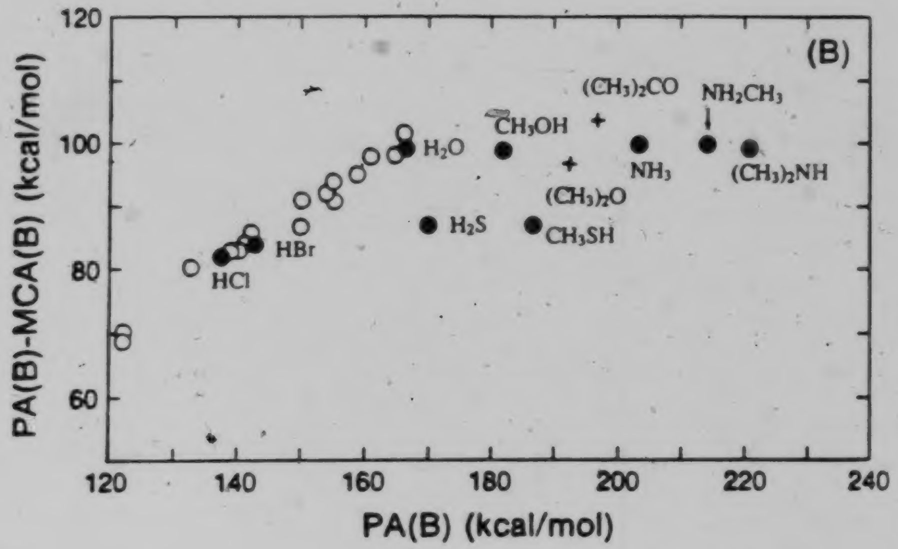

Figure 6.13 Plot of PA(B) - MCA(B) against PA(B) reaches a constant value at high PA(B). ○ Bases from Table 6.3, ● Bases XH, ✦ Bases from reference 144.

looks when MCA data becomes available for general bases B in the high affinity range.

6.3d Unique features of individual methyl cation affinities.

(i) SO_2F_2 and SO_2 Both SO_2 and SO_2F_2 have frequently been used as solvents of low nucleophilicity in the study of superacids (145). Gillespie (146) has shown that solutions of CH_3F/SbF_3SO_2 lead readily to formation of a new ionic species, CH_3OSO^+, which can be characterized by both NMR and X-ray crystallographic techniques (146). Both Gillespie (147) and Olah (148) have demonstrated that SO_2F_2 is a much more weakly coordinating solvent than SO_2 so that no $CH_3SO_2F_2^+$ is formed leaving only the $CH_3^+SbF_6^-$ complexes in SO_2F_2 solutions. This is in excellent agreement with the present data which shows SO_2 to bind Me^+ more strongly than SO_2F_2 by about 5 kcal/mol. The comparable gas phase basicities of SO_2F_2 and CH_3F towards Me^+ further suggests that under favorable conditions the dimethyl fluoronium ion, $(CH_3)_2F^+$, might be observable by NMR. The present methyl cation affinity scale also provides useful suggestions for other potential solvents for "magic methyl" experiments.

(ii) OCS and CS_2 The similarity of the methyl cation affinity of OCS and CS_2 and the larger difference between those of CO_2 and OCS suggests that OCS methylates at the sulfur. The comparable methyl cation affinities of CS_2 and SO_2 also indicate that CS_2 might be usefully exploited as a solvent in superacid systems where it is desirable to work at temperatures above the liquid range of SO_2. To the best our knowledge no such attempts have been made.

(iii) $(CF_3)_2CO$ and CF_3COCl The trifluoromethyl group is known to significantly weaken the C=O bond as evidenced by the substantially lower stretching frequency for these carbonyls compared to that in $(CH_3)_2CO$. This leads to a reduced basicity of CF_3 substituted compounds relative to their pure hydrogenic analogues. This reduction in basicity and the slightly lower methyl cation affinity of CF_3COCl relative to CH_3Cl give rise to the possibility that CF_3COCl may in fact be a chlorine, rather than an oxygen base towards CH_3^+.

(iv) CO_2 Holmes et al (149) have carried out collisional activation and metastable observation experiments of a variety of $C_2H_3O_2^+$ ions including CH_3OCO^+. In addition, ab initio calculations and appearance energy measurements were used to determine $\Delta H^\circ_f(CH_3OCO^+)$. Based on the appearance energy of 11.24 eV for CH_3OCO^+ from $ClCO_2CH_3$, a value of $\Delta H^\circ_f(CH_3OCO^+)$ of 126 kcal/mol was obtained corresponding to a methyl cation affinity for CO_2 of 41 kcal/mol. However, metastable peak observations indicated that formation of CH_3OCO^+ from $ClCO_2CH_3$ involves a significant reverse activation energy establishing 41 kcal/mol as a lower limit to the methyl cation affinity of CO_2. Ab initio calculations yielded $\Delta H^\circ_f(CH_3OCO^+)$ as 120 kcal/mol and a methyl cation affinity for CO_2 of 47 kcal/mol. However, the calculations did not involve a complete geometry optimization. Therefore, the value of 53 kcal/mol obtained in the present work appears to be quite reasonable.

(v) NF_3 Recent studies of protonation of NF_3 by both ICR and ab initio techniques have demonstrated that the most favorable site of protonation of NF_3 is at the fluorine rather than the nitrogen (150). As a result consideration must be given to possible methylation of NF_3 at both of these sites as well. A collision induced decomposition experiment in the CI source of a reverse geometry double focussing mass spectrometer showed dominant loss of CH_3F from $NF_3CH_3^+$ to yield NF_2^+ and a loss NF_2H to yield CH_2F^+. These data are consistent with initial attachment of CH_3^+ to a fluorine of NF_3 (150).

(vi) N_2O N_2O is isoelectronic with CO_2 and has a greater basicity toward both H^+ and CH_3^+ and again the possibility of ambient character must be considered. In a high resolution infra-red study of gaseous protonation of N_2O, Amano (151, 152) concluded that protonation takes place predominantly on oxygen. Collision induced decomposition studies reveal evidence of both possible protonated forms of N_2O. However, CID of methylated N_2O was more strongly suggestive of methylation at nitrogen since the major fragmentation under CID conditions led to NO^+ (150).

(vii) Rare Gases Methylated rare gas cations have previously been observed by Field et al (153) as ions of very low abundance in electron impact studies of CH_4/rare gas mixtures at high pressure in a conventional mass spectrometer. However, the means of formation of these species was not identified nor were any data obtained regarding their energetics. Reactions of Kr^+ with CH_4 at super-thermal kinetics energies in a chemical accelerator study demonstrated the formation of CH_3Kr^+ (154). Based on ICR observations of methyl cation transfer equilibria, Hovey and McMahon (125, 126) assigned methyl cation affinities of 55 ± 3 kcal/mol and 48 ± 3 kcal/mol for Xe and Kr respectively. Based on correlation of methyl cation affinity with proton affinity, it was suggested that the methyl cation affinity of Ar should be about 44 kcal/mol and might be observable by Me^+ transfer from CH_3FH^+.

The ICR data in Figure 6.7 was performed at the University of Waterloo by J. Hovey and Dr. T.B. McMahon. I would also like to acknowledge the assistance of Dr. T. Heinis for performing some the measurements presented in this chapter while a post doctoral fellow in this laboratory.

CHAPTER 7

The Electron Affinity of Perfluorobenzene, C_6F_6, and the Reaction of $C_6F_6^-$ with O_2[1]

7.1 Introduction

The negative ion $C_6F_6^-$ has been the subject of considerable study both in the gas phase and in solution (155-162). The studies have involved electron transmission spectroscopy (155, 156), ESR studies of the $C_6F_6^-$ in an adamantane matrix (158), and methyltetrahydrofuran glasses (157) as well as theoretical interpretation (155-160). Two electron affinity determinations for C_6F_6 can be found in the literature (161, 162). The more recent one by Lifshitz et al (162), $EA(C_6F_6) \geq 1.8$ eV, is generally quoted in the literature (155).

Kebarle et al (79, 163, 164, 166) have measured the electron affinities of a number of molecules by the determination of gas phase electron transfer equilibrium constants. This method can be readily applied to C_6F_6 and the present work reports a determination of $EA(C_6F_6)$ which differs substantially from that reported by Lifshitz (164).

7.2 Experimental

The electron transfer equilibria measurements were performed with the pulsed high pressure mass spectrometer with a magnet sector, which is described in Chapter 2. The procedures used were the same as in earlier studies of electron transfer equilibria (166-168). The compounds used were commercially obtained reagent grade and were used without further purification.

In general, the concentrations of the bases were varied and the resulting equilibrium constants measured to obtain an average K_{eq}. Also the equilibrium constants were measured at several different ion source pressures to ensure the equilibrium constant was not pressure dependant.

7.3 Results and Discussion

7.3a Electron affinity of C_6F_6

The electron affinity of C_6F_6 was determined by measuring the equilibrium constants of reaction 7.1.

$$C_6F_6^- + B = C_6F_6 + B^- \qquad [7.1]$$

A representative time dependance of the ion intensities observed with a reaction mixture containing methane as the bath gas (3 torr), C_6F_6 (19.3 mtorr), and 4-methoxynitrobenzene (4-MeONB) (0.3 mtorr) is shown in Figure 7.1. The neutral molecules capture near thermal secondary electrons, produced by the ionization of methane by a short (20us) electron pulse. In Figure 7.1a the time dependance of the log of the intensities is given, while Figure 7.1b gives the intensity changes as a percentage of the total ionization. The higher concentration of C_6F_6 leads initially to a higher $C_6F_6^-$ formation by electron capture. Electron transfer to 4-MeONB leads to a rapid decrease in the relative $C_6F_6^-$ intensity along with a corresponding rise in the MeONB$^-$ intensity. A constant ion intensity ratio is attained after about 0.7 ms. It is assumed to be due to the achievement of electron transfer equilibrium between C_6F_6 and 4-MeONB.

$$K_1 = \frac{[C_6F_6^-][A]}{[A^-][C_6F_6]} \qquad [7.2]$$

$$\Delta G^\circ_1 = -RT\ln K_1 \qquad [7.3]$$

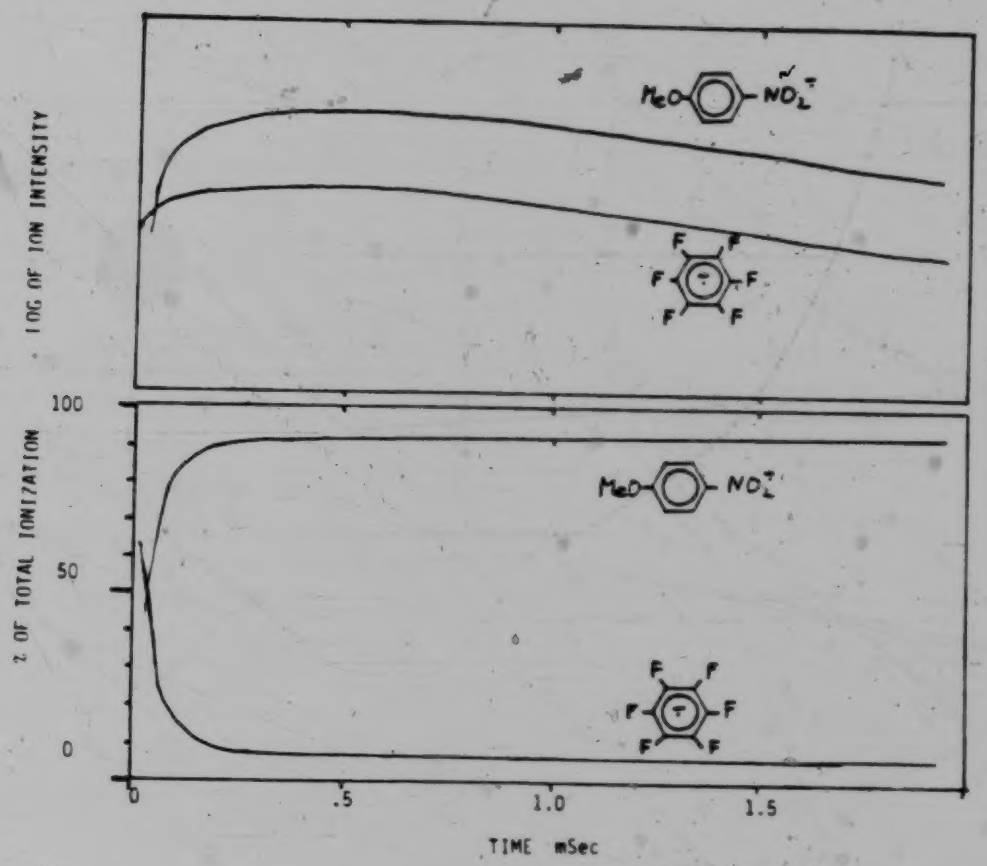

Figure 7.1 The time dependance of the ion intensities observed after a short (20 μs) electron pulse. Ion source temperature 150C, CH_4 3 torr, 4-methoxynitrobenzene 0.3 mtorr, C_6F_6 19.3 mtorr. Equilibrium (1): $C_6F_6^- + 4\text{-MeONB} = C_6F_6$ + [illegible]MeONB$^-$ established after about 0.4 ms, $K_1 = 855$, $\Delta G^\circ_1 = -0.246$ eV, which leads to EA(C_6F_6) = 0.55 eV. Figure 1a shows the log of the intensities. Figure 1b shows the intensities in % of total intensity.

ΔG°_1 can be determined from the equilibrium constant K_1 (See equations 7.2 and 7.3). ΔG°_4 for electron capture by various standard compounds, B, were determined earlier (79, 165-167).

$$B + e^- = B^- \qquad [7.4]$$

Equilibrium constants K_1 and corresponding ΔG°_1 were determined for the electron exchange equilibria of C_6F_6 with five different compounds for which ΔG°_4 had been determined previously. The results are summarized in Figure 7.2 which demonstrates the consistency of the determinations. The five determinations lead to a $\Delta G^\circ_4(C_6F_6)$ value of -13.1 kcal/mol (at 150C). In the determination of $\Delta G^\circ_4(B)$ of the standards, B, the stationary electron convention was used and the multiplicity of the spin of the free electron was neglected. This means that $\Delta S^\circ_4(B) = S^\circ(B^-) - S^\circ(B)$. Generally ΔS°_4 is small (less than 5 cal/mol) and ΔS°_1 is also small. Therefore, it can be assumed that $\Delta G^\circ_4(C_6F_6) = \Delta H^\circ_4(C_6F_6)$. Hence, the electron capture enthalpy of C_6F_6 and the electron affinity of C_6F_6 are as shown in equation 7.5.

$$\Delta H^\circ_4(C_6F_6) = -13.1 \pm 2 \text{ kcal/mol} \qquad [7.5]$$
$$EA(C_6F_6) = 13.1 \pm 2 \text{ kcal/mol or } 0.57 \pm 0.1 \text{ eV}$$

The present value for $EA(C_6F_6)$ is far smaller than the $EA(C_6F_6) \geq 1.8$ eV value determined by Lifshitz (163). The consistency of the present data, Figure 7.2, is very strong evidence for the reliability of the present result. Determinations of the electron affinities of several substituted C_6F_5X compounds, by measuring the electron transfer equilibria, have been performed by Kebarle et al (66). The electron affinities

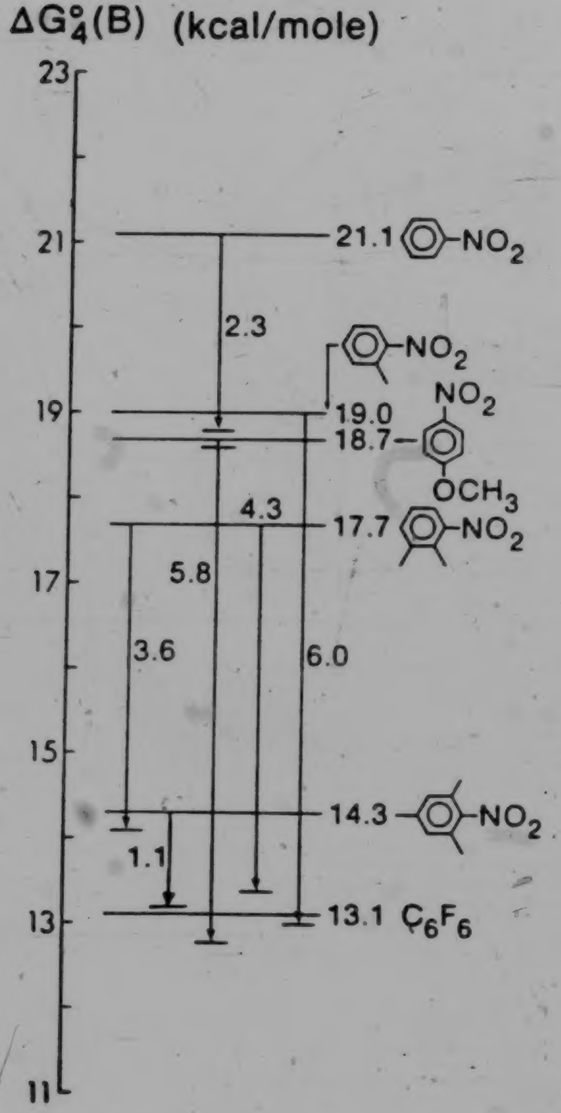

Figure 7.2 Summary of ΔG°_1 determinations with the five different reference compounds B. All values are in kcal/mol. $\Delta G^\circ_4(B)$ for reaction: $B + e^- = B^-$. All five reference compounds lead to a consistent $EA(C_6F_6) = 13.1 \pm 2$ kcal/mol or 0.57 ± 0.1 eV.

of all these compounds were generally below 1 eV and the individual values were consistent with the expected change due to the electron withdrawing power of the substituent. For C_6F_6, a determination of the temperature dependance of the equilibrium constants was performed (66). This gave, via van't Hoff plots, $\Delta H^\circ_4(C_6F_6) = -11.6$ kcal/mol, or $EA(C_6F_6) = 0.50 \pm 0.1$ eV, and a $\Delta S^\circ_4 = 7.4$ cal/mol·K in agreement with the results presented here. Furthermore, in experiments conducted with millitorr quantities of C_6F_6 in CH_4, the decay rate of $C_6F_6^-$ was found to be temperature dependant, and to increase dramatically above 150C. This was characteristic of ion loss due to thermal electron detachment from $C_6F_6^-$, the reverse of reaction 7.4. Thermal detachment had been observed earlier for the azulene negative ion (166). As thermal electron detachment is to be expected at 150C only for the negative ions formed from low electron affinity compounds, i.e. EA < 1 eV, this is additional, independent evidence for a low value of $EA(C_6F_6)$.

Difficulties and inconsistencies encountered in the C_6F_6 determination by the tandem mass spectrometer endothermic electron transfer method were reported by Lifshitz (164). Thus, the thresholds obtained with I^- projectiles did not agree with the thresholds obtained with the S^- beam, on which the determination was based. Considering that the same publication (164) reported an electron affinity of SF_6 which was too low by some 0.4 eV, one is forced to conclude that the beam method is not suitable for the determination of electron affinities of perfluoro compounds.

7.3b Reaction of $C_6F_6^-$ with O_2

While studying the electron affinity of C_6F_6, it was observed that the $C_6F_6^-$ ion was not the only peak in the mass spectrum of C_6F_6 in methane (Figure 7.3). One of the major peaks was at m/z 183, 3 mass units below $C_6F_6^-$, at m/z 186. This corresponds to an ion with the formula of $C_6F_5O^-$.

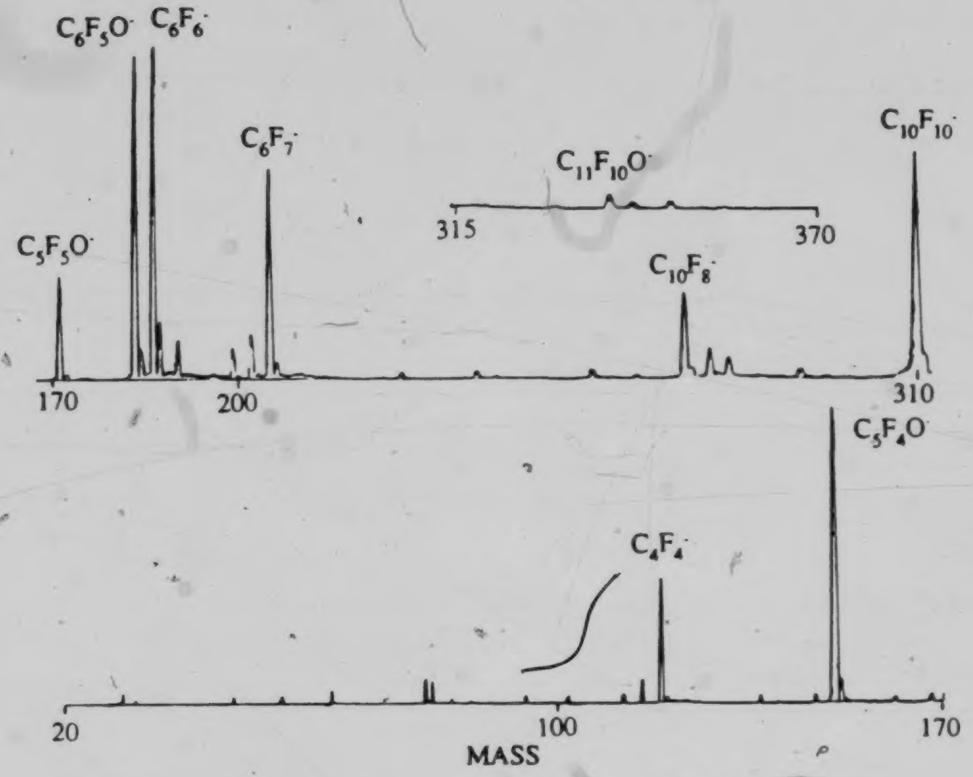

Figure 7.3 Mass spectrum of the reaction mixture: CH_4 = 3 torr, C_6F_6 = 19 mtorr, no O_2 was added, Temperature 121C. Even without the addition of O_2 numereous ions are observed in addition to the $C_6F_6^-$ ion.

$$C_6F_6^- + O_2 \longrightarrow C_6F_5O^- + \text{Products} \qquad [7.6]$$

This implies that the $C_6F_6^-$ is reacting with oxygen (reaction 7.6). Reaction 7.6 is probably not a single step but a series of reactions, as will be shown later. The oxygen had probably entered the gas handling plant through a leak in the system. A leak search was undertaken and a leak was found in the gas handling plant.

In order to further clarify the situation and also study the nature of the assumed reaction 7.6 and the origin of some other unexplained peaks in the C_6F_6 mass spectrum, an investigation of the reactions of $C_6F_6^-$ with deliberately added oxygen was undertaken, reaction 7.7.

$$C_6F_6^- + O_2 \longrightarrow \text{Products} \qquad [7.7]$$

The absence of any peak at m/z = 32, indicating the absence of O_2^- in the ion source, was taken as evidence that reactions between O_2^- and C_6F_6 could be discounted.

Reaction 7.7 was studied for several different concentrations of O_2 and C_6F_6 as well as at several different temperatures. For each set of conditions the time dependance of the 16 most intense ions was determined. In many cases there were more than 16 peaks (See Figure 7.3) in the mass spectrum, but the 16 ions collected usually made up more than 80%, and in most cases more than 90%, of the total ion intensity. Of the 16 ions, 5 ions (m/e= 186, 183, 152, 205, 310) usually made up more than 50% of the total ion intensity.

Figure 7.4 shows the time dependence of various ion intensities during a typical experiment; the logarithmic intensities shows all the ions but only the five major ions are sufficiently intense to be featured in the normalized plot. The rate of

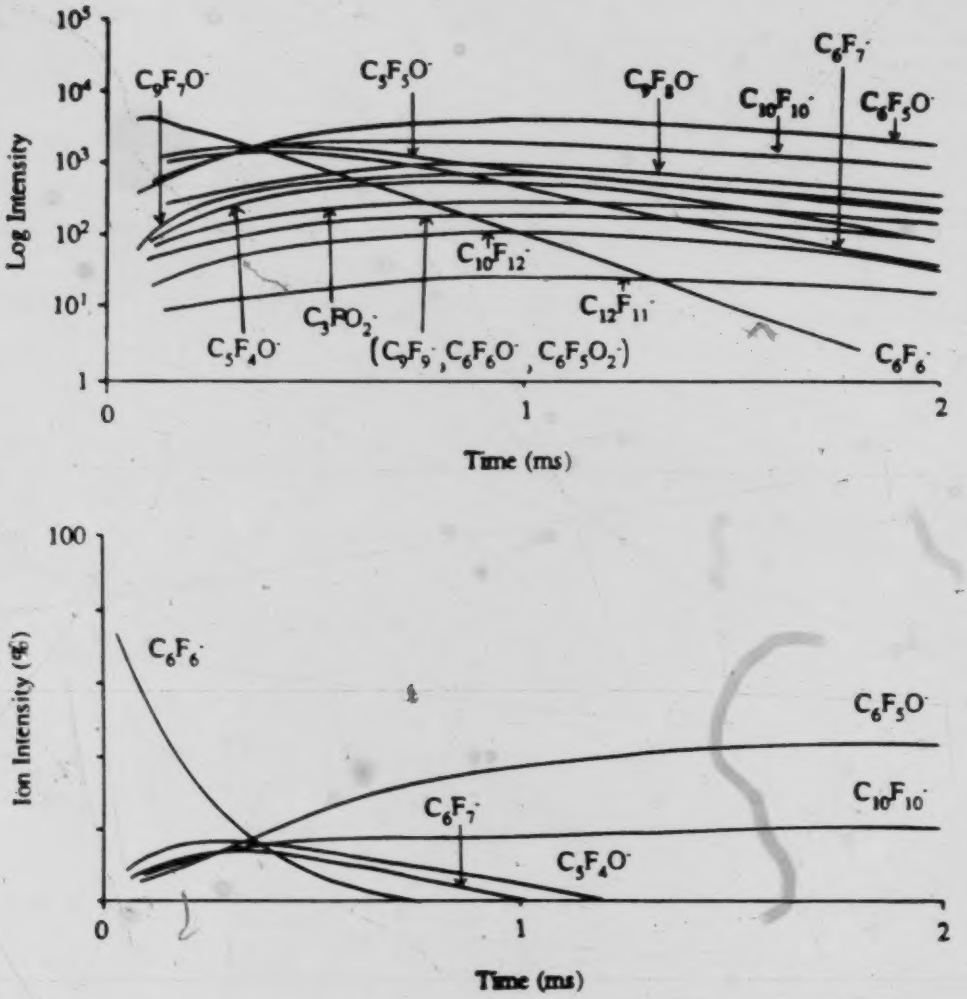

Figure 7.4 The time dependance of the ion intensities observed for the conditions: CH_4 = 3 torr, C_6F_6 = 19.3 mtorr, O_2 = 1.68 mtorr, Temp 70C.

Figure 4a shows the log of the intensities. In some cases two ion profiles fall on top of one another, as is the case for $C_9F_9^-$, $C_6F_6O^-$ and $C_5F_5O_2^-$. Figure 4b shows the percent of the total intensity. Here we only see the five major ions as the other ion profiles are crowded along the x-axis.

decay of the $C_6F_6^-$ ion was strongly dependant on the oxygen concentration, as shown in Figure 7.5. Figure 7.6 shows a plot of the pseudo-first order rate constant for the decay of $C_6F_6^-$ against the $[O_2]$ which demonstrates that the rate of loss of $C_6F_6^-$ increases linearly with oxygen concentration, and confirmed that a reaction with O_2 was taking place. From the slope of this plot, the rate constant for reaction 7.7, k_7, was determined to be 9.5×10^{-11} molecules^{-1} cm^3 s^{-1} at 70C. The background oxygen pressure was found to be 0.1 mtorr.

$$C_6F_6^- + C_6F_6 = \text{Products} \qquad [7.8]$$

The decay rate of $C_6F_6^-$ was found to increase slowly with the increase in neutral C_6F_6 concentration, reaction 7.8, Figure 7.7. Figure 7.8 shows the plot of the pseudo first order rate constant against the partial pressure of C_6F_6. Oxygen was added to the mixture (0.9 mtorr) so that variations in the background oxygen pressure would not be significant. The rate constant for reaction 7.8 was found to be 1.8×10^{-13} molecules^{-1} cm^3 s^{-1} at 70C. As this rate constant is so small relative to k_7, it was possible to neglect reaction 7.8 in most experiments especially when the concentrations of C_6F_6 and O_2 were approximately the same.

The effect of temperature on the $C_6F_6^-$ decay rate was also examined. Kebarle et al (166) saw, at temperatures greater than 150C, electron detachment, reaction 7.9.

$$C_6F_6^- = C_6F_6 + e^- \qquad [7.9]$$

With electron detachment occurring, the usual procedure of normalizing the data to eliminate the effects of diffusion are not valid. Therefore, we used the loss of $C_6F_6^-$ [illegible] the logarithm plots (Figure 7.9) and subtracted the diffusional loss of the ions to

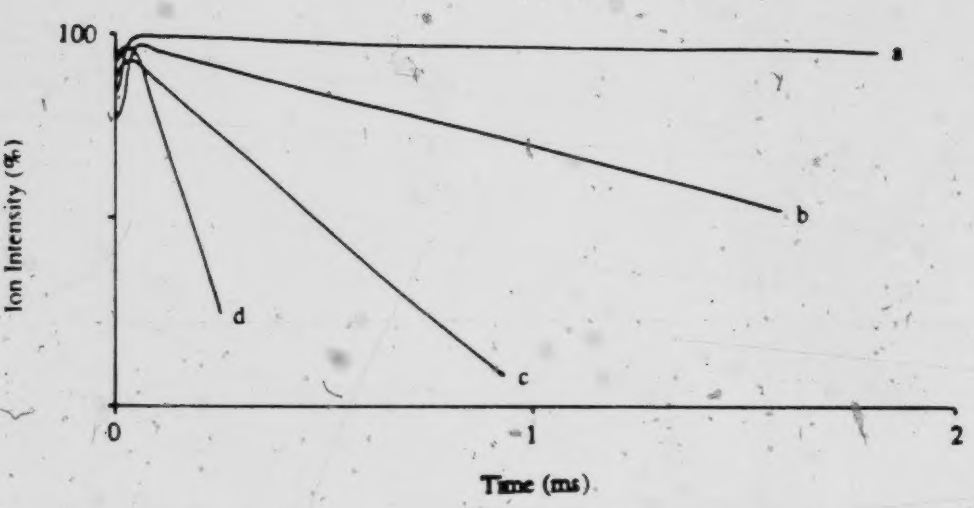

Figure 7.5 A plot of the log of the normalized intensities of $C_6F_6^-$ against time for several different O_2 concentrations. a) no oxygen added, b) O_2 = 0.42 mtorr, c) O_2 = 1.86 mtorr, d) O_2 = 4.3 mtorr. The plot of v_{C6F6^-} against $[O_2]$ is shown in Figure 7.6.

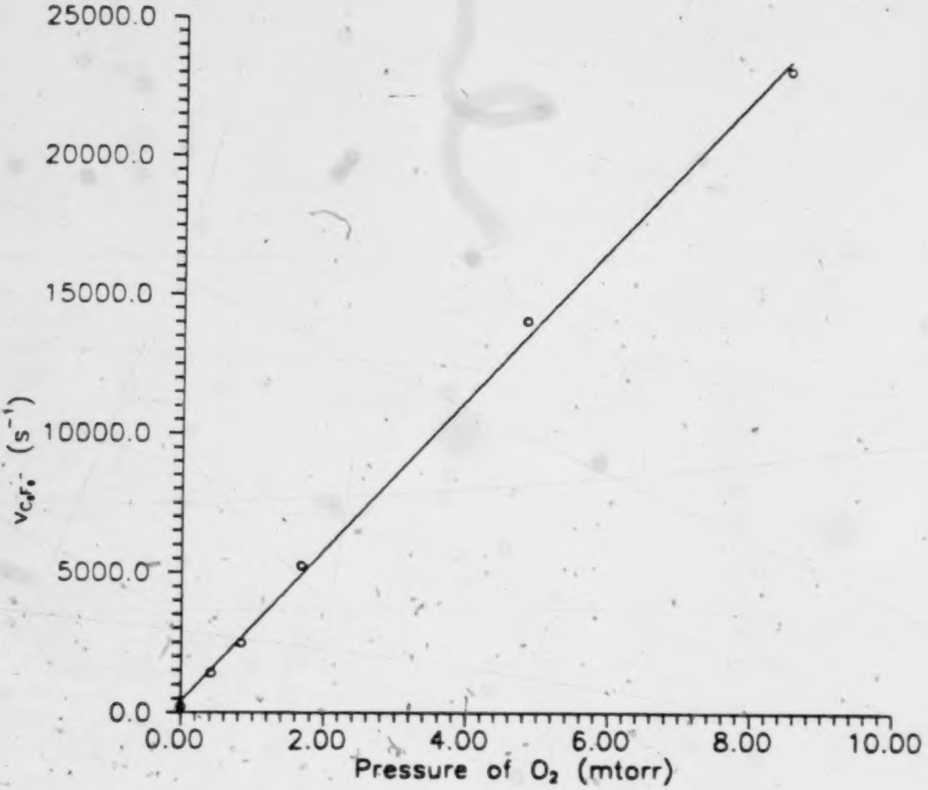

Figure 7.6 A plot of the pseudo first order rate constants for reaction 7.7 against the partial pressure of O_2. The slope of the line gives the rate constant for reaction 7.7 as $k_7 = 9.5 \times 10^{-11}$ molecules^{-1} cm^3 s^{-1}. Ion source temperature 70C. From the intercept, the background concentration of O_2 = 0.1 mtorr in the ion source.

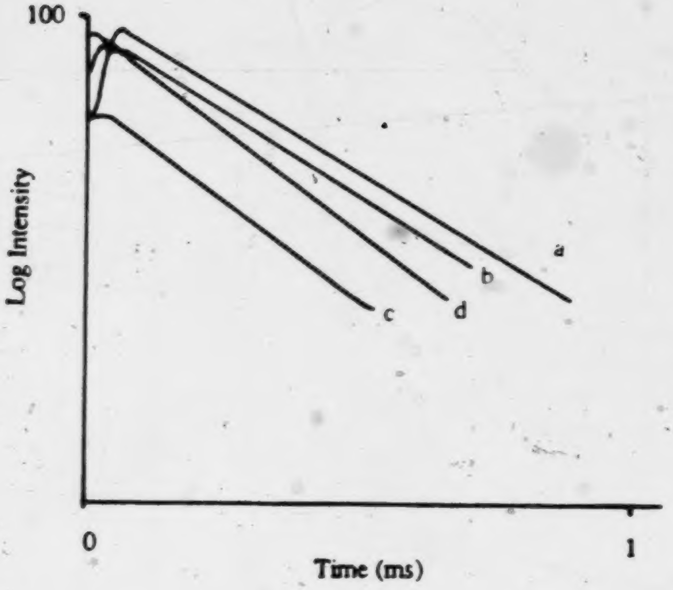

Figure 7.7. A plot of the log of the normalized intensities of C_6F_6 against time for several different C_6F_6 concentrations. a) 18.1 mtorr; b) 44.4 mtorr; c) 66.6 mtorr; d) 181. mtorr.

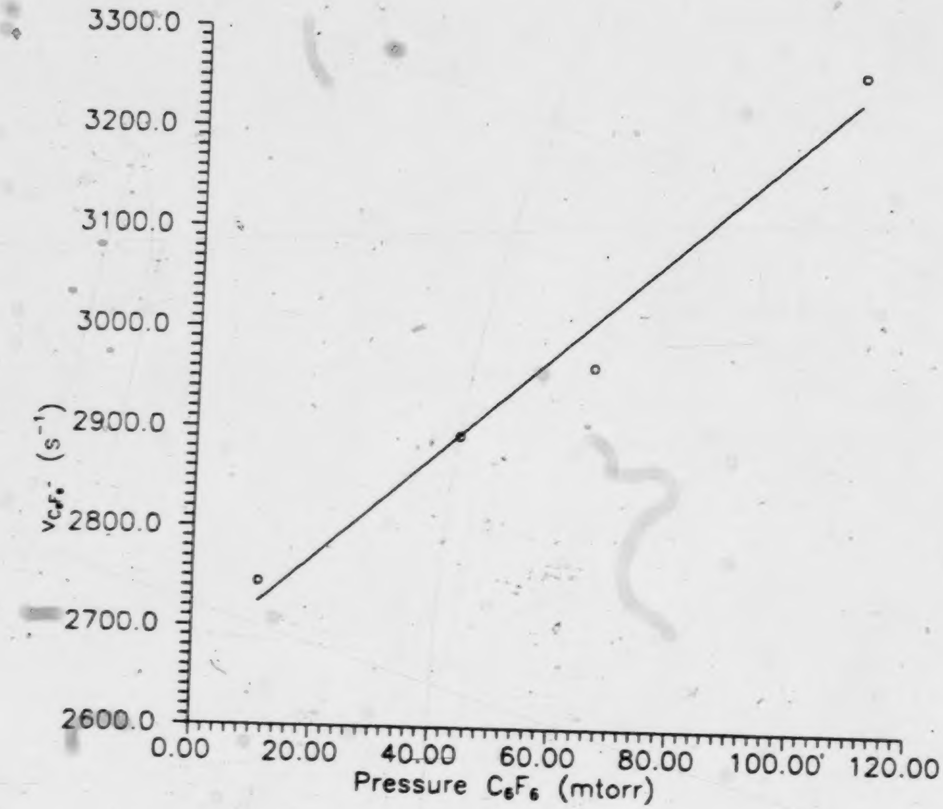

Figure 7.8 A plot of the pseudo first order rate constants for reaction 7.8 against the partial pressure of C_6F_6. The slope of the line gives the rate constant for reaction 7.8 as $k_8 = 1.8 \times 10^{-13}$ molecules^{-1} cm^3 s^{-1}. Ion source temperature 70C.

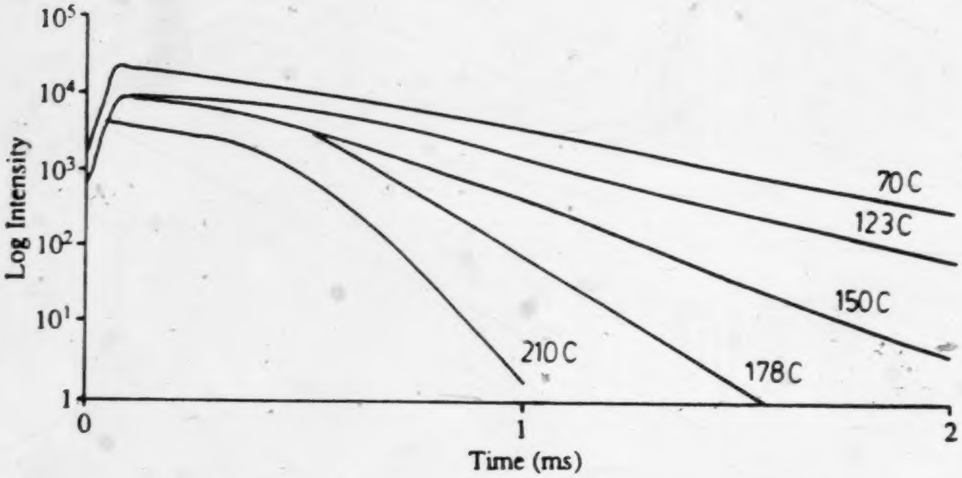

Figure 7.9 A plot of the intensity of $C_6F_6^-$ against time for several different temperatures. Conditions: CH_4 = 3 torr, C_6F_6 = 19.3 mtorr, O_2 = 0.88 mtorr. The slope of the straight line portion of the profile at latter time is taken as the pseudo first order rate constant which includes the diffusional rate loss, loss due to electron detachment and loss due to reaction 7.7.

obtain the pseudo first order rate constant of reaction 7.7. The diffusional loss of the ions, v_d, was calculated from the formula (166)

$$v_d = 1.81 \times 10^{-2}\, T^2/P$$

where T is the absolute temperature and P is the pressure in torr. In Figure 7.9 we see that there are two different areas of the graph, a small slope at short time and a steeper slope at longer times. In the region where $C_6F_6^-$ decreases more slowly, the C_6F_6 recaptures the electrons whose concentration is relativly high due to slow electron ambipolar diffusion (166). In the region where the $C_6F_6^-$ intensity decreases rapidly we assumed that there was no electron recapture taking place. Figure 7.10 shows a plot of the pseudo first order rate constant against temperature. From this plot we see that v_{C6F6^-} is almost constant at lower temperatures (slight decrease with increasing temperature) and increases at higher temperatures (>150C) as expected. If we assume that the pseudo first order rate constant at low temperatures (<100C) is due solely to reaction 7.7 (and is constant) and the rate constants at higher temperatures is due to both reaction 7.7 and electron detachment, by subtracting the average v_{C6F6^-} value for the three lowest temperatures from the high temperature values, a rate constant for thermal electron detachment from $C_6F_6^-$, v_{ed}, can be estimated. Figure 7.11 shows the plot of ln v_{ed} against 1/T. The slope of this plot is equal to the activation energy of reaction 7.9 divided by the gas constant and gives an activation energy of 15.6 ± 2.2 kcal/mol with a preexponential factor of 1.5×10^{11} s^{-1}. This compares to the electron affinity of 13.1 ± 2 kcal/mol determined by electron transfer equilibrium. The curvature of the Arrhenies plot is probably due to the assumption made in estimating the electron detachment rates. The value of 15.6

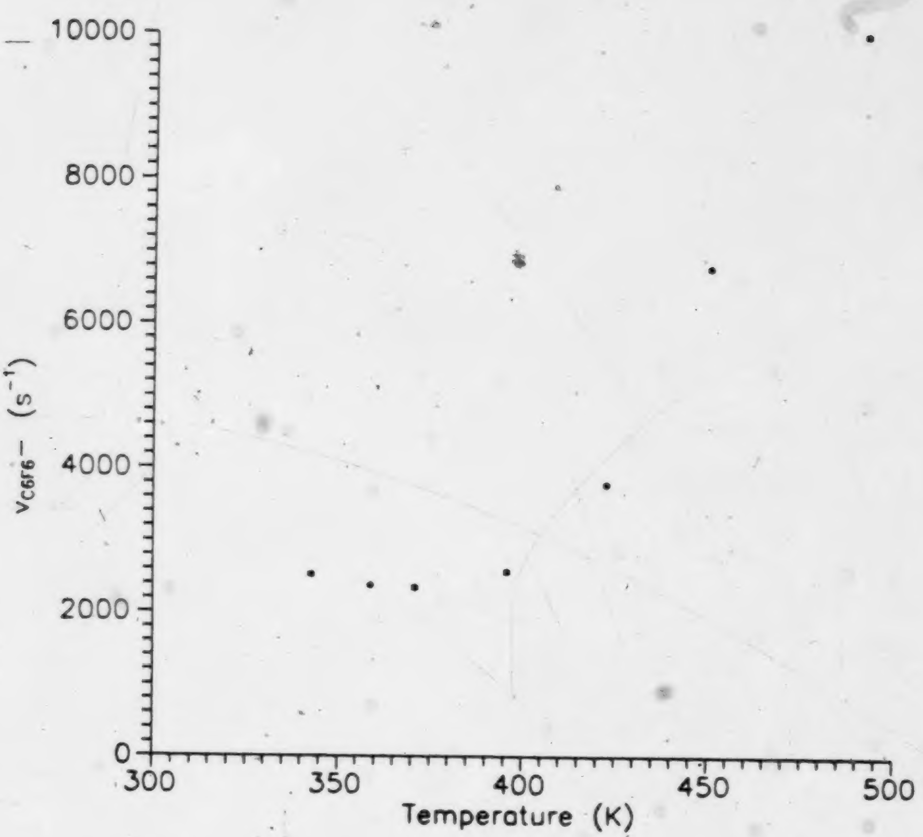

Figure 7.10 A plot of the pseudo first order rate constant for reaction 7.7 as a function of temperature. Conditions: CH_4 = 3 torr, C_6F_6 = 19.3 mtorr, O_2 = 0.96 mtorr. Below 120C the pseudo first order rate constant is constant with respect to temperature. Above 120C the change in the rate constant is due to thermal electron detachment

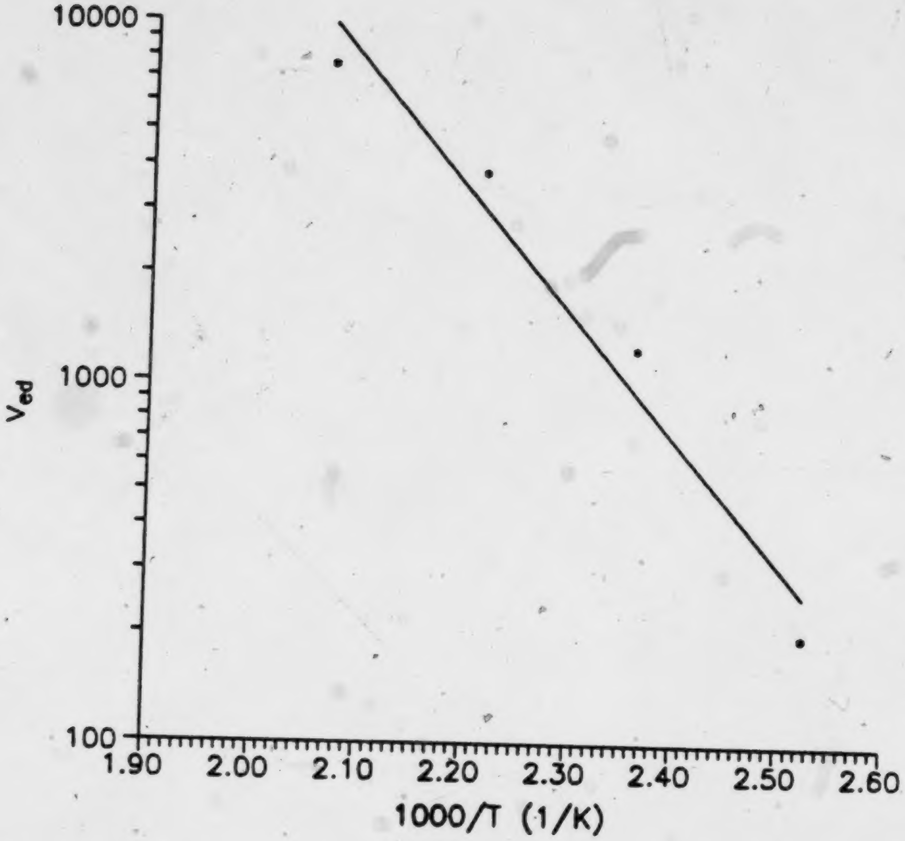

Figure 7.11 A plot of the rate of electron detachment as a function of temperature. The rate of electron detachment is determined by subtracting the pseudo first order rate constant for reaction 7.7 at temperatures less than 120C from v_{C6F6^-} at temperatures higher than 120C. (See text) The slope of this line should give the activation energy for reaction 7.9. Ea = 15.6 ± 2.2 kcal/mol as compared to the electron affinity of C_6F_6 of 13.1 ± 2 kcal/mol determined by equilibrium measurements. Curvature is due to assumptions made in estimatng v_{ed} (see text)

kcal/mol can only be considered a rough estimate but it is further evidence of the low electron affinity of C_6F_6.

From the time dependance of the ion intensity in Figure 7.4, it is seen that a complex set of reactions is taking place. The $C_6F_7^-$ and $C_5F_4O^-$ relative intensities increase initially and then fall off at longer time, indicating that these ions are intermediates in the reaction sequence. The $C_6F_5O^-$ ion reaches maximum intensity only after a relative long time, indicating that $C_6F_5O^-$ is not formed from reaction 7.6 directly but from a secondary reaction.

In hope of finding some clues to the mechanism of reaction 7.7, the reaction of oxygen with $C_6F_5CN^-$ (reaction 7.10) was examined.

$$C_6F_5CN^- + O_2 \longrightarrow \text{Products} \qquad [7.10]$$

Figure 7.12 shows a mass spectrum obtained with the conditions: CH_4 = 3 torr, C_6F_5CN = 1.6 mtorr, O_2 = 0.97mtorr, T = 150C. Figure 7.13 shows the time dependance of the observed ion intensities. From the rate of loss of $C_6F_5CN^-$ and the concentration of O_2, a rate constant for reaction 7.10 of approximately 7 x10^{-11} molecules^{-1} cm^3 s^{-1} is calculated. In comparing the mass spectrum of C_6F_6 (Figure 7.3) and C_6F_5CN (Figure 7.12) it is noteworthy that there is no M-3$^-$ ion ($C_5F_5CNO^-$) formed in the $C_6F_5CN^-$ reaction while this was one of the major products ($C_5F_5O^-$) in the $C_6F_6^-$ reaction. A second point of interest is the very much reduced intensity of the $C_6F_5CNF^-$ ion in Figure 7.12 as compared to the intensity of $C_6F_7^-$ in the C_6F_6 mass spectrum. As was noted earlier $C_6F_7^-$ is an intermediate in the $C_6F_6^-$ + O_2 reaction 7.7. With $C_6F_5CNF^-$ being of low intensity and no $C_6F_5CNO^-$ ion being detected, it is possible that the $C_6F_7^-$ ion is the precursor to the $C_6F_5O^-$ ion (reaction 7.11) in the C_6F_6 reaction scheme.

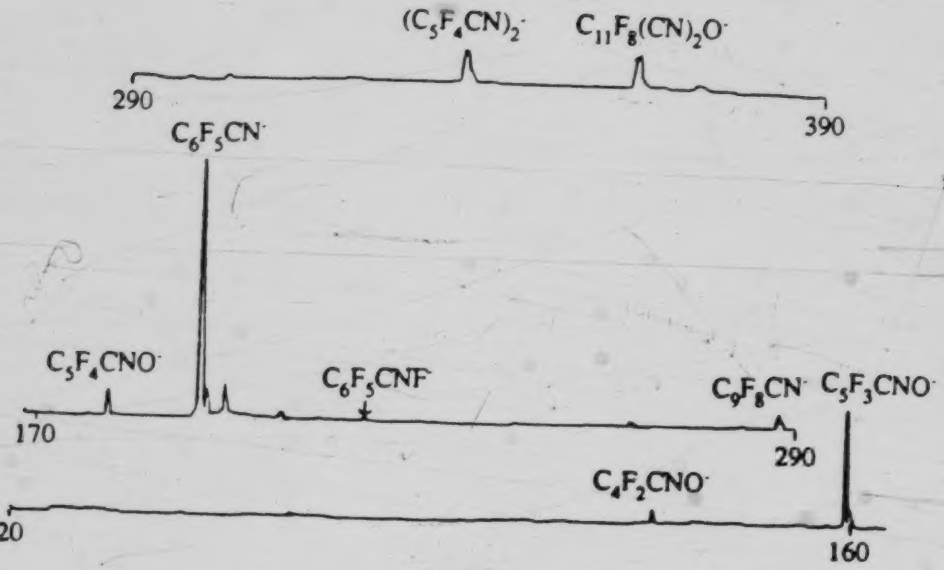

Figure 7.12 Mass spectrum of the reaction mixture: CH_4 = 3 torr, C_6F_5CN = 1.6 mtorr, O_2 = 0.97 mtorr, T 150C. Here we see that there is less fragmentation for the C_6F_5CN than for C_6F_6 (Figure 7.3) even though there is O_2 added in the C_6F_6 reaction mixture.

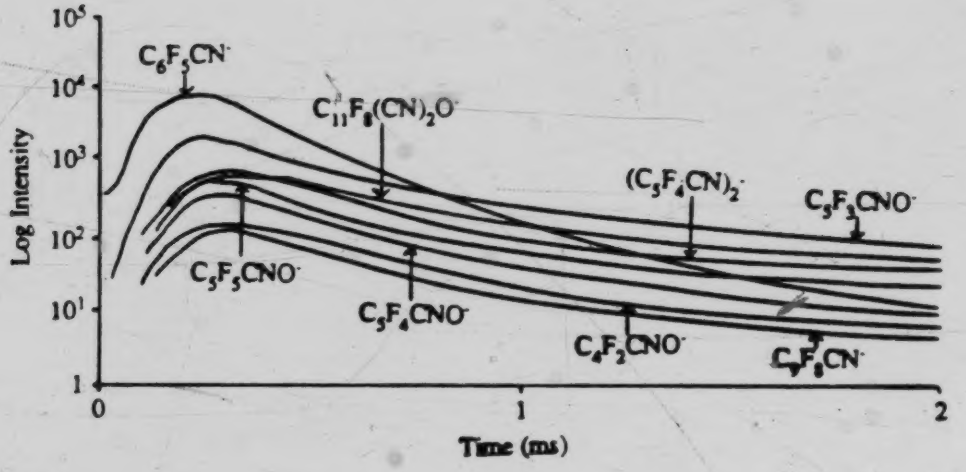

Figure 7.13 Time dependance of the observed ion intensities for reaction 7.10. Conditions: CH_4 = 3 torr, C_6F_5CN = 1.6 mtorr, O_2 = 0.97 mtorr, Temp 150C. The mass spectrum is seen in Figure 7.12.

$$C_6F_7^- + O_2 \longrightarrow C_6F_5O^- + OF_2 \qquad [7.11]$$

However, reaction 7.11 may be a series of reactions and not a single step.

The mass spectrum of $C_6F_6^-$ (Figure 7.3), contains several pair of ions separated by 34 mass units. This 34 amu mass difference could result from the loss of a CF_2 unit in association with the incorporation of an oxygen atom into the ion. The most prominent examples of this 34 mass loss are: $C_6F_6^-$(m/e 186) --> $C_5F_4O^-$ (m/e 152); $C_6F_7^-$(m/e 205) --> $C_5F_5O^-$(m/e 171); $C_{10}F_{10}^-$(m/e 310) --> $C_9F_8O^-$(m/e 276). Due to the complexity of the problem, no further work was conducted into the reactions of $C_6F_6^-$ with O_2.

Appendix A

Description of the data analysis program developed for the IBM computer

This chapter will describe the multichannel analyser program (MCA) developed in collaboration with Norman Osborn for the analysis of the time profile data collected with an EG&G ORTEC-MCS 913 board mounted on an IBM PC personal computer.

A.1 MCA Program for Analysis of Data from the EG&G MCS-913 Multi Channel Scaler

The MCA program is stored on the hard disk in the directory \DOS\MCA\. To call the program enter "MCA" and press "return" key. This will bring up the main menu A (Figure A.1) which is described later.

The MCA program can be used to plot the ion intensity time profiles obtained from the MCS program in logarithm (natural and base 10), linear or normalized (linear and natural log) fashion. The program also allows the recorded time profile data to be manipulated in various ways. For example, calculation of the best fit straight line over a region of the time profile, the intensity ratio of two ion profiles, summation of two profiles and other functions can be performed.

Another function of the program is to transfer the data to a file which can be used in a basic program created by the user. A sample of this type of program is the EXTANLYZ.EXE which is used to determine the rate constant of a reaction as it approaches equilibrium. The program subtracts a constant (entered by the user) from all the data in the file such that a plot of the $\ln(I-I_e)$ against time can be obtained, where I_e is the equilibrium intensity. This and the other functions will be described in more detail later. The following is a brief comment on each of the different

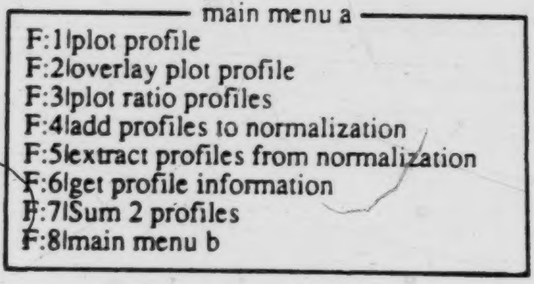
main menu a
F:1|plot profile
F:2|overlay plot profile
F:3|plot ratio profiles
F:4|add profiles to normalization
F:5|extract profiles from normalization
F:6|get profile information
F:7|Sum 2 profiles
F:8|main menu b

Figure A.1

functions that are available in the MCA program. These functions are accessed through the two main menus, A and B.

A.1a Main Menu A

When the MCA program is started Main Menu A (Figure A.1) is displayed on the screen. The following is a brief description of the functions in Main Menu A and Main Menu B. For most functions, a more elaborate description will be given later.

"F:1 plot profile"--plots and processes one profile at a time

--ESC will return you to the Main Menu A.

"F:2 overlay plot profile"--plots one or more profiles on the screen at one time. The name of the profiles plotted appear at the top of the screen. The color that the profile is plotted in will match the color of the name of the profile; there is a unique color for each profile up to 14 profiles. The menu at the bottom of the screen can be seen in each of the colors of the profiles plotted. The color of the menu indicates which profile the function will act upon. The color of the menu, or the active profile, can be changed by using the <- or -> arrow keys. This is necessary as some of the functions act upon only one profile at a time; for example, linear regression.

The initial scale setting is chosen to encompass all the data in the profiles that are being plotted. Pressing ESC will return the user to Main Menu A.

"F:3 plot profile ratios"--plots two profiles on a log scale, the user then chooses a region (start and end channels) over which the average ratio between the two profiles is to be taken. Note, the ratio is found on the original data rather than the log data; the log data is displayed only to make it easier to determine the region in which the ratios are constant. One problem with this function is that it is necessary to recall it in order to determine the ion ratio over a different area of the profiles.

"F:4 add profile to normalization"--this function allows the user to choose which profiles, from the set of profiles in the memory, are to be normalized and to add one or more profiles to the set of profiles that have been normalized previously. Normalization is preformed by summing the intensities for each channel for all the profiles chosen. The intensity in each channel in each separate profile is then divided by the sum of the intensities for that particular channel. The normalization is plotted with a maximum of 1, not 100.

"F:5 extract profiles from normalization": removes one or more profiles from the set of profiles which were previously normalized.

"F:6 get profile information": gets profile(s) originally produced by the MCS program and brings them into the memory of the MCA program. This is described in more detail latter.

"F:7 sum 2 profiles": produces a new profile that is the sum of the two chosen files. The computer will prompt the user for a file name; if one is not entered then the default name of the new profile is derived by joining the names of the two original profiles.

"F:8 main menu b": switches to the main menu B (Figure A.2). This level has commands that are destructive, therefore the function keys are disabled.

A.1b Main Menu B

These functions can be called by moving the cursor with the up and down arrow keys or by pressing the first letter of the first word of the function. One problem with using the first letter is that more than one function may start with the same letter and therefore only the first function will be called. The only time that using the first letter is useful is for the quit function. The available functions are as follows:

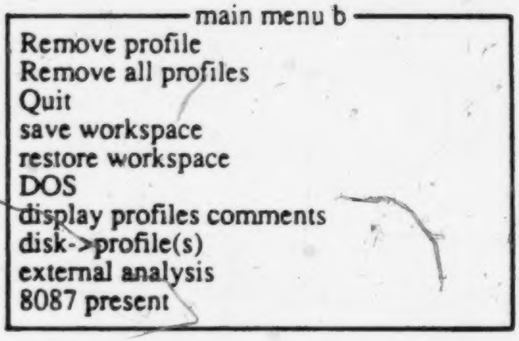
main menu b
Remove profile
Remove all profiles
Quit
save workspace
restore workspace
DOS
display profiles comments
disk->profile(s)
external analysis
8087 present

Figure A.2

"remove profile": this function will discard a profile from the memory of the program. If the profile was a part of a normalization the contribution of the profiles will be removed from the normalization automatically and the normalization will be recalculated.

"remove all profiles": remove all profiles from the memory and removes any normalization.

"QUIT": stops program and returns the user to DOS (disk operating system). To quit the program the computer prompts the user to type a lower case y. Any other entry will return the user to main menu A.

"save workspace": This function creates a file with the extension "DBA" (filename.DBA) in which all the profiles, normalizations, grid settings, plot point type, etc., are saved. The user will be prompted for a filename.

"restore workspace": this restores the program to the state before it was saved using the save workspace function. NOTE: Any profiles in the program memory will be erased when the function is called.

"DOS": returns the user to DOS. Type "EXIT" to return from DOS to the MCA program.

"display profile comments": allows the user to see the information stored in the header block on files produced by the MCS program. The information includes the time and date when the profile was recorded and other comments (Figure A.3). This function shows the comments of one profile at a time. If more than one profile is selected, the next set of comments can be seen by pressing any key. To exit from this function press any key after seeing all the comments from all the profiles of interest or press "Esc".

"disk-> profile": any profile on the disk that were created using the MCA program (this will be described later) can be read into the program memory using this

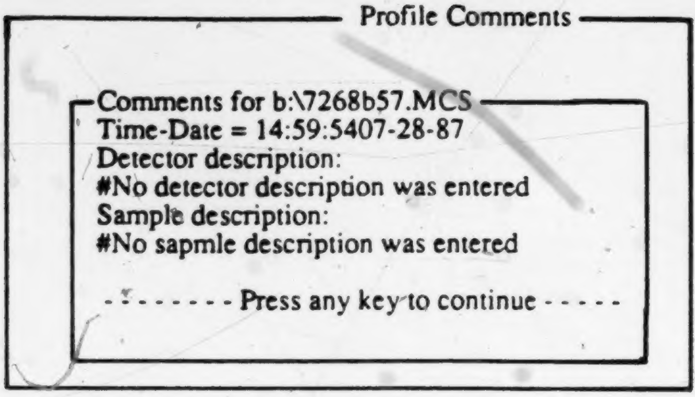

```
Profile Comments
Comments for b:\7268b57.MCS
Time-Date = 14:59:5407-28-87
Detector description:
#No detector description was entered
Sample description:
#No sapmle description was entered

-------- Press any key to continue -----
```

Figure A.3

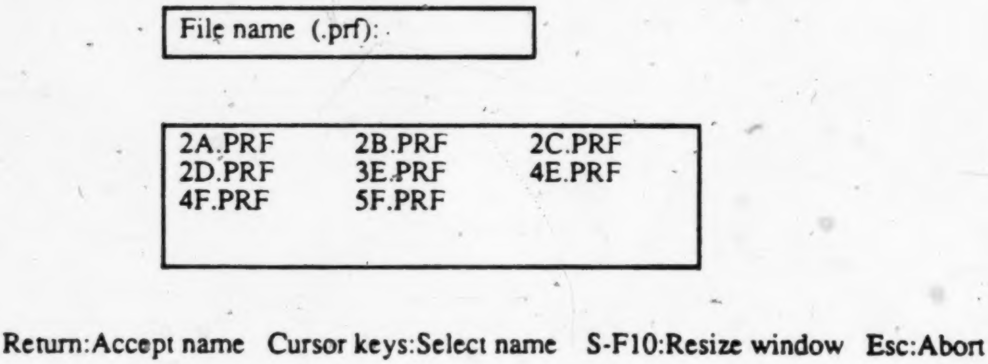

```
File name  (.prf):

2A.PRF        2B.PRF        2C.PRF
2D.PRF        3E.PRF        4E.PRF
4F.PRF        5F.PRF

Return:Accept name   Cursor keys:Select name   S-F10:Resize window   Esc:Abort
```

Figure A.4

command. The file on the disk must have the extension "PRF". The computer will prompt the user for a filename. To get a list of file names that are available to be read into the program, press return and the computer will give a menu listing all the files available (Figure A.4).

"external analysis": This allow the user to select a profile and runs a program called EXTANLYZ.EXE using the data in the profile chosen. This is the same function as on the plot menu and will be described later.

8087 preset--This will set the program to react to the 8087 chip once it is obtained.

A.2 Information on specific functions

In this section information for the operation of specific functions will be described. These functions include: reading data into the program; plotting the graphs; transfering the plots to a printer; as well as other functions.

A.2a F:6 To get Profile Information

To get the profile information into the memory of the program, first go to Main Menu A and press F:6.

The computer will look on disk A for any files ending in the extension .MCS created by the MCS program. The names are presented in a box menu (see Figure A.5) from which the user is able to choose profiles. To select the names of the files desired use the cursor keys (arrow keys) to move the cursor to the name of the desired file. Pressing the return key will highlight the filename. Repeat this process until all the files that are needed are highlighted and then press F:10 to have the computer read the files into the memory. If a file is highlighted by mistake, pressing return a second time while the cursor is at the file name removes the highlighting.

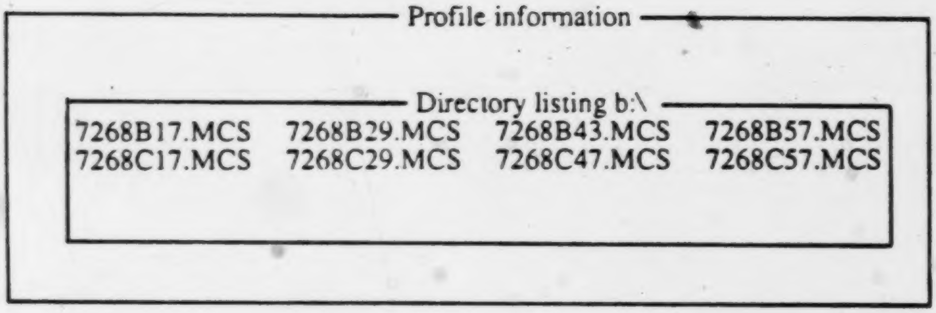

```
Profile information

Directory listing b:\
7268B17.MCS    7268B29.MCS    7268B43.MCS    7268B57.MCS
7268C17.MCS    7268C29.MCS    7268C47.MCS    7268C57.MCS
```

Figure A.5

Once the profiles are accepted the computer will prompt the user for a name for each profile. If no name is entered then the computer will use the file name that the data is stored under. The profile name can be changed by typing in a new name to be used with the program, or sections of the old name can be erased by using the delete key. As an example, if the file is stored under "1234test" and you want the name to be just "test" you would press the delete key 4 times to erase the 1234, then press enter. Once all the profiles chosen have been given names the computer returns to Main Menu A displaying the profiles which have been read into the memory (Figure A.6).

If no files were chosen when F:10 was pressed or ESC was pressed the computer looks at disk B: for any *.MCS files. If no files are chosen or ESC is pressed again the user is returned to the main menu A.

A.2b How to Plot Profiles

There are two ways to plot the profiles on the screen depending on whether the user wishes to plot one profile or more than one. From main menu A choose either "F:1-plot profile" to plot only one profile or "F:2-overlay plot profiles" to plot several profiles.

— Using the F:1-plot profile; to choose the profile to be plotted, press the F:# key where the # corresponds to the number beside the name of the profile of interest (see Figure A.7) or by moving the cursor up or down (with the arrow keys) until the cursor is on the name of a profile that is desired and then press the return key. This will select the profile to plotted. A second way to select the profiles is to simply press the F:# key associated with the profile name. This works only for numbers up to 9 (F:1-F:9). Once this is done a menu box will appear called "operations" (Figure A.8). From this menu the type of plot may be chosen (see type of plot below).

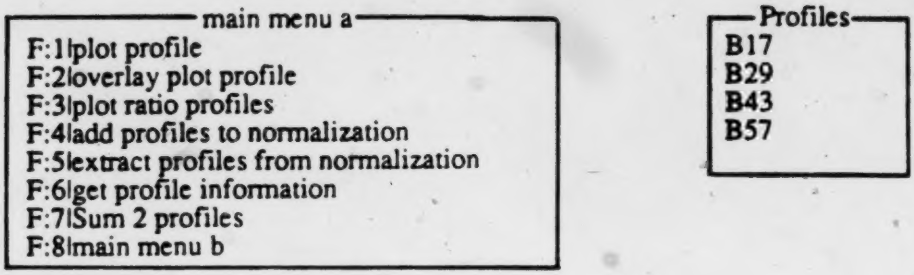

main menu a
F:1|plot profile
F:2|overlay plot profile
F:3|plot ratio profiles
F:4|add profiles to normalization
F:5|extract profiles from normalization
F:6|get profile information
F:7|Sum 2 profiles
F:8|main menu b

Profiles
B17
B29
B43
B57

Figure A.6

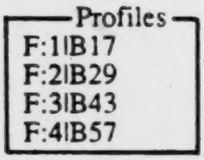

Profiles
F:1|B17
F:2|B29
F:3|B43
F:4|B57

Figure A.7

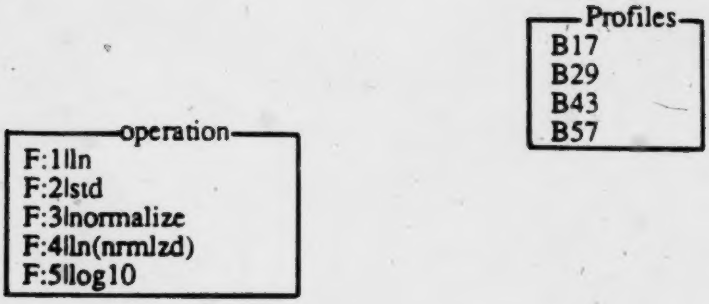

Profiles
B17
B29
B43
B57

operation
F:1|ln
F:2|std
F:3|normalize
F:4|ln(nrmlzd)
F:5|log10

Figure A.8

Using the F:2-overlay plot profile; use this function to plot a number of profiles at one time. To choose the profiles, move the cursor up or down until the cursor is on the name of a profile that is desired and then press the return key. This will highlight the profile name. A second way to highlight the profile name is to use the corresponding F:# key. Repeat this process until all the profiles that are desired are highlighted and then press the F:10 key. To unselect a profile simply select it a second time, this will remove the highlighted box from the name.

The profiles that are chosen will be remembered for the next time the user uses the overlay plot profile function.

Type of plots--there are 5 ways to plot the profile

F:1--ln:-natural logarithm

F:2--std:-does not change the values (linear)

F:3--normalized:-the ions are normalization and plotted linearly

F:4--ln(nrmlzd):-the ions are normalization and the natural log of the values are plotted.

F:5--log10:-log base 10

The maximum value for the x and y axes are chosen from the maximum value of x and y in the profiles chosen. The scale for the x and y axes can be changed as will be described later.

A.2c How to Normalize Ion Profiles

To normalize a number of profiles use the F:4 and F:5 keys. Start in main menu A and press F:4 key, this will change the screen to show 2 menu boxes both named "profiles" (Figure A.9a). The box on the right hand side will have F:# keys associated with the profile names. It is from these names that the profiles are chosen for the normalization process. To sellect the profiles of interest highlight the names of the profiles by pressing the F:# key associated with the profile or by moving the

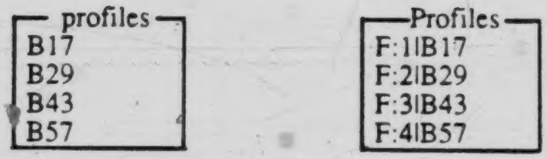
profiles
B17
B29
B43
B57
Profiles
F:1|B17
F:2|B29
F:3|B43
F:4|B57

Figure A.9a

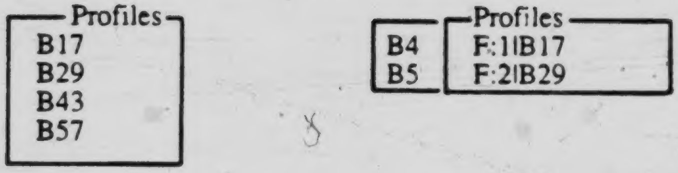
Profiles
B17
B29
B43
B57
B4
B5
Profiles
F:1|B17
F:2|B29

Figure A.9b

cursor to the profile name and pressing enter. Once all the profiles that are required for the normalization are highlighted, press F:10 to accept them. Only the profiles highlighted will be used in the normalization procedure. The profiles that are normalized will be remembered for future operations.

If some profiles have already normalized and F:4 is pressed, the screen will display two menu boxes (Figure A.9b), but in this case the right hand box will contain only the profiles that have not been normalized already. In this example, profiles B43 and B57 have already been normalized. Now profiles can be added to be included in the normalization procedure by highlighting them as before.

To remove profiles from the normalization procedure go to Main Menu A and press F:5. This will again give 2 menu boxes with the right hand box containing the profiles that are being used in the normalization procedure. From these choose the profiles to be removed from the normalization in the same manner as they were chosen i.e. using the arrow keys or the F:# keys.

A.2d How to get Profile Intensity Ratio

The F:3 key is used to get ion intensity ratios for use in calculating equilibrium constants.

To get intensity ratios start in main menu A and press F:3. The computer will show a menu box with the profile names and will prompt the user to choose the first profile for the ratio. To select the profile highlight it by using the F:# keys or move the cursor and press return. The computer will prompt for the second profile name in the same manner. Once the two profile are entered the program will plot the profiles (log I vs time). At the bottom of the screen there will be a menu box with F:1 integration; and F:2 cursor integration.

Using the F:1 key the computer will prompt the user for the start channel and end channel for the area that you want to take the ratio is to be taken over. The F:2 key will display a cursor on the screen which can be moved by using the (<-,->) arrow keys. Move the cursor to one side of the region that the intensity ratio is to be taken over and press return. A second cursor will appear; move this one to the other side of the region of interest. Even though the cursor can be moved in both the x and y directions, only the x direction has any effect on the region of interest. At the bottom of the screen the position of the cursor will be displayed as it is moved.

With both the start and the end channels entered, the program calculates the ratio of the two profiles. It does this by taking the ratio at each channel inside the region of interest and summing them. This sum is then divided by the number of channels over which the summation took place. At the bottom of the screen two values appear, the integral which is the sum of the ratio over the region of interest, and the average in the integral divided by the number of channels.

A.2e How to print ion profiles

One method is to use the print profile function found on the bar menus at the bottom of the screen when the profiles are plotted. This function will be described later. The best method to print a profile is to use the CAPTURE program. The instructions for this program are in the manual called "MICROSOFT SHOW PARTNER". CAPTURE allows the user to copy both graphics and text into a file. This file can then be edited and labels can be added or deleted to create a plot that has all the required information. This program must be started before calling the MCA program as it is a resident program; you cannot leave the MCA by the DOS command and call the CAPTURE program because there is not enough memory. Once the screens have been captured they then may be edited by the Graphics Editor Program called GED.EXE . Instructions to this program can also be found in the

MICROSOFT SHOW PARTNER manual. One problem with CAPTURE is the fact that it is a resident program and takes up a large area of the computers memory. Because of this only four or less profiles may be plotted at one time using the MCA program. This means a mass spectrum profile which has used all 4096 channels in the MCS program cannot be "captured" because of the memory requirement.

A.3 Functions available for the analysis of ion profiles

Once the profiles are plotted there are a number of functions available to the user. These are found in bar menus at the bottom of the screen in groups of three (Figure A.10). These function are called by pressing the F:# key corresponding to the function. Of the three functions shown at one time, one is the prompt to show the next series of functions. The up and down arrow keys also show the next series of functions in the forward and reverse directions.

Many of these functions can only be used on a single profile (eg. linear regression). In these cases, the functions will be performed on the plot which has the same color as that of the function. To change the color of the functions, press the <-, -> arrow keys.

Functions:

"set scale-keyboard": this allows the user to change the x and y axis scale and prompts the user with the old values for each. To change the scale, type in the new values when the old values appear at the bottom of the screen. To retain the old values (i.e. no change) press enter when these values appear.

"set scale-cursor": this allows the user to change the x and y axis scale by moving the cursor. The user selects the new x and y values for the new scale by using the cursor. Two points must be selected that do not have the same x or y value. The hypothetical box that can be drawn using the 2 selected points as diagonals

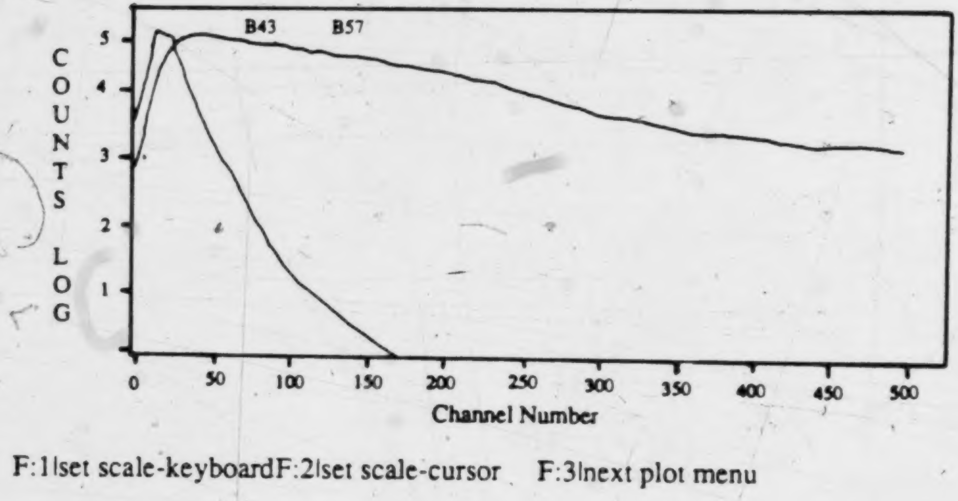
B43
B57
LOG COUNTS
0
1
2
3
4
5
0
50
100
150
200
250
300
350
400
450
500
Channel Number
F:1|set scale-keyboardF:2|set scale-cursor
F:3|next plot menu

Figure A.10

becomes the new scale. The new scale will be smaller than the old scale because the cursor must lie within the old scale. Pressing "Control arrows" at the same time moves the cursor quickly in the x direction while pressing the "shift" with the arrow keys causes the cursor to move slowly in either the x or y direction.

"next menu": this shows the next set of commands for the plot. This can also be done by pressing the up or down arrows.

"Best fit line": this function performs a least-squares linear regression fit on the plotted profile values. The user is prompted for the region that the best fit will be applied to and then a line will be drawn based on the best fit results. The best fit parameters will also be shown.

"best fit-keyboard": the region for the analysis is entered by the keyboard.

"best fit-cursor": The best fit region for the analysis is specified with moving the cursor by the arrow keys; two points must be selected to specify a region. Even though the cursor can move in both the x and y directions, only the x values are used to specify the region of interest.

"integration": integration is implemented as the sum of the y values over a specified region. The region can be specified by either the keyboard or the cursor keys, as for the best fit line. The value for y depends on the type of plot. This function does not take the original values but the values after the function that is applied for the plotting. For example, if the profile is plotted using the logarithm function, the intergration uses the log values and not the orginal data.

"grid on/off": toggles the grid on and off. The state of the grid is remembered between the return to main menu and return to the plot mode.

"change plot point": the plot point can be changed to 4 different types; a pixel, a cross, a solid box, a hollow box with a dot in the center. The size of the plotting point can also be varied except for the pixel. If a symbol other than the pixel is chosen, and there are more than one profile being plotted, each profile will be plotted using a different symbol (up to 4 profiles).

"save profile": the currently active profile (depending on the color) on the screen will be stored in the memory. The values saved will be the processed data and not the original data. The user will be prompted for a profile name; a default name is produced by combining the original name with the current operation that was being performed on the original profile. This is useful in order to plot the log of the normalized intensity for the same ion for several different conditions on the same plot.

"profile(s) to disk": all the profiles that are being looked at on the plot will be written on the disk in one file. The data values that are written out are not the original values but the processed values of the profiles that are displayed on the plot. The user will be prompted for a name for the file to which the data is written.

external analysis--this function automatically performs a "profile to disk" creating a file called EXTANLSW.PRF . Then, an external user supplied program of the name EXTANLYZ.EXE is started after which a file called EXTANLSR.PRF will be read and any profile in this file will be located in the profile storage area. Note that new profiles will not be seen without returning to the main menu. The files EXTRANLSR.PRF will be erased after the function is completed.

"print plot": is a preliminary printing routine that plots the screen display directly on the printer without having to use CAPTURE (described earlier). However, there are a number of bugs; if the printer is not present and online, the program will hang; also, the printing seems to go askew near the end of the plot. This routine is the only way to plot mass spectra that have been aquired with all 4096 channels from the MCS program.

A.4 Help Menus

There are help menus written to remind the user of the purpose of various functions. To call these help menus press 'Alt F:1' simultaneously. The help menus called up will have information on the functions that are available at that point in the program. That is at Main Menu A, the help menu will give information on Main Menu A only. If you are in the plot menus the help menus will only give you information on the menus visible on the screen at the time when the help menus are called.

A.5 Program for calculations not available in the MCA program

For functions not available, for example normalizing a mass spectrum so that the most intense peak is plotted as 100%, a program called PRFPROC.BAS can be modified to perform the desired calculation. This program is divided into three sections: the first section reads the data from the *.prf files created by the MCA program. The second section does the calculations desired and the third section write the calculated data to a new *.prf file which can be read into the MCA program with the disk->profile function in Main Menu B. The PRFPROC.BAS program can be found in the directory C:\DOS\MCA\HELPMCA using the Quick Basic Program. To create a program, modify the second section in the PRFPROC program and save it under a new name. In this way the program PRFPROC is not lost and can be used as a guide repeatedly. When the new program is created it will be stored in the C:\DOS\MCA\HELPMCA directory and should be copied to the C:\DOS\MCA directory to be used.

In order to use the program created, plot the profile of interest and use the function "profile->disk" to transform the profile to a *.PRF file. Leave the MCA program either by using the quit function or the DOS comand. Once in DOS, call the program that has been created for the calculation to be performed on. The program will ask for a file name. Make sure that the extension .PRF is included when the name is entered. After the program has completed the calculations, it will ask for a profile name. This name will be the one that will appear in the box in the MCA program once the file has been read into the MCA program's memory. The program created will then ask you for a file name. This name will be the one that the new profile will be stored under. Be sure to include the extension .PRF in the file name. This name will also be seen when the profile is read into the MCA memory using the "disk->profile" function in Main Menu b.

REFERENCES

1 Franklin, J.L.; Dillard, J.G.; Rosenstock, H.M.; Herron, J.T.; Draxl, K. and Field, F.H., "Ionization Potentials, Appearance Potentials and Heats of Formation of Gaseous Positive Ions" Nat. Stand. Ref. Data Ser. Nat. Bur. Stand. (US) (1969).

2 Rosenstock, H.M.; Buff, R.; Ferreira, A.A.; Lias, S.G.; Parr, A.A.; Stockbauer,R.L. and Holmes,J.L., J. Am. Chem. Soc. 1982, **104**, 2337.

3 Lossing, F.P. and Holmes, J.L., Can. J. Chem. 1982, **60**, 2365.

4 Tiedemann, P.W.; Anderson, S.L.; Ceyer, S.T.; Hiraoka, T.; Ng, C.Y.; Mahan, B.H. and Lee, Y.T., J. Chem. Phys. 1979, **71**, 605.

5 Baer, T., in "Ionic Processes in the Gas Phase", Ferreira, M.A. ed. Reidel, (1984).

6 Baer, T. in "Gas Phase Ion Chemistry", vol. 1, Bowers, M.T., Ed. Acad. Press, (1979)

7 Traeger, J.C. and McLaughlin, R.G., J. Am. Chem. Soc. 1981, **103**, 3647.

8 Schulz, P.A.; Mead, R.D.; Jones, P.L. and Lineberger, W.C., J. Chem. Phys. 1982, **77**, 1153.

9 Janoushek, B.K. and Brauman, J.I., in "Gas Phase Ion Chemistry", Bowers, M.T. Ed. Acad. Press, (1979).

10 Rosenstock, H.M.; Draxl, K.; Steiner, B.W. and Herron, J.T., J. Chem. Phys. ref. Data 6 Suppl. 1, 1977.

11 Hogg, A.M. and Kebarle, P., J. Chem. Phys. 1965, **43**, 499.

12 Hogg, A.M.; Haynes, R.N. and Kebarle, P., J. Am. Chem. Soc. 1966, **88**, 28.

13 Bowers, M.T.; Aue, D.H.; Webb, H. and McIver, R.T., J. Am. Chem. Soc. 1971, **93**, 4314.

14 Henderson, W.G.; Taagepera, D.; Holtz, D.; McIver, R.T.; Beauchamp, J.L. and Taft, R.W., J. Am. Chem. Soc. 1972, **94**, 4728.

15 Briggs, J.P.; Yamdagni, R. and Kebarle, P., J. Am. Chem. Soc. 1972, **94**, 4728.

16 Kebarle, P., Ann. Rev. Phys. 1977, **28**, 445.

17 Yamdagni, R. and Kebarle, P., J. Am. Chem. Soc. 1976, **98**, 1320.

18 Wolf, J.F.; Staley, R.H.; Koppel, I.; Taagepera, M.; McIver, R.T.; Beauchamp, J.L. and Taft, R.W., J. Am. Chem. Soc. 1977, **99**, 5417.

19 Aue, D.H. and Bowers, M.T., in "Gas Phase Ion Chemistry" Bowers,M.T. Ed. Acad. Press. (1070).

20 Collyer, S.H. and McMahon, T.B., J. Phys. Chem 1983, **87**, 909.

21 Baer, T., J. Am. Chem. Soc. 1980, **102**, 2482.

22 Lais, S.G.; Liebman, J.F. and Levin R., J. Phys. Chem. Ref. Data, 1984, **13**, 695.

23 McMahon, T.B. and Kebarle, P., J. Am. Chem. Soc. 1985, **107**, 2612.

24 Rains, L.J.; Moore, H.W. and McIver, R.T., J. Am. Chem. Soc. 1978, **68**, 3309.

25 Caldwell, G. and Kebarle, P., J. Chem. Phys. 1984, **80**, 577.

26 Meot-Ner, M., J. Phys. Chem 1980, **84**, 2724.

27 Meot-Ner, M.; Solomon, J.J. and Field, F.H., J. Am. Chem. Soc. 1976, **98**, 1025.

28 Solomon, J.J. and Field, F.H., J. Am. Chem. Soc. 1976, **98**, 1567.

29 Sharma, R.B.; Sen-Sharma, D.K.; Hiraoka, K. and Kebarle, P., J. Am. Chem. Soc. 1985, **107**, 3747.

30 McMahon, T.B.; Heinis, T.; Nicol, G.; Hovey, J.K. and Kebarle, P., Submitted to J. Am. Chem. Soc. 1988.

31 Kebarle, P. in "Ions and Ion Pairs in the Gas Phase" in Ions and Ion Pairs in Organic Reactions, Szwarc, M. Ed. Wiley Interscience, (1972).

32 Kebarle, P. in "Gas Phase Ion Equilibria and Ion Solvation" in Modern Aspects of Electrochemistry, vol 9, Conway, B.E. and Bockris, J.O.M. Ed. Plenum, (1974).

33 Mark, T.D. and Castleman, A.W., in " Experimental Studies on Cluster Ions" in Advances in Atomic and Molecular Physics, Bates, D.R. and Bederson, B. Eds. vol 20, (1984).

34 Su, T. and Bowers, M.T. in "Gas Phase Ion Chemistry" vol 1, Bowers, M.T. Ed. Academic Press, New York, (1979).

35 Chesnavich, W.A.; Su,T. and Bowers, M.T. in "Kinetics of Ion-Molecule Reactions", Ausloos, P. Ed., Plenum Press, New York,(1979).

36 Langevin, P.M., Ann. Chim. Phys. 1905, **5**, 245.

37 Gioumousis, G. and Stevenson, D.P., J. Chem. Phys. 1958, **29**, **294**.

38 Bass, L.; Su, T. and Bowers M.T., Int. J. Mass Spectrom Ion Phys. 1978, **28**, 389.

39 Theard, L.P. and Hamill, W.H., J. Am. Chem. Soc. 1962, **84**, 1134.

40 Moran, T.F. and Hamill, W.H., J. Chem. Phys. 1963, **39**, 1413.

41 Su, T. and Bowers, M.T., J. Am. Chem. Soc. 1973, **95**, 1370.

42 Bowers, M.T. and Laudenslager, J.B., J. Chem. Phys. 1972, **56**, 4711.

43 Su, T. and Bowers, M.T., Int. J. Mass Spectrom Ion Phys. 1973, **12**, 347.

44 Su, T. and Bowers, M.T., Int. J. Mass Spectrom Ion Phys. 1975, **17**, 211.

45 Su, T.; Su, E.C.F. and Bowers, M.T., J. Chem. Phys. 1978, **69**, 2243.

46 Su, T. and Bowers, M.T., Int. J. Mass Spectrom Ion Phys. 1975, **17**, 309.

47 Su, T.; Su, E.C.F. and Bowers, M.T., Int. J. Mass Spectrom Ion Phys. 1975, **28**, 285.

48 Payzant, J. "Kinetics and Thermodynamics of Ion-Molecule Reactions", Ph.D. Thesis, Chemistry Department, University of Alberta, (1973).

49 Durden, D.A. "Thermal Ion-Molecule Reactions at Pressures up to 10 torr with Pulsed Mass Spectrometry", Ph.D. Thesis, Chemistry Department, University of Alberta, (1969).

50 Lau, Y.K. "Gas-Phase Basicities and Proton Affinities", Ph.D. Thesis, Chemistry Department, University of Alberta, (1979)

51 Dawson, P.H. Ed. "Quadrupole Mass Spectrometry and its Applications", Elsevier, Amsterdam, (1976).

52 McDowell, C.A., Ed. "Mass Spectometry", McGraw-Hill, Toronto, (1963).

53 Kebarle, P.; Searles, S.K.; Zolla, A.; Scarborough, S. and Arshadi, M., J. Am. Chem. Soc. 1967, **89**, 6393.

54 Sunner, J.; Nicol, G. and Kebarle, P., Anal Chem 1988, , 1300.

55 Sunner, J.; Ikonomou, M. and Kebarle, P., Anal Chem 1988.

56 Lau, Y.K.; Ikuta, S. and Kebarle, P., J. Am. Chem. Soc. 1982, **104**, 1462.

57 Bohme, D.K.; Mackay, G.I. and Tanner, S.D., J.Am. Chem. Soc. 1979, **101**, 3729.

58 Raksit, A.B. and Bohme, D.K., Can. J. Chem. 1983, **61**, 1683.

59 Bohme, D.K. and Raksit, A.B., J. Am. Chem. Soc. 1984, **106**, 3447.

60 Mackay, G.I.; Raksit, A.B. and Bohme, D.K., Can. J. Chem. 1982, **60**, 2594.

61 Bohme, D.K.; Raksit, A.B. and Mackay, G.I., J. Am. Chem. Soc. 1982, **104**, 1100.

62 Smith, D.; Adams, N.G. and Henchman, M.J., J. Chem. Phys. 1980, **72**, 4951.

63 Hierl, P.M.; Ahrens, A.F.; Henchman, M.J.; Viggiano, A.; Paulson, J. and Clary, D.C., J. Am. Chem. Soc. 1986, **108**, 3140, 3142.

65 Arnold, F.; Krankowsky, O. and Marien, K.M., Nature, 1977, **267**, 30.

65 Fehsenfeld, F.C.; Dotan, I.; Albritton, D.L.; Howard, C.J. and Ferguson, E.E., J. Geophys. Res., 1978, **83**, 1333.

66 Kebarle, P. in Techniques for Study of Ion-Molecule Reactions, Techniques of Chemiries (series) Saunders Jr. Ed. Wiley Interscience (1988).

67 Keesee, R.G. and Castleman, A.W. Jr., J. Phys. Chem. Ref. Data 1986, **15**, 1011.

68 Davidson, W.R.; Sunner, J. and Kebarle, P., J. Am. Chem. Soc. 1979, **101**, 1675.

69 Hiraoka, K.; Takimoto, H. and Yamabe, S., J. Am. Chem. Soc. 1987, **109**, 7346.

70 Honriet, R.; Schwarz, H.;Zummack, W.; Andrade, J.G. and Schleyer, P.v.R., Nouveau Journal de Chemie 1981, **5**, 505.

71 Catalan, J. and Yanez, M., J. Am. Chem. Soc. 1984, **106**, 421.

72 Lau, Y.K.; Nishizawa, K.; Tse, A.; Brown, R.S. and Kebarle, P., J. Am. Chem. Soc. 1981, **103**, 6291.

73 Farneth, W.E. and Brauman, J.I., J. Am. Chem. Soc. 1976, **98**, 7891.

74 Meot-Ner, M., J. Am. Chem. Soc. 1984, **106**, 1265.

75 Olmstead, W.N. and Brauman, J.I., J. Am. Chem. Soc. 1977, **99**, 4219.

76 Hiraoka, K. and Kebarle, P., J. Am. Chem. Soc. 1976, **98**, 6119.

77 Meot-Ner, M. and Field, F.H., J. Am. Chem. Soc. 1978, **100**, 1356.

78 Sen Sharma, D.K. and Kebarle, P., J. Am. Chem. Soc. 1982, **104**, 19.

79 Grimsrud, E.P,; Chowdhury, S. and Kebarle, P., J. Chem. Phys. 1985, **83**, 1059.

80 Magnoli, D.E. and Murdoch, J.R., J. Am. Chem. Soc. 1981, **103**, 7465.

81 Dodd, J.A. and Brauman, J.I., J. Phys Chem 1986, **90**, 3559.

82 Morokuma, K.M., Acc. Chem. Res. 1977, **10**, 294.

83 Larson, J.W. and McMahon, T.B., J. Am. Chem. Soc. 1983, **105**, 2944.

84 Emsley, J., Chem. Soc. Rev. 1980, **9**, 91.

85 Umeyama, H.; Kitaura, K. and Morokuma, K., Chem. Phys. Lett. 1975, **36**, 11.

86 Hiraoka, K.; Sano, M. and Yamabe, S., Chem. Phys. Lett. 1982, **87**, 181.

87 Merlet, P.; Peyerimhoff, S.D. and Buenker, R.J., J. Am. Chem. Soc. 1972, **94**, 8301.

88 Desmeales, P.J. and Allen, L.C., J. Chem. Phys. 1980, **72**, 4731.

89 Long, J.W. and Franklin, J.L., J. Am. Chem. Soc. 1974, **96**, 2320.

90 Hiraoka, K. and Kebarle, P., Can. J. Chem. 1977, **55**, 24.

91 Payzant, J.D.; Cunningham, A.J. and Kebarle, P., Can. J. Chem. 1973, **51**, 3242.

92 Grimsrud, E.P. and Kebarle, P., J. Am. Chem. Soc. 1973, **95**, 7939.

93 Meot-Ner, M., J. Am. Chem. Soc. 1984, **106**, 1257.

94 Meot-Ner, M. and Deakyne, C.A., J. Am. Chem. Soc. 1985, **107**, 474.

95 Yamdagni, R. and Kebarle, P., J. Am. Chem. Soc. 1973, **95**, 3504.

96 Meot-Ner, M. and Sieck, L.W., J. Am. Chem. Soc. 1983, **105**, 2956.

97 Larsen, J.W. and McMahon, T.B., J. Am. Chem. Soc. 1982, **104**, 6255.

98 McMahon, T.B. and Kebarle, P., J. Am. Chem. Soc. 1986, **108**, 6502.

99 Caldwell, G.; Magnera, T.F. and Kebarle, P., J. Am. Chem. Soc. 1984, **106**, 959.

100 Weinkam, R.J., Biomed. Mass Spectrom. 1978, **5**, 334.

101 Meot-Ner, M.; Hamlet, P.; Hunter, E.P. and Field, F.H., J. Am. Chem. Soc. 1980, **102**, 6393.

102 Lau, Y.K.; Saluja, P.P.S.; Kebarle, P. and Alder, R.W., J. Am. Chem. Soc. 1978, **100**, 7328.

103 Meot-Ner, M., J. Am. Chem. Doc. 1983, **105**, 4906.

104 Morton, T.H. and Beauchamp, J.L., J. Am. Chem. Soc. 1972, **94**, 3671.

105 Sharma, R.B.; Blades, A.T. and Kebarle, P., J. Am. Chem. Soc. 1984, **106**, 510.

106 Winkler, F.J. and Stahl, D., J. Am. Chem. Soc. 1973, **95**, 3685.

107 Meot-Ner, M., J. Am. Chem. Soc. 1984, **106**, 278.

108 Warshel, A., Acc. Chem. Res. 1982, **14**, 284.

109 Larsen, J.W. and McMahon, T.B., J. Am. Chem. Soc. 1982, **104**, 6255.

110 Frisch, M.J.; Del Bene, J.E.; Binkley, J.S. and Schaefer, H.F., J. Chem. Phys., 1986, **84**, 2279.

111 Hiraoka, K.; Takimoto, H. and Yamabe, S., J. Phys. Chem, 1986, **90**, 5910.

112 Skull, D.R.; Westrum, E.F. and Sinke, G.C., "The Chemical Thermodynamics of Organic Compounds", Wiley, New York, (1969).

113 Taft, R.W., Prog. Phy. Org. Chem. 1983, **14**, 248.

114 Brauman, J.I., Annu. Rev. Phys. Chem. 19[illegible]3, **34**, 178.

115 Adams, N.G. and Smith, D., Chem. Phys. Lett. 1981, **79**, 563.

115a Smith, D. and Adams, N.G., Astrophys. J. 1978, **L87**, 220.

116 Keating, J.T. and Skell, P.S., in "Carbonium Ions" Vol II, Olah, G. and Schleyer, P.v.R., Ed. Wiley-Interscience, New York, (1970).

117 Zollinger, H., "Azo and Diazo Chemistry" Interscience, New York, (1961).

118 Zollinger, H., Acc. Chem. Res. 1973, 6, 335.

119 Kirmze, W., Agew. Chem. Int. Ed. Engl. 1976, **15**, 251.

120 Olah, G.A., "Halonium Ions" Wiley, New York, (1975).

121 Ford, G.P. and Scribner, J.D., J. Am. Chem. Soc. 1983, **105**, 349.

122 Ragharachari, K.; Chandrasekhar, J. and Burnier, R.C., J. Am. Chem. Soc. 1984, **106**, 3124.

123 Vincent, M.A. and Radom, L., J. Am. Chem. Soc. 1978, **100**, 3306.

124 Holtz, D.; Beauchamp, J.L. and Woodgate, S.D., J. Am. Chem. Soc. 1970, **92**, 7484.

125 Hovey, J.K. and McMahon, T.B., J. Am. Chem. Soc. 1986, **108**, 1719.

126 Hovey, J.K. and McMahon, T.B., J. Chem. Phys. 1987, **91**, 4560.

127 Good, A.; Durden, D.A. and Kebarle, P., J. Chem. Phys. 1970, **52**, 212.

128 Blint, R.J.; McMahon, T.B. and Beauchamp, J.L., J. Am. Chem. Soc. 1974, **96**, 1269.

129 Beauchamp, J.L.; Holtz, D.; Woodgate, S.D. and Patt, S.L., J. Am. Chem. Soc. 1972, **94**, 2798.

130 Herod, A.A.; Harrison, A.G. and McAskill, N.A., Can. J. Chem. 1971, **49**, 2217.

131 Asubiojo, O.I. and Brauman, J.I., J. Am. Chem. Soc. 1979, **101**, 3715.

132 Pellerite, M.J. and Brauman, J.I., J. Am. Chem. Soc. 1980, **102**, 5993.

133 Magnoli, D.E. and Murdoch, J.R., J. Am. Chem. Soc. 1981, **103**, 7465.

134 Magnera, T.F.; Caldwell, G.; Sunner, J.; Ikuta, S. and Kebarle, P., J. Am. Chem. Soc. 1984, **106**, 6140

135 Foster, M.S.; Williamson, A.D. and Beauchamp, J.L., Int. J. Mass Spectrom. Ion Phys. 1974, **15**, 429.

136 Traeger, J.C. and McMoughlin, R.G., J. Am. Chem. Soc. 1981, **103**, 3647.

137 Demontis, P.; Ercoli, R.; Gamba, A.; Suffritti, G.B. and Simonetta, M.J., Chem. Soc. Perkin Trans. 2 1981, 488.

138 Benson, S.W., "Thermochemical Kinetics" Second Edition, John Wiley & Sons, New York, (1976).

139 Sen Sharma, D.K.; De Hojer, S.M. and Kebarle, P., J. Am. Chem. Soc. 1985, **107**, 3757.

140 McManus, S.P., J. Org. Chem. 1982, **47**, 3070.

141 Pedley, J.B.; Naylor, R.D. and Kirby, S.P., "Thermochemical Data of Organic Compounds" Second Edition, Chapman and Hall, London (1986).

142 Wagman, D.D. et al., Selected Values of Chemical and Thermodynamic Properties (Technical Note 270-3), National Bureau of Standards, (1968).

143 McMahon, T.B. and Kebarle, P., Can. J. Chem. 1985, **63**, 3160.

144 Szulejko, J.E.; Fisher, J.J. and McMahon, T.B., Int. J. Mass Spectrom. Ion Phys. 1988, **83**, 147.

145 Olah, G.A.; Surya Prakash, G.K. and Sommer, J., "Superacids", John Wiley & Sons, New York, (1985).

146 Gillespie, R.J.; Ridell, F.G. and Slim, D.R., J. Am. Chem. Soc. 1976, **98**, 8069.

147 Calves, J.Y. and Gillespie, R.J., J. Am. Chem. Soc. 1977, **99**, 1788.

148 Olah, G.A. and Donovan, D.J., J. Am. Chem. Soc. 1978, **100**, 5163.

149 Blanchette, M.C.; Holmes, J.L.; Hop, C.E.C.A.; Lossing, F.P.; Postma, R.; Ruttink, P.J.A. and Terlow, J.K., J. Am. Chem. Soc. 1986, **108**, 7589.

150 Fisher, J.J. and McMahon, T.B., J. Am. Chem. Soc. Submitted.

151 Amano, T., Chem. Phys. Lett. 1986, **127**, 101.

152 Amano, T., Chem. Phys. Lett. 1986, **130**, 154.

153 Field, F.H.; Head, M.H. and Franklin, J.L., J. Am. Chem. Soc. 1962, **84**, 1118.

154 Wyatt, J.R.; Stratten, L.W. and Hierl, P.M., J. Phys. Chem. 1976, **80**, 2911.

155 Frazier, L.J.; Christophorou, L.G.; Carter, J.G. and Schwindler, H.C., J. Chem. Phys. 1978, **69**, 3807.

156 Burrow, P.D.; Micheda, J.A. and Jordan, K.D., J. Am. Chem. Doc. 1976, **98**, 6392, 7181.

157 Jordan, K.D. and Burrow, P.D., Acc. Chem. Res. 1978, **11**, 341.

158 Jordan, K.D. and Burrow, P.D., J. Chem. Phys. 1979, **71**, 5384.

159 Symons, M.C.R.; Selby, R.C.; Smith, I.G. and Bratt, S.W., Chem. Phys. Lett. 1977, **48**, 100.

160 Yim, M.B. and Wood, D.E., J. Am. Chem. Soc. 1976, **98**, 2053.

161 Millefiori, S.; Millefiori, A. and Granozzi, G., J. Molecular Structure 1982, **89**, 247.

162 Schegoleva, L.N.; Bilkis, I.I. and Schastnev, P.V., Chem. Phys. 1983, **82**, 343.

163 Page, F.M. and Goode, G.C. "Negative Ions and the Magnetron", Wiley, New York, (1969).

164 Lifshitz, C.; Tiernan, T.O. and Hughes, B.M., J. Chem. Phys. 1973, **59**, 3182.

165 Grimsrud, E.P.; Chowdhury, S. and Kebarle, P., J. Chem. Phys., 1985, **83**, 3983.

166 Grimsrud, E.P.; Caldwell, G.; Chowdhury, S. and Kebarle, P., J. Am. Chem. Soc. 1985, **107**, 4627.

167 Chowdhury, S.; Heinis, T.; Grimsrud, E.P. and Kebarle, P., J. Chem. Phys. 1986, **90**, 2747.

168 Chowdhury, S.; Grimsrud, E.P.; Heinis, T. and Kebarle, P., J. Am. Chem. Soc. 1986, **108**, 3630.